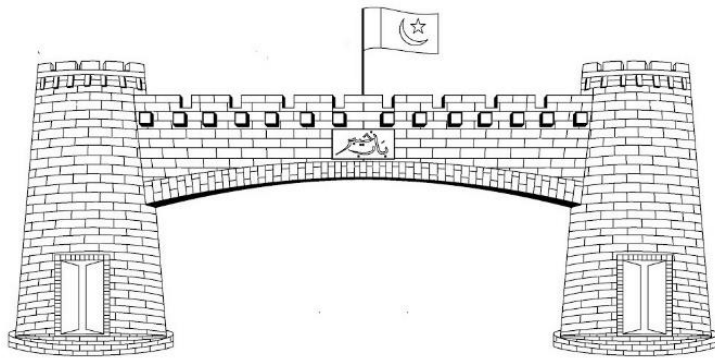


3rd Pak-Turk International Conference Proceedings (Local)



Organized by

**Ghulam Ishaq Khan Institute of Engineering
Sciences & Technology, Topi (GIKI)**



An Overview of Stability and Performance Analysis of Hybrid Vertical Take-off and Landing Unmanned Aerial Vehicle

Anas Manzoor Khan, Aamer Shahzad, Taimur Ali Shams
Department of Aerospace Engineering, College of Aeronautical Engineering
National University of Sciences and Technology, Pakistan
hazardchelsea933@gmail.com

Abstract—Hybrid vertical takeoff and landing unmanned air vehicles are nowadays under consideration because of their longer range, take-off and landing ability at any desired point and cruise capabilities. In this paper, different types of such vehicles and their configurations are explained. The flight regime of these vehicles is divided into three categories, that is, vertical take-off, transition and cruise flight. In addition, aerodynamic analysis of different hybrid vertical takeoff and landing unmanned aerial vehicles including tilt-wing, the tilt-rotor unmanned air vehicles and a separate lift and thrust unmanned air vehicles (having rotors at the mid-span of the wing) have been explained. In

most of the cases, essential aerodynamic characteristics are obtained from the six-degree freedom of equations derived from Newton's second law of motion and computational fluid dynamics. Since the two main parameters in hover mode are thrust co-efficient and the inflow ratio. Therefore equations for the calculation of these parameters are given in the paper. This paper also gives an overall brief of the methods used for the calculation of stability and performance parameters in both the hover and forward flight mode.

Keywords - Vertical take-off and landing; unmanned aerial vehicle; tilt-wing; tilt-rotor; blended wing; transition flight

I. INTRODUCTION

For the past several years, there is a great development in the field of Unmanned Aerial Vehicles (UAVs). Recently, UAVs have been used both for civil and military purposes such as

reconnaissance, surveillance, and security reinforcement. Basically, UAVs are of two types these are fixed-wing and rotorcraft UAVs. Fixed-wing UAVs are more suitable for high cruise speed,

Nomenclature

UAV	Unmanned aerial vehicle	C_m	Coefficient of moment
SLT	Separate lift and thrust	V_T	Flight speed (m/sec)
QTW	Quad tilt wing	T_{coax}	Coaxial fan thrust (N)
CFD	Computational fluid dynamics	i_T	Tilt angle (deg)
VTOL	Vertical take-off and landing	α	Angle of Attack (deg°)
C_D	Coefficient of drag	RPM	Revolution per minute
C_L	Coefficient of lift		

effective range, and endurance but actually needs runways for controlled take-off and landing. On the other hand the rotorcraft UAVs have a shorter range and endurance hence they are not suited for long range missions but are effective for short take-off and landing. Hybrid UAVs have the advantages of both fixed-wing and rotorcraft UAVs (i.e., vertical take-off, transition, and cruise) and they are, therefore, effective for longer range and endurance.

II. TYPES OF HYBRID VTOL UAVs

As mentioned in [1], there are basically two types of Hybrid UAVs these are convertiplane and tail-sitter. A convertiplane UAVs generally has transition mechanisms for transferring from vertical mode to cruise mode and from cruise mode to vertical mode for landing. While tail-sitter UAVs takes off and lands vertically on its tail, and the whole of the airframe is tilted in order to complete cruise flight.

A. *Convertdiplane*

Main types of these UAVs are: (a) tilt-rotor UAVs, (b) tilt-wing UAVs and c) Dual systems

a) *Tilt-Rotor*

In tilt-rotor UAVs there are a different numbers of rotors that are installed on tilting shafts. For a transition from hover to cruise flight, rotors actually get tilted in a horizontal until the cruise flight is achieved. Furthermore, these tilt-rotor UAVs are subdivided into three categories: a) bi-rotor, b) tri-rotor, and c) quad-rotor.

As mentioned by the name, bi-rotor convertiplane UAVs generally have two tilting rotors which help in thrust in the vertical direction and for providing sufficient lift during a cruise and several control surfaces for different kind of motions (yaw, pitch, and roll). An example is the Bell Eagle Eye UAV [2] having rotors mounted on the wingtips.

In tri-rotor convertiplane UAVs there are three rotors mounted at different places and are upward in direction. For the transition one or multiple rotors get tilted to providing thrust in the vertical direction and in cruise mode, it works similarly as the bi-rotors (i.e., lift is provided by the rotor and control surfaces are used for roll, pitch and yaw motions). Examples are TURAC and FireFLY6. Both are the type of tri-rotor convertiplane UAVs but the difference comes in flight mode i.e. hover mode where TURAC [3] uses a co-axial rear rotor while FireFLY6 [1] uses the Y-6 (i.e., three co-axial rotors) configuration.

b) *Tilt-Wing*

In tilt-wing convertiplane UAVs, complete or partial wing along with the rotors are tilted together during hover to cruise transition. For different flight regimes the wings are actually in the upward direction, which actually makes it susceptible to crosswind and thus greater work is required for developing a controlling procedure for attitude stability. There are two main types of tilt-wing convertiplane UAVs: single-wing configuration and tandem-wing configuration.

In the single-wing configuration, the commonly used UAVs are Harvee, AVIGLE, GLVTOL Drone and AT-10 Responder. In Harvee [4], there are two fixed-pitch motors which are placed below the wings of UAV. While for a transition from hover to cruise tilting of the whole wing is required. In hover-mode, the thrust for Harvee is provided in a similar manner as in a bi-rotor convertiplane UAV. In AT-10 Responder [7] there are two parts of the wing. Only the inner part with the rotors placed on the leading edge of the UAV can tilt. Whereas in AVIGLE [5, 16] in hover mode the thrust is actually provided by tilted propeller engines along with the deflected flaps. On the other hand, in GL VTOL Drone [6] for thrust in vertical direction and control mechanism, there are ten fixed-pitch rotors (out of which eight are located on the wings and the rest two are placed on horizontal stabilizers).

c) *Dual-System*

In this type of convertiplane UAVs [1] there are two sets of propulsion systems: one set of rotors for vertical take-off and landing while another set has tractor or pusher configuration for cruise flight. No tilting mechanism is needed for these UAVs. Whereas in cruise flight there is actually extra drag force on the UAV due to the non-usage of these fixed rotors in the cruise flight, results in putting more load on tractor or pusher propeller. The most commonly used types are multi-rotor with tractor configuration and multi-rotor with a pusher configuration. Tractor configuration is the one in which the propeller is placed in front of the wing. The flight of this configuration involves vertical take-off using quad-copter while the horizontal thrust motor remains powered off. The transition mode involves the turning off of quad-copter and starting of horizontal thrust motor simultaneously. Once the aircraft has attained horizontal velocity equal to stall velocity the quad-copter motors are turned off.

B. *Tail-Sitter*

In this type of the hybrid UAV tail is the major contributor for vertical take-off and landing and the entire airframe is actually tilted to achieve cruise flight. The flight can be summarized as follow:

At the start, power is supplied by the motors and the UAV rise vertically in the air at an appreciable height where it is slowly tilted through manipulation of the elevator devices and then proceeds further like a fixed-wing aircraft, the sustaining force of the propeller being replaced by the vertical reaction. During landing, the forward speed of the aircraft is reduced and the props are vertically tilted again, causing the UAV to act as a helicopter with the propeller supporting the complete load of the aircraft.

III. AERODYNAMIC ANALYSIS

Over the past ten to twenty years, the category of UAVs which has been under consideration for the stability and performance analysis are the tilt rotor and the tilt-wing UAVs in which the tilt angle of the rotors and the wings starts to decrease during transition and finally both the wings and rotors are in horizontal position during the cruise. The flight regime of the UAV is divided into a hover, transition and cruise flight [12].

Hover mode: For hover flight there are two factors that are under consideration: thrust and drag.

Transition mode: In transition phase, the important parameter is the changing speed of the propellers for transition and the use of control surfaces is thought to be secondary.

Forward flight mode: In this mode i.e. the airplane mode UAV has gained the required velocity (which is above the stall speed) so that it can generate enough aerodynamic forces to provide sufficient lift and is able to control the flight.

In another research done by Daud Filho et al.[9], multi-body equations of motion for Semi-tandem wing VTOL UAV are developed which are used to compute the trim curves (tilt angle vs flight speed, elevator angle vs velocity and angle of attack vs velocity) for the transition phase from hovering to cruise condition. These curves help us to determine tilt angles of the wing and the horizontal tail during hovering and cruise.

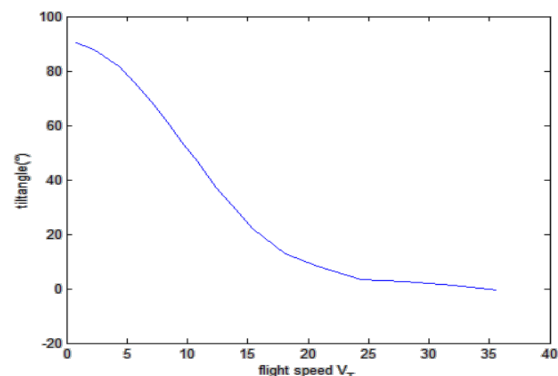


Fig. 1. Wing and horizontal tail tilt angles vs flight speed [9]

For mathematical modeling of the TURAC, the 3-D Computational fluid dynamics data [12] for forward flight at a different angle of attacks which includes the stall effect as well is obtained. Then at different forward velocities, same aerodynamic coefficients are used for calculations of transition phase.

In another research [12], aerodynamic analysis of tilt-rotor UAV i.e. TR-E2S1 was done by deflecting the control surfaces and by varying the angle of attack and sideslip angle the aerodynamic stabilities were analyzed then comparing these results with the wind tunnel testing results. The figure 2 [12] below tells us that as the elevator deflection angle increases lift increases linearly.

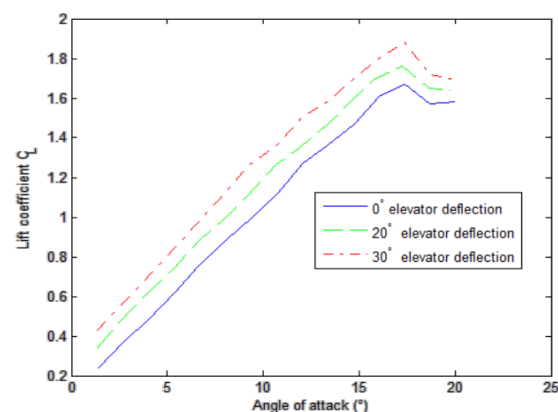


Fig. 2. Variaton of lift coefficient with control surface deflections [12]

In another research paper by Tomasz Kudala et al.[13] the Hybrid VTOL UAV is of the tilt rotors mechanism (only rear motors are tilted). In the transition phase the motors on the rear wing are gradually tilted into horizontal position (from vertical position in vertical take-off) for increasing forward speed whereas the front rotors are slowly turned off because they only disturb the airflow (in standard flight mode), without sufficiently increasing the lift that is produced on the wing. During cruise UAV acts like a simple conventional aircraft with control surfaces which are aileron,

elevator, and rudder for providing roll, pitch and yaw motions.

In another research done by Dewi et al. [14], a HYBRID UAV i.e. separate Lift and Thrust (SLT) UAV was first designed. This kind of UAV has five motors with two different functions. In separate lift and thrust model of hybrid UAV, there is no tilting rotor during the transition phase. One motor produces horizontal thrust like a normal fixed-wing to generate lift for forward flight. The other motors produce vertical thrust like a multi-rotor. Since it produces two kinds of thrusts with different direction (horizontal and vertical thrust), there will be overlapped thrust during the transition, when switching flight modes.

Then its 3D model was designed and imported as .stp file to other software, such as ANSYS to analyze airflow over the airframe.

Then Performance and stability analysis was carried out using XFLR-5. Both figure 3 and figure 4 describe static longitudinal stability. Graph of C_m versus α shows that this hybrid UAV is statically stable in longitudinal direction because the slope of the curve is negative. The more negative the slope is, the more stable the aircraft. Graph of C_m versus C_L shows us that at zero pitching moment, the lift is slightly positive.

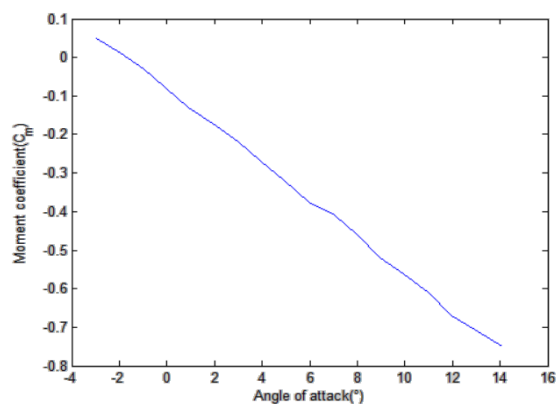


Fig. 3 C_m vs α curve [14]

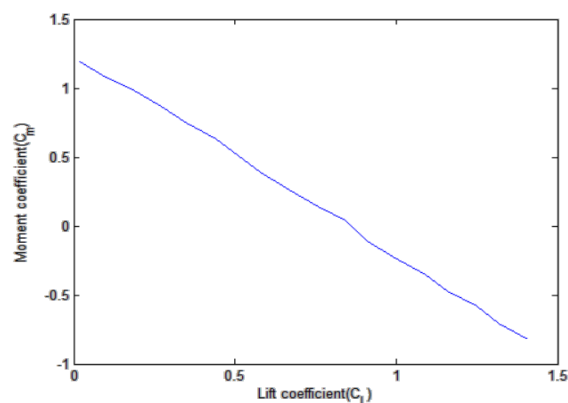


Fig. 4 C_m vs C_L curve [14]

Numerical simulations [14] are performed to analyze airflow around this hybrid UAV and to understand the effect of integrating multi-rotor equipment to the fixed-wing UAV. The basic information provided by CFD is the difference of forces (side force, lift, and drag) of UAV with propeller and without propeller. Therefore, there are two main cases which are analyzed and these are:

1. Case 1: airframe without propeller
2. Case 2: airframe with a propeller

Table 2 [14] tells that in both the cases side forces are not the same because of the different direction of the propellers and may be caused by asymmetric element built by unstructured meshing method. As far lift is concerned it is greater in case 1, but the drag on case 2 is much higher than case 1. One of the solutions for reducing the drag by propellers for hovering is by using folded propellers.

In another research done by J. Holsten et al. [16], tilt-wing UAV was designed and lift, drag and moment coefficients were measured using wind tunnel. The resulting values were then compared with the computed values of the softwares i.e., XFLR5 and Digital DATCOM. Because of the constraints in the softwares fuselage is assumed to be considered as a cylinder. Different parts of the UAVs which are engine pod, spinner and landing gear are neglected for computation. Landing gear increases the drag but does not increase lift. The spinner and engine pod disturb the air flow over the wing area. This tends to increase the drag and decreases the lift as compared to the computational results. The rise in the drag is mostly due to the landing gear and the engine pod (not because of the fuselage).

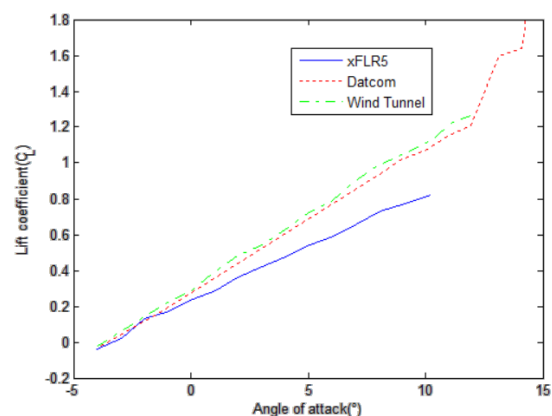


Fig. 5 Comparison of lift coefficients of the wind tunnel with computed data [16]

Also, change in elevator deflection with respect to the pitching moment coefficient and the effects of flaps on the lift coefficient were plotted. The results

of flaps deflection are in accordance with the DATCOM computational data. The trend of the computational data is not identical because of the tail-plane airfoil which is a symmetrical and, hence, the deflections should differ in their effect as seen from measurements.

Also, the measurements are done for different values of thrust in order to cater for greater overlap of propeller area and wing. For cruise flight, in order to ensure reproducibility, three different thrust levels were set and all the measurements were repeated once.

In another Research done by Muraoka et al. on QTW UAV [7], in which important aerodynamic parameters are measured from wind tunnel data. And lift coefficient was measured and its comparison with the tilt-angle of the front wing was measured. These lift coefficients include lift generated by both the wing and propeller thrust.

In another research done by Hong et al.[15], longitudinal flight characteristics of the single tilt-wing UAV are calculated. The methodology used is first aerodynamics forces and moments plus propulsive forces acting on the UAV are calculated by equations given in [16] which includes the forces and moments for the wetted area due to the slipstream, unwetted area, and free stream area. When the wing is tilted, then aerodynamic forces and moments are produced because of the wetted area in the slipstream and are effected by the change in induced velocity and not by change in the tilt angle.

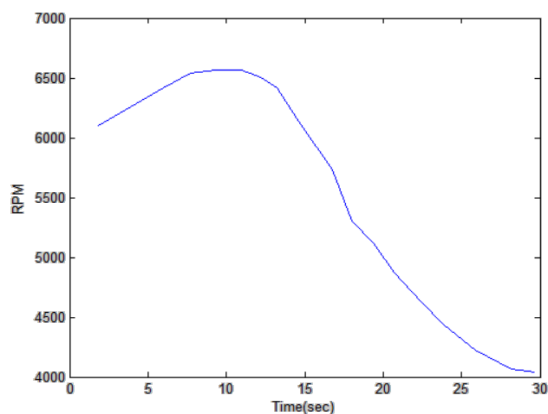


Fig.6 Longitudinal trim condition (RPM vs time) [15]

In another research done by Ozdemir et al. [17], aerodynamic analyses of the TURAC was carried out by using Vortex Lattice method in which first all the parameters were separately defined in the software and the geometry was created. Then each component was further separated into number of panels and the aerodynamic parameters i.e. lift coefficient, drag coefficient and induce drag coefficient were calculated across different angle of attack. Then CFD analysis was done for different

angle of attack and for open and close fan concept of the TURAC. Now in open fan design lift actually decreases but drag coefficient increases because of vortices that are present in the open fan design as compared to the close fan design.

Similarly momentum theory and blade element theory is used to calculate the performance in hover and vertical climb but they are not suitable because they have lot of assumptions like inflow is uniform, flow is incompressible as mentioned in [18]. Hence blade element momentum theory which is a hybrid of both momentum and blade element theory is used to compute the different performance parameters like coefficient of thrust, induce power and inflow ratio. Just like rotor power coefficient in hover flight can be calculated by using the following equation:

$$C_p = \frac{KC_w^{1.5}}{2} \frac{1}{2} + \frac{\sigma C_{do}}{8}$$

Where C_w is the weight coefficient, K is the induced power factor of the rotor, C_{do} is the parasite drag and σ is the solidity ratio. Similarly coefficient of thrust for optimum rotor can be calculated by using the equation given below:

$$C_T = \frac{N_b c_t C_l}{4 * p * R}$$

Where N_b is the number of blades, c_t is the tip chord which has different value for different rotors and C_l is the lift coefficient. Since blade element theory accounts for the losses of non-uniform inflow therefore its equation for the inflow in hover mode is:

$$\lambda = \sqrt{\left(\frac{\sigma C_{l\alpha}}{16}\right)^2 + \frac{\sigma C_{l\alpha} \Theta r}{8R} - \frac{\sigma C_{l\alpha}}{8}}$$

IV. CONCLUSION

The work done on the aerodynamic analysis of different type of UAVs suggest that methodology used for the calculation of aerodynamic parameters is the same i.e. six degrees of freedom equation are used to calculate the aerodynamic parameters (lift coefficient, drag coefficient and moment coefficient) for different flight regimes and the graphs are plotted to show that these UAVs are stable in those flight regime but the difference is the configuration of UAVs which have gone under consideration over the past years. Mostly tilt-rotor UAVs and tilt-wing UAVs are being investigated extensively. The tilt-wing UAVs have some advantages as compared to tilt-rotor UAVs because tilting of wing along with the rotor results in an increase in aerodynamic flow over wing which actually goes and help in transition flight regime plus reducing the loss of lift due to downward slipstream in hover. Similarly, tilt-rotor UAVs are

preferred over separate lift and thrust (SLT) UAVs because SLT UAVs produces more drag because of their rotors which are only helping in vertical take-off as compared to tilt-rotor UAVs in which these motors get tilted during the transition(helps in vertical take-off) and also then helps in the cruise flight.

V. REFERENCES

- [1] Saeed, A.S., Younes, A.B., Cai, C. and Cai, G. (2018). A survey of hybrid Unmanned Aerial Vehicles. *Progress in Aerospace Sciences*, 98, pp.91–105
- [2] UgurOzdemir, YasinDereli, Aktas, YucelOrkut,AslihanVuruskan, BurakYukse, Ahmed Farabi Tarhan, Aykut Cetin "A low-cost prototyping approach for design analysis and flight testing of the turac VTOL UAV." *Int. Conference on Unmanned Aircraft Systems (ICUAS)*, pp. 1029-1039, 2014.
- [3] ValanaL. Wells,Jeffrey J, Dickeson, David Miles, OguzhanCifdaloz,and Armando A. Rodriguez. "Robust lpv h gain-scheduled hover-to-cruise conversion for a tilt-wing rotorcraft in the presence of CG variations." *American Control Conference*, pp. 5266-5271, 2007.
- [4] Holsten, J., Ostermann, T. and Moormann, D. (2011). Design and wind tunnel tests of a tilt-wing UAV. *CEAS Aeronautical Journal*, 2(1–4), pp.69–79.
- [5] Ten-engine electric plane completes successful flight test, [Online], [cited 5 December 2017] (2015).
URL <https://www.nasa.gov/langley/ten-engine-electric-plane-completes-successful-flight-test>
- [6] M. Streetly, IHS Jane's all the world aircraft: Unmanned 2013-2014, IHS,2013.
- [7] Muraoka, Koji,Daisuke Kubo, and Noriaki Okada. "Quad tilt-wing VTOL UAV: Aerodynamic characteristics and prototype flight." *AIAAAerosp. Conference*, pp. 1834, 2009.
- [8] B. Coxworth."Quadshot RC aircraft combines quadcopter hovering with airplane flight", 2017.
URL <http://www.gizmag.com/quadshot-hovers-andflies/19449/>
- [9] DaudFilho, Antonio Carlos, and Eduardo Morgado Belo. "Flight Dynamics Modeling and Trim Curves of a conceptual Semi-Tandem Wing VTOL UAV."
- [10] R.C Nelson. "Flight Stability and Automatic Control." 2nd ed., Singapore, McGraw-Hill, ch.3-5, 1998.
- [11] Burak, Yuksek, UgurOzdemir, AslihanVuruskan M. A. Yukselen, and GökhanInalhan. "Transition flight modeling of a fixed-wing VTOL UAV." *J. Intelligent & Robotic Systems* 84, no. 1-4, pp. 83-105,2016.
- [12] Kim, C. and Chung, J. (2006). Aerodynamic analysis of tilt-rotor Unmanned Aerial Vehicle with computational fluid dynamics. *Journal of Mechanical Science and Technology*, 20(4), pp.561–568.
- [13] Czyba, R., Lemanowicz, M., Gorol, Z. and Kudala, T. (2018). Construction Prototyping, Flight Dynamics Modeling, and Aerodynamic Analysis of Hybrid VTOL Unmanned Aircraft. *Journal of Advanced Transportation*, 2018, pp.1–15.
- [14] Dewi, P.T., Hadi, G.S., Kusnaedi, M.R., Budiarto, A. and Budiyo, A. (2016). Design of Separate Lift and Thrust Hybrid UAV. *The Journal of Instrumentation, Automation and Systems*, 2(2), pp.45–51
- [15] Hong, S., Jeong, J., Kim, S., Suk, J. and Jung, J.I. (2013). Longitudinal Flight Dynamics of a Single Tilt-wing Unmanned Aerial Vehicle. *IFAC Proceedings Volumes*, 46(19), pp.60–65.
- [16] Holsten, J. and Moormann, D. (2014). Flight control law design criteria for the transition phase for a tiltwing aircraft using multi-objective parameter synthesis. *CEAS Aeronautical Journal*, 6(1), pp.17–30.
- [17] Ozdemir, Ugur, Yucel Orkut Aktas, AslihanVuruskan, YasinDereli, Ahmed FarabiTarhan, KaracaDemirbag, Ahmet Erdem, GanimeDuyguKalaycioglu, Ibrahim Ozkol, and GokhanInalhan. "Design of a commercial hybrid VTOL UAV system." *Journal of Intelligent & Robotic Systems* 74, no. 1-2 (2014): 371-393.
- [18] J.G Leishman. "Principles of Helicopter Aerodynamics." 2nd ed., Cambridge University press, 200

Critical Study on Design of High-Speed Weapon Capable Drone and Advancements in Drone Technology

Hammam Bin Shahab, Nadeem Hussain Shah, Muhammad Jameel
*Aerospace Engineering Department, College of Aeronautical Engineering
National University of Science & Technology, Pakistan*

hammasbinshahab@gmail.com
Nadeemhussain@cae.nust.edu.pk
mjkhurshid01@gmail.com

Abstract— In the last couple of decades, drone technology has advanced a lot and has become a branch of keen interest for students and research organizations. With these advancements, several new profiles and platforms for drones have been developed ranging from the military application to surveillance, reconnaissance, and agricultural purposes. This paper is an effort to study the multiple drone platforms available with a detailed study on quad-copter or quad-rotor. Quad-rotors are being frequently used by various researchers as this platform has a better tendency of performing tasks because of efficient and stable design configuration. The current utilization of this platform and its potential for Killer Drones is also discussed. The paper also covers multiple concepts approaches for damping or restricting motion due to the impact of fire from weapon mounted on a drone. The paper includes a feasibility study of these initially selected concepts i.e. varying propeller RPM of quad-copter for balancing the impact of weapon, use of damping mechanical structure & damping Fluid to reduce the impact and use of 3-D gimbals to constraint motion and stabilize Drone. The paper investigates the feasibility of all available platforms and mentioned approaches to predict the most appropriate combination for High-Speed Weapon Capable Killer Drone

Keywords – Platform, quad-copter, gimbals, feedback control, navigation, damping fluid

I. INTRODUCTION

In the past few years, an increasing interest is being invested in the development of small Unmanned Aerial Vehicles (UAVs). They are being employed by the civil sector for search and rescue during a disaster, geological surveying and mapping, agriculture and law enforcement. While the defense and military are utilizing UAVs for reconnaissance, intelligence data gathering as well as aerial targeting. Their main advantage is that they can be remotely piloted from any location, meaning the pilot is always safe. It also means that UAVs allow us to explore uncharted territories and perform missions that were humanly not possible.

II. LITERATURE REVIEW FOR PLATFORM

Based on the physical design and configuration, UAVs are classified into 3 major categories:

- Fixed-wing Aircraft
- Multi-Rotor Aircraft
- VTOL Hybrid Aircraft

The most commonly known platform is the fixed-wing aircraft. They are the simplest of all and have advantages of long endurance and range. However, they require runways to take-off and land. Some may be hand or catapult-launched and recovered in the net trap or land via parachute. This limits their operation in congested areas and requires an open field for take-off and landing. Rotary wing UAVs on the other hand, can vertically take-off and land almost anywhere.

III. FIXED-WING AIRCRAFT

Fixed-wing aircraft are conventional aircraft:



Figure 1 – Conventional Fixed Wing RC Aircraft

Table 1 – Classification of Flying Vehicle

UAV								
Heavier-than-air							Lighter-than-air	
Wing type			Rotor type				Blimp	Balloon
Fixed-wing	Flying-wing	Flapping-wing	Helicopter	Quadcopter	Hexacopter	Octocopter		

These aircraft have multiple advantages and disadvantages as discussed below:

ADVANTAGES

- Fixed-wing aircraft have longer endurance
- Fixed-wing aircraft can attain higher speeds
- They have a longer range

DISADVANTAGES

- Fixed-wing aircraft cannot hover
- Cannot work well space constraint environment

IV. MULTIROTOR AND ITS TYPES

Multirotor is the RC aircraft that provide thrust in the vertical direction and are capable of vertical take-offs and landings.



Figure 2 – Quadcopter Drone [2]

These aircraft have multiple advantages and disadvantages as discussed below:

ADVANTAGES

- It may Take-off/Land from any surface
- They can hover at a single point
- No landing approach is required

- They can provide security and surveillance in a time and space constraint environment

DISADVANTAGES

- Multi-rotors have short endurance

V. QUAD COPTERS

Quadcopters are primarily used to incorporate VTOL (Vertical Take-off and Landing) capabilities in fixed-wing RC aircraft. Quadcopters are inherently unstable and rely on four propellers for their control and maneuverability. Quadcopters are further divided into two categories:

- Fixed rotors
- Tilt rotors

A comparison between them can be made as:

- Fixed rotors are VTOL efficient
- Tilt rotors can have higher speeds.
- Tilt rotors have longer endurance time
- Tilt rotors can provide efficient in air braking

VI. VTOL FEATURE IN FIXED WING

Either tilt rotors configuration or fixed rotors configurations can be used to incorporate the VTOL mechanism in fixed-wing RC aircraft. Configurations which involve the use of tilt rotors in a fixed-wing to make them VTOL capable areas follow:

1. Quad Tilt wing
2. Bi-Tilt rotors
3. Quadcopter with all tilt rotors
4. Quadcopter with inverse tilt rotors

Fixed-wing RC aircrafts involving fixed rotors are

1. Multi-rotor with tractor configuration
2. Multi-rotor with pusher configuration
3. Tail setter configuration

Each of the tilt-rotor configurations is briefly explained below:

VII. QUAD TILT WING

In quad tilting wings configuration propellers are mounted at the mid-span of the wings capable of tilting. This configuration can provide all six-degree of freedom. The study involves the tandem wing configuration, which includes two wings. The forward wing, which is

comparatively larger than the aft wing also called the rear wing.



Figure 3 - Quad Tilt Wing Configuration for VTOL [3]

The most critical part of the flight is the transition. As the wings must be first tilt to a smaller angle so that the aircraft first attain the stall speed i.e. the minimum speed required to prevent the aircraft from stalling. Once the stall speed is attained, the wings can transit completely preventing the aircraft from stalling.

VIII. BI-TILT WING FOR VTOL

A simple bi-tilt rotor configuration involves the use of two tiltable rotors placed at the mid-way of the wing. This configuration is practically being applied in Boeing's V22 Osprey as shown below



Figure 4 - Boeing V-22 Osprey [4]

Two motors are in the vertical position providing thrust for the vertical take-off. During the transition mode, the motors change their orientation from vertical mode and once the stall speed is attained the motors are oriented in the

horizontal position providing thrust for the forward flight. Similarly, for the vertical landing, the motors change their orientation and provide thrust for the vertical land.

IX. QUAD ROTOR WITH ALL TILT ROTORS

These configurations involve the integration of tiltable quadrotors on a fixed-wing aircraft. The quad configuration provides a better VTOL efficiency and stable hovering as compared to the Bi-rotors configuration.

One important consideration while designing these VTOL multi-rotors is the clearance of the propellers and their direction of rotation concerning one another.

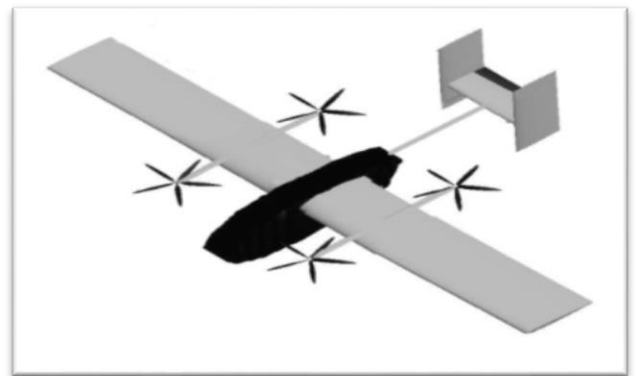


Figure 5 - Quad tilt rotor Configuration [5]

X. INVERSE TILT ROTOR

Quadcopters with inverse tilt rotors are essentially the same as simple quadcopters with tilt rotors except that in this configuration front motors are oriented in the upward direction while the rear motors are oriented in the downward direction.

As described above that fixed rotor configurations can also be used for designing vertical take-off and land RC aerial vehicles. A fixed-wing, fixed rotor RC aerial vehicle is equipped with quad-copter motors that are used for vertical take-off, landing, and a separate horizontal thrust motor for horizontal flight modes. A brief description of each configuration that can be involving the use of fixed rotors is explained below. These configurations differ based on the design of their forward flight while the mechanism for vertical take-off and landing remains the same.

XI. MULTIROTOR TRACTOR CONFIGURATION

Tractor configuration is the one in which the propeller is placed in front of the wing as shown. The characteristics of this configuration are:

- Tractor configuration has a better balancing
- Center of gravity ahead of the center of pressure.
- It is easy to fabricate
- It provides easier cooling of the motor
- Centre-line thrust is maintained



Figure 9: Tractor configuration [14]

The flight of this configuration involves vertical take-off using quadcopter while the horizontal thrust motor remains powered off. The transition mode involves the turning off of the quad-copter and the starting of the horizontal thrust motor simultaneously. Once the aircraft has attained horizontal velocity equal to stall velocity the quad-copter motors are turned off. During landing, the same process happens but in the opposite sequence. The horizontal thrust motor is turned off and the quad-copter is turned on simultaneously providing thrust in the vertical direction.

XII. TAIL SITTER

Tail sitter RC aircraft are the ones that take-off and land on their tail. This concept was first presented by Nicholas Tesla. This configuration is usually used in flying wing vertical take-off and land RC aerial vehicles.

Two motors are used along with three fins, two of them act as wings and one is used as vertical stabilizers.



Figure 6 - Tail Sitter Configuration [6]

These aircraft falls in the category of bi-quad fixed rotors RC UAVs. This configuration seems attractive, primarily because it can carry a greater payload with a relatively small expenditure of energy.

XIII. DISCUSSION ON PLATFORM

Based on the study [1, 22] different platforms were considered for the design and development of high-speed weapon capable killer drone. Keeping into consideration our design needs and requirements Multi-rotor in general and quad-copter, in particular, comes out to be the optimum solution for a reasonable compromise between speed, endurance, and design simplicity.

Table 2 - Overview of available platform

ATTRIBUTES	FIXED WING AIRCRAFTS	MULTI-ROTORS	HELI-COPTERS	VTOL PLANES
ENDURANCE	BEST	20-25 min	30-60 MIN	LESS
AREA COVERAGE	LARGE	MODERATE	MODERATE	LESS
HOVER	NO	YES	YES	YES
SIZE	LARGE	VARIABLE	SMALL	MODERATE
VTOL	NO	YES	YES	YES
SPEED	VARIABLE	50-60 KM/HR	70-100 KM/HR	LESS
STRUCTURE	SIMPLE	SIMPLE	COMPLEX	COMPLEX

XIV. WORKING OF MULTIROTOR

All Multi-rotor primarily work on the fundamental law of angular momentum conservation. To maintain the angular momentum the adjacent quadcopter motors rotate in opposite direction. To fly in steady-state hover case the thrust of all the motors should be equal to the weight of the flying vehicle, whereas in case of a climb and accelerated horizontal or vertical motion the thrust must be unevenly distributed with lesser thrust from motors in the direction of motion. Additional thrust for these segments is required, so therefore statistically the motor chosen should have the capability to provide twice the thrust than weight at 50% throttle for best efficiency [7]. The motions are controlled by varying throttle which reduces RPM of motors by controlling their current.

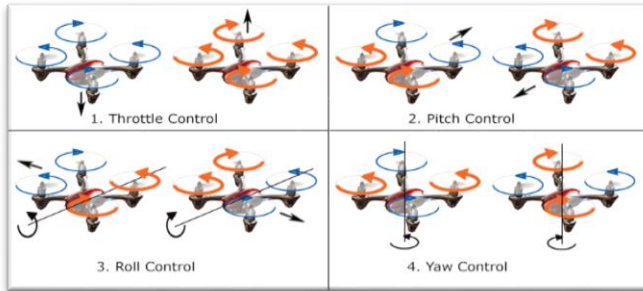


Figure 7 - Direction of Motors for Basic Motions [7]

Another important factor in determining efficiency is the ground effect. It is observed that when the multi-rotor is operating at the height of approximately $\frac{1}{2}$ of rotors

the diameter then the rotor tip vortices are avoided thus less thrust is required to overcome the drag due to them. In return, the efficiency and consequently multi-rotors efficiency is increased.

The roll, yaw and pitch motion of quadrotor changes with variation in RPM of motors. For motion along the roll axis, the throttle of rotors on one specific side is increased and the other side is decreased. Similarly, for motion along the pitch axis, the throttle of front or back motors is varied and for yaw, in the counter-clockwise direction, the counter-clockwise rotating rotor throttles are increased.

Quadcopter generally has two prominent configurations. 'X' configuration and '+' configuration. Both configurations have their own merits and demerits. Generally 'X' configuration comes out to be more stable whereas '+' Configuration is less stable and has more maneuverability.

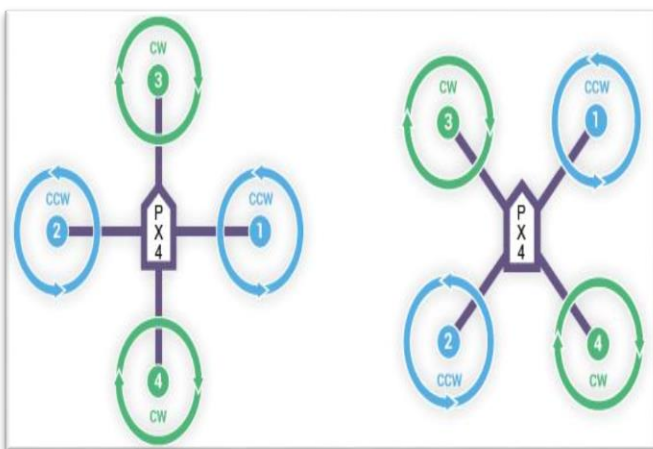


Figure 8 - 'X' and '+' Configuration [25]

XV. LITERATURE REVIEW FOR STABILIZATION

A weapon capable killer drone has to carry a firing weapon. This opens a complex domain of engineering issues because of the stabilization needed to balance the platform in response to the recoil of the weapon. In this regard, a lack of research on this specific aspect is a hindrance. The current problem of weapon capable drone is therefore simplified for a survey of the design of stabilization systems for quadcopter. The available stabilization methods widely used are:

- Gimbals
- Controls Systems
- Vibration Absorber

XVI. CONTROL SYSTEMS FOR STABILIZATION

With advancements in drone technology, the flight control systems and algorithms for stable drone flight have also increased. Control systems governed by basic PID [9, 10, 11, 14] to more complex systems [12, 13] have been developed and have proved to be significant.

General Methodology followed for the design of a control system is the estimation of the air vehicles' dynamic model. This dynamic model is a set of mathematical equations that consists of all aerodynamic flight affecting factors and factors acting on the quad-rotor in case of any disturbance. Research has been carried out for comparing different control techniques [15, 16, 17] but due to the underactuated nature of drones, it came out to be a complex dynamic model with various challenges.

Quadcopters carry an Inertial Measurement Unit (IMU) and microcontroller for simulating the control algorithm. IMU sensor identifies the orientation which is then interpreted by the control algorithm. In reply to any disturbance, the microprocessor from the control algorithm will send a rectifying signal to counter the disturbance and stabilize the platform. Research has been conducted in this regard but most of the effort is done lightweight drones [18], with settling time of almost 10 seconds. A major difficulty faced in designing a control system is to compensate for the response of nature. For this wind, parameters are required.

Some prominent Control board systems available are:

- Multi-Rotor Control Board (Atmega328 PA)
- Pixhawk – 4
- Arduino – Pilot Board (ATMega328)

MULTI-ROTOR CONTROL BOARD (ATMEGA328 PA)

Atmega328 PA – works on the same mentioned principle to stabilize the aircraft. The board has three gyroscopes available, which provide data to control board in case of disturbance for stabilizing the platform. The control board is programmable and may be modified by our dynamic model

Specifications:

- Dimensions: 50.5mm x 23.5mm
- Weight: 14.5 gram
- IC: Atmega328 PA
- Gyro: Murata Piezo
- Input Voltage: 3.3-5.5V
- Signal via Receiver: 1520 us
- Signal to ESC: 1520 us

PIXHAWK – 4

The Pixhawk 4 is a new version of Pixhawk having a 32-bit microprocessor along with a flash memory of 2 MB and also the RAM of 512KB. New Pixhawk P4 is even more powerful and is with more RAM resources. For stabilization purposes, low-noise and high-performance IMUs are designed on the board.

Pixhawk 4 comes with open-source firmware and also the software as well, for autonomous flying the new Pixhawk PX4 is undoubtedly one of the best flight controllers. The new Pixhawk PX4 can be assumed as a successor to the APM flight controllers but is much more powerful, making it worthy of being called one of the best flight controllers.

Features:

- Open-source software
- Autonomous flight
- 32-bit microprocessor
- A backup system in case of emergency

ARDUINO COMPATIBLE UAV CONTROLLER

It is an Arduino compatible controller with a feature of fully programmable autopilot. The input to the controller is from a GPS Module and infrared sensors in all three dimensions. It performs both navigation and stabilization using the stated combination of sensors [19].

Features:

- Built-in hardware for failsafe
- Multiple 3D waypoints
- Altitude controlled with the elevator and throttle
- 6-pin GPS connector for the 4Hz uBlox5
- Six spare analog inputs (with ADC on each)

- Size: 30mm x 47mm
- Four RC-in Channels

XVII. GIMBALS

Gimbal is a stabilization platform that dictates the movement of the object or payload that the drone is carrying. It is a pivoted support that allows rotation of the object in only a unilateral axis.

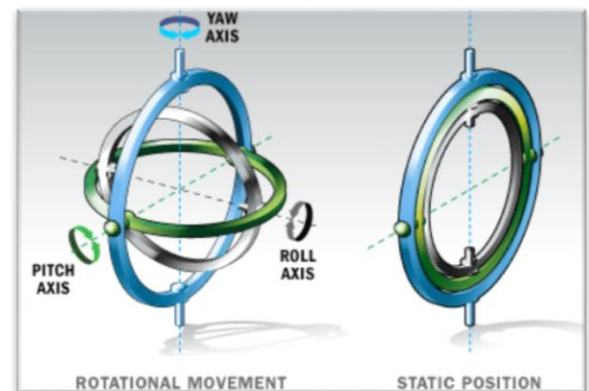


Figure 9 - Fundamental Principle for Gimbal [26]

Gimbal mounted on a drone is designed to give stability to the object by absorbing vibrations. It restricts the motion in specified axes for which it is designed, eliminating the noise and making the object stable, which is a weapon in our case.

Generally, Gimbals are powered by three brushless motors, each acting in one specified axis. An Inertial Measurement Unit is connected with Gimbal which reads the orientation, conditions the signal by applying calibrations and transmits it to Gimbal to generate a response to counter the vibration or disturbance and stabilizes the object and quad-copter. IMU for Gimbal comprises of three-axis accelerometer and gyroscope mounted on the object holder. In between the Gimbal and IMU is also a detailed algorithm in a microprocessor that acts as the main function and governs the response of Gimbal to any disturbance.

In Fig 10, a basic control loop for attitude heading and reference is shown. The attitude heading and reference system measure the orientation angles. Based on the correct orientation angles PID (Proportional Integral Derivative) angles are calculated and transmitted using Pulse Width Modulator (PWM) to the motor drive, which stabilizes the object.

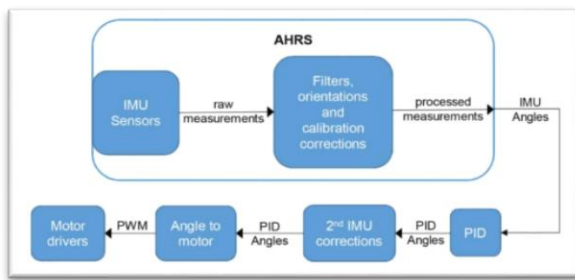


Figure 10 - Control Loop for Gimbal

The use of gimbal for the design of the stabilization system is an emerging concept that can be used in Weapon capable Drone but designing a specific gimbal based stabilization system demands decent engineering knowledge and skill. The significant factors in this phase of Gimbal System design are:

- Compatible Control Board for Gimbal
- Algorithm For Gimbal Response
- Mechanical Structure Design For Moderate Loads
- Design of Servo Module

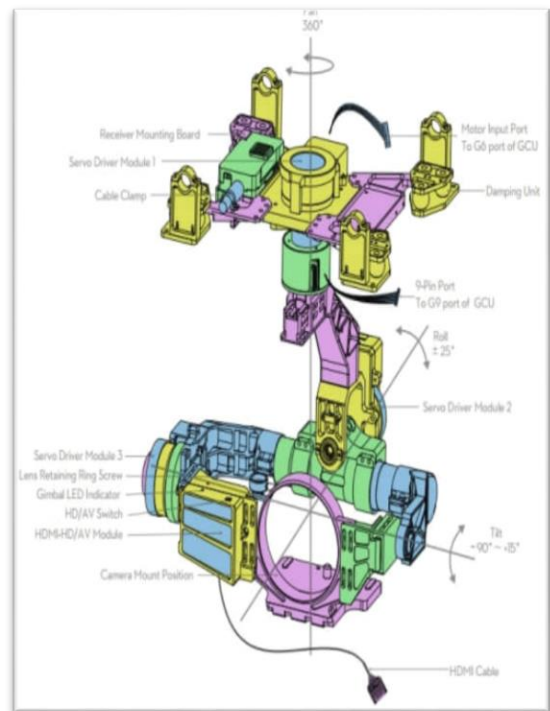


Figure 11 - Gimbal Design for Camera

XVIII. SHOCK ABSORBING MATERIAL

Mechanical energy manifests itself in the form of shock, impact, noise, and vibration and has the potential of becoming a source of a problem in aerial vehicles [27].

Shock reciprocates to a large magnitude short duration force or impact that can damage the platform. An effective solution to mitigate the damage of a Shock is to absorb the force magnitude and increase the time of impact as shown in Figure 12

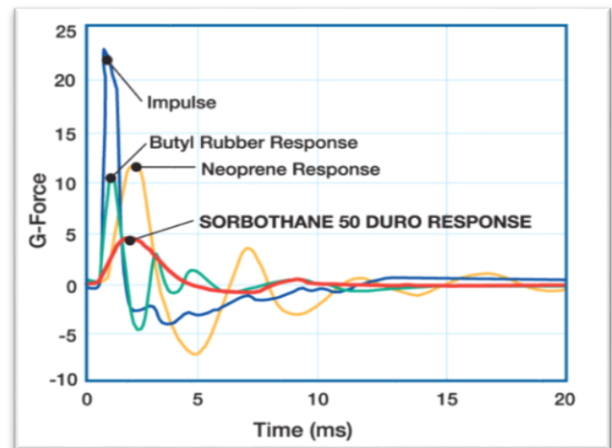


Figure 12 - Shock Absorbing Material [27]

Shock Absorbing Materials may be used to minimize the recoil of weapons [18]. One of the widely used Shocks absorbing material is Sorbothane which has the potential to absorb 94.7% of impact shock [27]. It is one of the highly damped, polymeric, visco-elastic material. Similarly, other materials that combine shock absorption, Vibration elimination, and damping characteristics may be used for reducing recoil impact in the quadcopter.

XIX. DISCUSSION

and-motors .html

Design of High-Speed Weapon Capable Killer Drone includes the design of a quad-copter platform and the design of a weapon recoil bearing stabilization system. This effort widens our horizon for designing such a system. For an efficient model, a system that utilizes all the three stabilizing mechanisms appears to be a decent concept that is a Gimbal based system that generates a response from an algorithm written after a detailed study of dynamic model imbedded in a control board. Shock-absorbing materials may be used for refinement of process and reduction of noise for accurate target detection and firing.

REFERENCES

- [1] David Hambling, "Disruptive Developments in Armed UAV Technology", United Nations Institute of Disarmament Research
- [2] S. Gupte, P. Teenu Mohandas, and J. M. Conrad, "Survey of quad-rotor UAVs," *2012 Proceedings of IEEE Southeastcon*, Orlando, FL, 2012, pp. 1-6. doi: 10.1109/SECon.2012.6196930
- [3] [Online], "Leaders in Emerging Drone Technologies" Available: <https://www.rit.edu/news/leaders-drone-technology-converge-rit>
- [4] [Online], "Unmanned Aerial Vehicle" Available: http://www.barnardmicrosystems.com/UAV/milestones/tilt_wing.html
- [5] [Online], "Boeing V 22 Osprey" Available: <https://winair.ca/blog/supreme-guide-bell-boeing-v-22-osprey-infographic/>
- [6] [Online], "Design and development of RC VTOL unmanned Aerial Vehicle" Available: <https://contest.techbriefs.com/2015/entries/aerospace-and-defense/6117>
- [7] Kimberly Hsu, "China's Military Unmanned Aerial Vehicle Industry" US-China Economic And Security Review, 2013
- [8] [Online], "Drone LiPo Battery calculator" Available: <https://www.translatorscafe.com/unit-converter/en/calculator/multicopter-lipo-battery/>
- [9] [Online], "Connect ESCS and Motors" Available: <http://ardupilot.org/copter/docs/connect-escs-and-motors.html>
- [10] S. Bouabdallah, P. Murrieri, and R. Siegwart, "Design and Control of an Indoor Micro Quad Copter", New Orleans, Proceedings of IEEE International Conference on Robotics and Automation, April 2004
- [11] B. Erginer and E. Altuğ, "Modeling and Proportional-Derivative Control of a Quadrotor Vehicle", Istanbul, Proceedings of IEEE Intelligent Vehicle Symposium, June 2007
- [12] A. Tayebi and S. McGilvary, "Attitude Stabilizer for a Quad rotor Aircraft", Vol. 14, No.3 Proceedings of IEEE Transactions on Control Systems Technology, May 2006
- [13] S. Bouabdallah and R. Siegwart, "Back-stepping and Sliding-mode Techniques Applied to an Indoor Micro Quadrotor", Barcelona, Proceedings of IEEE International Conference on Robotics and Automation, April 2005
- [14] J. Dunfied, M. Tarbouchi and G. Labonte, "Neural Network-Based Control of a Four Rotor Helicopter", Proceedings of IEEE International Conference on Industrial Technology, December 2004
- [15] Hoffinan F., Goddemeier N. and Bertram T. "Attitude Estimation and Control of a Quadcopter", IEEE/RSJ International Conference on Intelligent Robots and Systems, 2010
- [16] A. Benallegue, A. Mokhtari and L. Fridman, "Feedback Linearization and High Order Sliding Mode Observer For A Quadrotor", Alghero, Proceedings of IEEE International Workshop on Variable Structure Systems, June 2006
- [17] S. Bouabdallah, A. Noth, R. Siegwart, "LQ VS PID Control Techniques Applied to an Indoor Micro Quadrotor", Sendal, Proceedings of IEEE International Conference on Intelligent Robots and Systems, October 2004
- [18] [Willard M. Latime](#), "Shock Absorbing Pad for Rifle", Google Patent, US 20110113666A1
- [19] T. Madani and A. Benallegue, "Backstepping Control for a Quadrotor", Proceedings of IEEE International Conference on Intelligent Robotics and Systems, Beijing 2006
- [20] Eduardo Ansias and Domantas Brucas "Development of active camera stabilization system for implementation on UAV's", Mechanics, June 2012
- [21] [Online], "Drone Gimbal design, parts and top Gimbals" Available: <https://www.dronezon.com/learn-about-drones-quadcopters/drone-gimbal-design-components-parts-technology-overview/>

- 10.1007/978-94-6265-132-6_2, (2016)
- [22] Mateo Gašparovi'c and Luka Jurjevi'c, "*Influence of Gimbal on the Stability of Exterior Orientation Parameters of Unmanned Aerial Vehicle*", Faculty of Geodesy, University of Zagreb, Croatia [29] Kardasz, Piotr & Doskocz, Jacek, "*Drones and Possibilities of Their Using. Journal of Civil & Environmental Engineering*". 6. 10.4172/2165-784X.1000233, (2016)
- [23] N. J. Brake, "*Development of Control System for Small UAV Gimbal*" Ph.D. Thesis, California Polytechnic State University, San Luis Obispo, CA, USA, August 2012
- [24] Robert Lefebvre, "*UAV System Comparison*", NOVA Aerial robotics
- [25] Imad Aldieen, Mohamed, "*Design of a typical multi-role vehicle using quad-rotor theory*"
10.13140/RG.2.1.1631.1924.
- [26] [Online], "*What is a gimbal, Jonathan Strickland*"
Available: <https://science.howstuffworks.com/gimbal1.htm>
- [27] [Online], "*Shock Absorbing Material*"
Available: <https://www.sorbothane.com/shock-absorbing-material.aspx>
- [28] Vergouw, Bas & Nagel, Huub & Bondt, Geert & Custers, Bart, "*Drone Technology: Types, Payloads, Applications, Frequency Spectrum Issues, and Future Developments*".

Reverse Engineering of a Small Turbojet Engine

Abdul Rahim¹, Mohtashim Mansoor², Luqman Ahmed³

^{1,2,3}College of Aeronautical Engineering, National University of Science and Technology, Risalpur, Pakistan

¹Contact: arahim87eccae@student.nust.edu.pk, phone +92-320-9487943

²Contact: m.mansoor@cae.nust.edu.pk, phone +92-320-8801680

³Contact: luqmanahmed@cae.nust.edu.pk, phone +92-320-5770123

Abstract— This paper is aimed at creating an analytical model of a turbo jet engine with its parametric and performance analysis at on and off-design point to help reverse engineer the actual engine to be used in a drone. In the absence of the actual engine for testing, the analytical model was made by going through the design process for a new engine with certain parameters of the actual engine known and a few estimated based on historical trends. The performance and parametric analysis is performed for the better understanding of the engine's behaviour in different conditions. Computer simulations of the engine model are carried out on Gasturb software for the validation of analytical calculations followed by an attempt for the optimization of the model through the software to get an improved version of the actual engine. Lastly the virtual model of the engine is integrated into an algorithm and programmed into Arduino microcontroller to make a working engine control unit for the actual engine that can regulate the amount of fuel injected into the engine for its optimum functioning. The Engine Control Unit (ECU) thus designed is compatible with all types of micro jet engines requiring minor changes to the engine parameters section of the code like the component efficiencies.

I. INTRODUCTION

A gas turbine engine is a type of internal combustion engine in which power to drive the compressor is drawn from turbine which is driven by the flow of hot pressurized air flow. The engine comprises of a compressor which may be centrifugal type or axial type followed by the combustion chamber in which fuel is burnt to heat up and the pressurized air flow coming from the compressor. That pressurized air then flows through the turbine rotating it which is mechanically connected to the compressor wheel through a shaft hence turning it. An external motor is used to rotate the compressor wheel and fuel is pumped into the combustion chamber for burning of the pressurized air. The hot pressurized air then escapes through the turbine blades which turn the turbine and the turbine rotates the compressor hence it forms a closed cycle. Once an idle speed is achieved, the external motor shuts down and the engine keeps running as long as sufficient fuel is being provided to the combustion chamber. The speed is controlled by the rate of fuel

being provided. Greater the rate of fuel flow, faster the rotation and in turn more power is produced resulting in more thrust.

The reference engine is a micro jet single spool engine with a centrifugal compressor, annular combustion chamber and a radial turbine. Maximum thrust produced by this engine at sea level is 400 N. This paper covers the construction of a mathematical model of the engine for finding its performance parameters like specific thrust, specific fuel consumption, temperatures at different stages, exhaust gas temperature, engine rpms etc. Although the design parameters like compressor pressure ratio, compressor efficiency, turbine efficiency etc. are to be measured off the actual engine on a test bed, but the engine is not physically available for testing so in order to reverse engineer the actual engine, we proceeded through design process for building of new engine by incorporating the requirements, some measured parameters and some estimated parameters to get a very close if not the actual engine. These estimations are based on historical trends which were compiled by reviewing the works done on similarly designed engines with comparable characteristics. Parametric study of the engine is done by altering different design parameters in the mathematical model of the engine and observing its effect on the performance parameters. Then the model is tested at off design conditions and performance analysis is done. Gasturb simulation in the end approves the results obtained through analytical calculations.

Using the mathematical model thus made, a working ECU is developed in which the model is incorporated. As the only control input to a gas turbine engine is fuel flow rate so the ECU measures the ambient conditions, speed and the throttle position and controls the amount and rate of fuel to be injected into the engine so as to ensure its optimum functioning.

II. NOMENCLATURE

T_t = Total temperature
 P_t = Total pressure
 π_r = Recovery pressure ratio
 π_d = Diffuser pressure ratio
 π_c = Compressor pressure ratio
 π_t = Turbine pressure ratio
 π_f = Fan pressure ratio

τ_r = Recovery temperature ratio
 τ_d = Diffuser temperature ratio
 τ_c = Compressor temperature ratio
 τ_f = Fan temperature ratio
 τ_{ab} = After burner temperature ratio
 f_{ab} = Fuel to air ratio of after burner
 = Fuel to air ratio of main burner
 \dot{m} = Air mass flow rate
 C_p = Specific heat at constant pressure
 R = Specific air constant
 γ = Ratio of specific heats
 F_{gross} = Gross thrust

 D_{ram} = Ram drag

 ST = Specific thrust
 $TSCF$ = Thrust specific fuel consumption
 η_{th} = Thermal efficiency
 η_p = Propulsive efficiency
 η_o = Overall efficiency
 U = Rotational speed of rotor
 C_z = Absolute axial velocity
 C_θ = Absolute tangential velocity
 W = Relative velocity
 W_θ = Relative tangential velocity / Relative swirl
 a = Speed of sound
 T = Static temperature
 P = Static pressure
 MFP = Mass flow parameter
 A = Annulus area
 α = Absolute flow angle
 β = Relative flow angle
 M_w = Relative Mach Number
 T_{tw} = Relative total temperature
 P_{tw} = Relative total pressure
 $N_{b(s)}$ = Number of blades of stator

 $N_{b(R)}$ = Number of blades of rotor
 η = Adiabatic efficiency
 e = Polytropic efficiency
 D_R = Diffusion factor
 σ_s = Solidity ratio of stator
 σ_R = Solidity ratio of rotor
 ψ = Stage loading factor
 ϕ = Flow coefficient
 Γ = Circulation
 R^0 = Degree of reaction

III. LITERATURE REVIEW

1) *Radial flow turbomachines*: The type of turbomachinery where the path of the through-flow is mainly in a perpendicular plane to the axis of rotation, is known as radial flow turbomachinery. Hence, the radius change between the entry and the exit of fluid is finite. Depending on the purpose of use, a radial turbomachinery can be an inward or outward flow type. Inward flow type decreases the energy level of fluid while

outward flow type increases the energy level of the fluid. As the direction of fluid is changed, several stages of radial turbomachinery are not employed. The different components of a gas turbine engine are given below.

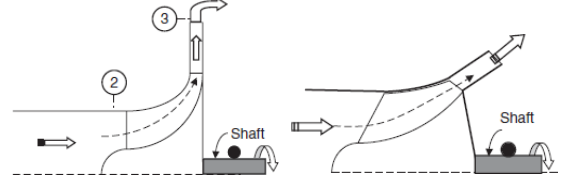


Fig. 1 Radial flow compressor(left) Hybrid flow compressor (right)

A. Compressors

The first component in jet engine's core is compressor. It consists of rotor and stator. Rotor works on the fluid by adding rotational energy into it, where stator acts as a diffuser and extracts that rotational energy from the fluid in the form of rise in static pressure. It runs on the power generated by the turbine. Through the compressor the temperature and pressure of the flow rises.

B. Turbines

The turbine is such type of turbomachine which extracts the energy from fluid by expanding fluid to a lower pressure. The turbine is consisting of nozzle and rotor. Nozzle accelerates the flow coming from combustor by decreasing its static pressure, while rotor extracts the energy from the flow. Fluid flow coming out of the combustor has higher energy, it goes into the turbine, where it causes the turbine blades to rotate, the turbine blades are linked by a shaft to turn the rotor in the compressor as well as other power consuming shafts. Turbine converts the translational energy of fluid flow into the rotational energy of turbine shaft. The rotational speed of jet turbine is thousands of time. The turbines are fixed on shafts having several sets of ball-bearing in between them.

C. Combustor Design

The simultaneous involvement of evaporation, turbulent mixing, ignition and chemical reaction in gas turbine combustion is too complex for complete theoretical treatment. Instead, large engine manufacturers undertake expensive engine development programs to modify previously established designs through trials and error. They also develop their own design rules based on the experimental results. The design rules provide a means of specifying the combustor geometry to meet a set of requirements at the given inlet conditions.

1) Gas Turbine Thermodynamic Cycle

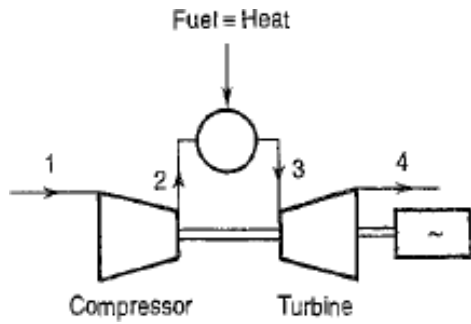


Fig. 2 Gas Turbine Thermodynamic Schematic

The primary advantage of this thermodynamic cycle is the high power generated to weight (or size) ratio, when compared to alternatives. Another advantage is the ability for it to quickly reach full power. A simple cycle combustion turbine has a lower thermal efficiency than a combined cycle machine. They may be less expensive to build simple cycle combustion turbines, due to their low efficiency.

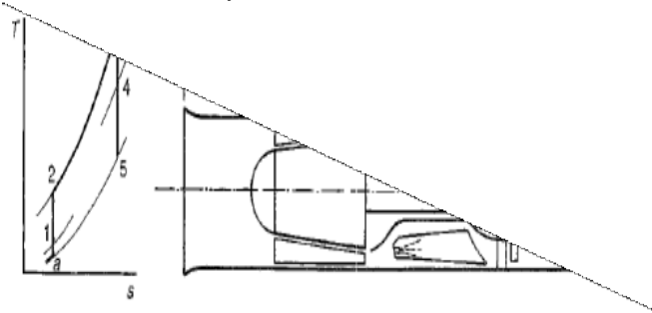


Fig. 3 The Brayton Cycle

The intake is a critical part in the aircraft engine, having a significant effect on both engine efficiency and aircraft safety. The prime requirement is to minimize the pressure loss up to the compressor face while ensuring that the flow enters the compressor with a uniform pressure and velocity, at all flight conditions. Non-uniform, or distorted, flow may cause compressor surge which can result in either engine flame-out or severe mechanical damage due to blade vibration induced by unsteady aerodynamic effects. Even with a well-designed intake, it is difficult to avoid some flow distortion during rapid manoeuvring.

Methodology

With the given characteristics of the engine we will follow the techniques for engine analysis given in the book “Gas Turbine Theory” by Henry Cohen to solve the engine analytically by calculating the engine parameters at every stage of the engine such as the compression and temperature ratios of the compressor and turbine, the temperature in the combustion chamber, the exhaust gas temperature, the rpms of the turbine etc. We will also refer to “Elements of Gas Turbine

Propulsion” by Jack D Mattingly to perform the on design and off design analysis of the engine. We will also work on the engine control unit design for this engine by integrating the algorithm for thermodynamic cycle of the engine and performance parameter calculation into the Arduino microcontroller. In the end, we will validate all the analytical solutions through simulations on GASTURB.

A. Approach

First of all, the dimensions of the reference engine were measured and the basic known parameters were acquired. Then the compressor configuration was matched to a market available compressor and its compressor maps were acquired in order to estimate the compression ratio of the compressor. Efficiencies of different components were estimated based on historical trends. Then a thermodynamic cycle of the engine was made. Afterwards on- and off-design analysis was carried out followed by simulation on GASTURB. Then an ECU model was made on Arduino microcontroller.

- Thermodynamic cycle analysis
- On design analysis
- Off design analysis
- Gasturb simulation
- ECU modeling

Fig. 4 Project Schematic

IV. ENGINE PARAMETERS

B. Published Data

Following Published data about the actual engine was provided by the sponsoring agency. Most of the data has either been calculated or estimated as the actual data of the engine is not provided by the maker. The compressor data was estimated with the help of compressor maps of similarly shaped compressor of a turbocharger.

Table 1 Engine Data Sheet

S.No.	Property	Value
1	Engine Diameter (mm)	154
2	Engine Length (mm)	420
3	Jet pipe exit diameter (mm)	70
4	Weight (kg)	7
5	Shaft speed (rpm)	91,000
6	Thrust (daN)	40
7	Pressure ratio	3.75
8	Air mass flow rate (kg/s)	0.75
9	Specific fuel consumption (kg/daN.hr)	1.45
10	Shaft power output (W)	1000
11	Exhaust gas temperature (°C)	600

12	Operating ambient temperatures (°C)	-40 to +50
13	Maximum altitude (m)	8,000
14	Maintenance cycle (hr)	20

21	Fs	413.8798	Ns/kg
22	SFC	0.155325	kg/hN

C. Estimations

As the maker does not provide any data of the engine whatsoever so some basic parameters are estimated based on the historical trends. These trends have been modelled based on the published data of some commercially available similarly sized and configured engines like Jetcat and Behotec engines. These estimated parameters are given in the table below.

Table 2 Estimated Parameters

S.No.	Property	Value
1	Turbine inlet temperature (T03)	1100
2	Isentropic compressor efficiency (η_c)	0.8
3	Isentropic turbine efficiency (η_t)	0.8
4	Isentropic intake efficiency (η_i)	0.93
5	Isentropic nozzle efficiency (η_j)	0.95
6	Mechanical transmission efficiency (η_m)	0.99
7	Combustion Efficiency (η_b)	0.98
8	Combustion pressure loss (ΔP_b)	4 %

D. Thermodynamic Cycle Analysis

Following the methodology stated in the book “Gas Turbine Theory” [1] we perform the thermodynamic cycle analysis of the engine and calculated the performance parameters. The results of the analysis is given in the table below.

Table 3 Results of thermodynamic cycle analysis

S.No	Parameter	Value	Units
1	Ca	240.75	
2	Ca2/2cp	28.8361	k
3	T01	284.8361	k
4	P01/Pa	1.417204	
5	P01	0.779462	bar
6	P02	2.922984	bar
7	T02-T01	163.3693	k
8	T02	448.2054	k
9	T03-T04	144.4639	k
10	T04	955.5361	k
11	P03	2.806065	bar
12	T04'	919.4201	k
13	P04	1.362144	bar
14	P04/Pa	2.476625	
15	P04/Pc	1.916815	
16	T5 = Tc	820.2027	k
17	P5 = Pc	0.710629	bar
18	Rho 5	0.301884	
19	C5	559.5351	m/s
20	A5/m	0.00592	

We performed iterative study of the engine by altering the different parameters in the algorithm and plotting it in excel to observe the behaviour of the engine which would mimic in the real-life scenario. We obtained the following results.

At different flight conditions like altitude, atmospheric pressure and temperature, air density etc the thrust and specific fuel consumption will vary, because of the variation in mass flow with the air density and the variation of momentum drag as the forward velocity changes.

Temperature to the turbine would alter with intake conditions. Hence any change in thrust and fuel consumption with change in altitude and Mach number, for our engine running at maximum rotational velocity, are shown in Fig. 10 and Fig. 11.

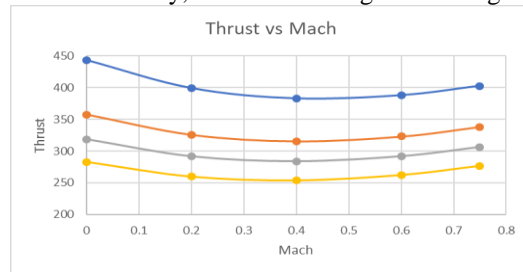


Fig. 5 Variation of thrust with altitude and Mach



Fig. 6 Variation of SFC with altitude and Mach

As we can see that the thrust is decreasing significantly with the increase in the altitude, because of the decreasing density and atmospheric pressure, although the specific thrust does increase with altitude from the favourable effect of the lower intake temperature. Specific fuel consumption however improves with the increasing altitude. It is evident from these graphs that the fuel consumption will be greatly reduced at higher altitudes. Fig 10 shows that with the increasing mach number at constant altitude the thrust initially decreases, because of the increasing momentum drag, and then starts increasing due to the effect of the ram pressure ratio.

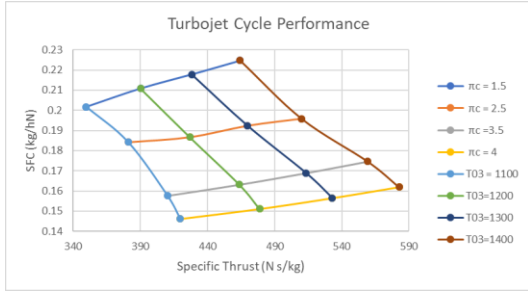


Fig. 7 Turbojet cycle performance

It is evident from the above figure that the specific thrust is mainly dependent upon the turbine inlet temperature (T_{03}), and using maximum temperature is in fact desirable so as to keep the size of the jet engine as small and light for the given amount of thrust. With constant pressure ratio, however, by increasing the turbine inlet temperature (T_{03}) will result in the increase in the specific fuel consumption. The increase in the specific thrust with the increase in temperature is more desirable that we can overlook the penalty we get in the form of rise in the specific fuel consumption, particularly at greater speeds where small jet engine size is crucial for reduction of both the weight and the drag. As is evident from the figure above figure by increasing the pressure ratio of the compressor (π_c) we can reduce the SFC. At constant turbine inlet temperature (T_{03}), if we increase the pressure ratio, the specific thrust initially increases as a result but for larger engines (not in our case) it eventually starts to decrease.

Figure 25 represents a particular case subsonic cruise. When we repeat such calculations for greater cruising speeds maintaining constant altitude, we find that generally, for any given pressure ratio (π_c), and TIT (T_{03}), the fuel consumption increases and the thrust decreases. Such effects are because of the combination of increased inlet momentum drag and increased compressor work resulting from the rise in the inlet temperature. The most noteworthy effect of increased design cruise speed is the reduction in the optimum compressor pressure ratio for the max specific thrust. It results from the larger ram compression in the engine intake. The greater compressor inlet temperature and the need for greater velocity make the use of a greater inlet temperature to the turbine more desirable and it is essential for the economy of the drone. Thermodynamic cycle optimization cannot be isolated from design considerations, and the choice of cycle parameters is greatly dependent on the type of aircraft system. Although greater turbine temperatures are desirable, they require the use of expensive and difficult to construct alloys and cooled blades of the turbine resulting in greater cost and complexity. The thermodynamic benefits of the increase in pressure ratio should cater for the increase in weight, cost and manufacturability due to the needs for greater number of stages of the compressor and turbine.

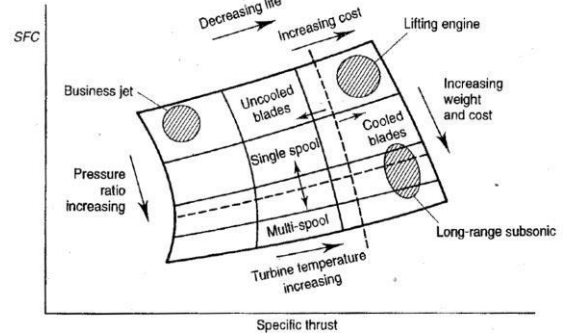


Fig. 8 Performance and design considerations

Figure 26 represents the relationship between design and performance considerations. For drones, a simple and reliable turbojet engine of low cost is needed and there's no definite need for a very fuel economical and high power engine for such UAVs. The fuel consumption is not that critical due to relatively little amount of flying, and their needs can be satisfied with engines having low compressor pressure ratios and the turbine inlet temperatures but what may matter to these drones is the size and the weight of the engine. The smaller and lighter the engine for same thrust output, the better it is.

E. EngineSim Simulation

EngineSim is an old java applet that was made by the NASA Glenn Research Centre in order to make basic calculations regarding gas turbine engines and rocket engines quickly and efficiently for research and education purposes. It's a simulator that creates a virtual design of the engine model as described by the designer and tests that model of the engine for different parameters.

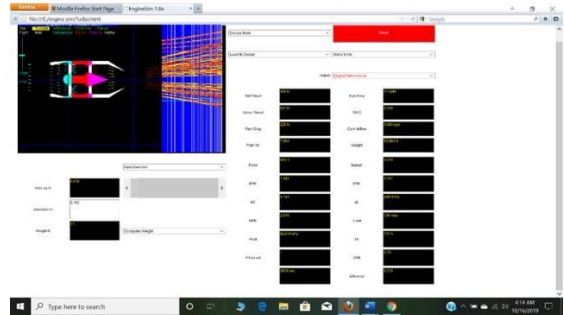


Fig. 9 EngineSim applet interface

Enginesim applet is a basic and outdated propulsion software and we cannot truly rely on its output. Its use was intended to see whether our direction for calculation of engine parameters analytical is right or not.

Table 4 Enginesim output vs analytical output

Parameter	Analytical Calculations	Enginesim
Thrust (Newtons)	402	400
SFC (kg/hN)	0.154	0.129
Fuel/air	0.017	0.016
Air mass flow rate (kg/s)	1.1	0.88
EGT (Kelvin)	760	737

F. Parametric Cycle Analysis:

Cycle analysis involves the study of the thermodynamic changes in the air and combustion products as it flows through the engine. The parametric cycle analysis involves the study of the performance of aircraft engine by varying the flight condition and parameters of the design choice for example the pressure ratios, burner pressure ratio, turbine efficiencies etc. one can say that the on design analysis depicts a rubber engine as the geometry for different combinations of an engine will be different from the one before. On design analysis is also called the parametric cycle analysis since in this kind of analysis we alter different parameters of an engine and observe the the effect on its performance.

Generally, in the On-Design analysis, I'll be altering the following parameters one by one and observing their impact upon the other parameters of the engine model.

- Compressor pressure ratio
- Burner exit temperature
- Aircraft Velocity
- Thrust
- SFC
- Efficiencies
- Fuel/air Ratio
- Altitude

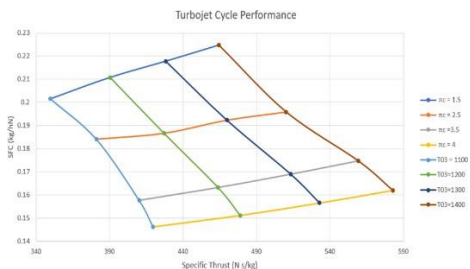


Fig. 10 Turbojet cycle performance

Increasing the pressure ratio of the compressor drastically decreases the fuel consumption and also increases the net thrust. And increasing the burner exit temperature very slightly

increases the Fuel consumption but also drastically increases the thrust of the engine.

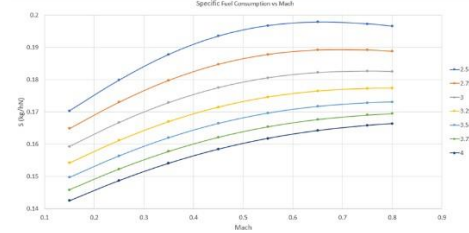


Fig. 11 Engine performance vs Mach: SFC

At constant compressor pressure ratio, SFC increases with increasing Mach numbers.

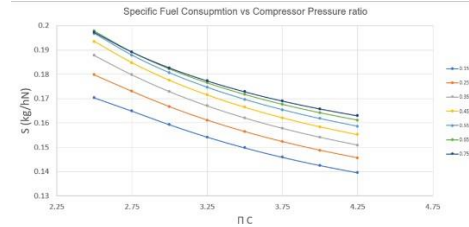


Fig. 12 Engine performance vs pressure ratios: SFC

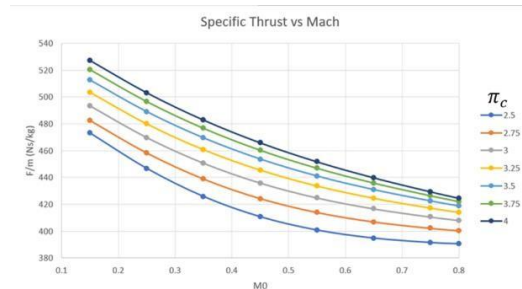


Fig. 13 Engine performance vs Mach number: Specific thrust

At a constant pressure ratio, specific thrust decreases when Mach number increased.

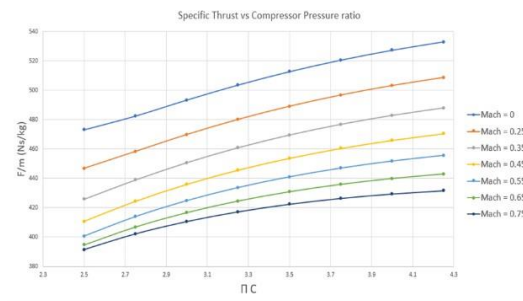


Fig. 14 Engine performance vs pressure ratios: Specific thrust

As we increase the compressor pressure ratio at constant Mach number the specific thrust also increases.

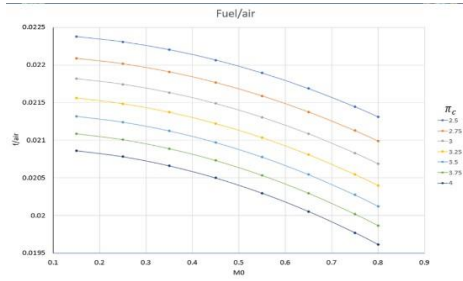


Fig. 15 Engine performance versus Mach: fuel-air ratio

At a constant pressure ratio, as we increase the velocity, the fuel to air ratio decreases.

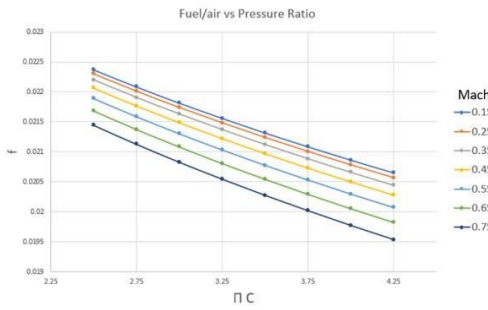


Fig. 16 Engine performance versus pressure ratio: fuel-air ratio

At constant Mach, if you increase the compression ratio of the compressor the fuel to air ratio decreases.



Fig. 17 Turbojet performance vs Mach: efficiency

Thermal, Propulsive and the Overall efficiencies, at a constant pressure ratio, increase with Mach number however the change is very little at higher Mach numbers.

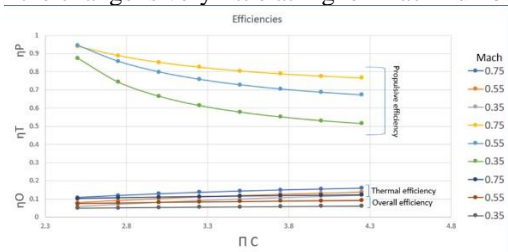


Fig. 18 Turbojet performance vs Compressor pressure ratio: efficiency

At a constant Mach, with increasing compressor pressure ratios, the propulsive efficiency decreases but thermal and overall efficiency increases

G. Performance Analysis:

When a turbo jet engine is modeled and constructed, the amount of variability of the gas turbine engine depends upon the technology already available, the requirements of the application for that engine, and the needs of the makers. Many turbojet engines contain fixed area flow passage and there is limited room for variation. In a basic fixed flow area engine, the performance (pressure ratio and the mass flow rate) of the compressor is dependent upon the power produced by the turbine and the conditions at the inlet to the compressor. In the off-design analysis, simple and basic analytical equations may be utilized to show a relation for the performance of engine compressor and the independent variable such as the throttle settings (T_{t4}) and the flight conditions (M_0, P_0, T_0).

Using the methodology stated in the book "Elements of Gas Turbine Propulsion for the off-design analysis of the our gas turbine engine we get the following plots for different parameters. The reference altitude was taken at 16000 ft and the off-design analysis was carried out at sea level, 8000 ft and 12000 ft.

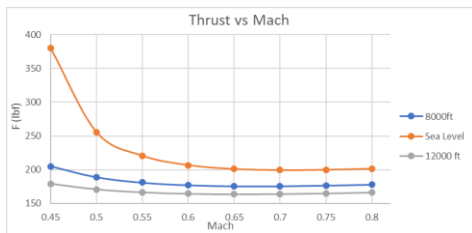


Fig. 19 Maximum Thrust vs Mach

This graph shows that as the speed increases the maximum thrust decreases down to almost 0.7 Mach than it slowly and gradually starts to increase. At constant speed the maximum thrust decreases with increase in altitude.

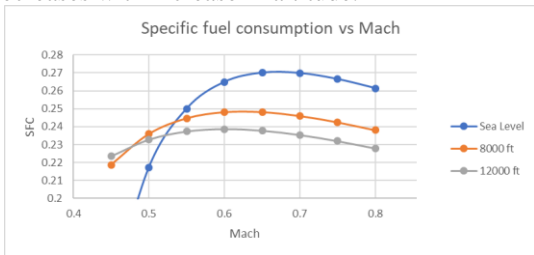


Fig. 20 Specific fuel consumption vs Mach

From this graph we can deduce that the SFC of our engines increases with the increase in the Mach number up till 0.65 to 0.7 mach. From there it starts to gradually decrease again. And at a constant Mach, SFC decreases when altitude is increased.

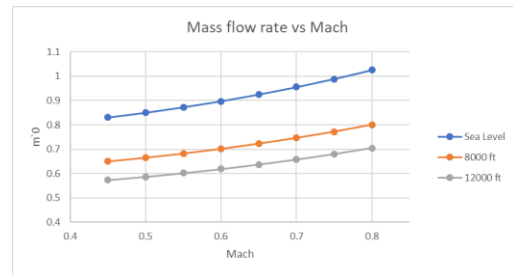


Fig. 21 Engine Mass Flow rate vs Mach

The curves in the above figure show us that as the Mach speed of the engine increases the amount of incoming air also increases hence the engine mass flow rate increases as a result. And at a constant Mach as we increase altitude, the mass flow rate of the air lessens because of the low air density at higher altitudes.

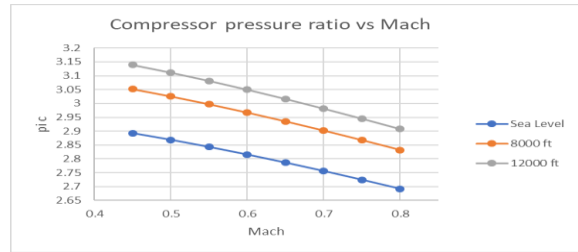


Fig. 22 Compressor pressure ratios vs Mach

From the above figure it is evident that as Mach increases the effective pressure ratio decreases and at a constant Mach if we increase the altitude, the compressor pressure ratio increases drastically.

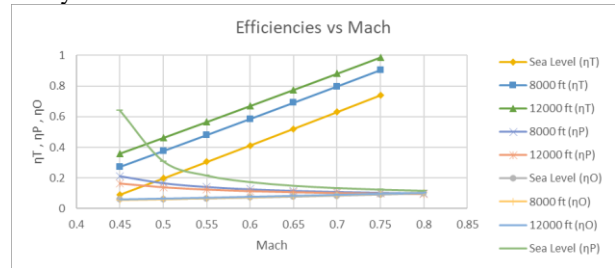


Fig. 23 Turbojet Efficiencies vs Mach

The trends for propulsive, thermal and overall efficiencies in the graph given above shows that the propulsive efficiency decrease with increasing speed and altitude. The thermal efficiency increases with speed increasing the air velocity and altitude. And the overall efficiency of the engine very slightly increase with speed and remains almost constant with the altitude.

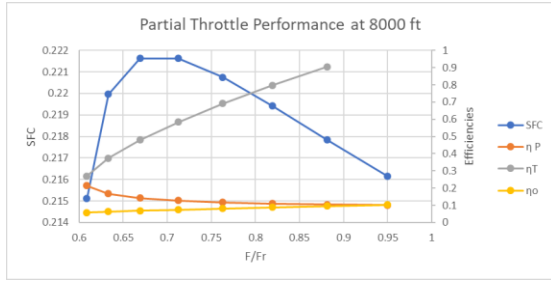


Fig. 24 Turbojet performance at partial throttle (8000ft)

The graph in the above figure represents the turbojet engine performance at partial throttle settings. It shows that as we reduce the throttle, our specific fuel consumption increases up till 0.65 and then starts to drastically decrease. This plot is commonly referred to as throttle hook plot because of its shape. The propulsive efficiency minutely increases while the thermal efficiency decreases by decreasing the throttle. As a result, the overall efficiency also very slightly decreases by decreasing the throttle.

V. GASTURB SIMULATION

We perform our cycle analysis and the on-off analysis of the engine on this software to see if our analytical calculation results agree with the output of this software.

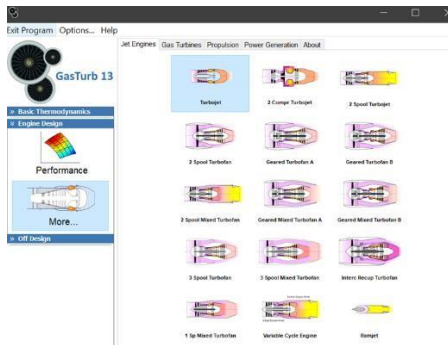


Fig. 25 Engine type selection page of GasTurb

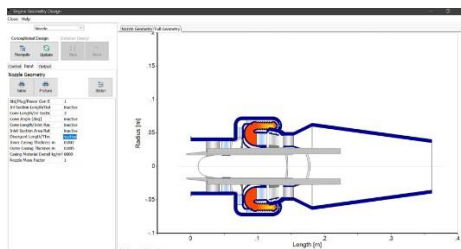


Fig. 26 Engine modeling in Gasturb

According to general trend of the aerospace industry and improvements in the technology Mach numbers as shown in Table 3 were supposed at different locations initially. They may vary after the analysis if results are not compatible or they can be evaluated by reverse engineering approach.

Table 5 Station Mach Numbers

Station #	2	3	4	5	6	8
Mach #	0.5	0.25	0.2	0.4	0.2	0

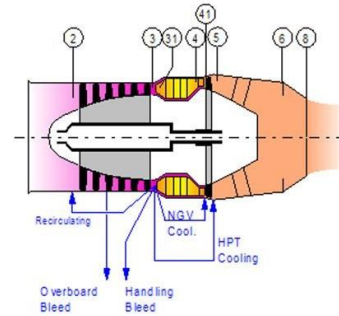


Fig. 27 Station numbering of turbojet

A. Output of GasTurb

After gathering all the information, we need, we modeled the reference engine on Gas Tub 13 and run the design point analysis. Results obtained were fulfilling the requirements like required thrust is greater than 270 N. We can also see the drop in the value of TSFC. Snapshot of the result sheet of GasTurb 13 is given in Figure 32.

Fig. 28 Reference engine's summary (At Design Point)

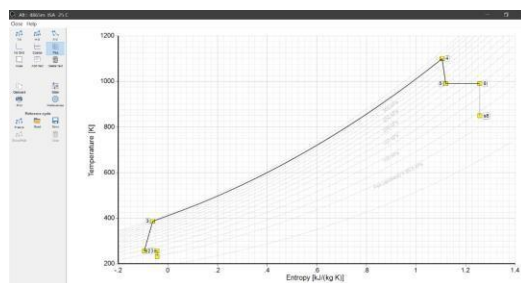


Fig. 29 Temperature vs Entropy Curve

This is the T-S curve made by Gasturb software. It represents the actual engine model. The temperatures at every station is given and are same as that calculated analytical. It shows that our analytical calculations are accurate.

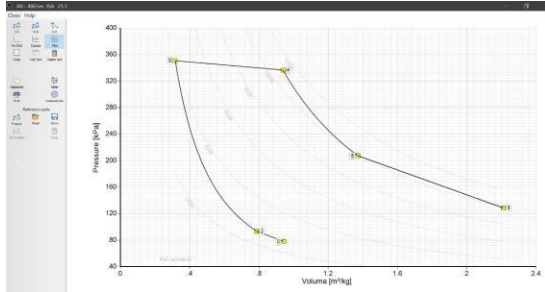


Fig. 30 Pressure vs Volume Curve

Similarly, the P-S curve is given in the above figure and represents the actual pressure and volume values at every station of our model engine. This ensures that our model is accurate and we can proceed forward with the trade studies of the engine in the next section.

B. Trade Studies

After modelling our baseline engine, we then perform the trade studies using the Gasturb program. Following engine trade studies were done to analyse the sensitivity of our engine corresponding to change in different parameters.

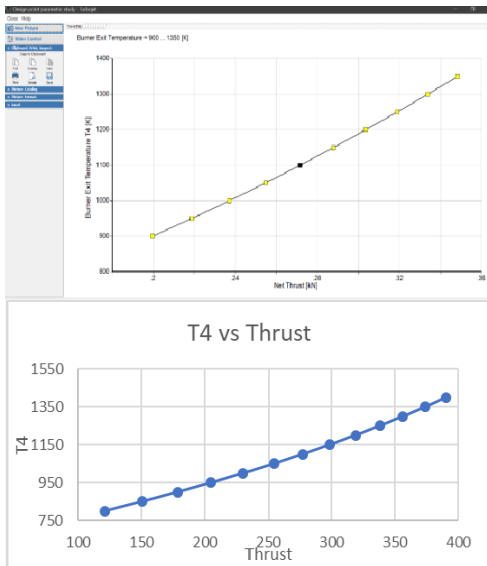


Fig. 31 Turbine Inlet Temperature vs Thrust

In the above figure we can see the variation of burner outlet temperature with the engine thrust. The trends of both the software and the analytical calculation agree to each other. The burner temperature varies exponentially with the thrust.

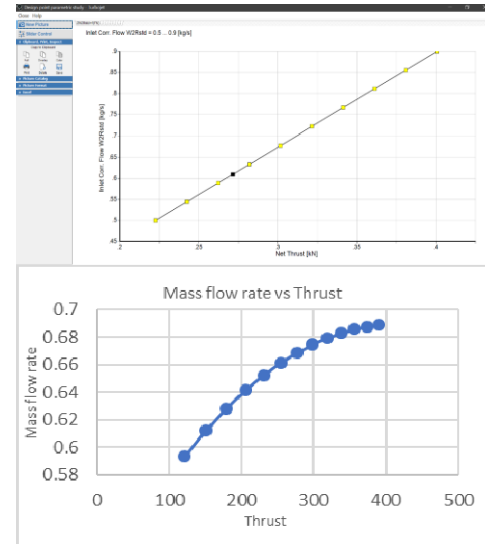


Fig. 32 Air mass flow rate vs Thrust

In these curves you can see that the output of the software is linear while that of the analytical calculation is exponential. That is because the software calculates corrected mass flow while our analytical algorithm gives the normal mass flow. But the output is same for both. The mass flow increases as we increase the thrust but the amount of increase decreases as we move to greater thrust values.

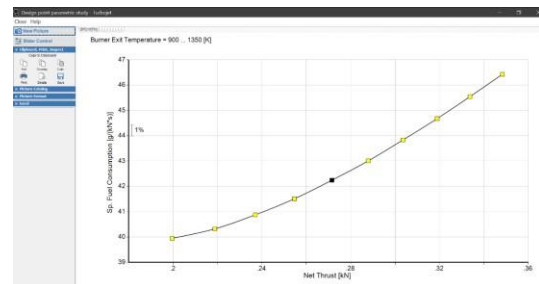


Fig. 33 Thrust vs Specific fuel consumption

This curve shows the exponential relationship between the thrust and the specific fuel consumption. As we increase the thrust our fuel consumption increases exponentially being greater at greater thrust values.

C. Optimization on Gasturb

Lastly, we perform optimization on Gasturb for our model to see if there's a better combination of design parameters of the engine which fulfil our requirements with greater efficiency.

Our constraints are net thrust, compressor efficiency, specific fuel consumption (SFC) and exit temperature of the combustion chamber. The variables are engine RPMs, inlet mass flow, burner exit temperature, isentropic compressor efficiency, isentropic turbine efficiency and the compressor pressure ratio. Following figure shows the optimization process take place and then the software gives an optimized model.

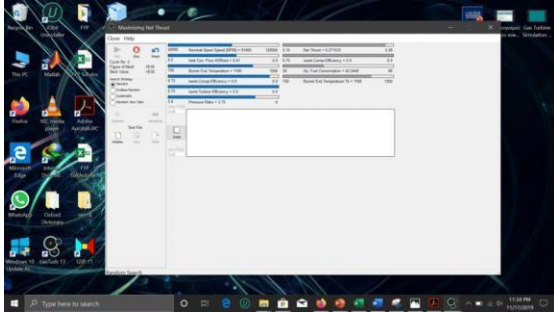


Fig. 34 Gasturb optimization process

The table in the above figure represents all the engine parameters thus calculated through our thermodynamic, parametric and performance analysis.

D. Optimized Results

After optimization process carried out by Gasturb following results are obtained.

Table 6 Gasturb optimization results

S.No.	Parameters	Values
1	RPM	83,440
2	Mass flow (kg/s)	0.695
3	Turbine Inlet Temperature (K)	1050
4	Compressor pressure Ratio	3.66
5	Compressor Efficiency	0.89
6	Turbine Efficiency	0.85
7	Specific fuel Consumption (kg/hN)	0.156

VI. FINAL SUMMARY OF ENGINE

Summary Data		
Design Mach	0.75	
Design Altitude	16000	ft
Design Mass Flow	0.668	kg/s
Design Net Thrust	276	N
Design TSFC	0.154	Kg/hN
Compressor Pressure Ratio	3.75	
Design T4	1100	K
Design Engine Pressure Ratio	2.47	
Design Compressor Efficiency	0.80	
Design Turbine Efficiency	0.80	
Design Engine Shaft RPM	91000	

VII. ECU MODELLING

An Engine Control Unit is a computer fitted on an aircraft engine that measures certain parameters of the engine in real time and controls the amount of fuel being injected into the engine. Gas turbine engines are controlled by injection of fuel into the combustion chambers. To increase thrust throttle is given which means greater amount of jet fuel is injected into the burner which causes a rise in combustion chamber temperature. To decrease the thrust throttle is reduced and the opposite effect takes place. Early jet engines featured a direct throttle which meant the fuel valve was directly controlled by the throttle stick which proved dangerous and difficult. If the fuel valve closes too quickly, it could result in engine die out. The fuel ratio decreases hence the flame can get distinguished as the airflow can blow out the flame. Increasing the throttle too quickly can cause a rich blow out. Meaning excess amount of fuel can soak the flame and extinguish it. Or can result in a greater fuel to air ratio meaning temperature rises to a point that may damage the turbine blades or could increase the burner pressure that may choke the engine causing stall.

These issues are resolved by the integration of an engine control unit. What an ECU does is that it acts as an intermediate between the throttle and the fuel valve. When the pilot moves the throttle stick the ECU gets that input and calculates how much fuel is needed to be ejected to meet the power needs of the pilot while avoiding all the above given problems and also get the best range and endurance. An ECU measures the RPMs and the exhaust gas temperature to regulate the fuel flow to the burner. In short, ECU is a computer that is fitted on modern jet engines that regulates the amount of fuel provided to the engine ensuring its optimum functioning.

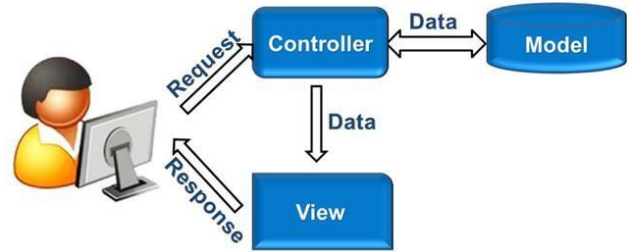
A. Arduino

The microcontroller used for our ECU is Arduino Uno and the program written is in Arduino IDE. The program is based on the algorithm given in section 3.1. The ECU algorithm is written in Arduino code that is given in appendix A. A testbed is made for testing of the Arduino with a motor, an RPM sensor, some controls using potentiometers, 20 x 4 LCD for displaying of output, and an Arduino Uno board itself.

The inputs to the Arduino ECU are

- Speed of the drone (Mach)
- Ambient Temperature
- Ambient Pressure
- Throttle Position

For testing, these inputs were emulated with the help of potentiometers. And the output is in the form of movement by the servomotor which emulates an actuator for opening and closing of the fuel valve.



VIII. LIMITATIONS

The analytical solution of the engine is based on the existent knowledge of the previous jet engines and a few estimations that are not specific to miniature jet engines. Furthermore, the parameters that were estimated for the engine are based on different similarly built engines that might alter our calculation from the actual value to some extent. Live testing of the engine is required to sync the virtual model with the actual one.

Furthermore the algorithm for ECU is for any micro jet engine however basic tweaking is required to make it compatible.

IX. CONCLUSION:

The analysis of this engine will result in

- Reverse Engineering of the Actual Engine
- Improvements in the Engine
- Development of newer and better Engines
- Development of ECUs

X. ACKNOWLEDGEMENTS

We would like to acknowledge the support and guidance provided by faculty members of Department of Aerospace Engineering, College of Aeronautical Engineering (NUST), towards fulfillment of this project.

XI. REFERENCES

- [1] Chauhan, Richa & Maity, Arnab & Paluri, Nataraj. (2018). Modeling, Simulation and Validation of Mini SR-30 Gas Turbine Engine. IFAC-
- [2] S. M. Haris, "Mini Turbojet Engine," DHA Suffa University, [Online]. Available: <https://www.researchgate.net/publication/317279288>
- [3] J. D. Mattingly, Aircraft Engine Design, United States: AIAA, 2002.
- [4] S. Farokhi, Aircraft Propulsion, UK: John Wiley & Sons Ltd, 2014.
- [5] S. Farokhi, Aircraft Propulsion, John Wiley & Sons Ltd, 2014.
- [6] D. J. Raymer, Aircraft Design A conceptual Approach, Washington: AIAA, 1992.

- [7] J. D. Anderson, Aircraft Performance and Design, AIAA..
- [8] David T. Pratt, AFTBNR Program User Guide, 2003.
- [9] N. Cumptsy, Jet Propulsion, New York: Cambridge University Press, 2009.
- [10] B. Dunbar, "NASA National Aeronautics and Space Administration," Glenn Research Center, [Online]. Available: <https://www.grc.nasa.gov/www/k-12/airplane/brayton.html>. [Accessed 16 03 2018].
- [11] P. G. Hill, Mechanics and Thermodynamics of Propulsion, Menlo Park, California: Addison-Wesley Publishing Company, 1992.
- [12] D. G. Hull, Fundamentals of Airplane Mechanics, Austin: Springer-Verlag Berlin Heidelberg, 2007.
- [13] J. Kurzke, "GasTurb 13.0 : On design and Off design Performance program for gas Turbine," GasTurb GmbH, Germany, 2012.
- [14] J. D. Mattingly, Aircraft Engine Design, AIAA , 2002 Virginia.
- [15] J. D. Mattingly, OFFX USER GUIDE, 1996.
- [16] J. D. Mattingly, AEDsys Program User Guide, 2014.
- [17] J. D. Mattingly, COMPR Program User Guide, 2016.
- [18] J. D. Mattingly, Elements of Gas Turbine Propulsion, New Delhi: Tata McGraw Hill Education Private Limited, 2013.
- [19] J. D. Mattingly, Elements of Propulsion: Gas Turbine and Rockets, Virginia: AIAA, 2006.
- [20] J. D. Mattingly, NOZZLE Program v4.0 User Guide, 2016.
- [21] J. D. Mattingly, ONX USER GUIDE, 1996.
- [22] J. D. Mattingly, PARA Program User Guide, 2016.
- [23] J. D. Mattingly, PERF Program User Guide, 2016.
- [24] J. D. Mattingly, TURBN Program User Guide, 2016.
- [25] H. Wordpress, "Machinery Equipment," hvac machinery, [Online]. Available: <http://machineryequipmentonline.com/hvac>
- [26] N. Cumptsy, Jet Propulsion, New York: Cambridge University Press, 2009.
- [27] Ujam, A.J., 2013. Parametric analysis of a Turbojet engine with reduced inlet pressure to compressor. IOSR Journal of Engineering, 3(8), pp.29.
- [28] Saravanamuttoo, H.I., Rogers, G.F.C. and Cohen, H., 2001. Gas turbine theory. Pearson Education.
- [29] Kamps, T., 2005. Model Jet Engines, Traplet Publications.
- [30] Trazzi, P.E., 2004. Design and Development of a 70 N Thrust Class Turbojet Engine. Revista de Engenharia Térmica, 3(1), pp.09-14.
- [31] Polat, C., 2009. An electronic control unit design for a miniature jet engine. Master of Science Thesis in Mechanical Engineering Graduate School of Natural and Applied Sciences of Middle East Technical University.
- [32] Ujam, A.J., Ifeacho, F.C. and Anakudo, G., 2013. Modeling Performance Characteristics of a Turbojet Engine. International Journal of Manufacturing, Material and Mechanical Engineering Research, 1(1), pp.1-16.

DESIGN OF ROCKET ASSISTED TAKEOFF FOR DRONES

Asees Siddiqui¹, Mohtashim Mansoor², Luqman Ahmed³

^{1 2 3} College of Aeronautical Engineering, National University of Science and Technology, Risalpur, Pakistan

¹Contact: asiddiqui87eccae@student.nust.edu.pk, phone +92-320-9487943

²Contact: mohtashimmansoor@gmail.com, phone +92-320-8801680

³Contact: luqmanahmed@cae.nust.edu.pk, phone +92-320-5770123

Abstract—Conventional runway takeoff is not available in many situations especially for small drones in inhospitable terrain. In that case one may resort to catapult launch system or zero length rail launch system in which rocket motor is used to launch the aircraft in a very short distance. The aim is to design a small rocket motor using easily available propellant for launching drones in a very short distance. The rocket's motor sizing, nozzle and structure will be designed and trajectory and stability will be analyzed

Keywords—Rocket Assisted Takeoff; Propellants; Rail launch.

I. INTRODUCTION

Rocket engines obtain thrust in accordance with Newton's third law and are mainly reaction engines. Thrust in rocket engines is obtained by expulsion of matter through a nozzle. This matter consists of high-speed fluid which is mostly gaseous in nature which is created by high pressure combustion of solid or liquid propellants, consisting of fuel and oxidizer components, within a combustion chamber. The main components of a chemical rocket are, rocket motor or engine propellant consisting of fuel and oxidizer, a frame to hold the components, control systems and a cargo such as satellites.[2]

There are three types of rocket propulsion systems, which are chemical, nuclear, and

solar, the basic functions include booster, sustainer, altitude control. The type of vehicle rockets carry are aircrafts, space shuttles and small drone. Type of propellant, type of construction, or number of rocket propulsion units used in a given vehicle [6]

II. ROCKET FUELS

The fuels used in rocket motors can either be liquid or solid. The liquid fuel consists of fuel and oxygen in liquid state. The fuel and oxygen are combined in a combustion chamber and ignited. The fuel flow to the engine can be controlled, the amount of thrust can be altered according to the requirement and the engine can be turned off or on at will. [5] Solid-fuel rockets consist of a fuel and oxidizer that are mixed with the help of a binder in the solid form. Once the solid fuel is ignited, the thrust cannot be controlled and the propellant burns to the end. Solid rockets are cheap to manufacture, simple to operate and safe to use unlike liquid rockets. Specific impulse (usually abbreviated Isp) is a measure of how effectively a rocket uses propellant or a jet engine uses fuel. By definition, it is the total impulse (or change in momentum) delivered per unit of propellant consumed.. [5]

Table 1. Types of Propellant

III. Assisted Take-off

Assisted take-off is a system for helping aircraft get into the air when the aircraft loaded with excessive weight, or has insufficient power or insufficient runway length.

It has two main types

1. Catapult launch
2. Rocket Assisted Take-off or Jet Assisted Take-off

In catapult launch, a piston, known as a shuttle, is pushed forward under the steam pressure in a cylindrical chamber. the tow bar or launch bar is attached to the front landing gear of the aircraft which attaches it to the shuttle which propels the aircraft at the deck at about 15 knots above minimum flying speed, which is achieved in approximately four seconds.



Figure 13. F/A 18 attached to steam catapult

In Rocket assisted take-off additional engines are mounted on the air frame which are only used during the takeoff. After the takeoff the engines are usually jettisoned.

Solid propellants	Liquid propellants
Solid propellants have low specific impulse [4]	Liquid propellants have high specific impulse [4]
Storage, handling and transport are comparatively easy. [4]	storage, handling and transport are comparatively difficult. [4]
Engines used have simple designs. [4]	Engines used have delicate design and cannot withstand rough handling. [4]
Economical in use. [4]	Costly to use. [4]
Manipulation of the fuel and calibration of the engine is difficult. [4]	Fuel is versatile and engine calibration is easy [4]
Once ignited solid propellants cannot be stopped [5]	Liquid propellants can be used in different proportions and can be controlled [5]



Figure 14HESA Karrar

IV. METHODOLOGY

The approach for project is that firstly a suitable propellant for the requirement of the mission will be selected. The basic design of the rocket motor would be carried out which would include the calculation of total impulse, the weight of the selected propellant to be used, the volume required by the propellant in the motor casing and the web thickness of the propellant grain. Next the case would be designed for the rocket motor, the material for the casing would be selected and the wall thickness for the selected material would be determined by taking in consideration the stresses being applied on the casing. Grain configuration would be selected later depending on the mission requirement. After that the nozzle would be designed according to the chamber

pressure, burn rate and the coefficient of specific heat of the propellant used

V. DESIGN REQUIREMENTS

Table 2. Design Parameters

Known Parameters	SI	
	Mass Of Drone	120
Stall Velocity (est.)	60	m/sec
Take-off Velocity (est.)	69	m/sec
Stall Velocity(calc.)	53.3	m/sec
Take-off Velocity (est.)=1.15 x Vs	61.3	m/sec
Mass of Rocket	10	kg
Mass of Rocket & UAV	130	kg
Time	2.3	sec
Chamber Pressure	8.50	MPa
Thrust	5200	N
Max. acceleration	60	m/sec ²
Burning Rate	0.889	cm/s
Outer Dia	0.115	m

VI. SELECTION OF PROPELLANT

A number of solid propellants are available which can be used for the mission requirement. For this mission we would use HTPB+AP+Al as propellant. It has the following advantages and disadvantages.

Table 3. Advantages Disadvantages of Propellant

Advantages	Disadvantages
------------	---------------

Better Performance	Moisture sensitive
Widest ambient temperature limits	High flame temperature
Good burn rate control	Toxic
Stable combustion	Smokey exhaust
Medium relative cost	
Good physical properties	
Good experiences	

Following concentration of the propellant would be used

Ammonium Perchlorate (oxidizer) 68%

Aluminum (fuel) 20%

Hydroxyl-Terminated Polybutadiene (binder) 12%

VII. BASIC DESIGN

The total Impulse of the rocket motor was calculated as

$$I_t = Ft_b = I_s w_b = 7969 \text{ N-s}$$

Next the propellant weight required was determined from the specific impulse value of the propellant

$$w_b = \frac{I_t}{I_s} = 33.20 \text{ kg-m/s}^2$$

The volume required for this weight of propellant is calculated using the formulation

$$V_b = \frac{w_b}{\rho_b} = 1.86 \times 10^{-3} \text{ m}^3$$

Lastly, we calculate the web thickness of the propellant grain using

$$b = rt_b = 2.05 \times 10^{-2} \text{ m}$$

VIII. CASE DESIGN

A number of materials are available for the manufacturing of rocket motors, according to our requirement we would use metal casing for our rocket motor. The materials are

Table 4. Case Materials

Material	Tensile strength (N/mm ²)	Modulus of elasticity (N/mm ²)	Density (gm/cm ³)
Alloy steel	1400-2000	207,000	205
Aluminum 2024	455	72,000	165
Titanium alloy	1240	110,000	270

We would firstly select alloy steel as it has higher strength and a medium density value.

Also, the graph plotted for the change in yield strength with temperature tells us that alloy steel shows much resistance to changes in temperature

Now we will determine the wall thickness of the casing using the formulation of hoop stress

$$t = \frac{p_1 D}{2\sigma} = 3.22 \times 10^{-4} m$$

IX. GRAIN CONFIGURATION

The propellant grain is the geometric shape a solid propellant is processed into. It is usually cylindrical in shape. It determines the burn rate of the propellant

We will use a cartridge loaded grain as it is simpler to use and the rocket motor casing can be reused

For the insulation of the casing from the propellant grain we will use the ablative material and the thickness would be determined using the formulation

$$a = c \left[\frac{2kt}{R_r R_v C_p \rho} \ln \left(1 + \frac{R_r R_v C_p (T_{aw} - T_d)}{Lp} \right) \right]^{0.5} \left[\frac{P_c}{100} \right]^{0.4}$$

The grain outside diameter is calculated as

$$D_o = D - (2 \times t) - (2 \times t_i) = 0.11m$$

The grain inside diameter is calculated as

$$D_i = D_o - (2 \times b) = 0.07m$$

The grain length would be calculated using the total volume of the propellant used which was calculated earlier

$$V_b = \frac{\pi}{4} L (D_o^2 - D_i^2)$$

Solving the equation for $V_b = 1.86 \times 10^{-3} m^3$ we get $L = 0.33m$

Next, we find the average burn area of the propellant grain to meet the requirements of the burn rate and burn time

$$A_b = \frac{F}{\rho_b r I_s} = 1.31 m^2$$

The mass flow rate of the gasses is given as

$$\dot{m} = m/t = 1.4 \text{ kg/s}$$

X. NOZZLE DESIGN

As the chamber pressure requirement is given in the design conditions so from the formulation of chamber pressure for isentropic flow relations of nozzles, we find the Mach number at the end of the C-D nozzle

$$P_o = P \left[1 + \frac{1}{2} (k-1) M^2 \right]^{\frac{k}{k-1}}$$

For $P_o = 8.5 \text{ MPa}$; $P = 101325 \text{ Pa}$; $k = 1.2$ (for selected propellant)

The mach number comes out to be $M = 3.3$

Using this mach number and the pressure ratio of chamber and atmosphere we can find the area ratio using the following relation

$$\frac{A_2}{A_1} = \frac{1}{M} \left[\frac{1 + \left[\frac{k-1}{2} \right] M^2}{\frac{k+1}{2}} \right]^{\frac{(k+1)}{2(k-1)}}$$

The area ratio comes out to be $\frac{A_2}{A_1} = 9.9$

The thrust coefficient C_F is a function of gas property k , the nozzle area ratio e ,

and the pressure ratio across the nozzle P_1/P_2 , but independent of chamber temperature. It is calculated as

$$C_F = \sqrt{\frac{2k^2}{k-1} \left(\frac{2}{k+1}\right)^{\frac{k+1}{k-1}} \left[1 - \left(\frac{p_2}{p_1}\right)^{\frac{k-1}{k}}\right] + \frac{p_2 + p_3}{p_1} \times \frac{A_2}{A_t}}$$

For idea conditions, P2=P3 so the C_F value comes out to be

$$C_F = 1.67$$

Now from the above calculated values we can calculate the throat area as

$$A_t = \frac{F}{p_1 C_F}$$

$$A_t = 3.66 \times 10^{-4} m^2$$

From this throat area the throat diameter is calculated as

$$D_t = \sqrt{\frac{4A_t}{\pi}}$$

$$D_t = 1.94 \times 10^{-2} m$$

Using the area ratio, the exit area of the nozzle is calculated as

$$A_e = \frac{A_e}{A_t} A_t$$

$$A_e = 3.63 \times 10^{-3} m^2$$

And the exit diameter from this exit are is calculated as

$$D_e = \sqrt{\frac{4A_e}{\pi}}$$

$$D_e = 6.80 \times 10^{-2} m$$

XI. PERFORMANCE

The total mass of the case is found by using the total volume of the metal casing which comes out to be

$$\text{Mass of case} = 3.11 \text{ kg}$$

The mass of propellant is calculated before which came out to be 3.32 kg

Total mass of the rocket motor comes out to be 6.5 kg

The total thrust acting on the rocket motor is given in design conditions as 5200N

So, the thrust to weight ratio comes out to be T/W=81.6

XII. COMPARISON WITH OTHER COMBINATIONS

A number of casing material and propellant combinations are used in a MATLAB code used for calculations and a comparison between their cost and performance is done

Table 5. Comparison of Rocket Motors

Rocket Motor		Thrust to Weight Ratio	Cost
Propellant	Casing		
HTPB+AP+Al	Alloy Steel	81.6	66\$
HTPB+AP+Al	Aluminum 2024	117	105\$
HTPB+AP+Al	Titanium	102	92\$
AN+Al+Binder	Alloy Steel	76.3	64\$
AN+Al+Binder	Aluminum 2024	93.4	103\$
AN+Al+Binder	Titanium	83.6	90\$
KN-Sucrose	Alloy Steel	56.6	54\$
KN-Sucrose	Aluminum 2024	71.5	93\$
KN-Sucrose	Titanium	65.7	80\$
KN-Dextrose	Alloy Steel	64.7	56\$
KN-Dextrose	Aluminum 2024	85	95\$
KN-Dextrose	Titanium	76.8	82\$

From the table it is clear that HTPB+AP+Al with aluminum gives the best thrust to weight ratio but the cost is highest, but in comparison to titanium with the same propellant the cost difference is not that much so it would be better to select aluminum as the casing and HTPB+AP+Al as the propellant

XIII. CAD MODEL

The CAD model for the designed rocket motor was made in CATIA V5

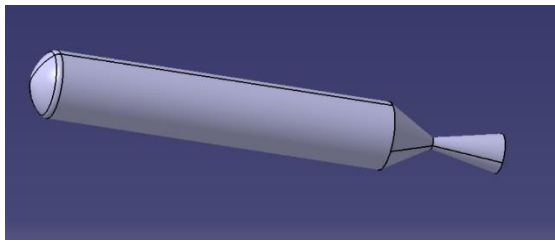


Figure 15. Rocket motor

The casing was designed as follows

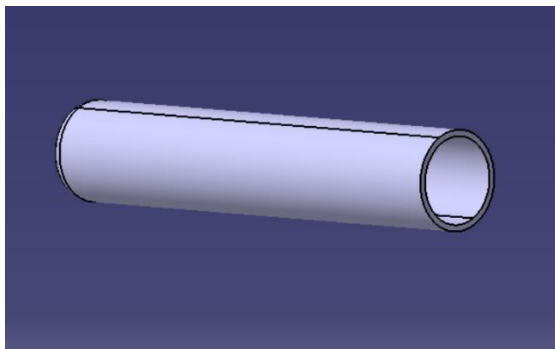


Figure 16. Casing

The nozzle was designed as follows

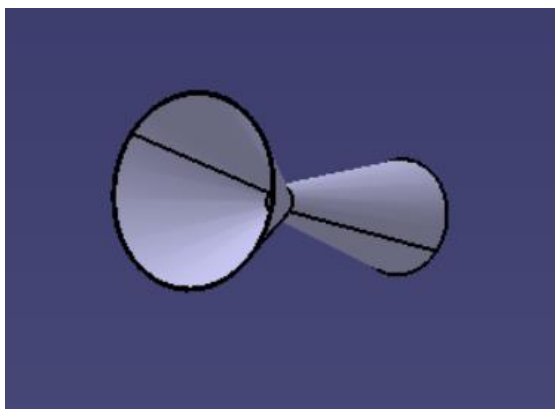


Figure 17. Nozzle

XIV. VALIDATION OF RESULTS

The given design conditions were analyzed in some rocket propulsion software and the results were compared with the analytically calculated values

COMPROP:

This is a software which gives results using one of the ratios either pressure ratio, area ratio or mach

number and using isentropic flow relations gives the value of the unknown ratios and terms.

The given pressure value was entered into the software which gave the results for the area ratio, mach number and density ratio

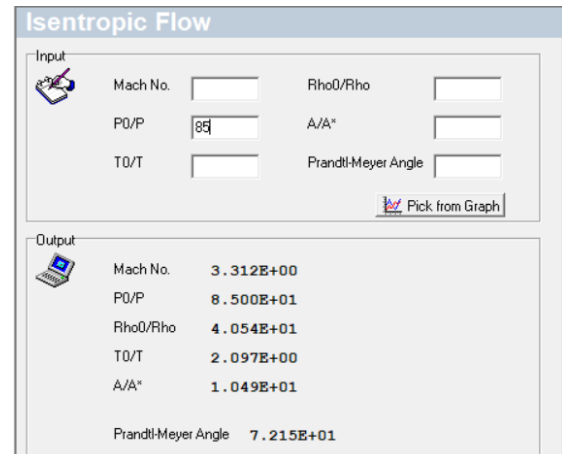


Figure 618. COMPROP Results

The results are quite close to the calculated values of area ratio and the Mach number

Rocket Propulsion Analysis

It is a software which gives the ideal results for the design of a specific rocket motor, and gives an estimation quite close to the original rocket to be designed.

The analytical results were compared to the results obtained from the software

Thermodynamic properties (O/F=4.000)

Parameter	Injector	Nozzle inlet	Nozzle throat	Nozzle exit	Unit
Pressure	8.5000	8.5000	4.9518	0.1013	MPa
Temperature	3831.6452	3831.6452	3662.0520	2668.2058	K
Enthalpy	-2013.9111	-2013.9111	-2452.3729	-5008.6668	kJ/kg
Entropy	8.1592	8.1592	8.1592	8.1592	kJ/(kg-K)
Internal energy	939.4053	939.4053	692.3717	-917.0702	kJ/kg
Specific heat (p=const)	4.5721	4.5721	4.4708	3.3528	kJ/(kg-K)
Specific heat (V=const)	3.9215	3.9215	3.8554	2.9857	kJ/(kg-K)
Gamma	1.1659	1.1659	1.1596	1.1229	
Isentropic exponent	1.1109	1.1109	1.1102	1.1053	
Gas constant	0.2175	0.2175	0.2157	0.2032	kJ/(kg-K)
Molecular weight (M)	38.2211	38.2211	38.5484	40.9206	
Molecular weight (MW)	0.03364	0.03364	0.03384	0.03554	
Density	10.1977	10.1977	6.2691	0.1869	kg/m ³
Sonic velocity	962.2640	962.2640	936.4421	774.1111	m/s
Velocity	0.0000	0.0000	936.4421	2447.3478	m/s
Mach number	0.0000	0.0000	1.0000	3.1615	
Area ratio	infinity	infinity	1.0000	12.8347	
Mass flux	0.0000	0.0000	5870.6559	457.4049	kg/(m ² -s)
Mass flux (relative)	0.000e-04	0.000e-04			kg/(N-s)
Viscosity	0.0001149	0.0001149	0.0001118	9.012e-05	kg/(m-s)
Conductivity, frozen	0.3213	0.3213	0.3096	0.226	W/(m-K)
Specific heat (p=const), frozen	1.777	1.777	1.773	1.709	kJ/(kg-K)
Prandtl number, frozen	0.6354	0.6354	0.6402	0.6814	
Conductivity, effective	1.645	1.645	1.621	0.9649	W/(m-K)
Specific heat (p=const), effective	5.808	5.808	5.802	4.407	kJ/(kg-K)
Prandtl number, effective	0.4056	0.4056	0.4002	0.4316	

Fractions of the combustion products

Figure 19. RPA Results

The results obtained from RPA were close to the analytical calculations made which validates the results

XV. CONCLUSION

A rocket motor was designed with the required specifications given initially using MATLAB and a comparison was made between certain combination of rocket motor materials. Then a cost analysis was done based on the materials chosen, the machining done and the propellant used. After that a CAD model was designed using CATIA V5. Using the CAD model, the fabrication of the rocket motor is in progress and the development of the propellant has been completed.

XVI. REFERENCES

[1] Numerical Investigation of Launch Dynamics for Subscale Aerial Drone with Rocket Assisted Take-Off (RATO), Timothy A. Eymann and John D. Martel

[2] Rocket Propulsion Elements by George P. Sutton and Oscar Biblarz.

[3] <https://www.nakka-rocketry.net/>

[4] <http://www.polytechnichub.com/different-solid-liquid-propellants/>

[5] <https://howthingsfly.si.edu/ask-anexplainer/what-difference-between-liquid-and-solid-fuel-rockets>

[6] Rocket Propulsion Analysis V2.3 Standard

[7] Surface Launch Simulations of an Unmanned Aerial Vehicle Loaded with Jet Assisted Takeoff Motors, David R. González *Naval Surface Warfare Center, Indian Head*

[8] CATIA V5

[9] Compressible Fluid Flow by Patrick H Oosthuizen & (2nd Edition) by William E Carscallen

[10] Introduction to Heat Transfer by F P Incropera & D P DeWitt (5th Edition) 2007

Effect of Different Grades of Carbon Black on Compressive Strength of Mortar

Muhammad Saeed Qasim^{1,a}, Faisal Shabbir^{2,b}

¹Research Assistant, Department of Civil Engineering, University of Engineering and Technology, Taxila, 47050, Pakistan

²Associate Professor, Department of Civil Engineering, University of Engineering and Technology, Taxila, 47050, Pakistan

Email address: ^a saeedqasim55@gmail.com, ^b faisal.shabbir@uettaxila.edu.pk

Abstract—The progress in the field of additives also upgraded the construction field. Use of additives plays the key role in improving the different properties of cement mixes. They are being used in the fields of strength, structural health monitoring and durability etc. Carbon Black (CB), one of additives, attracted the researchers in the field of health monitoring but very less research has been done on their effect on the strength of the cement mortar composites. In this research different grades of CB has been studied to find an optimum grade for the strength of CB based cement composites. The compressive strength behavior of three grades of CB (N330, N550 and N660) has been studied by replacing cement content by 5%, 7.5%, 10%, 12.5% and 15% by weight. Compressive strength was investigated at the age of 14, 28 and 120 days. The result showed that the compressive strength of CB based cement composites was more than control mix at the age of 28 and 120 days.

Keywords— Carbon Black, Grade, Compressive strength, N330, N550, N660

I. Introduction

Cementitious composites exhibit many properties including physical, mechanical, chemical and durability etc. Mechanical property like compressive strength is most important property of these materials.

Different types of additives and mineral admixtures were investigated in past to improve the physical and mechanical properties of cementitious materials like mortar and concrete. The most common of them were silica fume, fly

ash, ZnO, nanoSiO₂ and nanoFe₂O₃ [1–5].

Haruehansapong et al.[6] observed that the optimum particle size of nanosilica (40 nm) when replaced with 9% of cement gives max increase in strength. Pathak et al. [7] suggest that 1% replacement of ZnO with cement gives 18% more strength than normal concrete. Liu et al.[8] found that strength increase in concrete and mortar by use of nanoparticles depends on the particle size and its optimum percentage replacement with cement. Alyhya et al. [9] studied the behavior of waste carbon black (CB) in self compacting concrete as filler and observed that the optimum percentage is 5% when used as replacement of cement. Fly ash, silica fume and blast furnace slag were investigated by Demirboga [10] to find their effect on compressive strength of cement mortar. He concluded that 10 percent silica fume increase compressive strength by 17% at 120 days. Above that %age, it causes reduction in compressive strength. Fly ash slightly increases strength at 56 days when replaced by 20 percent of cement. Blast furnace slag increased the strength by 14 percent when 30 percent of cement is replaced at 120 days. The authors also concluded that fly ash, silica fume and blast furnace slag are less effective in mortar than in concrete.

CB also affects the compressive strength of mortar and concrete. Furthermore, it is one of those additives which are considered to develop some of

the desired properties in cement composites by different researchers [9, 11–14]. According to Chitra et al. [15, 16], CB used up to 8% in cement replacement can increase the compressive strength of concrete. Nagavkar [17] investigated the effect of CB on various properties of concrete. Due to its ability of heat resistance, its composites can be used to reduce the fire effect [18–20]. CB changes the resistivity, so it was also investigated by different authors that it can be used as strain sensing or pressure sensing in health monitoring field [21–23].

Due to its cheap cost, being readily available and highly effective in mortar, it is economical to use CB to increase compressive strength of cement mortar.

Few studies have been carried out to investigate the strength of mortar cubes by using CB as an additive. Further research efforts are needed on strength of mortar by comparing the effect of different grades of CB available in market for partial replacement of cement in different cement percentages by weight. This research shows a comparison between the grades of CB i.e. CB 330, CB 550 and CB660 used as a partial replacement in mortar, and depicts their effect on the compressive strength of mortar cubes. The optimum percentage of cement replacement by weight has been recommended for the three grades.

II. Experimental Methodology

A. Sample Preparation

Three grades of CB (i.e. N330, N550 and N660) having specific gravity of 1.8 were used to prepare mortar cubes. CB was passed through sieve #100 to get the CB powder. Ordinary Portland cement was used as binder and fine sand having size <1 mm was used. The ratio of cement-aggregates was maintained at 1:3 and the water-cement ratio was maintained at 0.55. Super plasticizer (SP) SP 470 was used as water reducing agent in percentage varying from 0%-4% depending upon the cement replacement by CB. The aggregates and cement

were added in water and mixed for 5 minutes in the auto mortar mixer. SP was added in mixture and mixed for 3 minutes. CB was then added to it and mixing was done for another 5 minutes. Moulds of size 2” x 2” x 2” were oiled and mix was poured into them. Good compaction was ensured to reduce voids. The homogenous dispersion of CB was ensured by proper mixing.

Control samples were prepared without any CB and is referred as control mix (CM). *Table VI* shows the mix proportion for each composition prepared. Five mixes were prepared for each CB grade. A total of 15 mixes for three grades have been prepared. Different nomenclature for CB grades was adopted: The samples with N330 named as A, N550 named as B and N660 named as C. The percentages of each grade in replacement of cement were 5%, 7.5%, 10%, 12.5% and 15% in different mixes.

Table VI. Mix Proportion for Each Composition (g)

Mix	Cement (g)	Sand (g)	Water (g)	CB (g)	SP (g)	CB grades
CM	1000	3000	550	-	-	-
A5	950	3000	550	50	20	CB330
A7.5	925	3000	550	75	25	
A10	900	3000	550	100	30	
A12.5	875	3000	550	125	35	
A15	850	3000	550	150	40	
B5	950	3000	550	50	20	CB550
B7.5	925	3000	550	75	25	
B10	900	3000	550	100	30	
B12.5	875	3000	550	125	35	
B15	850	3000	550	150	40	
C5	950	3000	550	50	20	
C7.5	925	3000	550	75	25	

C10	900	3000	550	100	30	CB660
C12.5	875	3000	550	125	35	
C15	850	3000	550	150	40	

A total of nine samples were tested for the compressive strength at the age of 14, 28 and 120 days for each mix, Curing was done at humidity level >95% and room temperature. Fig. 1 shows the sample placed in tank for curing.



Fig. 20. Curing of samples

B. Testing

After the age of 14 days, three samples from each mix A, B and C were taken out of curing tank and wiped out to saturated surface dry condition. Same was done for the samples tested at the age of 28 and 120 days. The samples were placed in compression testing machine and compressive strength of cubes was found out. Loading rate of 1 KN/sec was applied by the compression testing machine. Fig. 2 shows the apparatus for testing compressive strength of specimen.



Fig. 21. Computer controlled universal testing machine

III. Results And Discussions

Compressive strength of cement composites was found at the age of 14, 28 and 120 days. Average of compressive strength of three samples for defined mixes at a specified age was considered in results for the comparison.

Strength performance was calculated by taking CM as a reference as it is made of conventional mortar. Strength performance was calculated for each mix strength at age of 120 days as shown in formula in (1). The value greater than 100% shows better performance than conventional mix.

$$\text{Strength performance (\% age)} = 100 \times \frac{\text{Strength of mix}}{\text{strength of CM}} \quad (1).$$

Table VII shows the results of compressive strength and performance of all mixes A, B and C at different ages

Table VII. Compressive Strength of Mixes and Their Strength Performance

Mix	Compressive Strength (MPa)			Strength Performance (%age)
	14 days	28 days	120 days	
CM	9.6	12.8	14.0	100.00
A 5	12.4	14.0	17.2	122.86
A 7.5	15.6	21.2	23.2	165.71
A 10	12.8	16.4	18.0	128.57
A 12.5	9.2	13.6	14.0	100.00
A 15	6.8	9.2	10.0	71.43

Mix	Compressive Strength (MPa)			Strength Performance (%age)
	14 days	28 days	120 days	
B 5	8.4	10.0	12.0	85.71
B 7.5	12.8	17.6	18.8	134.29
B 10	12.4	15.2	16.8	120.00
B 12.5	11.2	15.6	16.0	114.29
B 15	7.2	9.6	10.0	71.43
C 5	8.0	9.2	11.2	80.00
C 7.5	11.2	15.2	16.4	117.14
C 10	11.6	14.4	15.6	111.43
C 12.5	8.0	11.2	11.6	82.86
C 15	6.4	8.4	8.8	62.86

The graph between percentage replacement of CB N330 (A) and compressive strength at different ages is shown in Fig. 3. It is clear from the results that A5, A7.5 and A10 shows greater compressive strength by +22.86%, +65.71% and +28.57% respectively as compared to CM at age of 120 days. Also, A12.5 shows +6.25% more strength than CM at age of 28 days whereas A15 is the only sample which shows -28.57% less strength than CM. A7.5 shows the maximum strength in all mixes when N330 used at age of 120 days.

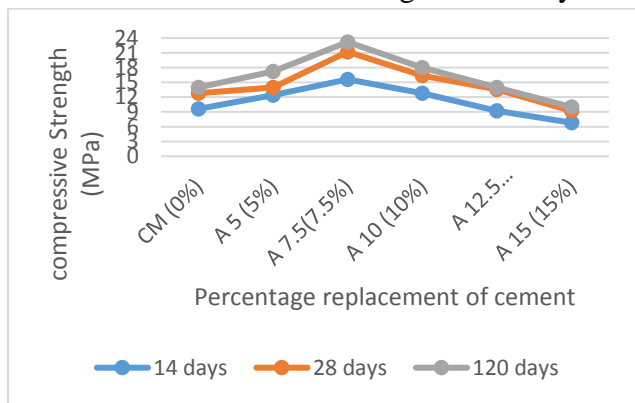


Fig. 22 Percentage replacement of cement vs. compressive strength for type A (CB N330 mix)

Fig. 4 shows the behaviour of percentage

replacement of CB N550 (B) and compressive strength at different ages. It can be found that B7.5, B10 and B12.5 show +34.29%, +20% and +14.29% greater compressive strength than CM at age of 120 days. When CB 550 content of less than 7.5 or more than 12.5 percent in cement replacement is used, the strength of cement composite is reduced. So it was found that B7.5 shows the maximum compressive strength of all mixes at age of 120 days when N550 used.

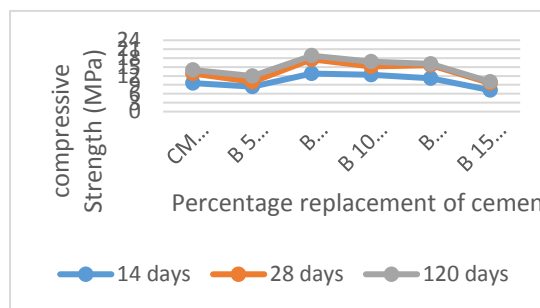


Fig. 23. Percentage replacement of cement vs. compressive strength for type B (CB N550 mix)

The relation between percentage replacement of CB N660 (C) used and compressive strength at different ages is shown in Fig. 5. The results show that C7.5 and C10 show +17.14% and +11.43% greater compressive strength than CM at age 120 days. When N660 content of less than 7.5% or more than 10% in replacement of cement is used the strength of composite is reduced. It was noted that C7.5 gives the maximum compressive strength when N660 was used at the age of 120 days.

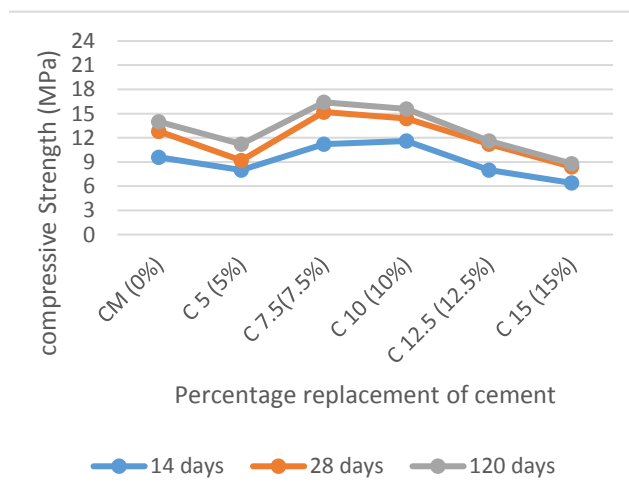


Fig. 24. Percentage replacement of cement vs. compressive strength for type C (CB N660 mix)

Possible reason behind increase in the strength is

the filling of micro pores in the cement mortar. In the CM, cement and sand is used and their size differ a lot as the average size of sand is around 0.5 mm and average cement is 15 micron having 95% particles below 45 micron. So a gap or void is created when paste is made and their bond can be improved by adding some material to fill the pores between cement and sand. Having particle size between cement and sand CB acts as a filler resulting in occupying the space between cement and sand. Due to this, the strength increases and the porosity of composites decreases. This trend continues to a certain percentage of CB normally called threshold content. Above the threshold value, the fillers are overloaded and proper textural binding of composites is not achieved hence reducing the strength. This threshold percentage to achieve maximum possible strength is known as optimum percentage of CB. Furthermore, among the grades of CB used, N330 is hard grade as compared to N550 and N660. Therefore it shows good compressive strength as compared to soft grades i.e. N550 and N660.

IV. Conclusions

From this research, it can be concluded that the CB can be used to increase the strength of cement composites. Any CB grade gave better results as compared to CM. Out of the three grades investigated in this study, N550 is better than N660 and N330 is better than N550. It has been noted that all the CB grades show their best compressive strength results at 7.5% replacement with cement. Among the grades, N330 is best in terms of compressive strength when cement is replaced at 7.5% by weight.

REFERENCES

- [1] B. Ali, L. A. Qureshi, M. A. Nawaz, and H. M. U. Aslam, "Combined Influence of Fly Ash and Recycled Coarse Aggregates on Strength and Economic Performance of Concrete," *Civ. Eng. J.*, vol. 5, no. 4, pp. 832–844, 2019, doi: 10.28991/cej-2019-03091292.
- [2] H. Li, H. gang Xiao, and J. ping Ou, "A study on mechanical and pressure-sensitive properties of cement mortar with nanophase materials," *Cem. Concr. Res.*, vol. 34, no. 3, pp. 435–438, 2004, doi: 10.1016/j.cemconres.2003.08.025.
- [3] P. Chindaprasirt, S. Homwuttiwong, and V. Sirivivatnanon, "Influence of fly ash fineness on strength, drying shrinkage and sulfate resistance of blended cement mortar," *Cem. Concr. Res.*, vol. 34, no. 7, pp. 1087–1092, 2004, doi: 10.1016/j.cemconres.2003.11.021.
- [4] J. Vera-Agullo et al., "Mortar and Concrete Reinforced with Nanomaterials," *Nanotechnol. Constr.* 3, pp. 383–388, 2009, doi: 10.1007/978-3-642-00980-8_52.
- [5] X. Shi, Z. Yang, Y. Liu, and D. Cross, "Strength and corrosion properties of Portland cement mortar and concrete with mineral admixtures," *Constr. Build. Mater.*, vol. 25, no. 8, pp. 3245–3256, 2011, doi: 10.1016/j.conbuildmat.2011.03.011.
- [6] S. Haruehansapong, T. Pulngern, and S. Chuchepsakul, "Effect of the particle size of nanosilica on the compressive strength and the optimum replacement content of cement mortar containing nano-SiO₂," *Constr. Build. Mater.*, vol. 50, pp. 471–477, 2014, doi: 10.1016/j.conbuildmat.2013.10.002.
- [7] A. Pathak, "Effect of Zinc Oxide Nanoparticle on Compressive Strength and Durability of Concrete," *Int. J. Res. Appl. Sci. Eng. Technol.*, vol. V, no. VIII, pp. 683–687, 2017, doi: 10.22214/ijraset.2017.8098.
- [8] J. Liu, Q. Li, and S. Xu, "Influence of nanoparticles on fluidity and mechanical properties of cement mortar," *Constr. Build.*

- Mater., vol. 101, pp. 892–901, 2015, doi: 10.1016/j.conbuildmat.2015.10.149.
- [9] W. Shober Saheb Alyhya, S. S. A. Alaa Abed Alameer, L. Mohammed Ridha Mahmmod, and ..., “Experimental Investigation on Self-Compacting Concrete with Waste Carbon Black,” *Int. J. Eng. Technol.*, vol. 7, no. 4.20, p. 414, 2018, doi: 10.14419/ijet.v7i4.20.26233.
- [10] R. Demirboğa, “Influence of mineral admixtures on thermal conductivity and compressive strength of mortar,” *Energy Build.*, vol. 35, no. 2, pp. 189–192, 2003, doi: 10.1016/S0378-7788(02)00052-X.
- [11] A. O. Monteiro, A. Loredo, P. M. F. J. Costa, M. Oeser, and P. B. Cachim, “A pressure-sensitive carbon black cement composite for traffic monitoring,” *Constr. Build. Mater.*, vol. 154, pp. 1079–1086, 2017, doi: 10.1016/j.conbuildmat.2017.08.053.
- [12] A. O. Monteiro, P. B. Cachim, and P. M. F. J. Costa, “Electrical Properties of Cement-based Composites Containing Carbon Black Particles,” *Mater. Today Proc.*, vol. 2, no. 1, pp. 193–199, 2015, doi: 10.1016/j.matpr.2015.04.021.
- [13] Y. Wang, Y. Zhao, X. Zhao, and R. Hai, “Mechanical and strain-sensing properties of cement-matrix composite containing nano-sized carbon black,” *Key Eng. Mater.*, vol. 815 KEM, pp. 203–209, 2019, doi: 10.4028/www.scientific.net/KEM.815.203.
- [14] S. Wen and D. D. L. Chung, “Partial replacement of carbon fiber by carbon black in multifunctional cement-matrix composites,” *Carbon N. Y.*, vol. 45, no. 3, pp. 505–513, 2007, doi: 10.1016/j.carbon.2006.10.024.
- [15] G. Chitra, P. V. Selvi, and D. Vijayalakshmi, “Carbon black as an additive in conventional concrete,” *Int. J. Emerg. Technol. Adv. Eng.*, vol. 4, no. 2, pp. 194–201, 2014.
- [16] T. M. Jeyashree and G. Chitra, “Experimental studies on concrete elements using waste carbon black as filler material,” *Asian J. Civ. Eng.*, vol. 18, no. 1, pp. 21–30, 2017.
- [17] G. N. Nagavkar, “Effect on properties of concrete with partial replacement of additives cement,” *Int. J. Eng. Sci. Res. Technol.*, vol. 6, no. 2, pp. 784–790, 2017.
- [18] J. Song, W. Yang, X. Liu, W. Zhang, and Y. Zhang, “ASA/graphite/carbon black composites with improved EMI SE, conductivity and heat resistance properties,” *Iran. Polym. J. (English Ed.)*, vol. 25, no. 2, pp. 111–118, 2016, doi: 10.1007/s13726-015-0404-6.
- [19] S. Mingqing, M. Xinying, W. Xiaoying, H. Zuofu, and L. Zhuoqiu, “Experimental studies on the indoor electrical floor heating system with carbon black mortar slabs,” *Energy Build.*, vol. 40, no. 6, pp. 1094–1100, 2008, doi: 10.1016/j.enbuild.2007.10.009.
- [20] M. I. N. Bin Yahya, “The Effect of Mixing Carbon Black N330 and N660 in Fiber Reinforcement Plastic Matrix System for Fire Retardance in Marine Application,” *J. Polym. Sci. Appl.*, vol. 2017, pp. 2–5, 2017, doi: 10.4172/JPSA.1000105.
- [21] H. Li, H. gang Xiao, and J. ping Ou, “Effect of compressive strain on electrical resistivity of carbon black-filled cement-based composites,” *Cem. Concr. Compos.*, vol. 28, no. 9, pp. 824–828, 2006, doi: 10.1016/j.cemconcomp.2006.05.004.
- [22] T. N. Tallman, S. Gungor, K. W. Wang, and C. E. Bakis, “Damage detection via electrical impedance tomography in glass fiber/epoxy laminates with carbon black filler,” *Struct. Heal. Monit.*, vol. 14, no. 1, pp. 100–109, 2015, doi: 10.1177/1475921714554142.

- [23] M. G. Pârvan, G. Voicu, and A. I. Bădănoiu,
“Study of hydration and hardening
processes of self-sensing cement-based
materials with carbon black content,” *J.
Therm. Anal. Calorim.*, vol. 8, 2019, doi:
10.1007/s10973-019-08535-8.

Effect of temperature on behavior of concrete with e-waste as partial replacement of aggregates

Muhammad Farrukh Javaid^{1,a}, Muhammad Irshad Qureshi^{1,b} and Shahzad Saleem^{1,c}
¹*Department of Civil Engineering, University of Engineering and Technology Taxila*

Email address: ^afarrukh000webs@gmail.com, ^birshad.queshi@uettaxila.edu.pk and ^cshahzad.saleem@uettaxila.edu.pk

Abstract—Plastic waste is an environmental hazard due to its low biodegradability and minimal recycling (only around 7% globally). With the ever-increasing advancement of technology, the proportion of electronic waste (E-waste) is also increasing significantly. This is specially an important issue for developing countries where most of E-waste is dumped now a days. Building and construction industry, on the other hand, account for almost 40% of energy related CO₂ emissions globally and is also responsible for depleting natural resources. Recycling of E-waste as an alternative construction material has the potential to address these issues. Past studies have explored the mechanical properties of plastic concrete and found that a 20% replacement of aggregates is feasible with some reduction in compressive strength. One important aspect of plastic concrete is its thermal properties and resistance to fire. The current study is focused on the fire resistance of concrete made with E-waste as partial replacement of aggregates i.e. coarse and fine aggregates. The concrete specimens were heated at 150° C and 300° C for 1 hour and the effect of fire on the mechanical properties of plastic concrete are explored and recommendations are presented regarding the decrease of strength properties due to fire.

Keywords—*e-waste aggregate, plastic concrete, waste management, temperature effects*

V. Introduction

The rapidly growing world's population and increased rate of urbanization has a huge impact on construction industry. It has increased the demand of construction making concrete the most widely used man-made construction material. Concrete is often said to be the second most utilized substance after the water on earth [1, 2]. The causes of this huge demand of concrete are its low cost, ease of application and high compressive strength. Now a days, construction without the use of concrete cannot be even imagined [3]. Such demand of concrete needs the resources from which its constituents i.e. cement, sand, gravel etc. are obtained. When the rate of extraction of resources like cement, sand or crushed aggregates exceeds the generation of natural resources, it causes environmental problems. This enormous consumption of concrete is resulting in eradication of natural sources of its constituents [1]. As the population is growing and the technology is advancing rapidly, the demand, utilization and waste is also increasing

[2]. Plastic materials had a vital role in progress of the society for the last 150 years. It is considered as a necessary part of our today's life as it meets a wide variety of public needs because of its useful properties such as good strength, ease of design, low density, durability, process-ability and low cost [4]. Many plastic materials that were beyond the reach in the past are now available at affordable prices. People now a days are changing themselves with the advancing technology and the old technology is being trashed. This trash is exerting pressure on environment creating the disposal issues [5]. One major plastic waste type is the waste generated from the trash of electronic appliances called as electronic plastic waste (E-waste). E-waste is increasing exponentially as the markets and industries of electronic appliances are increasing day by day.

United States Environmental Protection Agency (US-EPA) report categorized video, audio and information devices as means of electronic waste. Video devices include televisions (TV), flat panel TVs, DVD, Cathode Ray Tubes (CRT) and videocassettes recorder decks etc. Similarly, audio devices include compact audio systems, CD players, home radios and mp3 players. Information devices include mobile telephones, facsimile (fax) machines, laptop computers, printers, cordless/corded telephones, desktops and other computer monitors, laptops tablets and computer accessories like mice and keyboards. According to US-EPA estimate in 2007, 29.9 million desktops and 12 million laptops were discarded as a waste. According to EPA estimate 2008, about 3.16 million tons of e-waste was generated and the recycled amount was 13.6% or 430,000 tons of total waste. In 2013, about 366,000 tons were reported across 21 states in United States and

in 2014 volume increased by 6% about 390,000 tons [6, 7, and 8].

This waste needs to be dumped and disposed but due to its very low biodegradability it creates a serious waste management issue for the authorities. This electronic waste needs to be recycled just like some other recyclable waste materials. Plastic loses strength with number of recycling. So, an efficient approach is much needed in order to utilize this waste in a proper way and overcome the disposal issues. This can be helpful in sustainable growth. To save the natural resources of filler materials and to deal with the utilization of plastic waste are the two of the major concerns at present [9]. In order to meet the demands of filler material, researchers are trying to incorporate a variety of alternative materials in concrete now a days.

Similarly, some researches worked on the substitution of plastic waste in concrete in the form of aggregates (coarse or fine) or fibers. Zainab Z. Ismail has worked on the mechanical behavior of concrete made with percentage replacement of natural fine aggregate with plastic waste aggregate by 0%, 10%, 15% and 20%. As a result, compressive strength tends to decrease with increase in waste plastic ratio. The substitution of plastic waste in fabrifom shape showed crack propagation but this work is proved to be a good approach to reuse the waste plastic [10]. Likewise, some other authors also worked on the mechanical properties of concrete made with partial substitution of e-waste aggregate with natural fine aggregates. They replaced the natural fine aggregate with e-waste at different varying percentages up to 25%. Some researchers incorporated the e-waste in the form of thin fibers and some in the form of fine aggregate. A slight decrease in

compressive, tensile and flexural strength was observed with increase of plastic content. But they suggested the feasibility of utilizing the plastic waste as a construction material [1, 3]. Strength properties of concrete made with e-waste is also investigated using silica fume with replacement of cement and the resulting strength was higher than reference concrete mix [2].

Similarly, some researchers studied the properties of concrete made with e-waste as coarse aggregate substitution. A wide range of replacement ratio up to 40% is utilized in concrete replacing natural coarse aggregates. Same as fine plastic aggregate replacement, the decrease in strength is also observed in case of coarse aggregate replacement with e-waste aggregate. But the results are in permissible limits showing the feasibility to utilize the e-waste as aggregate in concrete [11, 12, 13 and 14]. K. Senthil Kumar investigated the effects of temperature and thermal shock on concrete made with partial replacement of coarse aggregate. The replacement ratio of High Impact Polystyrene (HIPS) used were 10%, 20%, 30%, 40% and 50%. Samples were exposed to 100, 200 and 300°C and then cool down with water. Concrete was observed under destructive and non-destructive tests. This type of concrete is recommended for non-structural applications and this is also suggested for thermal insulation and advantageous from energy point of view [15].

Researchers have recently worked on strength properties of concrete made with e-waste aggregate and suggested that 15-20% substitution of e-waste aggregates is feasible with slight reduction in strength. However, thermal behavior/fire resistance is a very important aspect to be investigated which has not been yet studied in case of concrete

made with e-waste aggregates. The current study is focused on thermal behavior/fire resistance of concrete made with partial replacement of e-waste aggregates.

VI. Materials and Methods

A. Cement

In this research work, locally and commercially available ordinary Portland cement (OPC Type-1 Fauji brand) is used. The nominal size of cement is 50um with specific gravity of 3.15 and bulk density 1440 kg/m³. The cement used in this study is according to international standards (ASTM C-150) and its properties provided by the manufacturer are given in the Table I below [16].

TABLE I. PROPERTIES OF ORDINARY PORTLAND CEMENT

Properties of Ordinary Portland Cement (Type I)		
<i>Properties</i>	<i>FCC L valu es</i>	<i>Standard Requireme nt ASTM C-150</i>
Initial setting time (minutes)	110	45 min (Min.)
Final setting time (minutes)	180	375 min (Max.)
3-days Compressive strength (Psi)	3259	1740 (Min.)
7-days Compressive strength (Psi)	5039	2760 (Min.)
28-days Compressive strength (Psi)	5844

B. Natral Fine Aggregate

Locally available Lawrencepur sand is used as fine aggregate in this research work. Various standard tests were performed on the sand to find out the properties which are given in Table II.

C. Natural Coarse Aggregate

The natural coarse aggregates used in this study are obtained locally from the Margalla Quarry. The coarse aggregates having maximum size of 20 mm are adopted for this work. Different standard test were carried out according to ASTM specifications to find properties which are mentioned in Table II.

D. Plastic Waste Aggregate

Electronic waste is purchased and the plastic from the whole scrap is separated mostly the computers, monitor bodies and keyboards. It is then processed in recycling plants. The plastic is heated and then crushed to the required size after cooling down. In the present study we incorporated the e-waste plastic aggregate both as a partial replacement of fine and coarse aggregates. The maximum size of plastic coarse aggregate is 19mm and that of plastic fine aggregates is below 4.75mm. Some other properties of natural fine aggregate, natural coarse and plastic aggregates are given in table II.

TABLE II. PROPERTIES OF NATRAL SAND, COARSE AGGREGATES AND PLASTIC AGGREGATES

Properties of Materials			
Properti es	Natur al Sand	Coarse Aggrega te	Plastic Aggregat es
Fineness Modulus	2.2	8.4
Specific Gravity	2.67	2.68	0.97

Water Absorpti on	4%	1.4%	0%
Bulk Density	1600 kg/m ³	1518 kg/m ³	620 kg/m ³
Impact Value	10.9%	2.24%
Abrasion Value	13%	8.68%

VII. Experimental program

In this study, concrete of M20 grade is prepared using mix ratio of 1:1.5:3 and a water-cement ratio of 0.45. Batching of concrete constituents is done. Concrete specimens are prepared by using the partial replacement percentages of 0%, 10%, 15% and 20% e-waste fine and coarse aggregates separately. Concrete mix groups, specimen IDs, standards size of specimens and temperatures are mentioned below in Table III.

The quantities of cement, sand, coarse aggregates and e-waste aggregates are calculated with w/c ratio of 0.45. Estimation of water is done based on w/c ratio which in this case is kept at 0.45. Also, a super-plasticizer is also added about 2% of cement but in addition to cement while mixing the water.

Mixing is done according to the standard ASTM C-192 in an electric mixer. The ingredients of concrete are dry mixed in the mixer or 2-3 minutes so that a homogeneous mix is formed then water and super-plasticizer are added and it is further left for 3-4 minutes to mix properly and poured out and checked for slump of every mix according to standard ASTM C-143.

The slump values are given in above Table III and slump values are observed to be increasing as the plastic aggregate content

increases. As the plastic has 0% water absorption and lighter in weight as compared to natural aggregate so the workability of concrete mix made with e-waste increases.

Then concrete is poured into standard size moulds (150mm X 300mm) for compressive strength according to ASTM C-172. Moulds are filled with concrete in three layers and compacted with tamping rod. Concrete moulds are left for 24 hours to set and then specimens are removed from the moulds and placed in water for curing of 28 days according to ASTM C192. After curing, samples are removed from the water and placed in open air and left for a day to dry the water or moisture. A set of samples is tested at room temperature against compressive strength according to ASTM C39. As the present study is about the thermal behavior/fire resistance of concrete made with partially replaced e-waste, the samples are placed in a muffle furnace. And the target temperature is set to 150°C with heating rate of 20°C/min and kept in the furnace for 1 hour after the target temperature is achieved. Similarly, the samples are also placed in furnace for the target temperature of 300°C and kept for 1 hour at elevated temperature. Concrete specimens after heating are shown in fig. 1 (a) and (b) below where the plastic aggregate can be seen bulging out of specimens.

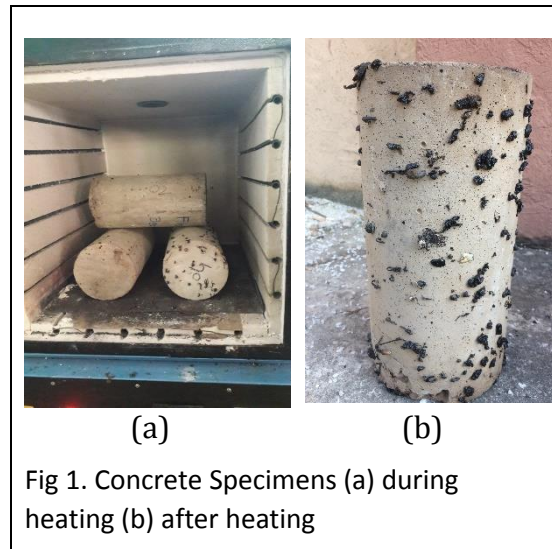


Fig 1. Concrete Specimens (a) during heating (b) after heating

After the exposure to heat, samples are taken out of furnace and placed in open air for 24 hours to cool down to the room temperature. Then compressive strength test is performed on the heated samples. Results of compression strength are show in Fig. 2 and Fig. 3.

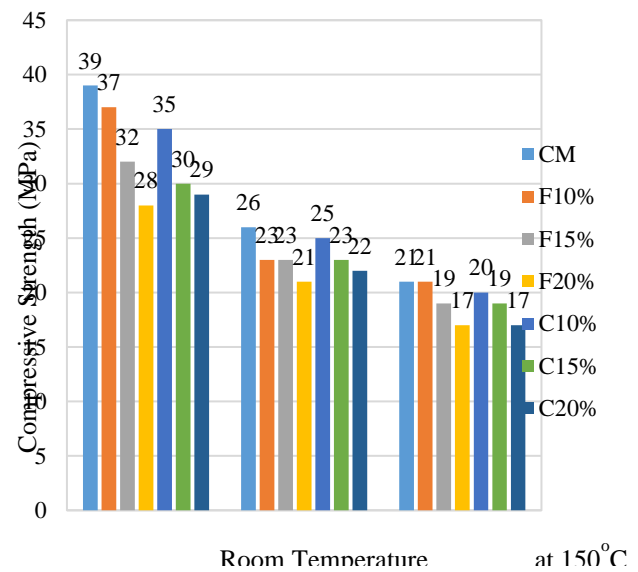


Fig. 2 Compressive strength of concrete samples at different temperatures

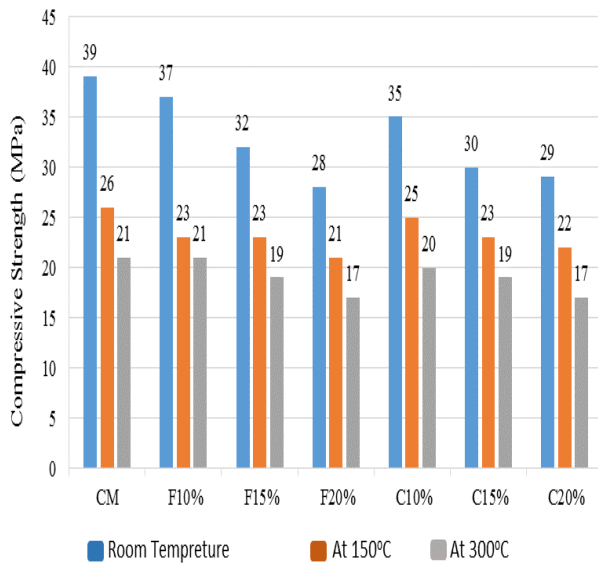


Fig.3 Reduction in Compressive Strength

From the results, a decrease in compressive strength can be observed with increase in plastic aggregate content and a decrease in strength with increase in temperature. As the plastic has low melting temperature so it gets melted when subject to higher temperatures. There is a reduction of about 23% to 34% in compressive strength when samples were tested after heating at elevated temperature of 150°C and about 36% to 46% reduction when the exposure temperature is 300°C. During the current study, plastic aggregates seemed to bulge out of concrete specimens making cavities inside the concrete when we heat samples about 300°C for 1 hour. Strength reduction between room temperature and 150°C is quite significant while the strength reduction between 150°C and 300°C is at slower rate. But still the e-waste concrete specimens possessed more than 50% residual strength after heating at elevated temperatures. The reduction in strength with e-waste substitution is because of weaker bond strength between plastic aggregate and the cement paste. The melting of plastic also causes the decrease in strength.

VIII. Conclusions

The current research work was aimed at finding the effect of temperature on strength of concrete made with e-waste aggregates. Overall 63 samples were tested at room temperature, at 150°C and at 300°C. When we simply replace the natural aggregates with e-waste aggregate, there is a decrease in compressive strength after 28 days curing but in permissible limit. The percentage reduction in strength at 150°C lies in range of 23% to 34%. And the percentage reduction of strength at 300°C is observed between 36% and 46%. The strength reduction is because of relatively weaker bond strength between plastic aggregates and cement paste. When samples are subjected to higher temperatures, they exhibit lessor compressive strength as compared to that at room temperature same as conventional concrete. We intended to go further beyond 300°C but due to low melting point of plastic aggregates, this is the limiting temperature. Plastic aggregate melts and tries to bulge out of concrete making cavities inside the concrete. Besides this effect, the concrete specimens showed more than 50% residual strength. That's why e-waste concrete is suggested to be used in non-structural member. A lot of research is still needed on every aspect regarding fire resistance and thermal behavior to introduce this technique and its frequent usage. The slight reduction in the compressive strength of concrete with e-waste can be overcome using admixtures. Research must be done on strengthening of e-waste aggregate concrete for its applications where fire damage may exist.

REFERENCES

- [24] J. K. S. R. Shamili, C. Natarajan, "An Overview of Electronic Waste as Aggregate in Concrete," *World Acad. Sci. Eng. Technol. Int. J. Struct. Constr. Eng.*, vol. Vol:11, no. No:10, pp. 1423–1427, 2017.
- [25] B. Harini and K. V Ramana, "Use of Recycled Plastic Waste as Partial Replacement for Fine Aggregate in Concrete," *Int. J. Innov. Res. Sci. Eng. Technol.*, vol. 4, no. 9, pp. 8596–8603, 2015, doi: 10.15680/IJIRSET.2015.0409106.
- [26] H. A. Bulut and R. Şahin, "A study on mechanical properties of polymer concrete containing electronic plastic waste," *Compos. Struct.*, vol. 178, pp. 50–62, 2017, doi: 10.1016/j.compstruct.2017.06.058.
- [27] M. Záleská, M. Pavlíková, J. Pokorný, O. Jankovský, Z. Pavlík, and R. Černý, "Structural, mechanical and hygrothermal properties of lightweight concrete based on the application of waste plastics," *Constr. Build. Mater.*, vol. 180, pp. 1–11, 2018, doi: 10.1016/j.conbuildmat.2018.05.250.
- [28] S. M. Ahirwar Pratiksha Malviya Tech Scholar Professor and V. Patidar Vikash Kumar Singh Professor Professor, "An Experimental Study on Concrete by using E-Waste as Partial Replacement for Course Aggregate," *IJSTE-International J. Sci. Technol. Eng. |*, vol. 3, no. 04, p. 7, 2016.
- [29] S. Pramila, M. H. Fulekar, and P. Bhawana, "E-Waste- A Challenge for Tomorrow," vol. 1, no. 3, pp. 86–93, 2012.
- [30] United States Environmental Protection Agency, "fact and figure sheet," United States Environmental Protection Agency, 2019. [Online]. Available: https://www.epa.gov/sites/production/files/2019/11/documents/2017_facts_and_figures_fact_sheet_final.pdf.
- [31] United States Environmental Protection Agency, "Electronic products generation and recycling," United States Environmental Protection Agency, 2016. [Online].
- [32] Dr. K. Tajne and Mrs. P. Bhandari, "WASTE PLASTIC USED AS A COARSE AGGREGATE IN CONCRETE" vol. 2, no. 01, 2016
- [33] Z. Z. Ismail and E. A. AL-Hashmi, "Use of waste plastic in concrete mixture as aggregate replacement," *Waste Manag.*, vol. 28, no. 11, pp. 2041–2047, 2008, doi: 10.1016/j.wasman.2007.08.023.
- [34] A. A. C. S. dhar, K. Mehraj Pasha, "E-Waste Management by Utilization of E-Plastics in Concrete Mixture as Coarse Aggregate Replacement," *Int. J. Innov. Res. Sci. Eng. Technol.*, vol. 04, no. 07, pp. 5087–5095, 2015, doi: 10.15680/ijirset.2015.0407008.
- [35] B. T. A. Manjunath, "Partial Replacement of E-plastic Waste as Coarse-Aggregate in Concrete," *Procedia Environ. Sci.*, vol. 35, pp. 731–739, 2016, doi: 10.1016/j.proenv.2016.07.079.
- [36] B. Mishra and R. S. Mishra, "A Study on Use of Plastic Waste Aggregate as Partial Replacement of Natural Coarse Aggregate in Cement Concrete Mix," pp. 11232–11238, 2015, doi: 10.15680/IJIRSET.2015.0411068.
- [37] R. Lakshmia and S. Nagan, "Investigations on durability characteristics of E-plastic waste incorporated concrete," *Asian J. Civ. Eng.*, vol. 12, no. 6, pp. 773–787, 2011.
- [38] K. S. Kumar and K. Baskar, "Effect of temperature and thermal shock on concrete containing hazardous electronic waste," *J. Hazardous, Toxic, Radioact. Waste*, vol. 22, no. 2, pp. 8–13, 2018, doi: 10.1061/(ASCE)HZ.2153-5515.0000387.
- [39] Fauji Cement, "Ordinary portland cement," Fauji Cement, 2019. [Online]. Available: <http://fccl.com.pk/products/ordinary-portland-cement/>.

TABLE III. EXPERIMENTAL PROGRAM DETAILS

Group	Slump (mm)	Specimen ID	Cross Section	Dimensions (mmxmm)	%age E-waste Replacement		No. of Specimens	Temperature
					Fine Aggregate	Coarse Aggregate		
1	65	CM-TR	Circular	150x300	0	0	3	Room Temp.
		CM-T-150	Circular	150x300	0	0	3	150°C
		CM-T-300	Circular	150x300	0	0	3	300°C
2	65	F10TR	Circular	150x300	10	0	3	Room Temp.
		F10-T-150	Circular	150x300	10	0	3	150°C
		F10-T-300	Circular	150x300	10	0	3	300°C
3	70	F15-TR	Circular	150x300	15	0	3	Room Temp.
		F15-T-150	Circular	150x300	15	0	3	150°C
		F15-T-300	Circular	150x300	15	0	3	300°C
4	75	F20-TR	Circular	150x300	20	0	3	Room Temp.
		F20-T-150	Circular	150x300	20	0	3	150°C
		F20-T-300	Circular	150x300	20	0	3	300°C
5	80	C10-TR	Circular	150x300	0	10	3	Room Temp.
		C10-T-150	Circular	150x300	0	10	3	150°C
		C10-T-300	Circular	150x300	0	10	3	300°C
6	130	C15-TR	Circular	150x300	0	15	3	Room Temp.
		C15-T-150	Circular	150x300	0	15	3	150°C
		C15-T-300	Circular	150x300	0	15	3	300°C
7	180	C20-TR	Circular	150x300	0	20	3	Room Temp.
		C20-T-150	Circular	150x300	0	20	3	150°C
		C20-T-300	Circular	150x300	0	20	3	300°C

CM= Control Mix, TR = room temperature, T= Temperature, F=plastic fine aggregate, C=plastic coarse aggregate

Techno-Economic Analysis of an Off-Grid Eco-Friendly Flywheel Based Bicycle Generator

Arsal Mehmood^{1,a}, Dr. Nayyar Hussain Mirjat^{2,b}, Prof. Dr. Zubair Ahmed Memon^{3,c}, Faraz Baig^{4,d}, Muhammad Ammar Jatt^{5,e}, Muhammad Saad Khan^{6,f}, Suhail Ahmed Shaikh^{7,g}

¹Department of Electrical Engineering, Mehran University of Engineering & Technology, Jamshoro, Pakistan

²Faculty of Electrical Engineering, Mehran University of Engineering & Technology, Jamshoro, Pakistan

³Faculty of Electrical Engineering, Mehran University of Engineering & Technology, Jamshoro, Pakistan

Email Address: ^{a)} arsalmehmood0713@gmail.com, ^{b)} nayyar.hussain@faculty.muett.edu.pk,

^{c)} zubair.memon@faculty.muett.edu.pk

I. INTRODUCTION

ABSTRACT---According to the Global Long-Term Climate Risk Index (CRI) 2020 by the German Watch, Pakistan is 5th among 10 countries affected most by climate change. Global warming and scarcity of Conventional resources are becoming major problem in the current scenario. Pakistan's most of the energy is produced by using conventional sources, but these sources are responsible for pollution and global warming which ultimately result in climate change. That's why today we need alternative non-conventional sources which are eco-friendly and sustainable. Solar and other renewable sources are several forms of energy which are used alternatively today. Along with those sources, Human Power is one of lasting source of energy which is wasted during workout. In this paper, a prototype modelling of an OFF-Grid Green Energy Harvesting Flywheel Based Bicycle Generator which could be used as an OFF-Grid Battery Charging System is developed to minimize the lighting load demand of MUET Gymnasium fitness facility. In this mechanism, efficient flywheel energy storage technology is implemented on KERS (Kinetic Energy Recovery System) static workout bicycle generator. Additionally, a relative cost analysis of prototype model, comparative analysis of present with proposed LED luminosity system in terms of CO₂ emission, energy unit saving, and its cost saving is analyzed. Feasibility analysis for the implementation of Energy and Climate Change (EC) indicators of Universitas Indonesia Green Metric World University Ranking (UIGM) is also undertake.

KEYWORDS--- Global Long-Term, Climate Risk Index, German Watch, Climate Change, Conventional Sources, Global Warming, Alternative, Renewable Sources, Human Power, Off-Grid, Green Energy, Kinetic Energy Recovery System, Bicycle Generator, Relative Cost Analysis, Comparative Analysis, LED Luminosity System, CO₂ Emission, Energy Unit Saving, Cost Saving, Feasibility Analysis, Sustainable, Energy and Climate Change (EC) Indicators, Flywheel, Universitas Indonesia Green Metric World University Ranking .

Pakistan is fifth most populous country in the world [1]. Electricity is the basic need of human life. With an on growing population, the needs of renewable electrical power and their usage is also increasing day by day. Every year the consumption rate of electricity is increasing globally, but in Pakistan the production rate is not growing sufficiently which consequently resulted in load shedding and increase in electricity price levels. Besides, fossil fuel cost is increasing day by day as well as government is also taking steps to make use of renewable sources. Today climate change is the biggest thread we faced. So, now it is time to gives attentions to generate power through renewable energy sources, instead of conventional energy source. According to National Electric Power Regulatory Authority (NEPRA) annual report 2018-2019 [2].

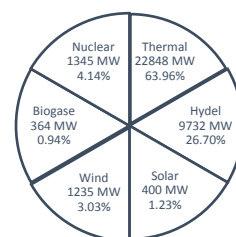


Figure 25: Represents overall installed capacity of Pakistan

From Fig.1, this is one of the main element that Pakistan is listed in Global Long-term Climate Risk Index (CRI) top 10 countries [3, 4].

In Paris Agreement 2015, United Nations Framework Convention on Climate change (UFCCC) presents an idea that developing countries needed to utilized environment friendly technologies to contribute in reducing emissions and prevent the world from global warming [5]. For that we need to focus on find an alternative renewable energy power plants, especially environmentally green and eco-friendly [6]. One type of an environmentally friendly clean and green energy power plant is an off-grid eco-friendly flywheel fitness exercise static KERS bicycle generator.

Human body can produce a significant amount of energy and Human muscles activity has the potential to produce power which can be used for low power application specially lighting load application. Use of exercise equipment for green energy source would be an exciting experience for participants as well as it provides a mean to generate power along with cycling exercise [7].

Flywheel-Based KERS Bicycle Generator has an ability to tap human energy to produce electricity quickly and efficiently. The primary function of flywheel is to works as an energy accumulator and to reduce the fluctuation in speed. It absorbs the energy when demand is less and releases the same when it's required, which is the technical and engineering aspect of harvesting energy [8, 9]. This flywheel technology inherits many advantages that are environmentally friendly and has low maintenance, long life with no degradation. That's why even NASA (National Aeronautics and Space Administration) Glenn Research center has employed Flywheel energy storage systems for over three decades [10].

The objective of this research is to develop a practical prototype of an OFF-Grid Green Harvesting Bicycle Generator with highly efficient flywheel energy storage system, which could act as well as an OFF-Grid Battery Charging System. This model will be proposed as a technological solution to minimize and to overcome the lighting load demand dependency of MUET Gymnasium on WAPDA and it will be suggest as a proposal for the implementation of UI Green Metric (UIGM), Energy and Climate Change (EC) indicators [11].



Fig 26: Represents Energy and Climate Change Indicator of Universitas Indonesia Green Metric World University Ranking



Fig 27: Represents Criteria and Indicators of Universitas Indonesia Green Metric World University Ranking [12]

According to the Ranking released by Universitas Indonesia Green Metric in 2019, MUET is 271st Worldwide, 2nd in all over Pakistan while 1st in Sindh Province University rankings. Although, in terms of implementing Energy and Climate Indicators of UIGM they listed MUET 275th best Globally [13].

Ranking	University	Country	Total Score	Setting & Infrastructure	Energy & Climate Change	Waste	Transportation	Water	Education & Research
271	Mehran University of Engineering & Technology	Pakistan	5625	1050	1100	675	1100	425	1275

Fig 28: Represents Global Ranking of Mehran University of Engineering & Technology in Green Metric World University [14]

Ranking	University	Country	Total Score	Setting & Infrastructure	Energy & Climate Change	Waste	Transportation	Water	Education & Research
275	Mehran University of Engineering & Technology	Pakistan	5625	1050	1100	675	1100	425	1275

Fig 29: Represents Global Ranking of Mehran University of Engineering & Technology in Green Metric World University for the Implementation of Energy and Climate Change Indicators [15]

Our proposed mechanism is beneficial in maintaining sustainability and improving global ranking through the implementation of EC indicators.

Alternatively, this research also gives a comparative analysis of present less-efficient 60 Watts tube light Lighting System with the highly efficient 6 Watts LED lighting System in terms of Electrical Energy Unit Consumption Saving, its Cost Saving and its related Green House Gases (GHG) emission saving.

II. LITERATURE REVIEW

Literature review suggests that there is considerable work done towards the utilization of bicycle generator as renewable energy source globally. However, there is limited evidences in the literatures about any techno-economic study which undertaken for the designing, development and implementation of an “Off-Grid Flywheel Based Bicycle Generator” as renewable green energy source to meet the Lumosity demand of a Gymnasium Fitness Facility through an efficient lighting system as some of the literature are as follows:

Flywheel based Bicycle Generator can be used as a mode of transportation as it provides low cost mobility facility along with some health benefits the working principle is to convert the rotational energy of the rare wheel into kinetic energy to recharge the battery [16].

Bicycle-based human power generation system can harvest power of 50 W which can be utilized for the low power off-grid rural electrification to charge battery for the purpose of lighting the home with low wattage LED lamp during the periods of necessity [17].

Gymnasium bicycle is an Electro-Mechanical system which tap harvest electrical energy by using alternator by the conversation of pressure energy of human muscles to kinetic energy [18].

Riding bicycle is a good source of Power as well as a good exercise. According to a research, humans are capable to generate around 100 W of power while riding bicycle. However, this power is wasted without our knowledge. The dynamo or alternator can harvest cyclers generated energy while riding which could be used to charge small devices, laptops, and mobiles [19].

Human powered gyms are those gyms which uses equipment’s like treadmills, stationary bikes and rowing machine to generate green and sustainable energy which not only benefits environmentally but also economically [20].

Green Energy Harvesting (EV) by using wastage energy during activity through Gymnasium bicycle is an economical generation of electricity since conventional sources decreasing day by day [21].

Power Generation by pedaling bicycle is a great resource of clean energy as well as it serves as a

mode of transportation to power the un-electrified village by using either alternator or dynamo [22].

Pedaling bicycle helps in maintaining a good physic as well as it serves as a good source of green energy generation by using dynamo which is then used to charge mobiles, iPod, Laptops [23].

III. METHODOLOGY

In human’s life, electricity is the basic requirement. Every year electricity consumption is increasing by 10% but when there is no simultaneous increase in production, then the consequences resulted in the form of increase electricity prices and load shedding Alongside the availableness of fossil fuels are getting reduced. In this case study we have proposed the general technique to produce electricity from mechanical energy. The concept of this study is

to use the wasted kinetic energy in gymnasium while work out to produce electricity.

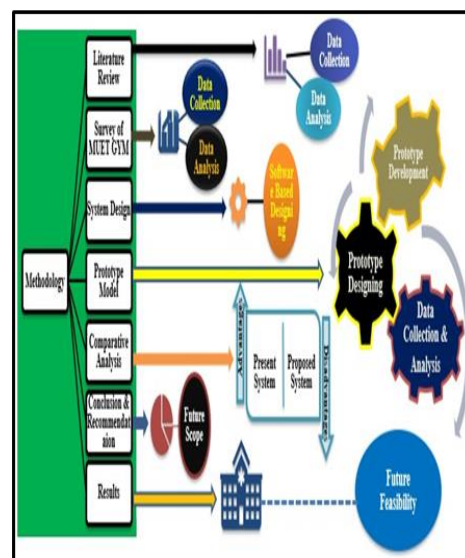
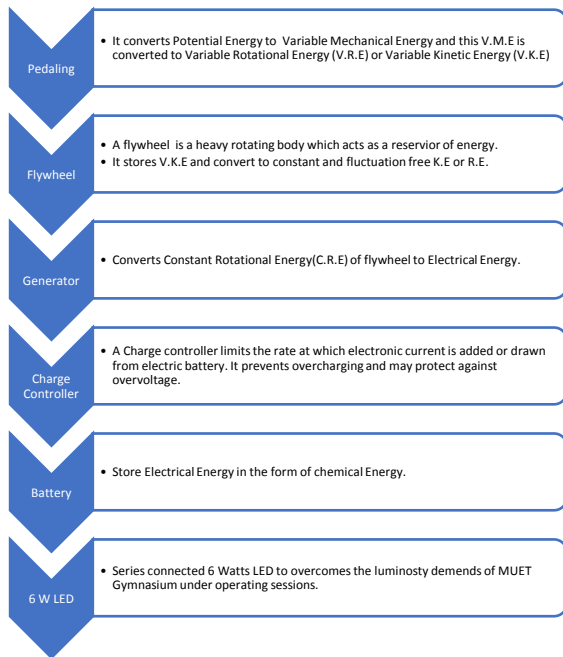


Fig 30: Research Methodology Framework

Table 8: Research Flow Diagram



I. DATA COLLECTION & SURVEYS

In this review, a survey is performed for the data collection from MUET Gymnasium fitness facility.

Questionnaire method is used for the determination of GYM operating hours, Operating sessions, Power ratings present appliances, Overall load demand, Lighting load demand in the respective sessions, Quantity of luminosity appliances, Frequency of peoples in the respective sessions and their equipment's of concern.

Table 9: Data collection from Gymnasium fitness facility

DATA	SPECIFICATIONS
NO. OF TUBELIGHTS	30
ENERGY CONSUMTION OF TUBELIGHT	60-70 W
TOTAL LIGHTENING CONNECTED LOAD	1.8 KW

Table 10: Represents operating hours of Gymnasium

GYMNASIUM OPERATING HOURS	
1 SESSION	9 AM - 2:30PM
2 SESSION	3:30 PM – 9 PM
TOTAL OPERATION HOURS	11 HOURS

Table 11: Represents load demand of fitness facility

LOAD CONSUMPTION DURING TOTAL OPERATING HOURS	
1 SESSION	1 hr. (IN BED LIGHT) 8 TUBLIGHT
2 SESSION	6 PM– 9:30 PM
TOTAL LOAD CONSUMPTION HOURS	480W + 6.3KW=6780W

II. DATA ANALYSIS

The results of collected data analysis are as follows:

Table 12: Represents classifications of PMDC Generators with present and proposed lighting capacity

Classification of DC PMDC GENERATOR	PRESENT TUBELIGHT 60W TUBELIGHT SYSTEM 1 TUBELIGHT= 60W	PROPOSED 6W LED LIGHTING SYSTEM 6 WATTS 1 LED = 6W
50 WATTS	NOT A SINGLE TUBELIGHT	8 LED
100 WATTS	1 TUBELIGHT	16 LED
250 WATTS	4	41 LED
300 WATTS	5	50 LED
500 WATTS	8	83 LED
1000 WATTS	16	166 LED

III. SYSTEM DESIGNING

Design of the proposed system is given by:

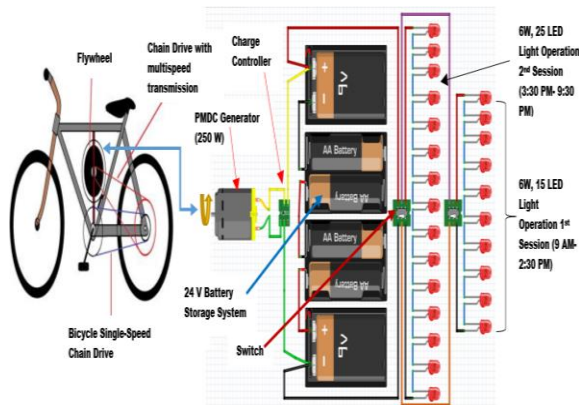


Fig 31: Represents Proposed System Design with 250W PMDC, 24 V battery, Charge Controller, Switches and Series connected 6W 40 LED (1st session 15 LED + 2ND session 25 LED) fitness facility through Frizing Software



Fig 33: Represents Hardware model of an Off-Grid Eco-friendly Green Energy Harvesting (EH) Flywheel Based Bicycle Generator.

IV. PROTOTYPE INTERNAL MECHANISM

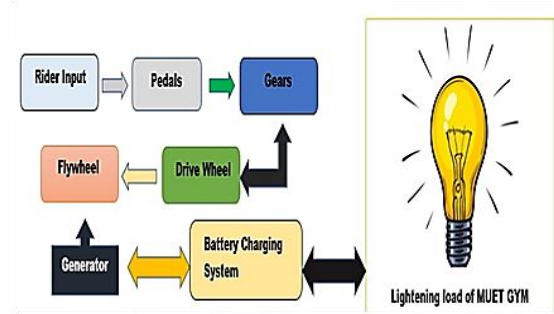


Fig 32: Represents prototype model internal mechanism

V. HARDWARE MODEL COMPONENTS CONFIGURATION

The below figure represents the basic configuration of “Off-Grid Green Energy Harvesting (EH) Flywheel Based Bicycle Generator” with specialized and unique flywheel energy accumulation technology integration.

IV. RESULTS & ANALYSIS

The main objective of this prototype development research is to initiate a self-sufficient gymnasium phenomenon which can sustain its all lighting load by the utilization of waste mechanical energy during workout and convert it down into electrical energy.

This project presents an economical and technological solution of load shedding and as well as it could serve as a backup energy resource or uninterruptable power supply (UPS) by using battery.

Additionally, power production by the flywheel-based bicycle generator provides us opportunity to minimize the atmospheric pollution which is nowadays a government policy.

Flywheel-based bicycle generator is very cheap. Since, we know that cost of fossil fuel is increasing day by day and this project is not depending on those.

It serves dual purposes benefits simultaneously. Firstly, physical fitness through exercise of muscles, and legs. Secondly, green, and eco-friendly power generation through those healthy activities at the same time.

The initial result of the study for energy saving and its cost saving is given by the formula as:

I. Calculations for Energy Saving

Energy Saving,

$$C = A - B \quad (1)$$

A = (1st session operating hours × Sum of 60 W connected load operates in 1st session) + (2ND session operating hours × Sum of 60 W connected load operates in 2ND session)

B = (1st session operating hours × Sum of 6 W connected load operates in 1st session) + (2ND session operating hours × Sum of 6 W connected load operates in 2ND session)

Table 13: Represents initial results of the study for Energy Saving

Comparison	60 W Tube light System Load Consumption (A)	6 W LED Lightening System Load Consumption (B)	Energy Consumption Saving by using 6 W LED System C = (A-B)
Daily	6.780 KW	250 W	6530 KW
Weekly	47.46 KW	1.750 KW	47.21 KW
Monthly (29 Days)	196.62 KW	7.250 KW	196.370 KW
Annually (305 Days)	2067.9 KW	76.250 KW	2067.65 KW

II. Calculations for Cost Saving

Comparison	CO ₂ Emission in 60 W Tube Light System for Wind and Solar Emission Factor=0.501tco ₂ Per MWH (Other Source)	CO ₂ Emission in 6 W LED System for Wind and Solar Emission Factor=0.600 tco ₂ Per MWH (Wind & Solar)
Daily	0.00339 Ton of CO ₂	0.004068 Ton of CO ₂
Weekly	0.02377 Ton of CO ₂	0.0284 Ton of CO ₂
Monthly (29 Days)	0.09850 Ton of CO ₂	0.1220 Ton of CO ₂
Annually (305 Days)	1.0360 Ton of CO ₂	1.484 Ton of CO ₂

Cost Saving D,

$$D = C \times \gamma \quad (2)$$

C = Energy unit saving(daily/weekly/monthly)

γ = Cost Per Price of single unit of Energy

Table 14: Represents initial results of the study for Cost Saving

Comparison	Saving (1 Unit = 18 Rupees in Pakistan)
Daily	117.54 Rupees
Weekly	849.78 Rupees
Monthly (29 Days)	3534.66 Rupees
Annually (305 Days)	37217.7 Rupees

Daily	117.54 Rupees
Weekly	849.78 Rupees
Monthly (29 Days)	3534.66 Rupees
Annually (305 Days)	37217.7 Rupees

III. Calculations for CO₂ Emission Saving

Primary electricity production in Pakistan from thermal (oil, natural gas, etc.) as shown in fig:1, and

$$1\text{KWH} = 0.001\text{MWH}$$

Since,

Energy produce in this proposed “Off-Grid Eco-Friendly bicycle generator” is 100% green. So, there is no CO₂ emission.

Therefore,

The amount of CO₂ Emission saving through proposed idea as compare to 60 W tube light system is given by the formula as:

$$\text{CO}_2 \text{ Emission Saving} = \text{Energy consume while 60W system operates in KWH} \times \text{CO}_2 \text{ Emission factor for solar, wind or other sources} \times 0.001 \text{ MWH Per KWH}$$

CO₂ Factor for wind and solar is 0.600 ton CO₂ per Megawatt hours .While its value for other source is 0.501 ton CO₂ per Megawatt hours according to the Asian Development Bank [24].

Table 15: Represents initial results of the study for Co₂ Emission Saving

V. CONCLUSION

Pakistanis are facing electricity crisis whereas higher electricity tariffs are another burden for the consumers. Higher Education Commission of Pakistan provides students’ academic as well as some extra curriculum opportunities for the grooming of generation. However, they fetch funding from Government. Mehran University has a gymnasium fitness facility where enough electricity is consumed which could be met through a unique and innovative alternative energy

generation prospective to save energy, cost, Green House Gas (GHG) Emission by an implementations of UIGM Energy & Climate indicators through a feasibility analysis approach .

REFERENCE

- [1] "Worldometer," [Online]. Available: <https://www.worldometers.info/world-population/pakistan-population/>.
- [2] "NEPRA Annual Report 2018-19," National Electric Power Regulatory Authority of Pakistan, 2018-2019.
- [3] "German Watch," [Online]. Available: <https://germanwatch.org/sites/germanwatch.org/files/publication/20432.pdf>.
- [4] "Ministry Climate Change Pakistan," 2010. [Online]. Available: <http://mocc.gov.pk/moclc/userfiles1/file/ECCO/Chapter-07.pdf>.
- [5] "United Nations Climate Change Conference," Paris, 2015.
- [6] P. P. a. D. D. F. S. Prabowo, "Eco-electric energy generator system using human exercise activities," vol. 197, p. 11010, 2018.
- [7] "Youtube," [Online]. Available: <https://www.youtube.com/watch?v=OZQz59NpIS8>.
- [8] "Clubtechnical," [Online]. Available: <https://clubtechnical.com/flywheel>.
- [9] "Wikipedia," [Online]. Available: <https://en.wikipedia.org/wiki/Flywheel>.
- [10] "Wikipedia," [Online]. Available: https://en.wikipedia.org/wiki/Flywheel_energy_storage.
- [11] "UI GreenMetric," [Online]. Available: <http://greenmetric.ui.ac.id/criteria-indicator/>.
- [12] "UI Green Metric," [Online]. Available: http://www.ireg-observatory.org/ireg-8/presentations/V/Riri-Fitri-Sari-UI-GreenMetric-PPT_IREG8_06052016.pdf.
- [13] "Mehran University of Engineering & Technology," [Online]. Available: <https://www.muett.edu.pk/sustainability>.
- [14] "UI GreenMetric," 2019. [Online]. Available: <http://greenmetric.ui.ac.id/overall-rankings-2019/>.
- [15] "UI GreenMetric," 2019. [Online]. Available: <http://greenmetric.ui.ac.id/rankingindicator2019/?indicator=2>.
- [16] P. S. J. P. K. Yadav R, "Flywheel Based Bicycle Generator," *IJARIE*, vol. 2, no. 5, 2017.
- [17] T. L. U. S. A. a. J. M. B. B. Shenoy, "Human Muscles Energy Harvesting : Model and Application for low power load," in *8th IEEE India International Conference on Power Electronics (IICPE)*, 2018.
- [18] K. M. U. M. M. A. K.M Ahsan-uz-Zaman, "Generation of Electrical Power using Gymnasium Bicycle," in *IEEE Region 10 Humanitarian Technology Conference (R10-HTC)*, Dhaka, 2017.
- [19] B. S. a. D. Reddy, "Generation of Power from Bicycle Pedal," *International Journal of Advanced Research in Electrical Electronics and Instrumentation Engineering*, vol. 4, no. 10, pp. 8429-8434, 2015.
- [20] N. S. O. S. a. B. R. B. Chalermthai, "Recovery of useful energy from lost human power in Gymnasium," in *IEEE 15th International Conference on Environment and Electrical Engineering (EEEIC)*, Abu Dhabi, 2015.
- [21] M. T. K. M. A. B. U. M. H. & T. G. M. Ullah, "Harvesting green Energy from wastage energy of human activities using gymnasium bicycle at Chittagong City," in *3rd International Conference on Green Energy and Technology (ICGET)*, Chittagong, 2015.
- [22] P. S. V. R. M. P. a. R. K. R. K. Megalingam, "Pedal power generation," *International Journal of Applied Engineering Research*, vol. 7, no. 11, pp. 699-704, 2012.
- [23] M. C. K. K. K. S. a. A. S. R. Suhalka, "Generation of Electrical Power using Bicycle Pedal," *International Journal of Recent Research and Review*, vol. 7, no. 2, pp. 63-67, 2014.
- [24] "Asian Development Bank," 2017. [Online]. Available: <https://www.adb.org/documents/guidelines-estimating-ghg-energy-projects>.

Appraisal of Stone Processing Industry Wastage as an Admixture for Soil Improvement

Qammar Abbas^{1,a}, Muhammad Usman Arshid^{1,b}, Syed Shujaa Safdar^{2,c} and Raja Abubakar Khalid^{3,d}

¹ *University of Engineering and Technology Taxila*

² *Capital University of Science and Technology Islamabad*

³ *The University of Lahore Islamabad Campus*

Email address: ^a) qammarabbas175@gmail.com, ^b) usman.Arshid@uettaxila.edu.pk, ^c) dr.shujaasafdar@cust.edu.pk and ^d) abubakr_rajah@hotmail.com

Abstract— Removal and replacement is technique being employed for the projects encountered with A-6 or A-7-5 types of Soils, but it require extra financial support along with requirements of considerable time for its implementation. The current research work explore in-situ improvement of such soils using marble stone dust as an admixture. Marble stone dust was added in variable percentages (0%,5% and 10%) and the resulting effect was assessed by comparing index properties, Engineering properties and shear strength parameters. The soil properties considerably improved with the addition of marble stone dust. The outcome of the study established the suitability of proposed admixture for the in-situ improvement of soil. It may not only reduce the cost of the projects but also shorten the time consumed for the soil improvement.

Keywords— *Expansive soil, admixture, marble stone waste, CBR, UCS*

I. Introduction

Soils having expansive characteristic are the problematic soils that experience huge volume changes when they come into contact with water and severely impair the light and heavily loaded structure. Soil of Expansive nature are found in many parts of world, and these type of soil caused severe damage to the pavement subgrade layer due to the action of capillary rise or poor drainage system, which may lead to the failure of pavement[1].

Expansive soil have a concern of research for many investigations especially for road projects. The pavement may undergo cracking due to the uneven heave because of wetting and shrinkage of subgrade during drying. To rehabilitate the existing pavement laid on the bed made up of expansive soils, geosynthetic layer was being placed on existing pavement over which asphalt layer is laid [2]. [1] studied the volume expansion effect on road pavement system using Oedometer and CBR mold, CBR tests were performed to predict the swell percentage and swelling/expansion pressure of subgrade soil with different moisture content. As a result it was concluded that with the increase in the moisture content, swell percentage and swelling pressure decreases at a given surcharge load.

Different materials have been explored to stabilize the expansive soil in different parts of the world. Apart from many techniques addition of admixtures has been widely accepted. [3] suggested that expansive nature of the soils can be reduced using additives like Fe₂O₃, CaO, and some polymers. Many researchers have said that marble stone dust has very high lime content of calcium oxide up to 55 % by total weight [4]. The amount of marble stone waste discharged as during block and tiles production at the quarries is equal to 40-60% of the total production out of that very small portion of the waste stone marble products is used economically[5]. [6] had practically proved that marble dust powder is effective waste material obtained from stone processing industry for the stabilization of expansive nature soil. Index properties as well as engineering properties of weak soil could be improved. [7] made a research effort to evaluate the recovery and reuse of byproducts obtained from marble processing industries quarries as well as processing plants produce large amount of waste during excavation, sawing, polishing and water treatment. It was concluded that calcium carbonate dust particles are very fine particles and have no impurities can be used as an admixture.

Marble stone waste is a solid waste that is produced by the marble stone processing industry, which are available in Pakistan abundantly. Studies showed that the marble production throughout the world was almost 21.7 million tons in 1986; However in 1998, this was significantly increased up to 51 million tons [8]. Expansive soils are abundantly available in Pakistan especially in the areas like Dera ghazi khan, Dera Ismail Khan, Lahore and Rawalpindi. Different techniques are required to stabilize such type of soil such as chemical stabilization and addition of different admixture.

II. materials & methodology

In order to carry out the research work, Material collection and lab tests were performed after detailed literature review.

A. Materials

Soil samples was taken from two sources Kangota Syedan, Sihala zone -V, Islamabad and Dandi Gujran near Rawalpindi Pakistan.



Figure II-1 Collection points of Expansive Soils

B. Marble Stone Waste

Marble stone waste was collected from marble industry located at T-chowk Rawat Pakistan.



Figure II-2 Collection point of Marble stone waste

C. Soil properties

Following soil properties of the proposed soil were examined using marble stone dust as an admixture.

Index properties

Engineering properties

Shear Strength parameters

III. RESULTS AND DISSCUSION

The collected samples were analyzed in the laboratory. The study results have been discussed in subsequent section below.

A. Index propertis

Basic index properties (L.L, P.L & P.I) as well as sieve size analysis test ASTM D-6913 was performed for the classification of collected soil samples. Both soil were found to be of expansive nature (A-7-5 and A-6). Tests results are given in Table 1.

TABLE 16. SOIL PROPERTIES

Sample Location	Grain Size Analysis			Atterberg's Limits			Soil Classification
	Percent Passing %			L.L	P.L	P.I	
	#10	#40	#200	%	%	%	AASHTO Classification
Dandi Gujran	99.36	98.77	96.13	45	28	17	A-7-5
Kangota Saidan Sihala	98.72	96.29	92.63	37.8	21.9	15.9	A-6

1) *Liquid Limit test results*

Figure 1 shows the combine results of A-6 and A-7-5 soil liquid limit test (ASTM D-4318) result by addition of marble stone waste in varying percentage. Results shows that liquid limit of A-6 soil and A-7-5 soil was decreased by the addition of marble stone waste up to 15% and 20% after liquid limit of both soil was decreased.

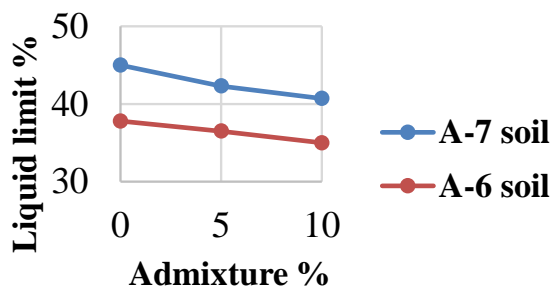


Figure III-1 Combine result of Liquid limit with varying %age of marble stone waste

2) *Plastic Limit*

Figure 2 shows the plastic limit test results of A-6 and A-7-5 soil sample prepared after addition of marble stone waste in different percentages. Results shows that plastic limit of A-6 soil and A-7-5 soil was decreased by the addition of marble stone dust.

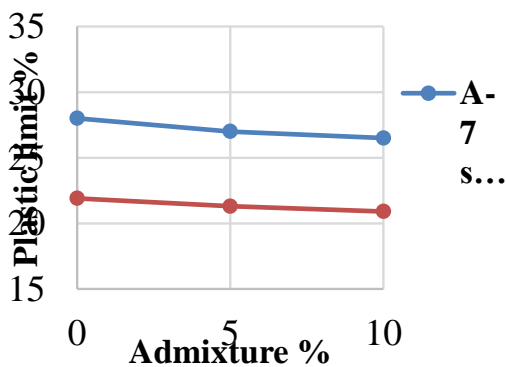


Figure III-2 Combine result of Plastic limit with varying %age of marble stone waste

3) **Plasticity Index**

Figure 3 shows the plasticity Index results of A-6 and A-7-5 prepared soil samples after addition of marble stone waste. Results shows that plasticity index of A-6 soil and A-7-5 soil was decreased by the addition of marble stone waste.

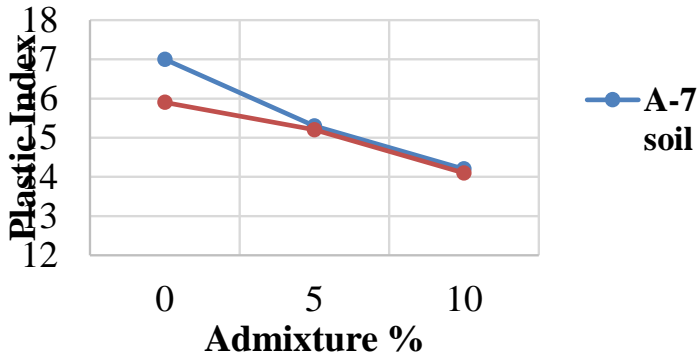


Figure III-3 Combine result of Plasticity index with varying %age of marble stone waste

B. **Engineering properties**

1) **MDD**

Modified AASHTO T-180 compaction test was performed to find out the effect of marble stone waste on MDD of both A-6 and A-7-5 soil. From results it is observed that the optimum value of marble stone waste to increase the MDD of A-6 soil is 15% and for A-7-5 soil it is 20%.

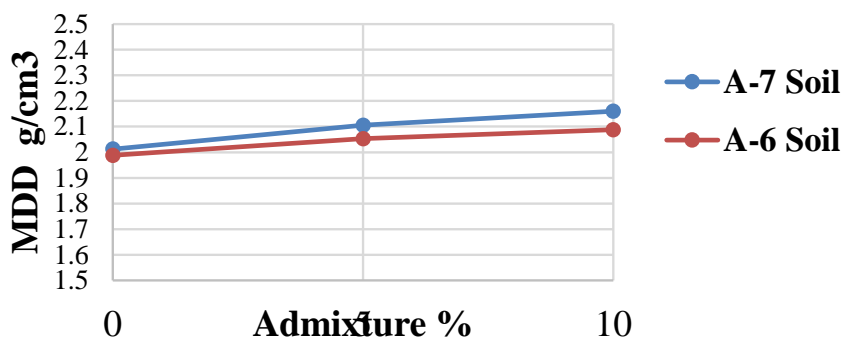


Figure III-4 Combine result of MDD with marble stone waste

2) **OMC**

Decrease in OMC value of both expansive nature soils was observed with the addition of marble stone waste.

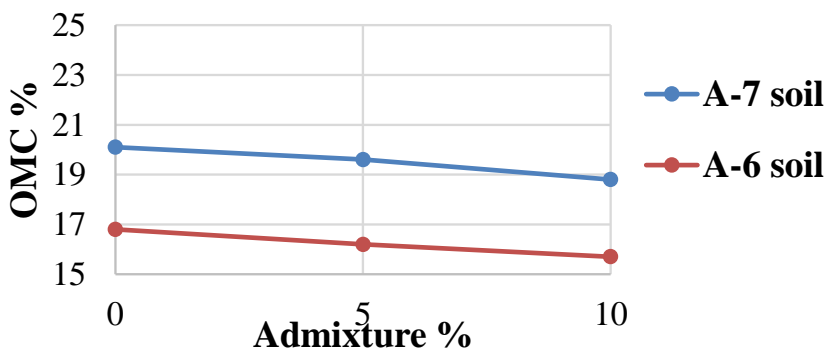


Figure III-5 OMC result with varying %age of marble stone waste

3) *Swell Potential*

Swell potential of the tested soil samples were constantly decreased by adding marble stone waste.

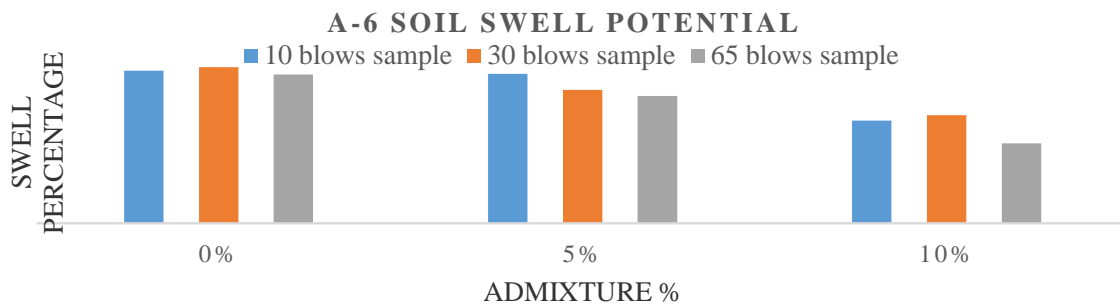


Figure III-6 A-6 soil swell potential result at different dosage of marble stone waste

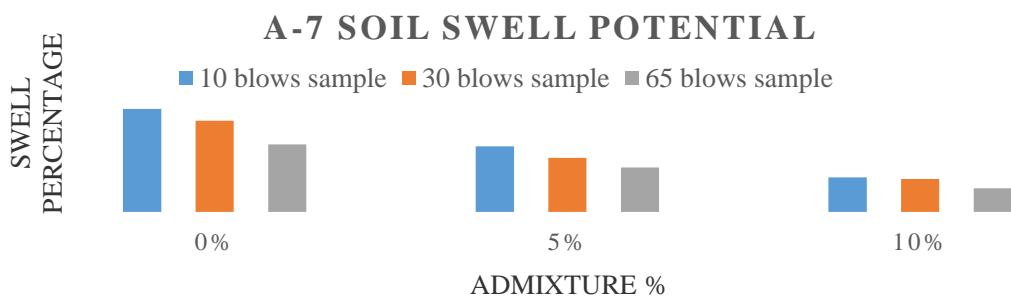


Figure III-7 A-7-5 soil swell potential result at different dosage of marble stone waste

4) *CBR*

Combine CBR test AASHTO T-193 result of tested soil samples is shown below. Constant increase in CBR of tested soil samples was observed. CBR of A-6 soil obtained using marble stone waste is more than the A-7-5 soil.

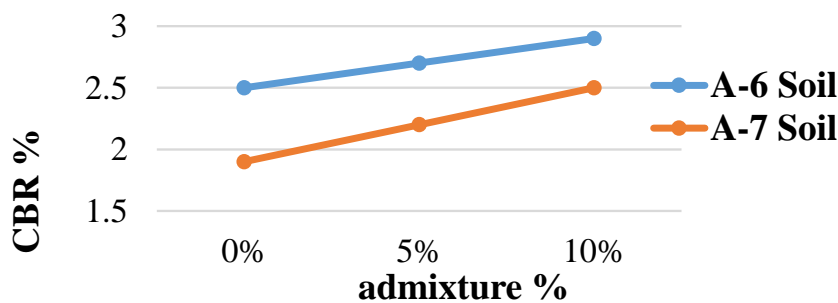


Figure III-8 CBR at different dosage of marble stone waste

5) *Unconfined Compressive Strength Test Result*

Unconfined compressive strength test ASTM D-2216 was performed on expansive soil samples, combine result of prepared soil samples with marble stone dust in varying percentage is given

below. It is clear from the results obtained after UCS test that UCS value of tested soil was increased by adding marble stone waste.

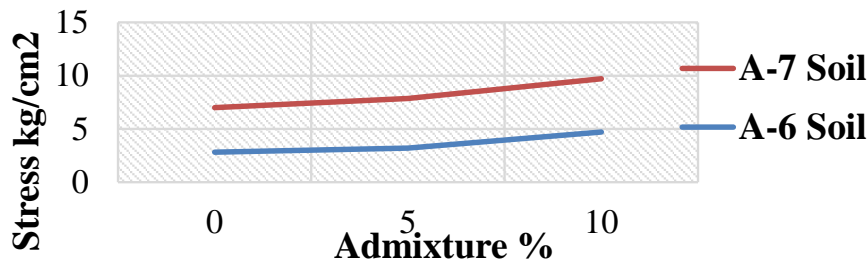


Figure III-9 UCS result after addition of marble stone waste

C. Shear Box Test Results

Effect of marble stone waste on shear strength parameters C and Φ ASTM D-3080 is shown in figure 4-69. Results shows that Cohesion of both type of soil was decreased by adding marble stone waste. Slight increase in the value of angle of internal friction of both soil was observed.

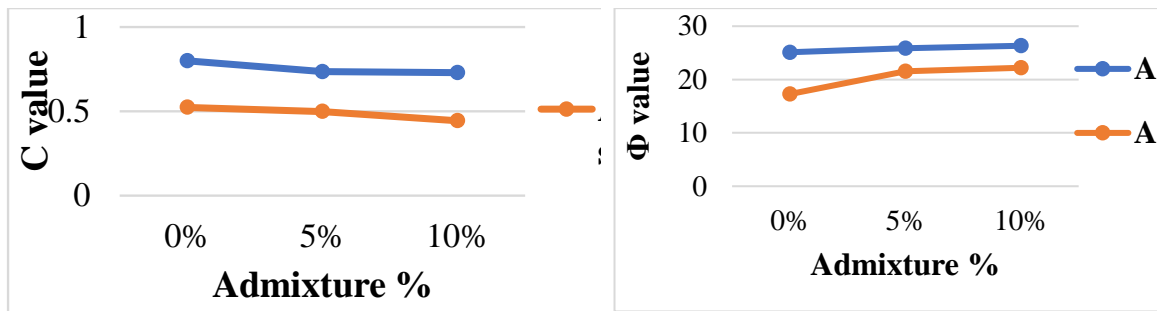


Figure III-10 Cohesion and Φ variation at different percentage of marble stone waste

IV. Conclusion

From the study it has been concluded that,

- With increasing marble stone waste percentage, Liquid limit, plastic limit and Plasticity index of soil samples reduced.
- OMC as well as MDD reduced by the addition of marble stone waste.
- Strong correlation with increasing marble stone dust percentage has been observed.
- A-6 soil observed significant increase in CBR value with increase in marble stone waste this depict that expansive soil with lower values of CBR can be used as subgrade soil after stabilizing through marble stone waste.
- Swell potential of both type of soil constantly decreased by the addition of marble stone waste.
- Results of direct shear test highlighted that cohesion of both soils was reduced by the increase of marble stone waste along with increase in cohesion of soil samples was observed.
- Angle of internal friction also observed to be increased.

- Comparative analysis yielded that marble stone waste could be used to reduce the swell potential as well as to enhance the strength characteristics of expansive soil. However the research work is still in progress to observe further %age of adopted admixture.

REFERENCES

- [40] Al-qayssi, Mahmood R M. 2014. "Effect of Swelling of Subgrade Soil on the Flexible Pavement." Geotechnical Aspects of Underground Construction in Soft Ground – Yoo, Park, Kim & Ban (Eds) © 2014 Korean Geotechnical Society, Seoul, Korea, ISBN 978-1-138-02700-8 Effect of Swelling of Subgrade Soil on the Flexible Pavement Mahmood R.M. Al-Qayssi Geote, no. 1377: 141–46.
- [41] Steinberg, Malcolm L. 1985. "Geogrids as a Rehabilitation Remedy for Asphaltic Concrete Pavements." TRANSPORTATION RESEARCH RECORD 1369, no. 2.
- [42] Petry, Thomas M., and J. Clyde Armstrong. 1989. "Stabilization of Expansive Clay Soils." *Transportation Research Record*, no. 1219: 103–12.
- [43] Karaca, Zeki, Abdülkerim Pekin, and Ahmet Hamdi Deliormanlı. 2012. "Classification of Dimension Stone Wastes." *Environmental Science and Pollution Research* 19 (6): 2354–62. <https://doi.org/10.1007/s11356-012-0745-z..>
- [44] Johnson, L D, and A D Pengelly. 1983. "Scholars' Mine Chemical and Lime Stabilization of Expansive Clay Chemical and Lime Stabilization of Expansive Clay" 19
- [45] Baser, Onur. 2009. "Stabilization of Expansive Soils Using Waste Marble Dust." *Middle East Technical University*, 1–116.
- [46] Marras, G, N Careddu, C Internicola, and G Siotto. 2010. "Recovery and Reuse of Marble Powder By-Product." Global Stone Congress, no. August: 1–5.
- [47] N.d., 2008 "An Overview of Environmental Pollution S'An Overview of Environmental Pollution Status.,'" no. i.

Measurement of Thermal Conductivity of Copper Metal Foam Saturated with Phase Change Material

Ijaz Ahmad^{1,a}, Abid Hussain¹, Awais Ahmed¹, Hanzala Shahid¹, Izhan Sajid¹

¹Department of Mechanical Engineering, University of Engineering and Technology Taxila, Pakistan

Email address: ^{a)} ijazahmad672@yahoo.com

Abstract—Heat transfer and storage properties are important characteristics of the phase change material (PCMs) which perform a major role in the storage system of thermal energy. The minimum thermal conductivity of phase change materials significantly lowers its performance in terms of energy storage and release rate. Metal foam can be used to increase the low thermal conductivity of the paraffin. In this research work, the thermal conductivity of the phase change material was increased by using the metal foam paraffin composite. The heat transfer enhancement of the paraffin metal foam composite was studied in comparison to pure paraffin. The infiltration technique was used to infiltrate the paraffin in the metal foam. The result showed that the thermal conductivity of the composite was enhanced as compared to pure paraffin. Thermal conductivity and porosity of metal foam have an inverse relationship with each other. The maximum thermal conductivity of 8.6 (W/m.K) has seen at a porosity of 0.90.

Keywords—heat storage capacity, thermal conductivity, paraffin/metal foam composite, heat transfer rate, phase transition process

V. Introduction

During recent years, great attention has been paid towards renewable energy due to the gradual depletion of fossil fuels. Solar energy is a suitable alternative to fossil fuels as it is easily available and is friendly to the environment [1]. Therefore, an efficient storage system is required to store the excess amount of heat. Passive thermal management of phase change materials are attractive for thermal management as they are efficient, have a long working life, compact and require less maintenance. Phase change materials (PCM) can absorb, retain and release a large quantity of energy while maintaining the temperature uniformity during the phase change process [2]. The phase transition process of PCM

during melting or solidification takes place nearly at a constant temperature during latent heat storage. The usage of PCM has some additional advantages over other storage materials of being non-corrosive, non-poisonous and low volume expansion [3]. However, the less thermal conductivity of the PCM severely disrupts its efficiency of energy storage and limits its usage in engineering applications. For better heat transfer rates, the higher thermal conductivity of PCM is required. Different techniques are reported in the existing literature to enhance the heat conduction properties of PCM. Tian et al. [4] formed a composite PCM by the combination of eutectic composed of three parts carbonate salt with the magnesium particles. There was no comprehensive change in the composite

PCM melting temperature relative pure carbonate salt. An enhancement of about 145% was seen in thermal conductivity of 2 wt.% of magnesium was added. Abid et al. They have investigated practically work to study the heat management of batteries using PCMs/graphene-coated nickel (GCN) foam PCM composite. The thermal conductivity was increased up to 23 times with the corresponding decrease to specific thermal capacity by 34%. Rehman et al. [5] studied the behavior of heat sink at different heat fluxes with different PCMs. They observed the operational time for heat sink without PCMs and with PCMs composites. Different PCMs/composites were investigated by changing heat fluxes from 800 W/m² to 2400 W/m². They pointed out that as the power provided increased, there was a reduction in maximum temperature across the heat sink. Copper foam/PCMs composites were least proficient at 2400 W/m² based on the performance of aluminum heat cavity [6]. Furthermore, the study revealed that increasing the PCMs volume fraction decreased the base temperature of the thermal cavity. Since the copper foam is characterized by high conductive materials, the presence of copper increased the heat transfer rate within composites. When the copper foam is embedded in PCMs, the melting time of PCM reduced and there was a 36% increase in heat transfer rate [7]. Heat storage properties of paraffin mixtures can be improved when nanoparticles of Al₂O₃ are encapsulated in paraffin by the direct-synthesis method [8]. Metal filler and carbon-based filler materials both added in PCMs largely improve the thermal conductivity. However, carbon additives show excellent stability compared to metal-based PCMs composites [9]. R. Baby et al.

[10] studied the properties of copper foam/PCM based submerged heat. They found that spinning does not effect the heat transfer rate.

Heat transfer enhancement has a major influence on the thermal properties of PCM. Rapid heat transfer effects the heat-storing and release rate. Hence it is very necessary to increase the low thermal conductivity of the phase change material composite. Different approaches used through researchers were focused on using graphite, nanoparticles, and enclosing of PCM. However, the thermal conductivity of copper PCM composite utilizing the infiltration technique was rarely focused. This article focuses on the increase of thermal conductivity of copper/PCM composite along with the heat storage properties.

VI. Materials and methods

In this study Paraffin (Rubitherm-42) was used as a PCM having temperature range and thermal conductivity of (38-41) °C and (0.2 W/m.K) respectively, through the Ruhr Technology China. The thermal properties of materials are given in the Table below.

Table XVII: Thermal conductivities of samples

Material	Thermal conductivity W/m.K
Copper	398
Paraffin (38-41°C)	0.2

The composite PCM is prepared by the infiltration of molten paraffin wax into a copper foam. The paraffin was placed in a metal container and heated uniformly through the heater until the wax was melted

completely. The copper foam was lowered in the metal container through the wire mesh for the infiltration of molten paraffin wax. When the paraffin was completely penetrated, the heat source was removed and left the wax to solidify. The metal container was then gently heated to separate the saturated coated metal foam paraffin composite from the container.

VII. Infiltration Ratio

To find the infiltration ratio the sample was weighted using the electronic mass balance (JM10002) with a precision of 0.01 g provided by Zhejiang Ltd China. The mass reading was taken before and after the infiltration of the paraffin. Metal foam bulk porosity was found by the following equation [12].

$$\varepsilon_b = 1 - \frac{m_{f_0}}{\rho_{sk}V_t} \quad (1)$$

In the above equation, the ε_b is the bulk porosity of metal foam. V_t represents the volume of the metal foam, ρ_{sk} represent the density of the metal skeleton and m_{f_0} represents the mass of metal foam. The following equation was then utilized to find the infiltration ratio [12].

$$\alpha = \frac{m_{actual}}{m_{ideal}} = \frac{\Delta m_i}{\varepsilon_b \rho_{pcm} V_t} \quad (2)$$

Where ρ_{pcm} is represent the density of PCM when it is in solid form. Δm_i is the difference in masses of metal foam before and after the infiltration. The α is a dimensionless parameter and show the actual value of paraffin wax infiltrated into the metal foam as compared to the ideal mass which could be infiltrated. If the value is 100% it implies that all the paraffin has infiltrated into the metal foam and all the pores are filled with the paraffin.

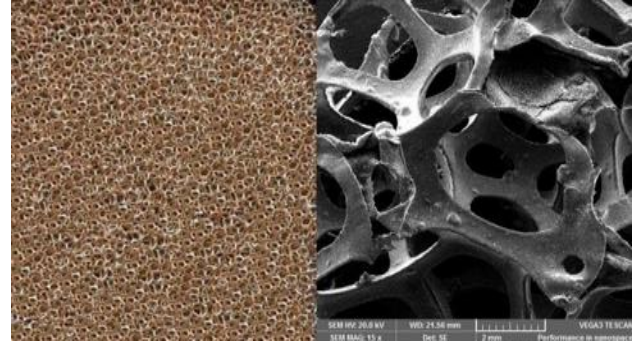


Fig. 11: Isometric view of copper foam.[13]

VIII. Experimental setup configuration

Thermal conductivity of copper paraffin composite wax measured indirectly by thermal diffusivity, defined as heat move rate by conduction during changing specimen temperature with the passage of time and denoted by (α). Where diffusivity is measured by using an apparatus designed based on laser flash technique at 25 °C. The apparatus consists of a metal rod with an inside electric heater for heating purpose and temperature of the metal rod is constantly maintained by 35 °C throughout the experiment and infrared radiator (IR detector) of (FLIR SC660) type is used for temperature measurement without any physical contact with apparatus or sample material. The samples of the composite of copper foam with paraffin wax is tightly attached with metal rod along the length through the thermal tape (thermal interface material) to overcome interface resistance between metal rod and test samples. During the experiment, the sample temperature for each specimen is recorded by the IR detector (FLIR SC660) from top to bottom at 5 mm, 25 mm, and 45mm. The working temperature range of the IR detector was from -40 °C to 1500 °C. It has a temperature sensitivity of 0.05 °C and an accuracy of ± 1 °C. The thermal diffusivity is measured by using the following relation [12].

$$\alpha = \frac{1.38 d^2}{\pi^2 t^{1/2}} \quad (3)$$

Where on the left side, there is α in (m²/s) and on the right side denotes the sample length in (m) and $t^{1/2}$ as time in (seconds) for half-maximum temperature on the rare side of specimens. This value of time for half-maximum temperature on the rare side is the main parameter for thermal diffusivity measurement. By using thermal diffusivity value from the above equation, thermal conductivity for each specimen is determined through the following equation [14].

$$\kappa = \alpha \rho c \quad (4)$$

Where, on left side κ denotes thermal conductivity in (W/ m.k) and on the right side, c denotes specific heat capacity in (J/kg.K) of the respective specimen determined through calorimeter (DSC Q1000) determined in above section with ρ as density in (kg/m³). The density of the respective specimen is determined by mass/volume relation. Where the mass is determined by using the electronic mass balance (JM10002) with a precision of 0.01 g provided by Zhejiang Ltd China and volume by (L × W × H) mm relation for each specimen.



Fig. 12: Laser flash method

IX. Results and discussions

The graph in Fig. 3 below shows the relation between the porosity and the thermal conductivity of copper/paraffin composite. The outcome tells that the thermal conductivity of the copper/paraffin composite is inversely proportion to the porosity of the foam. Maximum thermal conductivity was seen at a porosity of 0.90 which was 8.6 W/(m.K) while low thermal conductivity of 3 W/(m.K) was seen at a porosity of 0.98. The thermal conductivity was enhanced by 286.6% as porosity was varied from 0.98 to 0.90

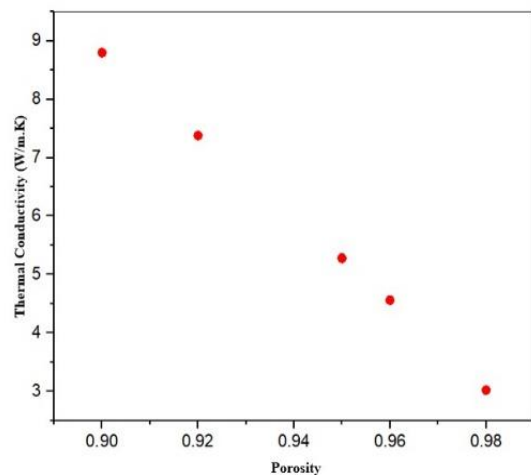


Fig. 3: The relation between porosity and thermal conductivity of copper foam/paraffin composite

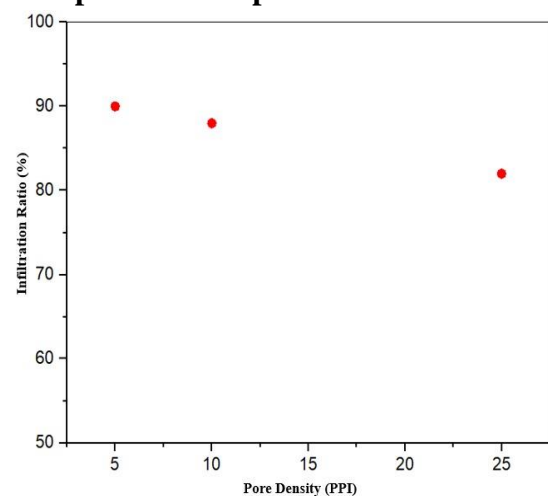


Fig. 4: The relation between the pore density (PPI) and the infiltration ratio
The graph in Fig. 4 above shows the inverse

relation between the pore density (PPI) and the infiltration ratio. As the pore density increased, the infiltration ratio of the paraffin decreased. A maximum infiltration ratio of 90% was achieved. A 100% infiltration ratio cannot be achieved due to the slight difference in the solidification rates of PCM. The solidification of the paraffin on the outer side of the metal foam starts early as compare to the inner side of the metal foam. There is also a slight difference in the density of the paraffin when it in solid form as compare to paraffin that is in liquid form. When the PCM cools down this density difference causes the shrinkage of PCM and the small cavity is formed on the inner side of PCM which does not allow complete infiltration of PCM in a metal foam.

X. Conclusions

The test was performed to find out the thermal conductivity of copper/paraffin composite. The composite sample was prepared by the infiltration of paraffin into the metal foam. Laser flash phenomena were used to find out the thermal conductivity of the composite sample. It is concluded that copper metal foam is a suitable candidate for thermal conductivity enhancement due to its high porous design and high thermal conductivity. High thermal conductivity value (8.6 W/m.K) of the composite sample was obtained as compared to paraffin (0.2 W/m).

- The thermal conductivity was highest at the porosity of 0.9 and decreased gradually as the porosity increases with all the above cases.
- The infiltration ratio and pore density had an inverse relation. As the pore density increased, the infiltration ratio decreased.

- Metal foam efficient thermal conductivity was enhanced significantly compare to pure paraffin. The thermal conductivity of the paraffin was increased to 43 times.

REFERENCES

- [48] Z. Khan, Z. Khan, and A. Ghafoor, "A review of performance enhancement of PCM based latent heat storage system within the context of materials , thermal stability and compatibility," *Energy Convers. Manag.*, vol. 115, pp. 132–158, 2016.
- [49] A. Sharma, V. V Tyagi, C. R. Chen, and D. Buddhi, "Review on thermal energy storage with phase change materials and applications," vol. 13, pp. 318–345, 2009.
- [50] L. Liu, D. Su, Y. Tang, and G. Fang, "Thermal conductivity enhancement of phase change materials for thermal energy storage : A review," vol. 62, pp. 305–317, 2016.
- [51] H. Tian, L. Du, X. Wei, S. Deng, W. Wang, and J. Ding, "Enhanced thermal conductivity of ternary carbonate salt phase change material with Mg particles for solar thermal energy storage," *Appl. Energy*, vol. 204, pp. 525–530, 2017.
- [52] T.- Rehman, H. Muhammad, A. Saieed, W. Pao, and M. Ali, "International Journal of Heat and Mass Transfer Copper foam / PCMs based heat sinks : An experimental study for electronic cooling systems," *Int. J. Heat Mass Transf.*, vol. 127, pp. 381–393, 2018.
- [53] T.- Rehman, "Experimental investigation on para ffin wax integrated with copper foam based heat sinks for electronic components thermal cooling," vol. 98, pp. 155–162, 2018.
- [54] H. T. Cui, "Experimental investigation on the heat charging process by paraf fi n fi lled with high porosity copper foam," *Appl. Therm. Eng.*, vol. 39, pp. 26–28, 2012.

- [55] A. Babapoor and G. Karimi, "Thermal properties measurement and heat storage analysis of paraffin nanoparticles composites phase change material: Comparison and optimization," *Appl. Therm. Eng.*, vol. 90, pp. 945–951, 2015.
- [56] Y. Lin, Y. Jia, G. Alva, and G. Fang, "Review on thermal conductivity enhancement, thermal properties and applications of phase change materials in thermal energy storage," *Renew. Sustain. Energy Rev.*, vol. 82, no. May 2017, pp. 2730–2742, 2018.
- [57] R. Baby and C. Balaji, "Experimental investigations on thermal performance enhancement and effect of orientation on porous matrix filled PCM based heat sink," *Int. Commun. Heat Mass Transf.*, 2013.
- [58] H. Zheng and C. Wang, "Numerical and Experimental Studies on the Heat Transfer Performance of Copper Foam Filled with Paraffin," 2017.
- [59] X. Hu, F. Zhu, and X. Gong, "Experimental and numerical study on the thermal behavior of phase change material in infiltrated in low porosity metal foam," *J. Energy Storage*, vol. 26, no. July, p. 101005, 2019.
- [60] R. Hafiz and M. Ali, "Thermal performance analysis of metallic foam - based heat sinks embedded with RT - 54HC paraffin: an experimental investigation for electronic cooling," 2019.
- [61] T. Lian et al., "Rapid thermal conductivity measurement of porous thermal insulation material by laser flash method," *Adv. Powder Technol.*, vol. 27, no. 3, pp. 882–885, 2016.

Temperature control of battery using Phase change material infiltrated in metal foam

Waqas Ahmed^{1, a}, Abid Hussain^{1, b}

¹Department of Mechanical Engineering, University of Engineering & Technology Taxila,
Pakistan.

*Email address: ^awaqasahmadbutt33@gmail.com , ^babid.hussain@uettaxila.edu.pk

Abstract--- Energy plays a significant aspect in the advancement of nation both socially and financially. Utilization of energy from renewable source is the main research focus in order to reduce dependency on conventional fuels. Keeping in view the fact, battery hybrid vehicles are rapidly replacing conventional vehicles. Lithium ion battery is an integral part of battery electric vehicles due to their high energy and power density. Their efficiency is affected due to rise in temperature of battery pack. An effort is made to maintain battery within permissible temperature limits. In current study efficient thermal management (graphene coated nickel foam paraffin composite) are examined experimentally for highly powered Li-ion batteries. Experimental model carries six Panasonic 18650B 3400 mAh lithium ion energy cells which were connected in series. Four other thermal management modes were compared, and their results were evaluated. By utilizing graphene coated nickel foam paraffin composite, 34% reduction in temperature of battery pack is achieved. While 1% decreases in temperature of battery enhances the life of battery for two months. So, graphene coated nickel foam paraffin composite is feasible option to maintained battery temperature within permissible limits.

Keywords---thermal management, hybrid electric vehicle, passive cooling, graphene composite

I. INTRODUCTION

Lithium ion batteries are integral part of electric vehicles because of their high energy and power density. Li-ion batteries are light in weight and more efficient as compared to other type of batteries [1]. However, lithium ion batteries produce extreme heat during operation. Their efficiency decreases due to rise in temperature of battery. Also the performance and life of battery is concerned by rise in temperature [2]. Managing this rise in temperature remains a challenge. There are the following methods for thermal management of battery that are used for temperature control. It includes active cooling system which consists of pump, fan and heat exchanger whereas passive cooling system contains PCM. Active cooling system is expensive, bulky and makes the system heavy [3]. So passive cooling system which contains PCMs is compact, light in weight and is more efficient [4]. PCM enhances thermal energy storing ability of the system by using latent heat and effectively control the rise in temperature. Phase change materials (paraffin wax) that are utilized in thermal management have latent heat, low cost, environment friendly but possess poor rate of heat transfer (0.19 W/m K) [5]. Various techniques for improving the heat transfer are introduced (a) By adjoining additives like nano materials with PCMs [6]. (b) By employing metal fins/foam [7]. Researcher focused to work for enhancing thermal conductivity by various methods.

Goli et al. [8] discovered that rate of thermal mobilization of pure PCMs can be raised by spending graphene paraffin composite. He developed PCMs by using graphene composite and thermal conductivity of PCM was raised to 45 W/ (m. K) rather than 0.19 W/ (m. K) by pure paraffin.

Sedeh et al. [9] employing graphite foam composite with phase change material. Pores of foam penetrated with PCM (cyclohexane) and thermal analysis was done at experimental setup which contained lithium ion batteries. Surface temperature of battery pack reduced to 11.2°C using graphite foam paraffin composite. Temperature gradient of module is kept in permissible limits due to sufficient increase in thermal conductivity. Samimi et al. [10] had done experimentation using carbon fiber with paraffin wax composite and showed that thermal conductivity raise to (81-273%) of paraffin wax. There was 15 °C decrease in temperature of lithium ion batteries so that results were effective for battery thermal management system.

Al-Hallaj et al. [11] investigated a technique for passive cooling of Li-ion batteries using graphite matrix infiltrated with phase change material. Experimentation was performed utilizing a cylindrical shape battery cells at different ambient temperature of 30 °C and 45 °C. By this study they concluded that

battery life is improved efficiently by using PCM composite.

Sabbah et al. [12] studied temperature uniformity using natural air at 1.5C rate. They developed experimental model and reported that PCM composite with metal foam gives good dissipation of heat as related to active air-cooling system at discharge ratio of 6.66C for 18650B Li-ion batteries.

Lithium ion battery thermal control was achieved by the use of metal foam (copper, aluminum) or paraffin wax graphite composite. Graphene heat transfer rate (2000-3000 W / m. K) is very high. In fact, graphene coating on nickel foam improves the transfer of heat from phase-change product infiltrated in a nickel foam [13, 14] .

By afore mentioned literature survey, it is concluded that specific heat of nickel foam is more reliable and it extracts more heat from battery pack. But the issue is that nickel foam increases just six times paraffin's thermal conductivity. Graphene thermal conductivity is very high (3000 W / m K) [13]. Nickel foam has ability to extracts more carbons from graphene. Herein, the objective of current research is to evaluate the temperature of battery pack by utilizing graphene coated nickel foam paraffin composite. Benefits of graphene composites include enhanced mechanical strength and reduced thermal expansion with no extra expanses. It is investigated that nickel foam is never used with graphene coating. Novelty is established in recent work by studying and comparing four other modes of thermal management i.e. natural air circulation, pure phase change material, phase change material infiltrated in nickel foam and phase change material infiltrated in graphene coated nickel foam. In this paper temperature uniformity along with battery pack will be analyzed by comparing their results.

II. EXPERIMENTAL SETUP

A Battery Pack Properties

Different types of lithium ion batteries are available with various configurations so after a thorough literature review, we have selected such kind of batteries which satisfy its rating. The experimental setup carries six Panasonic 18650B 3400 mAh lithium ion energy cells which were connected in series. Complete specification of battery pack is shown in Table 1.

B Nickel Foam Paraffin Composite

Paraffin wax and nickel foam were evaluated for performance to proper control the temperature battery pack. Paraffin wax RT-42, exhibit large latent heat capacitance as well as must have high thermal conductivity and it should melt consistently and with minimal sub cooling, non-corrosive, and non-toxic and have low cost. A small (0.1%) uncertainty arises in a sample and neglected due to thickness of metal foam.

C Testing of battery pack

The temperature of Li-ion battery pack was examined under four modes of thermal management: (a) nickel foam (b) pure PCM (c) nickel foam PCM composite (d) PCM infiltrated in graphene coated nickel foam composite. The experiment was performed under varying load inputs Thermocouples were utilized to observe the temperature of battery pack. One thermocouple was engaged at 1st positive junction of battery pack and two thermocouples were engaged at mid of 3rd and 5th battery, after passing every 30 sec data acquisition system recorded the surface temperature of battery module. The step by step obtained data was evaluated and manipulated when the expected results were justified.



Figure 1: Nickel Foam



Figure 2: Battery Panasonic NCR 18650B

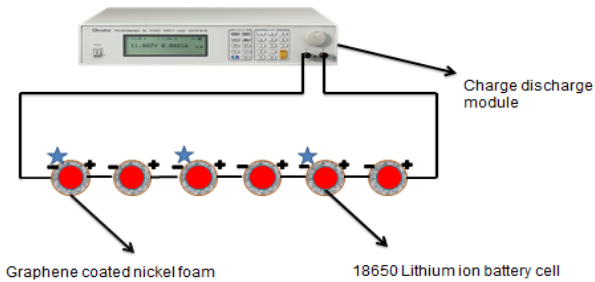


Figure 3: Schematic diagram of Experimental Setup

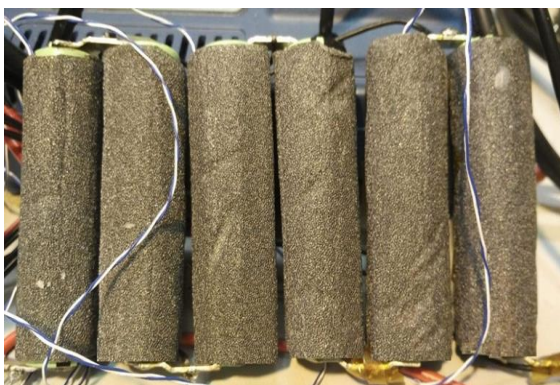


Figure 4: Battery Pack Wrapping with Nickel Foam



Figure 5: Experimental Setup connected with System

III. RESULTS & DISCUSSION

A Discharging at 0.5C using natural air

A complete charge-discharge cycle was carried using natural air as cooling medium. Temperature distinction varied linearly with time under 0.5C discharge rate.

Maximum rise in temperature took place at the mid of battery pack so cell number 3 was selected and connected with T type thermocouple. Temperature response of cell no 3 are shown in Figure 6. The battery pack charged and discharged at constant rate 0.5C and it began to heat and reached at 35°C during (205 min < t < 290 min) discharging phase. Sudden rise in temperature was due to convection at the same time rate of heat transfer of air was low.

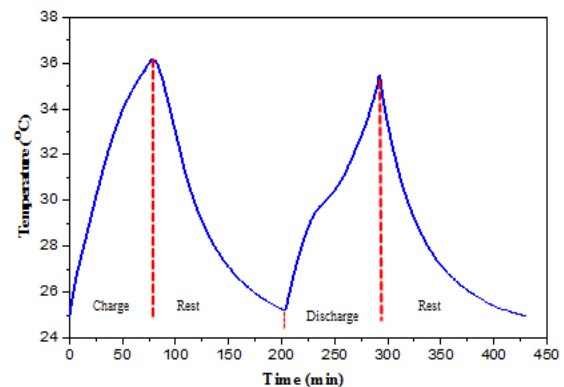


Figure 6: Discharging at 0.5C using natural air as cooling mode

B Discharging at 0.5C using PCM

Paraffin wax exhibits conduction mode of heat transfer. Discharging of battery pack was done at 0.5C rate and temperature increased gradually and went to maximum at 33°C during (415 min < t < 480 min). Comparing with natural air circulation mode there was 7% drop in temperature of PCM as cooling medium which clarified that heat transfer rate of paraffin (conduction) is more than natural air (convection). The point to emphasize that increase in temperature of battery pack was lower than melting range of paraffin wax, so in this case only thermal conduction parameter of compact paraffin was used as shown in Figure 7.

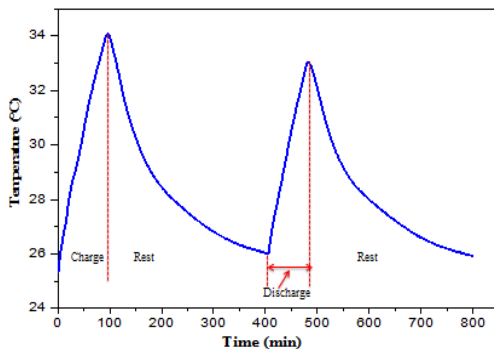


Figure 7: Discharging at 0.5C using paraffin wax as cooling mode

C Discharging at 0.5C using nickel foam PCM Composite

Paraffin wax infiltrated in porous nickel foam. Discharging of battery pack initiated and temperature profile went to maximum at 31°C during time (300 min < t < 380 min). In present study phase change material cannot be melted during charge and discharge process and only conduction phenomenon of heat transfer worked efficiently, that there is immense increase in thermal conductivity due to use of nickel foam composite as shown in Figure 8. Its determined that there was 9% and 13% drop in temperature profile as compared with pure PCMs and air circulation.

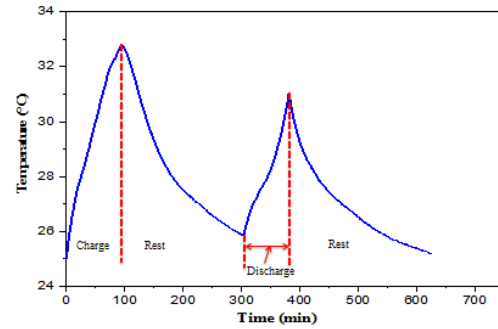


Figure 8: Discharging at 0.5C using nickel foam paraffin composite as cooling mode

D Discharging at 0.5C using graphene coated nickel foam PCM composite

Graphene has immense thermal conductivity Therefore battery pack temperature was further reduced utilizing graphene layers on nickel foam saturated with paraffin wax. At same discharge rate 0.5C battery pack is examined using GCN composite and studied that during charging phase maximum temperature increased to 32°C and 30°C in discharging phase which is lowest as compared to without graphene coating as shown in Figure 9. Passive temperature control of batteries proved more effective and kept battery temperature within limits by using graphene coated nickel foam.

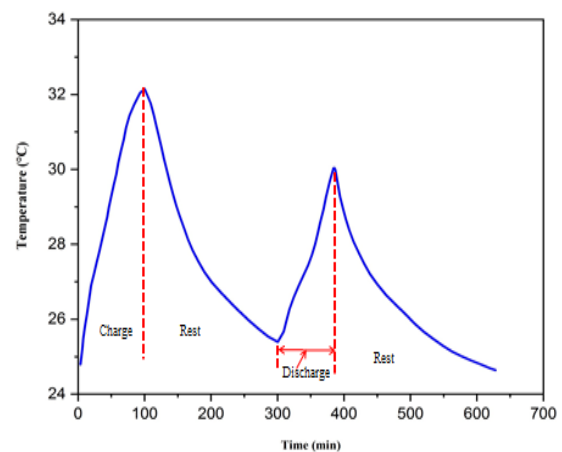


Figure 9: Discharging at 0.5C using paraffin wax infiltrated in graphene coated nickel foam as cooling mode

E Discharging at 2C rate using graphene coated nickel foam PCM composite

The experiment was repeated again, and module was discharged at 2C (6.8A) to check the sensible heat effect on all three cooling modes. The figure 10 showed the temperature profile at 2C discharge rate. It can be seen from graph that temperature by natural cooling is 65.45°C that can damage the battery pack. 24.69% temperature drop with paraffin application. At the point when graphene coated nickel foam composite is used temperature goes to 43.19°C which is 34% lower when contrasted with common air cooling. A 34% reduction in surface temperature of battery pack is accomplished by utilizing paraffin wax infiltrated in graphene coated nickel foam than common air convection. This temperature decrease demonstrates that the graphene coated nickel foam paraffin composite is a feasible choice for efficiently temperature control of lithium ion batteries.

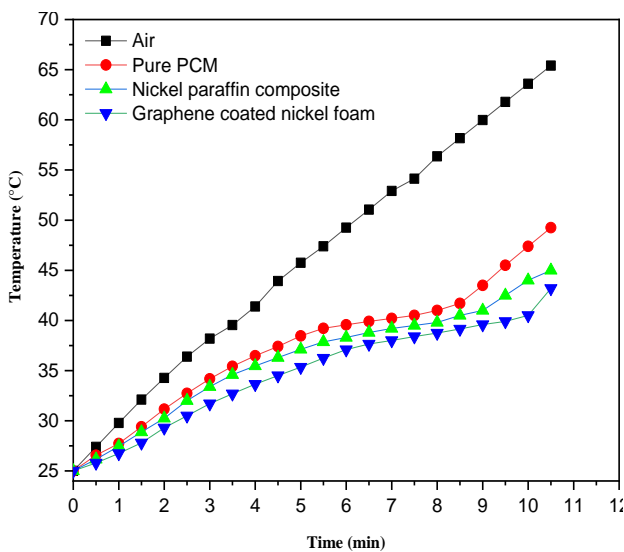


Figure 10: Discharging at 2C rate comparing all cooling modes

F Temperature uniformity using graphene coated nickel foam PCM composite

Keeping discharge rate same as 1.5C for temperature control of battery pack was carried by employing GCN paraffin composite. Identical temperature distribution inside the battery pack is essential for achievement and life of battery pack. Temperature uniformity

between cell no 1 and cell no 3 is shown in Figure 11. This smallest temperature difference 0.5°C ensures that graphene enhanced the dissipation of heat through conduction mode.

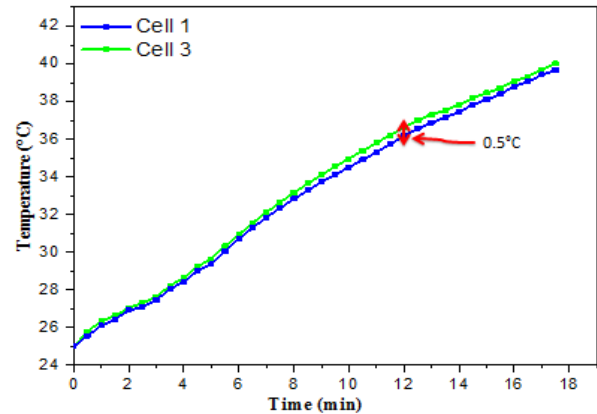


Figure 11: Temperature uniformity using graphene coated nickel foam PCM composite

IV. CONCLUSION

- Experimental survey on thermal management of high-powered lithium ion batteries was conducted by employing graphene coated nickel foam paraffin composite.
- The results indicated that nickel foam enhanced the heat transfer rate of PCM by 6 times while graphene coated nickel foam increased heat transfer by 23 times of PCM. By employing GCN paraffin composite as a cooling medium, the surface temperature of battery pack was reduced to 34% as compared to natural air and PCM under 2C discharge conditions.
- The temperature difference along battery pack was only 0.5°C, while 1% decreases in temperature enhanced the life of battery for 2 months. So paraffin wax infiltrated in graphene coated nickel foam was viable option for thermal management of lithium ion batteries.

REFERENCES

- [1] H. Maleki, "Thermal Properties of Lithium-Ion Battery and Components," *J. Electrochem. Soc.*, vol. 146, no. 3, p.

- 947, 2002.
- [2] R. F. Liang, Z. X. Wang, H. J. Guo, X. H. Li, W. J. Peng, and Z. G. Wang, "Fabrication and electrochemical properties of lithium-ion batteries for power tools," *J. Power Sources*, vol. 184, no. 2, pp. 598–603, 2008.
- [3] M. R. Giuliano, A. K. Prasad, and S. G. Advani, "Experimental study of an air-cooled thermal management system for high capacity lithium-titanate batteries," *J. Power Sources*, vol. 216, pp. 345–352, 2012.
- [4] L. Ianniciello, P. H. Biwolé, and P. Achard, "Electric vehicles batteries thermal management systems employing phase change materials," *J. Power Sources*, vol. 378, no. December 2017, pp. 383–403, 2018.
- [5] Z. Rao and S. Wang, "A review of power battery thermal energy management," *Renew. Sustain. Energy Rev.*, vol. 15, no. 9, pp. 4554–4571, 2011.
- [6] P. Chandrasekaran, M. Cheralathan, V. Kumaresan, and R. Velraj, "Enhanced heat transfer characteristics of water based copper oxide nanofluid PCM (phase change material) in a spherical capsule during solidification for energy efficient cool thermal storage system," *Energy*, vol. 72, pp. 636–642, 2014.
- [7] Y. Lin, Y. Jia, G. Alva, and G. Fang, "Review on thermal conductivity enhancement, thermal properties and applications of phase change materials in thermal energy storage," *Renew. Sustain. Energy Rev.*, vol. 82, no. October 2017, pp. 2730–2742, 2018.
- [8] P. Goli, S. Legedza, A. Dhar, R. Salgado, and A. A. Balandin, "Graphene-Enhanced Hybrid Phase Change Materials for Thermal Management of Li-Ion Batteries," *J. Power Sources*, 2013.
- [9] M. M. Sedeh and J. M. Khodadadi, "Thermal conductivity improvement of phase change materials / graphite foam composites," *Carbon N. Y.*, vol. 60, pp. 117–128, 2013.
- [10] F. Samimi, A. Babapoor, M. Azizi, and G. Karimi, "Thermal management analysis of a Li-ion battery cell using phase change material loaded with carbon fibers," *Energy*, vol. 96, pp. 355–371, 2016.
- [11] S. Al-Hallaj, R. Kizilel, A. Lateef, R. Sabbah, M. Farid, and J. Rob Selman, "Passive thermal management using phase change material (PCM) for EV and HEV Li-ion batteries," *2005 IEEE Veh. Power Propuls. Conf. VPPC*, vol. 2005, pp. 376–380, 2005.
- [12] R. Sabbah, R. Kizilel, J. R. Selman, and S. Al-Hallaj, "Active (air-cooled) vs. passive (phase change material) thermal management of high power lithium-ion packs: Limitation of temperature rise and uniformity of temperature distribution," *J. Power Sources*, vol. 182, no. 2, pp. 630–638, 2008.
- [13] K. M. F. Shahil and A. A. Balandin, "Thermal properties of graphene and multilayer graphene: Applications in thermal interface materials," *Solid State Commun.*, vol. 152, no. 15, pp. 1331–1340, 2012.
- [14] X. Xiao, P. Zhang, and M. Li, "Preparation and thermal characterization of paraffin/metal foam composite phase change material," *Appl. Energy*, vol. 112, pp. 1357–1366, 2013.
- [15] L. M. Malard, M. A. Pimenta, G. Dresselhaus, and M. S. Dresselhaus, "Raman spectroscopy in graphene," *Phys. Rep.*, vol. 473, no. 5–6, pp. 51–87, 2009.

Energy Improvement Strategies in Coal Fired Chain Grate Boiler.

M. Khalil^{1, a}, Abid Hussain^{1, b}

¹ Department of Mechanical Engineering, University of Engineering and Technology Taxila, Pakistan

Email address: ^{a)} khalilakhtar23@gmail.com, ^{b)} abid.hussain@uettaxila.edu.pk

Abstract—*Properties of coal are characteristics which perform an essential role in the boiler energy system. Boiler efficiency increase when the less calorific values of coal is used for burning. Addition the size of coal has the significant effect on the combustion process as well as in the performance of the boiler efficiency. In this paper, the production of steam in chain grate boiler against different gross calorific values of coal were experimentally examined. The behaviors of coal combustion and steam production at different gross calorific values of coal was studied. At the lowest gross calorific value of coal, production of steam increases and also attain the highest efficiency of boiler. A comparative analysis of coal and steam is made. The mass of steam produced and the mass of coal combustion is experimentally considered. Experimental results show that a minor development in the productivity of the boiler with the lowest gross calorific value of coal increases the efficiency of the boiler by 10-15% and also get the highest heating capacity of coal.*

Keywords—*Energy, Gross calorific value, Coal fired Boiler, Heat Input, Heat Output, Efficiency, Steam Flow Rate.*

I. Introduction

Boiler is a closed vessel in which water is boiled and converted to steam. Boiler is a machine to produce the steam. By burning of petroleum in the boiler is used to production of steam at defined temperature, pressure and steam flow rate [1].

The purposes of experimentation assessment of operation of boiler is to get the real performance and productivity of the boiler and associate it with design effectiveness and other factors. It is fact day to day modification in boiler design and increasing in energy demands and also in burning of petroleum,

gross calorific value (GCV) enhancements to get the highest thermal efficiency [2].

For increasing the boiler efficiency by minor fraction changes, will be minimize the fuel consumption in steam generation. Again, regardless of remnant coal assets in environment and environmental safety subjects, the lubricant, natural gas and coal petition is likely to rise to 47.5%, 91.6% and 94.7% correspondingly amongst 2003 and 2030 [3]. First, examine how efficient the boiler is at plant. Start by checking the design efficiency rating of boiler. This is usually published in product catalogues and/or safety data sheets. It is keeping in mind, however,

that this rating describes the efficiency of the boiler when operating under ideal conditions, and may not be an accurate reflection of the efficiency at which the boiler is operating at your plant. The efficiency rating of your boiler should be taken as an ideal level, and plants should work to make their boiler's operational efficiency as close to this rating as possible [4].

Amari et al. researched on the energy economics of the Hamadan steam control plant were studied and the energy consumption and energy loss of the mechanisms of the command plant were estimated. In command to improvement good vision into the investigation, the effects of load changes and ambient temperature were calculated. Estimation of the energy efficiency of the boilers, turbines, heaters, condensers at unlike ambient temperatures. From the energy analysis it was found that the condenser had a maximum energy loss (about 70.5%) and an energy loss of 15.5% was found in the boiler. On the other hand, in terms of energy, the main energy loss (about 81%) of the boiler's total energy loss is only 5% of the total energy loss. From an energy economic point of view, it has been observed that the energy consumption of boilers and turbines is higher than the cost of another component [5-7].

The main reason of energy deficient in the boiler is the temperature loss. The wide range of heat loss in the boiler take place through the chimney smoke. The most important parameters for the loss of heat are the temperature and volume of chimney fume. So that decrease in any one of these will reduces the heat loss. To minimize chimney temperature loss, temperature of chimney fume should be cheap to the nearby heat of boiler. But due to the cost-effective inaccessibility and limitation in heat transmission standard these damages are unavoidable [8, 9].

Burning process of coal to transfer the temperature is the straight forward method to practice the fuel. For temperateness, culinary and engineering procedures to get generated heat from burning of coal. The china is using the firewood as primary as 1000 BC [10]. From the fourth century expenditure of coal first time documented by the Greek philosophers Pliny, Aristotle and Theophrastus in the western world (Moore, 1922), the coal is used to burn and the coal is usually recycled by antediluvian man, meanwhile coal can be establish at boulders [11].

The understanding of coal ignition in three methods: as outsized piece in a static bed or on a grate, for example crushed or tiny parts in a fluidized bed, or as very sufficient elements in postponement. Ideally, a few mass of particle can be burning the coal through any one of the three techniques, but industrial limitations found chosen size of constituent part for the three methods. With respect to leading answer appliance and other warm air processes (i.e. ratio of heating system, which can regulator volatiles produce and structure), particle has also been found to be the most important parameter. (Elliot, 1981) [10]. Studies have also been organized and carry out to evaluate energy savings and production and discharge of flue gas degree opportunities and their cost effectiveness in industrial boilers and associated steam systems. Einstein, et al calculated energy usage and energy competence upgrading capacities in steam methods in the U.S. by way of calculating the cost of conserved energy (CCE) to estimate the cost-effectiveness of relevant retrofit measures [12]. Best use of fire procedure with regards of boiler productivity and discharge of air contaminants is of crucial importance in reducing effective and repairs expenditures.

There are countless techniques for such improvement, in which there are some

varieties from boiler apparatus e.g. new capacity tools, connected software systems.

Throughout past few centuries' contactless heat amount expertise have developed more standard in the production. There are two main skills, which are used in firewood boilers to calculate heat division-acoustic equipment [13-15] and laser machinery [16, 17]. In [18] writers extant rewards of acoustic structure in estimation of incineration value in minced petroleum afire boiler. Going on the further pointer, in [19] the significance of laser equipment in fire optimization tasks is obtainable. Heat splitting up in parallel cross-section of a boiler is an excessive gauge of worth of fire procedure. This sign could be recycled in boiler controller to finest usage the incineration progression.

- Steam flow meter
- HMI flow chart display
- HMI control parameters common.

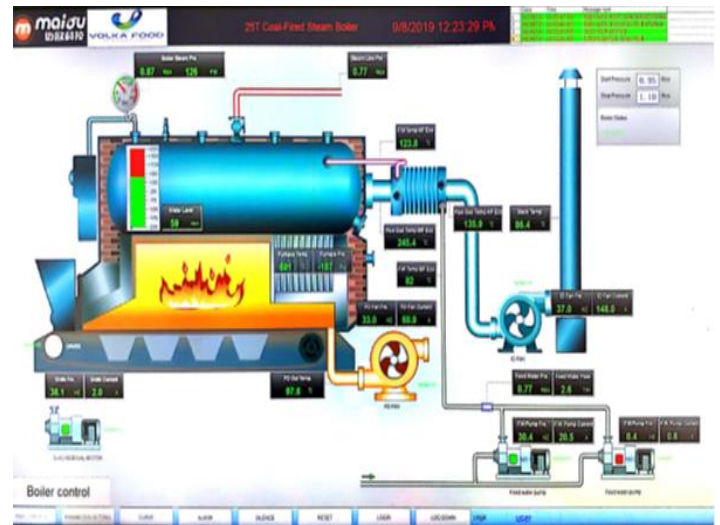


Figure.1 Flow Chart of Boiler Process.

II. Experimental Setup

For the current research experiment, an experimental setup was available to analyze and compare the steam production and coal combustion with different gross calorific values of coal. The special apparatus was available also used to give measurements of gross calorific value of coal for analysis of mass of steam production along the different GCV of coal and at various mass of coal combustion with the different temperature's series of feed water and pressure of steam.

The experimental set consists of following components

- Boiler in operation
- Pressure gauges
- Thermocouples
- Temperature sensors

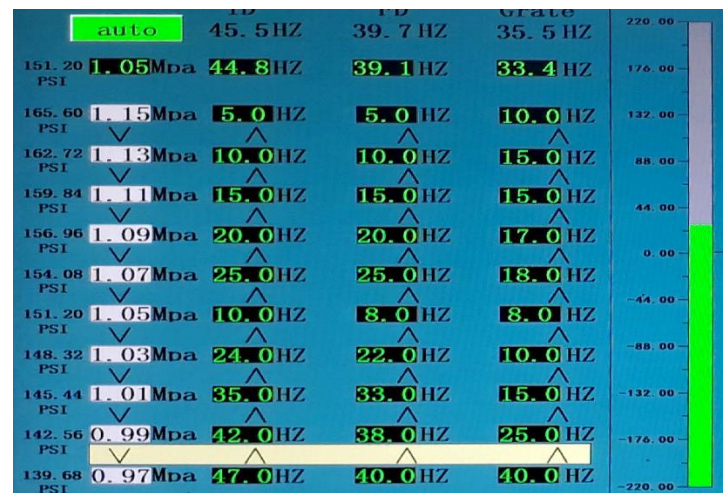


Figure.2 Different Controlled Parameters.



Figure.3 Steam Flow Meter.

III. Results and discussions

Current study will be helpful while carrying out thermal management of boiler especially developing steam system.

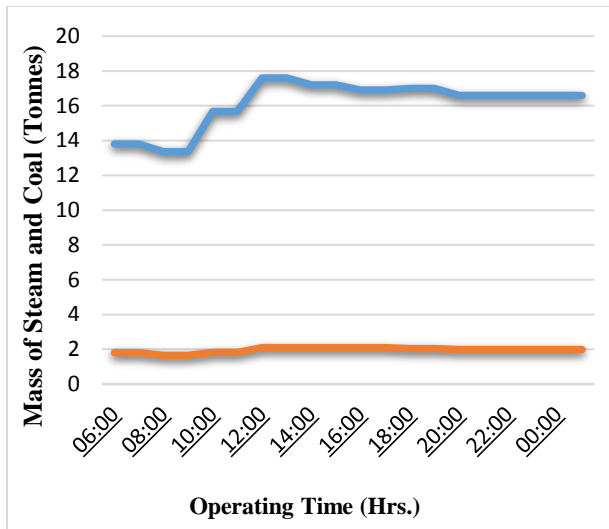


Figure 4: The relation between mass of steam and mass of coal

It is the maximum opportunity to be achieved useful work and able to be used for a practical purpose or in several ways that could be acquired from the system at a given state in identified and cleared surrounding. In the figure.4 the graph relation between the steam and coal shows that steam production rate (tonnes/hr.) changes with the minimum change in the mass of coal for combustion.

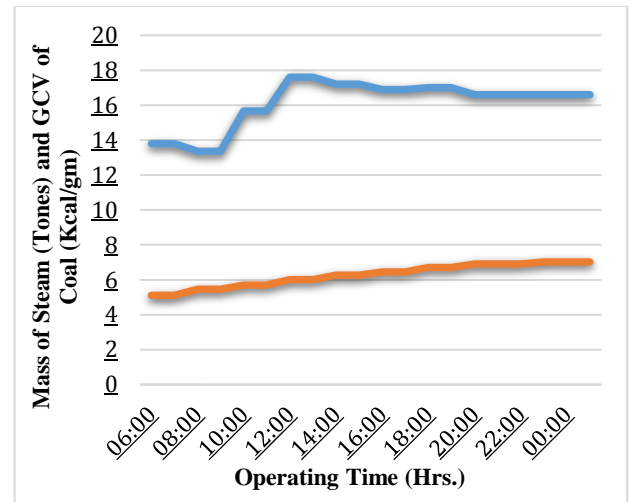


Figure 5: The relation between the mass of steam and the gross calorific value of Coal

The work done during an operation determined on the initial state, the final state, as well as the working order of the condition. The relation in the figure 5 shows the curve of mass of steam and the gross calorific value of coal. This graph shows that due to the increase in the gross calorific value of coal, decreases the mass flow rate (Tonnes/hr.) of steam. It shows that the steam production rate decreases at the same rate of mass of coal in the combustion process with the highest gross calorific value of coal.

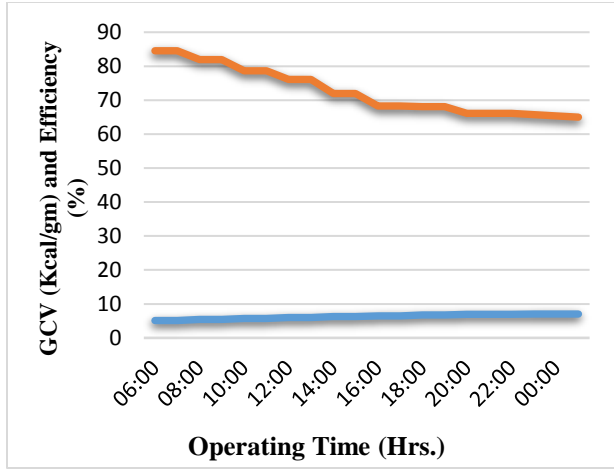


Figure 6: The relation between the gross calorific value and the efficiency of the boiler

In figure 6, the graph shows the relation between the gross calorific value of coal and the efficiency of the boiler. The increase in the gross calorific value of coal decreases the efficiency of the boiler. It means that the gross calorific value of coal effected the performance of the boiler. At the lowest gross calorific value of coal, the performance of the boiler will be better. We should select the proper coal for steam generation in the boiler.

IV. Conclusions

The study reveals that energy efficiency measures are cost effective in saving energy used and thus emissions from coal-fired industrial boilers. To develop the wide adoption of energy efficiency measures in Pakistan, strategies and plans are required to remove the information, capacity, and financial barriers and to create better standards and greater opportunities for capturing system-wide potentials. The efficiency calculation procedures are helpful for coal fired boilers in production of use of steam and in thermal power plants by straight and unintended technique commencing the Agency of energy proficiency [20] are for a short time explained in the paper. The energy efficiency and the heat losses through boiler for the production of steam is a wide scope. The scope work exists in the insulation and material of structure for calculation the heat losses in the boiler and steam flow directions. Instead of the gross calorific value of coal, also the moisture content, air dried sulfur and ash (%) effect the combustion heat capacity of the coal.

REFERENCES

- [1] <http://powerelectrical.blogspot.Com/2007/03/thermal- power-plant- Layout-and.html>.
- [2] Power Plant engineering by P K Nag, third edition.
- [3] Renewable and Sustainable Energy Reviews journal. Homepage:www.Elsevier.com/locate/rsr.
- [4] <https://www.tlv.com/global/TI/steam- theory/what-is-steam.html>.
- [5] Ameri M., Ahmadi P., Hamidi A. (2009). Energy, energy and energy-economic analysis of a steam power plant: A case study. International Journal of Energy Research, 33:499–512.
- [6] Rosen MA, Dincer, I. Energo-Economic analysis of power plants operating on various fuels. Applied Thermal Engineering 2003;23:643-658.
- [7] Silvera JL, Tuna CE. Thermo economic analysis method for optimization of combined heat and power systems. Part 1. Progress in Energy and Combustion Science 2003; 29:479–485.
- [8] ERC I. How to save energy and money in boilers and furnace systems. Energy Res Cent (ERC) 2004.
- [9] Hisatome M. Power generation system, Google Patents; 1993.
- [10] Elliot, M.A (Ed.), 1981. Chemistry Of coal utilization secondary Supplementary volume. John Wiley & Sons, New York.
- [11] Moore, E.S., 1922. Coal: its Properties, Analysis, Classification, Geology, Extraction, Uses and Distribution. John Wiley & Sons. p. 124.

- [12] Einstein D, Worrel E, Khrusch M. Steam systems in industry: Energy efficiency improvement potentials[R]. Lawrence Berkeley National Laboratory, 2001. available at <http://escholarship.org/uc/item/3m1781>
- [13] D. Husson, S.D. Bennett, G.S. Kino, Remote temperature measurement using an acoustic probe, *Appl. Phys. Lett.* 41 (1982)915,<http://dx.doi.org/10.1063/1.93334>
- [14] Hua Yan, Zhen Peng, Kexin Cui, Liang Zhang, Acoustic travel-time measurement in acoustic temperature field monitoring, in: 2008 7th WorldCongress on Intelligent Control and Automation, Chongqing, China, June 2008,pp. 4947–4951.
- [15] Kousuke Kudo, Koichi Mizutani, Temperature measurement using acousticreflectors, *Jpn. J. Appl. Phys.* 43 (5B) (2004) 3095–3098.
- [16] Hajime Arimoto, Nobuo Takeuchi, Sachio Mukaihara, Toru Kimura, Ryuzo Kano, Takeo Ohira, Shinji Kawashima, Kazuya Iwakura, Applicability of TDLAS gas detection technique to combustion control and emission monitoring under harsh environment, *Int. J. Technol.* 2 (1) (2011) 1–9.
- [17] Pei-jin Liu, Bin Huang, Bin Yang, Guo-qiang He, TDLAS for measurement of temperature in combustion environment, in: *Proceedings of SPIE – The International Society for Optical Engineering*, 2013, vol. 8796; <http://dx.doi.org/10.1117/12.2011262>.
- [18] D. Nabagło, P. Madejski, Combustion process analysis in boiler OP-650K based on acoustic gas temperature measuring system, in: 3rd International Conference on Contemporary Problems of Thermal Engineering CPOTE 2012,18–20 September 2012, Gliwice, Poland.
- [19] Andrew D. Sappey, Pat Masterson, Eric Huelson, Jim Howell, Mike Estes, Henrik Hofvander, Atilio Jobson, Results of closed-loop coal-fired boiler operation using a TDLAS sensor and smart process control software, *Combust. Sci. Technol.* 183 (11) (2011) 1282–1295.
- [20] Energy performance assessment of boilers. Bureau of Energy. Efficiency (2005).<http://www.beee.com/>; <http://www.em-ea.org/>.

Passive Thermal Management of Lithium Ion Batteries using Metal foam Saturated with Phase Change Material

Wajid Ali^{1,a}, Abid Hussain^{1,b} and Ali Hasan^{1,c}

¹*Department of Mechanical Engineering, University of Engineering and Technology Taxila.*

Email address: ^{a)} wajid.alimemon@gmail.com ^{b)} abid.hussain@uettaxila.edu.pk

Abstract— Li-ion battery pack utilized in the Electric vehicles (EVs) and Hybrid electric vehicles (HEVs) require a very effective thermal management system (TMS), to keep the working temperature of the battery pack in the safe range. In this research, a passive thermal management system (PTMs) is developed by utilizing unique composite (Aluminum foam and paraffin wax) to maintain the operating temperature of highly powered li-ion batteries. Comparison has also been made with three other cooling modes i.e. nickel foam-paraffin, natural air-circulation and phase change material (Paraffin wax). The results signify that the safety requirements of the lithium-ion battery cannot met through natural air circulation as a cooling mode. After using aluminum foam/paraffin composite as medium of cooling, results show a decrease of 32.6% in the temperature comparing with natural air cooling, 5.1% by nickel/paraffin composite as a medium of cooling and 11.8% in comparison to the pure PCM at 2C discharge rates.

Keywords— Charge & Discharge rates; TMS; li-ion batteries; PCM material, Aluminum foam.

XI. Introduction

The Electric vehicles (i.e. EVs & HEVs) demand is rising on daily basis because of issues related to the emissions, limited

resources of fossil fuels and price hike of hydrocarbon. The fuel used to power EVs and HEVs is the li-ion batteries which have more energy & power density. The problem which frequently occurs in using the high-powered batteries of li-ion in EVs and HEVs is the temperature rise at the time of charge and discharge. This temperature rise causes the production of heat in the battery pack and there is the possibility of an explosion if the battery temperature reaches its critical limit.

Different methodologies are used for efficiency enhancement of PCM for temperature management of the lithium-ion battery pack. Wu et al.[1] developed a self-type heat contained duct enclosed with battery pack superficial area for the control of excess temperature throughout the discharge. They discovered that using the heat pipe with air strained convection has decreased the temperature and caused extra uniform temperature supply.

Pesaran et al. [2] discovered a liquid-based temperature control system. They computed the temperature throughout the discharge procedure. Previously the organic phase change materials were also given preference

due to their higher latent heat, good chemical properties and inexpensiveness [3]. Sabah et al. [4] did comparative research between the PCM and forced air circulation methodology at a constant discharge rate for both the methodologies. They used 1.5 Ah 18650 commercial lithium-ion battery cells. Their research demonstrated that the phase change material cooling methodologies and effective temperature distribution was greater in comparison to the active cooling methodology at 1.3 C discharge rate & ambient temperature of 40 °C. PCMs are also better choice for battery thermal management, because of its advantages as a thermal energy storage use. As they have a drawback of having very less thermal conductivity, therefore it has limited utilization in heat storage applications. [5]. To overcome this drawback different kinds of methodologies are presented for thermal conductivity enhancement of PCMs. Fan and Khodadadi [6] researched to enhance the PCMs thermal conductivity, they used the spread fins, mixing the higher thermal conductivity bits, or using the porous metal foams. For the electric vehicles. Khateeb et al.[7] researched the 4 modes of heat transfer for 18650 (2.20 Ah) battery pack. They found that the temperature of aluminum foam/PCM composite decreased an extra 5 °C temperature comparing with PCM material. Another research conducted by li et al. [8] methodology for encapsulating of phase change material with the copper metal foam. They showed in their research that PCM material’s thermal conductivity was enhanced greatly using copper metal foam and heater surface temperature was also decreased.

The purpose of this research is the development of a TMS for the harmless working condition of lithium-ion battery pack applied in the HEVs & EVs by employing Aluminum foam saturated with PCM (Paraffin wax). This research has also been compared with the three other methodologies, i.e. natural air, PCM & nickel foam/paraffin composite.

XII. Experimental setup

A. Setup of Battery Packs

The lithium-ion battery cells utilized for this research has been tested and those having above 90% efficiency are utilized. Cells used in this research are 18650 B NCR type Panasonic their operating voltage range is 3.0 Volts - 4.2 Volts. Whereas pack capacity is 3.40 Ah. The diameter of the cell is 18.40 mm, the height of each cell 65.0 mm and nominal voltages are 3.70 Volts. The connection is made in the series and the configuration of the cells is 6S (six cells in series). For battery pack safety, a safety circuit is also installed. The specifications are listed in Table No 1.

Table 18 Battery Pack Specification.

Arrangement of Cells	6 cells in Series
Capacity (Pack)	3.40 Ah
Cells Space	5.740 mm
Rate of Charging	0.50C rate (1.70 A) galvanostatic mode and 100 mA potentiostatic mode
Rate of Discharge	0.50C rate (1.70 A), 1.50C rate (5.10 A) & 2.0C rate (6.80 A)
Voltage limit cut off	Charing 4.2 Volts per cell & Discharging 3.0 Volts per cell.

PCM properties (thermo-physical) utilized in this research are: specific heat capacity (2000.0 J/Kg.K), its density in liquid & solid state is 760 kg/m³ & 880 kg/m³ respectively, melting temperature 38.0 °C to 41.0 °C, Paraffin thermal conductivity is 0.20 W/m.K. Aluminum foam sample having porosity (ϵ) 0.950 and pore density (w) 20.0 PPI (Pore Per Inch) with a measurement of L=165.0 mm, W=65.0 mm and H=25.0 mm, (L x W x H). Aluminum foam thermal conductivity 91.40 [W/ (m.K)]. The drilled cavity diameter is 18.3 mm and space between two cells is 24.04 mm from their centers. After dividing the foam into two parts the cells have been placed in the drilled holes, the sole purpose of this structure is to decrease the weight of a battery pack.

B. Aluminum metal foam/PCM (paraffin) Composite.

Aluminum foam-paraffin was made through penetrating liquid PCM (paraffin) in the pores of Aluminum foam using a water bath (hot). For calculation of thermal conductivity of composite, equation used is equation No 1. [9].

$$Ke = A [(1 - \epsilon_b) k_{foam} + \epsilon_b k_{pcm}] + \frac{1 - A}{\frac{\epsilon_b}{k_{pcm}} + \frac{1 - \epsilon_b}{k_{foam}}} , \quad (1)$$

Expressions used in this equation are, effective thermal conductivity ke. A being the coefficient of correlation. ϵ_b for bulk porosity. k_{foam} is thermal conductivity of foam & k_{pcm} is PCM thermal conductivity. The calculated quantities of bulk porosity 0.970 and foam thermal conductivity is 91.40 [W/m.K] [10]. Bhattacharya et al.[9] proposed coefficient of correlation (A) to be 0.350, he highlighted that

through this Equation (1), the calculating range of porosities and pore density of the foam is from 0.905 to 0.978 & 5 to 40 Pore Per Inch respectively. As the Pore density and porosities of foam lies within the suggested range, the operational thermal conductivity of Aluminum foam composite is also calculated through the same equation and the value is 1.802 [W/ (m-K)]. The “Fig 1”. of Aluminum foam before and after permeation is shown below. Leica microscope (Leica-M205C) was used to take the pictures.

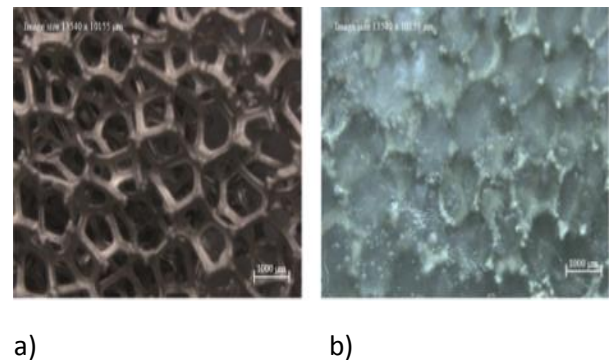


Figure 1 Aluminum metal foam (a) before PCM infiltration (b) After PCM infiltration.

C. Battery Pack Testing.

These tests are performed on four methods i.e. Natural air circulation, Pure phase change material, Nickel foam/paraffin composite & Aluminum foam/paraffin wax composite. Three thermocouples having an accuracy of 0.10 °C has been used in this research to investigate battery surface temperature. Two thermocouples are in the mid of fifth & third cells and the other one is placed on the battery cell +ve side terminal. Another thermo-couple is also used to check the environmental air temperature. Laboratory environment temperature was thermostatically kept at 25.0 °C. The charging

of the battery was done on the galvanostatic & potentiostatic modes, constant rate was 0.50 C (1.70 A) and 100 mA respectively and limit of voltage cut off was 4.20 Volt/cell. Charge time continued after a break till the pack reaches the environmental temperature. Discharge has been done 1.50 C (5.10 A) & 2.0 C (6.80 A) rate till it reduces to 3.0 Volts each battery cell. Lastly, break time was continued for the complete cycle till the temperature reaches the environmental temperature. The temperature has been recorded after passing every 30 seconds with the help of DAQ (National Instrument NI USB-9162). These values are shown in Table. 2.

Table 19 Load Cycles Parameters

Parameters	Test 01	Test 02
Charge	0.5 C (1.7 A) rate	0.5 C (1.7 A) rate
Rest	up to ambient temp.	up to ambient temp.
Discharge	1.5 C (5.1 A) rate	2 C (6.8 A) rate
Rest	up to ambient temp.	up to ambient temp.



Fig.2 Research arrangement.

The battery pack research arrangement and charging, discharging module can be seen in “Fig 2”.

XIII. Results and discussion

A. Performance Of Different Cooling Mediums (Passive TMS).

For classification of natural air flow, the Rayleigh number used is the equation No. 2.

$$Ra = \frac{g\beta(T_s - T_o)L^3}{\nu^2} Pr, \quad (2)$$

In equation β [1/K] thermal expansion coefficient, ν [m²/s] viscosity (Kinematic), g is the gravity that is 9.8 m/s², L is length of battery cell (6.5 cm), T_s [K] is battery cell surface temperature and T_o [K] the ambient temperature. For this research T_o is kept constant, which is equal to 298.150 K, whereas the T_s surface temperature is calculated via experiment. The range of Rayleigh number, $10^3 < Ra < 10^9$ is considered as the laminar flow, while for turbulent flow the range is $10^9 < Ra < 10^{14}$.

The experiment was conducted for the Aluminum foam/paraffin composite at 0.50 C, 1.50 C & 2.0 C rate. During charge & discharge process the temperature was increased up to 32.1 °C and 30.4 °C respectively at 0.5 C. This

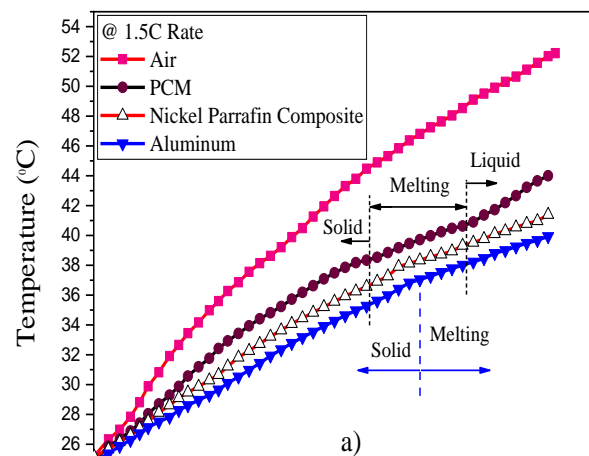


Figure 4. Temperature variations with respect to time using four cooling modes, i.e. Air, PCM, Nickel/paraffin composite and aluminum foam paraffin, a) at 1.5 C.

temperature is less than the melting point range of the paraffin (i.e. 38 °C to 41 °C). From these results the aluminum foam/paraffin composite thermal conductivity has increased. The developed composite had played a vital role for raising the paraffin thermal conductivity that caused good quantity of heat exchange of the battery pack. For the observation of sensible heat influence, the experiment was repeated at 1.50 C (5.1 A) & 2.0 C (6.80 A) rate. These results are shown in "Fig 4. a & b". The natural air-circulation mode temperature is 52.22 °C and 64.544 °C, at the 1.5 C and 2.0 C discharge rates respectively. While the temperature using the pure paraffin is, 44.001 °C, 49.331 °C at 1.5 C and 2 C discharge rates respectively. For nickel /paraffin composite the results are 41.392 °C, 45.84 °C at the same discharge rates. While using the aluminum foam/paraffin composite the results are 39.94 °C, 43.5 °C at 1.5 C and 2 C discharge rates respectively. Figure shows a decrease in temperature from 45.6 °C to 43.5 °C after utilizing aluminum foam/paraffin composite as thermal mode instead of nickel paraffin composite. If we further analyze these results for observations, it shows that there is the reduction of temperature about 32.6% utilizing aluminum foam-PCM (paraffin) composite in comparison to mode of natural air cooling. If we compare the results of PCM cooling medium, there is also temperature decrease about 12%. Also, the aluminum foam/paraffin composite has an advantage over the nickel/paraffin composite. This comparison shows a decrease in temperature of about 5% at C/2 discharge rate. From these results, it is concluded that aluminum foam/paraffin composite can be used as a TMS to maintain the lithium-ion batteries

operating temperature utilized in the EVs & HEVs.

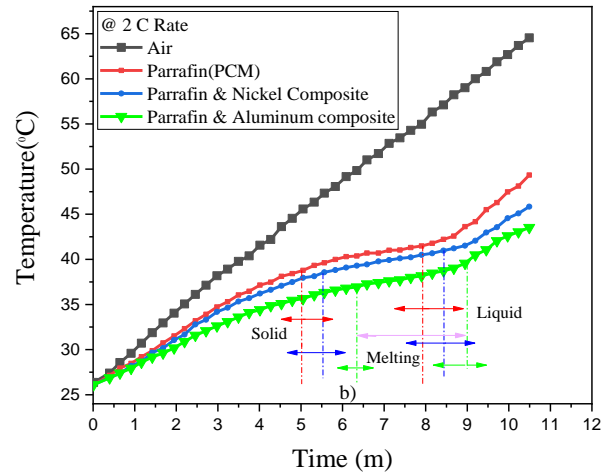


Figure 4. Temperature variations with respect to time using four cooling modes, i.e. Air, PCM, Nickel/paraffin composite and aluminum foam paraffin b) 2.0 C discharge rate.

XIV. Conclusion.

Aluminum foam/PCM (paraffin) composite is used to make thermal management system (TMS) for highly powered li-ion battery pack. It is concluded that by using this composite, lithium-ion batteries temperature drops of 32.6%, 12% & 5% has been noticed in comparison to other cooling modes i.e. natural air circulation, PCM and nickel foam/paraffin composite respectively. The increase in li-ion battery surface temperature has been reduced more in comparison to the other three cooling modes (i.e. natural air, pure paraffin, & nickel foam-PCM (paraffin) composite). This decrease in battery surface temperature highlights the importance of aluminum metal foam/PCM (paraffin) composite as a cooling mode for development of lithium-ion battery pack TMS (thermal management system).

XV. References:

- [1] M. Wu, K. H. Liu, Y. Wang, and C. Wan,

- “Heat dissipation design for lithium-ion batteries,” vol. 109, pp. 160–166, 2002.
- [2] A. A. Pesaran, “Battery Thermal Management in EVs and HEVs : Issues and Solutions,” 2001.
- [3] F. Agyenim, N. Hewitt, P. Eames, and M. Smyth, “A review of materials , heat transfer and phase change problem formulation for latent heat thermal energy storage systems (LHTESS),” vol. 14, pp. 615–628, 2010.
- [4] R. Sabbah, R. Kizilel, J. R. Selman, and S. Al-Hallaj, “Active (air-cooled) vs. passive (phase change material) thermal management of high power lithium-ion packs: Limitation of temperature rise and uniformity of temperature distribution,” *J. Power Sources*, 2008.
- [5] M. M. Farid, A. M. Khudhair, S. Ali, and K. Razack, “A review on phase change energy storage : materials and applications,” vol. 45, pp. 1597–1615, 2004.
- [6] L. Fan and J. M. Khodadadi, “Thermal conductivity enhancement of phase change materials for thermal energy storage : A review §,” vol. 15, pp. 24–46, 2011.
- [7] S. A. Khateeb, S. Amiruddin, M. Farid, J. R. Selman, and S. Al-Hallaj, “Thermal management of Li-ion battery with phase change material for electric scooters: Experimental validation,” *J. Power Sources*, 2005.
- [8] W. Q. Li, Z. G. Qu, Y. L. He, and W. Q. Tao, “Experimental and numerical studies on melting phase change heat transfer in open-cell metallic foams filled with paraffin,” vol. 37, pp. 1–9, 2012.
- [9] A. Bhattacharya, V. V Calmidi, and R. L. Mahajan, “Thermophysical properties of high porosity metal foams.”
- [10] X. Xiao, P. Zhang, and M. Li, “Preparation and thermal characterization of paraffin/metal foam composite phase change material,” *Appl. Energy*, 2013.

Mechanical Properties of Concrete with E-Waste as Partial Replacement of Natural Aggregate

Khawar Ali^{1, a, 2, b} Dr. Irshad Qureshi
¹*Research Assistant*
²*Assistant Professor UET Taxila*

Email address: ^{a)} khawarali187@gmail.com, ^{b)} irshad.qureshi@uettaxila.edu.pk

Abstract— Concrete is a fundamental constitute of construction industry across the globe. The bulk of concrete is made up of aggregates, hence structural behavior of concrete significantly relies on the quality and properties of aggregates. Natural resources are depleting due to continuous production of concrete resulting in stringent environmental impact. To endeavor this challenging situation, several studies have been conducted to opt the sustainable and eco-friendly by-products generated by automobiles, packaging industries, electronics goods etc. as alternative construction material. This paper presents partial replacement of natural aggregates with plastic aggregates and the effect of plastic aggregates on fresh and hardened properties of concrete. Three replacement percentages are adopted which are 10%, 15%, 20%. Also, silica fume is used in three percentages to enhance the properties of concrete with plastic aggregates. Effects of these parameters on the strength properties of concrete are discussed in detail and the suitability of recycling electronic waste in construction industry is discussed.

Keywords—concrete, natural aggregate electronic waste, slump, mechanical properties

I. Introduction

Amount of concrete produced is constantly increasing, requiring an increasing amount of natural resources to be used to meet the demand. Major Portion in the concrete is aggregate, it may be fine or coarse. Source of coarse aggregates are natural stones and mountains. Plastic is a highly sought-after material due to its excellent properties, resulting in an increase in its production worldwide. Plastic is used in population-oriented industries such as automobiles, packaging industries, electronics goods and agriculture. As the population is increasing day by day, the production of plastic waste is also increasing. This is resulting into a huge problem as the most of waste plastic is not recycled and is creating an environmental hazard. Electronic waste (E-waste) on the other hand has even more environmentally hazardous materials and is mostly dumped in developing countries like Pakistan. One solution to this problem is to reuse the E-waste in construction industry which will not only save the natural resources but also will help in

recycling E-waste. Total mass of concrete contains 60-70% of the aggregates and replacing the aggregates partially or fully will help to preserve the natural sources [1]. There have been few studies where plastic has been used to produce aggregates. Formation of artificial or plastic aggregate has been done by shredding the plastic. To characterize the fracture energy of concrete and mortar having plastic aggregate, tensile test is performed [2, 3, 4]. The addition of Plastic aggregate in concrete reduced the strength of the concrete but enhanced the fracture energy. Hannawi et al. [3] reported that mortar having plastic aggregate reduce the tensile strength but increase the fracture energy up to 6% as compared to conventional sand. Addition of plastic aggregate slow down the crack propagation and thus increase the fracture energy and made the structure more resilient. Although there are studies which are focused on the use of plastic aggregates in concrete, the current study is focused on the use of E-waste aggregates as partial replacement of natural aggregates.

II. Materials

Material testing is the process to determine the engineering properties and the characteristics of material. Aggregate play important role in the strength of concrete so their properties really matter a lot. Therefore, it is necessary to test them in the lab for determining their shape, size, gradation, fineness modulus, specific gravity and the water absorption. This article describes the procedure as well as the mix proportion of the materials used in the research work. The section also elaborates the material properties of concrete mix. Ordinary Portland Cement (OPC), provided from Fauji Cement Company according to the requirements of ASTM C-150 was used. Natural Coarse aggregate from margalla crush, sand from lawrancepur and tap water was used in research. Artificial aggregate was manufactured from waste plastic. Size of artificial aggregate was greater than 4 mm and less than 25mm which was quite like natural aggregate.

III. Sieve Analysis Test

Sieve analysis is widely used test in civil engineering for finding the gradation of aggregates whether they are capable to be used in concrete or not. The test includes the sieving of aggregates through the standard designated sieves. The sieve analysis of fine aggregates was performed according to ASTM C 136, and the fineness modulus of lawrancepur sand is 2.76 which tells its good capability to be used in concrete for better results. Nominal size of natural coarse aggregate and plastic aggregate was 20mm.

IV. Water absorption Density, and Specific Gravity Test

Water absorption values are helpful in determining the water absorbed by the pores available in aggregate particles. The Tests were performed as per ASTM C127 – 15 [5]. The values of specific gravity and water absorption are presented in table 2

V. Preparation of Mixes:

In this study, total seven mixes were considered. One of them was control mix while others had 10%, 15%, 20% replacement of natural coarse aggregate with and without addition of silica fume. Mix ratio used in this study was 1:1.5:3 and water cement ratio was 0.45. Ultra-Super Plast was used to improve the workability of concrete which was 1.25 % of the weight of the cement. PA stands for plastic aggregate and SF stands for silica fume. For example, 10% PA corresponds ten percent replacement of natural aggregate to Plastic aggregate and 10%PASF means ten percent replacement of coarse aggregate with natural aggregate and ten percent silica fume with cement.

VI. Slump Test

Workability ensures the handling of concrete and controls the strength and durability. Workability of the fresh concrete were examined using slump test according to ASTM [8]. The effect of replacing coarse aggregates with plastic aggregates on slump is shown in Fig. 1. The increase in slump of PA mixes ranged from 96mm to 130mm as the replacement level increased from 10 to 20%. These results also confirmed in a work by Ferreira et al [9], Silva et al [10], de Brito et al [11] and Hadipramana et al [12] that showed using plastic aggregate increases the workability with the increase of plastic content. This could be still beneficial in casting and pumping of such type of

Table VI.1 Specific gravity , Water absorption and Density

Source Name	Specific Gravity	Water absorption	Density(kg/m ³)
Margallah Crush	2.61	0.97	1518
Plastic Aggregate	0.88	0	620

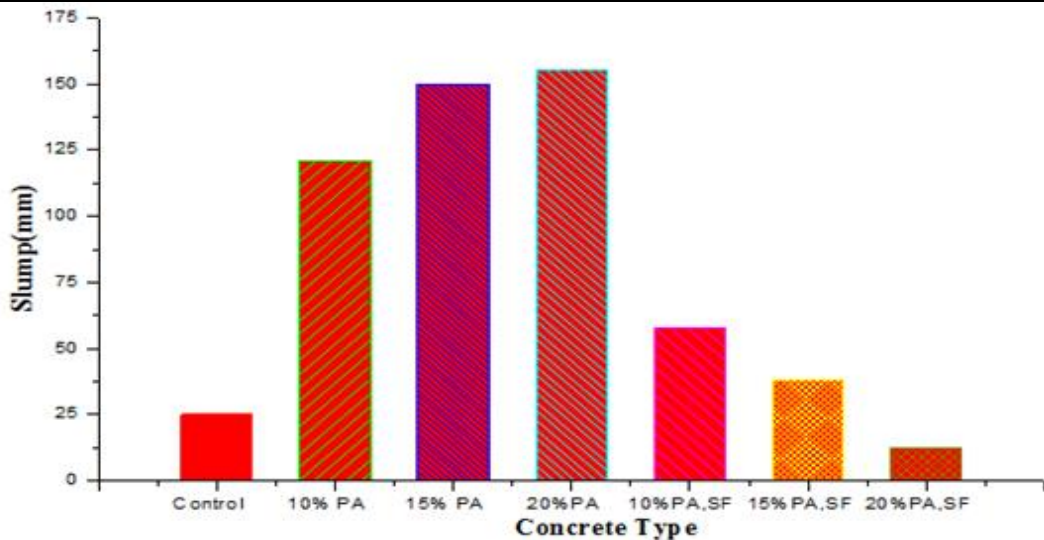


Figure 13 Slump Result

concrete over congested reinforcement or long distance. Choe et al also reported that increase in slump is not only attributed to spherical shape with smooth surface but also due to zero water absorption capacity. The decline in slump of PASF as compared to PA with the addition of silica

fume from 97mm to 142.5 due small particle size and large surface area of silica fume.

VII. Casting and curing of Concrete Specimens

All the samples were made with standard concrete cylinders of 12” height and 6” diameter. The mix was placed in the mold in three layers of equal depth and compacted using stand size rod with 25 blows on each layer. A total of 42 samples were casted with 6 nos. of samples for each formulation. Fig 2 shows the casted samples.



Figure 14 Casting and Curing of Concrete Sample

The test samples were remolded after 24 hours and then placed in curing tank for 28 days at room temperature.

VIII. Testing Method

The samples were tested for their compressive and tensile strengths using compression testing machine and universal testing machine. The compressive strength of 28 days cured hardened cylinders was measured according to the ASTM specification using standard compressive testing machine (CTM) having a loading rate of 100 KN/min. For each combination, three samples were tested for compressive strength and three were tested for split cylinder test[6-7].

A. Compressive Strength

Fig. 3 shows the compressive strength results for the concrete mixes considered in this study. The CPA0 and CPA10SF10 had a compressive strength of 42.07 and 34.28 MPa, respectively, whereas the result of CPA10 to CPA20SF20 are ranging from 31.54 to 27.98 MPa. Decrease in compressive strength of concrete mixes having plastic aggregate and silica fume compared with control concrete ranged from 18% to 33% as the replacement level was increased from 10 to 20 % with the interval of 5.

The reduction in compressive strength of concrete mixes having plastic aggregate without silica fume ranged from 25% to 37% and with silica fume from 18% to 33% as the replacement level increased from 10 to 15%. With the addition of silica fume reduction in compressive strength reduced due its pozzolanic activity and smaller particle size as compared to cement. Previous research agreed with the results that compressive strength increased as the replacement level of silica fume increased. The reduction in compressive strength of concrete mixes is due to weak interfacial transition zone between the cement paste and plastic. Decrease in compressive strength is due to more bleeding water in the concrete containing plastic aggregate as compared

to conventional concrete mixes because plastic aggregates are hydrophobic. This water is located near the plastic aggregate and produced weak bond between plastic and cement matrix. The results were consistent with the previous research works done on other kinds of plastic aggregates [13, 14, 15-17]

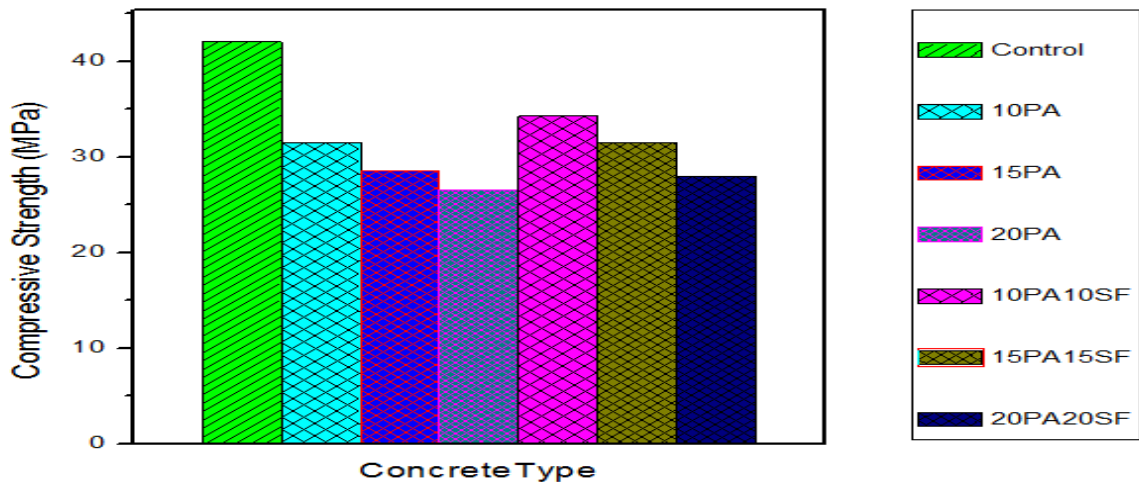


Figure 15 Compressive Strength Result

B. Tensile Strength

Fig.4 presents the splitting tensile strength results of concrete mixes. The CPA0 and CPA10SF10 had tensile strength 4.45 and 3.41 MPa, respectively. The concrete mixes containing silica fume showed tensile strength from 3.41 to 3.041 MPa and 3.17 to 2.88 MPa without silica fume as the replacement level increase from 10 to 20%.

The tensile strength of CPA0 compared with the other formulations containing plastic aggregate was reduced up to 29 to 35% as the replacement level increase from 10 to 20%. Moreover, the decline in tensile strength of concrete mixes having silica fume ranged from 23 to 32%. The downward trend of relative splitting tensile strength of concrete mixes was consistent with previous studies [18-20]. Decline in compressive and splitting tensile strength of concrete mixes is due to weak bond of plastic aggregate with concrete. It is also due to the hydrophobic, smooth spherical shapes and zero water absorption of plastic aggregate.

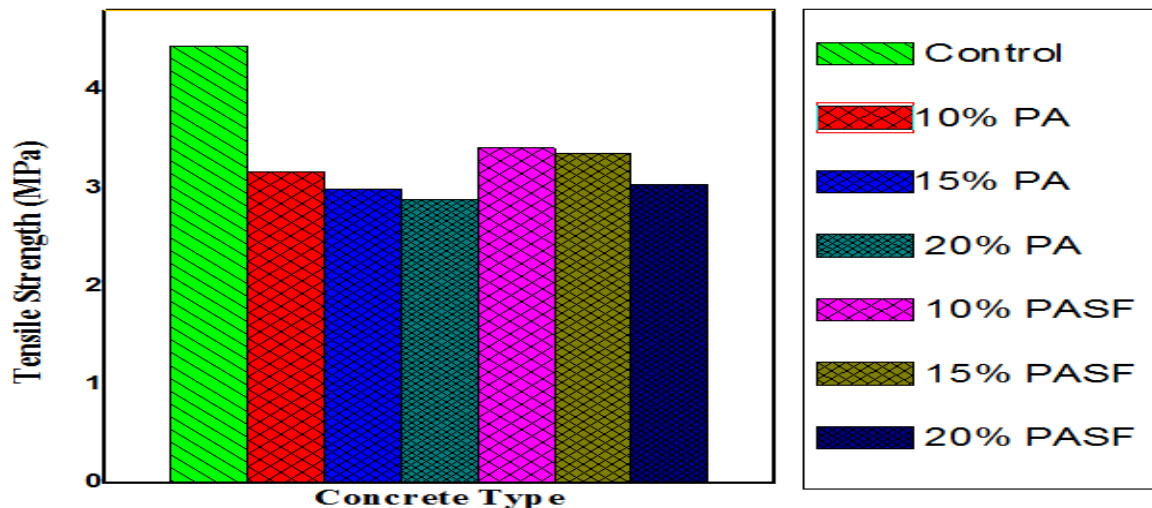


Figure 16 Tensile Strength Result

CONCLUSION

- The value of slump increase with the replacement of plastic aggregate due to zero water absorption and hydrophobic nature of the plastic aggregate. Concrete having plastic aggregate was used in such type of construction where more workable concrete mixes are required. At 20% replacement of plastic aggregate with natural aggregate, value of slump increases 84% which is the suitable value for more workable concrete.
- Concrete Samples reduced the value of slump after replacement of silica fume and plastic aggregate with cement and natural aggregate respectively. Value of slump was 12mm at maximum replacement of 20% while control have 25mm slump. Such type of concrete is recommended in pavement and shoulders.
- With the replacement of plastic aggregate, compressive strength of concrete mixes was reduced up to 31%, 38% and 43% as compared to control mix but it was reasonable and more than structural strength for construction.
- With the replacement of plastic aggregate and silica fume with conventional aggregate and cement respectively, decrease in strength was 26%, 28%, and 22% for 6, 12 and 18%.
- Tensile strength of control mix was 652 psi while at 10, 15 and 20% replacement of plastic aggregate strength was 4.49, 3.064 and 3.0008 MPA respectively. Concrete having 10, 15 and 20% replacement of cement and natural aggregate with silica fume and plastic aggregate was 3.413, 3.348 and 3.0468 MPA respectively, increase in strength was due to replacement of silica fume with cement.
- Use of e-waste in concrete make significant contribution towards reduction in pollution of the environment. In parallel due to increase in global demand for construction aggregates, it is an effort to use of electronic waste to contribute more sustainable construction.

- Although decremental effect on mechanical properties of different formulation but at maximum replacement (20% PA), but results suggest that it can be used for structural and non-structural applications.

References

- [62] M. Gesoğlu, E. Güneyisi, R. Alzebaree, and K. Mermerdaş, "Effect of silica fume and steel fiber on the mechanical properties of the concretes produced with cold bonded fly ash aggregates," *Construction and Building Materials*, vol. 40, pp. 982-990, 2013
- [63] Fredonia. (2012). "Global demand for construction aggregates in 2015, demand and sales forecasts." (<http://www.fredoniagroup.com>) (May 23,2015).
- [64] K. Hannawi, S. Kamali-Bernard, W. Prince, Physical and mechanical properties of mortars containing PET and PC waste aggregates, *Waste Manage.* 30 (11) (2010) 2312–2320.
- [65] Z.Z. Ismail, E.A. AL-Hashmi, Use of waste plastic in concrete mixture as aggregate replacement, *Waste Manage.* 28 (11) (2008) 2041–2047.
- [66] A. International, "Standard Test Method for Relative Density (Specific Gravity) and Absorption of Coarse Aggregate , ASTM C 127-15."
- [67] ASTM, C. "39/C39M-03 (2003)," "Standard Test Method for Compressive Strength of Cylindrical Concrete Specimens".
- [68] In American Society for Testing and Materials, pp. 21-25. ASTM, C. (1989). 496-86, "Standard Test Method for Splitting Tensile of Cylindrical Concrete Specimens". *Annual Book of ASTM Standards*, 4(02), 259-262.
- [69] ASTM, C. (2012). Standard test method for slump of hydraulic-cement concrete.
- [70] Y. Ghernouti, B. Rabehi, B. Safi, and R. Chaid, "Use of recycled plastic bag waste in the concrete," *Journal of International Scientific Publications: Materials, Methods and Technologies*, vol. 8, 2011.
- [71] R. V. Silva, J. de Brito, and N. Saikia, "Influence of curing conditions on the durability-related performance of concrete made with selected plastic waste aggregates," *Cement and Concrete Composites*, vol. 35, no. 1, pp. 23-31, 2013.
- [72] R. V. Silva, J. De Brito, and R. Dhir, "Properties and composition of recycled aggregates from construction and demolition waste suitable for concrete production," *Construction and Building Materials*, vol. 65, pp. 201-217, 2014.
- [73] J. Hadipramana, S. Mokhatar, A. Samad, and N. Hakim, "An exploratory compressive strength of concrete containing modified artificial Polyethylene aggregate (MAPEA)," in *IOP Conference Series: Materials Science and Engineering*, 2016, vol. 160, no. 1, p. 012065: IOP Publishing.
- [74] Lamond, J. F. (1994). *Making and Curing Concrete Specimens*. In *Significance of Tests and Properties of Concrete and Concrete-Making Materials*. ASTM International.

- [75] S. Kou, G. Lee, C. Poon, and W. Lai, "Properties of lightweight aggregate concrete prepared with PVC granules derived from scraped PVC pipes," *Waste Management*, vol. 29, no. 2, pp. 621-628, 2009.
- [76] ASTM, "Standard Test Method for Static Modulus of Elasticity and Poisson's Ratio of Concrete in Compression."
- [77] J. N. Farahani, P. Shafigh, B. Alsubari, S. Shahnazar, and H. B. Mahmud, "Engineering properties of lightweight aggregate concrete containing binary and ternary blended cement," *Journal of cleaner production*, vol. 149, pp. 976-988, 2017.
- [78] A. Al-Manaseer and T. Dalal, "Concrete containing plastic aggregates," *Concrete International*, vol. 19, no. 8, pp. 47-52, 1997.
- [79] Y.-W. Choi, D.-J. Moon, J.-S. Chung, and S.-K. Cho, "Effects of waste PET bottles aggregate on the properties of concrete," *Cement and concrete research*, vol. 35, no. 4, pp. 776-781, 2005.
- [80] A. B. Fraj, M. Kismi, and P. Mounanga, "Valorization of coarse rigid polyurethane foam waste in lightweight aggregate concrete," *Construction and Building Materials*, vol. 24, no. 6, pp. 1069-1077, 2010.
- [81] M. Frigione, "Recycling of PET bottles as fine aggregate in concrete," *Waste management*, vol. 30, no. 6, pp. 1101-1106, 2010.

Hybrid Thermal Management of Heating Element using Forced Air Convection and Phase Change Material Soaked in Copper Foam

Sohaib Nazar^{1, a}, Abid Hussain^{1, b} and Tanzeel-ur-Rehman^{1, c}

¹Department of Mechanical Engineering, University of Engineering & Technology, Taxila

Email address: ^{a)}sohaibnazar7@gmail.com, ^{b)}abid.hussain@uettaxila.edu.pk,

^{c)}tanzeel_atk@yahoo.com

ABSTRACT—*The current study includes the comparison of hybrid thermal management system designed for heating element with active and passive thermal management system. The effectiveness and usefulness of hybrid thermal management system is evaluated and compared experimentally. All the experiments are performed under constant ambient temperature of 25°C. It can be concluded from experimental results that alone active and passive thermal management system is not sufficient to keep the temperature of heating element within the safety limits. Moreover, combination of active and passive thermal management system gives more Steady temperature distribution and have the ability to maintain the temperature of heating element for long time interval as compared to active as well as passive thermal management system.*

Key words: *Active, Passive, Thermal Management, Hybrid.*

I. INTRODUCTION

To keep the temperature of electrical and electronic devices within the safety limits different techniques are utilized. Plenty of researchers worked on different thermal management system to evaluate and to suggest the best system for severe ambient conditions. Pesaran reported that the function of thermal management system is to sustain the temperature at an optimum range with even temperature variation and to prevent the occurrence of thermal runaway [1]. Irregular temperature distribution and overheating of battery module result in reduction of life span of battery pack [2]. According to US air force premature failure of more than 55%

electronic devices occur due to overheating and non-uniform temperature distribution [3]. Excess operating temperature of lithium ion battery not only result in reduction the life span of battery but also result in serious accidents like fire and explosion [4,5]. Samimi et al. experimentally assessed the thermal function of phase change material saturated with carbon fibers and concluded that presence of carbon fibers with PCM give more uniform temperature distribution [6]. Rao et al. experimentally explored the thermal management system comprised of copper foam embedded in paraffin their results show that the local temperature difference is 2.85°C and maximum temperature difference is 38.94°C which indicate the suitability of this system for challenging ambient conditions [7]. Wang et al. experimentally tested the thermal management system comprised on paraffin and paraffin/aluminum foam composite results show that if heat storage time of PCM is 74.4% and 73.6% under heat flux of 7000 W/m² and 12000 W/m² the use of aluminum foam result in smooth and steady temperature variation [8]. Hussain et al. experimentally investigated the nickel foam paraffin based thermal management system and also examined the geometric properties of metal foam it can be predicted from results that the combination of nickel foam and paraffin reduce the temperature of

battery pack about 24% and 31% compared to pure PCM. Decrease in permeability and pore density of metal foam also reduce the surface temperature of battery module [9]. Li et al. made the comparison between the thermal management system based on copper foam /PCM composite combined with natural air-convection and pure PCM. Results exhibit that natural air cooling is not enough for maintaining the temperature within safety limits. Due to lower thermal conductivity of pure PCM metal foam saturated with PCM is more reliable [10]. Zhao et al. explored the consequence of inserting heat pipe into phase change material through experimentation. Their results show that by inserting heat pipe into PCM have the capability to keep the temperature below 50°C for time period as compared to natural air-convection and the temperature variance can be achieved more than 33.6% by injecting heat pipe into PCM [11]. Wang et al. carried out simulation-based study to explore the thermo physical characteristics of pure paraffin, composite material and copper foam/paraffin results show that paraffin reduces the heat storage time by more than 40% and dramatically recover the linearity of paraffin internal heat transfer [12]. Shahabeddin et al. use numerical simulation to predict the effect of using metal foam in air flow channels. Results show that decrease in porosity result in reduction of surface temperature and to obtain smallest ratio of standard deviation of temperature it is recommended that 70% of air flow channel should be occupied with metal foam having porosity of 0.85 [13]. Javani et al. modeled the PCM embedded foam through simulation and concluded that temperature drop of 7.3 K is achieved as compared to dry foam [14]. Hemery et al. experimentally compared PCM, natural and forced air cooling based thermal management system and concluded that advantage of using PCM is that the weight ratio of about 13.4% and more uniform temperature distribution is achieved as compared to natural and forced air cooling mode [15]. PCMs are commonly used material for thermal management because PCMs dissipate and absorb great amount of heat during phase shifting process [16]. Yang et al. executed the numerical simulation to explore the function of air for cooling in axial direction for Li ion battery pack and predicted that more even temperature distribution can be attained by increasing radial interval [17]. Hasan Fathabadi numerically assessed the performance of thermal management system comprised of combined effect of natural air cooling and expanded graphite and explored that the temperature remains in safety limits under ambient temperature of 55°C [18].

II. EXPERIMENTAL SETUP

To perform the experimentation flat plate heating element having capacity of 5 W and dimensions of 100 mm x 100 mm is used. Plexiglass cavity having dimensions of 100 mm x 100 mm is manufactured and utilized as heat sink. Hole is provided at top of the cavity to permit thermocouples and wires of heating element to pass through. For purpose of forced air convection, the variable speed fan is used. Four K type thermocouples are connected at different spots of heating element to carefully measure the temperature. Phase change material is soaked in copper foam by infiltrating paraffin wax in the holes of metal foam. To record the temperature accurately the DAQ (National Instruments) is used. To regulate the current and voltage properly digital AC power supply is used.

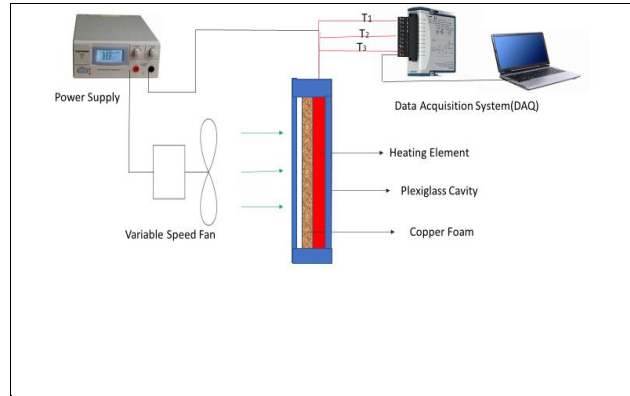


Figure 1. Schematic of Experimental Setup

III. RESULTS AND DISCUSSION

Passive Thermal Management System

Fig.1 show the temperature profile recorded for passive thermal management system. It can be observed from temperature profile that temperature reach beyond the permissible range in 1800 S which is very short time period. Results show that due to lesser thermal conductivity of PCM PTMS is not sufficient to keep the temperature within acceptable range.

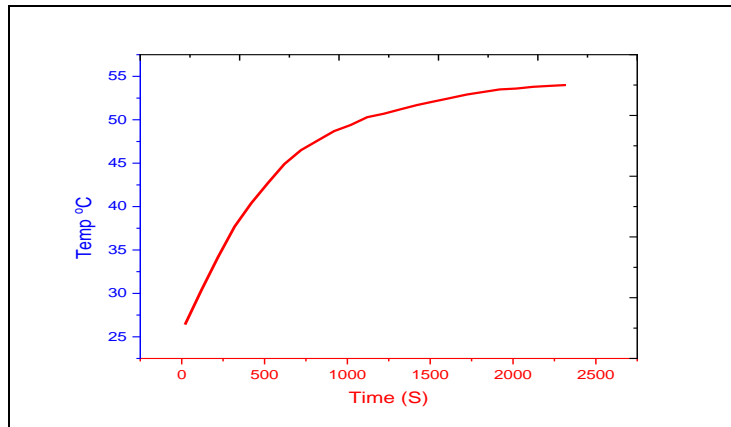


Figure 2. Distribution of temperature with time using Passive thermal management system

Active Thermal Management System

Fig.2 show the temperature variation with time in case of active thermal management system. It can be predicted from curve that the temperature of heating element can be maintained within allowable range up to 1400 S. Experimental results depict that the active thermal management system is not capable to cope with severe environmental conditions.

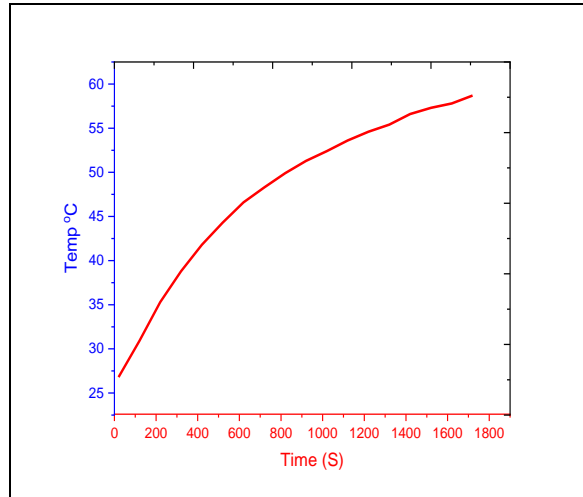


Figure 3. Distribution of temperature with time using active thermal management system

Hybrid Thermal Management System

Fig.4 show the function of hybrid thermal management system in terms of temperature variation with time. The experimental results exhibit that HTMS can maintain the temperature of heating element within safety limit for long time period of about 6000 s, which show the effectiveness of HTMS. It can be predicted from experimental results that hybrid thermal management system is best suitable option for maintaining the temperature of heating element within the permissible range for long time period as compared to active and passive thermal management system.

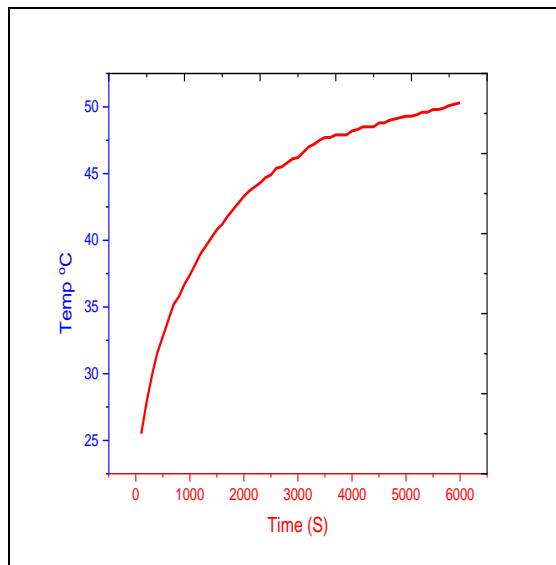


Figure 4. Distribution of temperature with time using hybrid thermal management system

IV. CONCLUSION

The purpose of this research is to experimentally examine and assess the active, passive and hybrid thermal

management systems. The use of PTMS fail due to lower thermal conductivity of PCM. Uniform distribution of heat flux can be achieved by using copper foam saturated with PCM but the time period to maintain the temperature within safety limits is almost same for both PTMS and ATMS. Therefore, combination of ATMS and PTMS is more effective and suitable. The problem associated with PTMS is the large solidification time of PCM which can be overcome by using forced air convection and copper foam can be supportive in recovering the latent heat of PCM. It can be concluded from experimental results that HTMS is the best suitable option for maintaining the temperature within permissible range.

V. REFERENCES

- [1] A.A Pesaran, "Battery Thermal Models for Hybrid Vehicle Simulations" *Journal of Power Sources*, vol-110, pp-377-382,2002.
- [2] Sabbah R, Kizilel R, Selman JR, Al-Hallaj, "Active (air-cooled) vs. Passive (phase change material) Thermal Management of High-Power Lithium-Ion Packs: Limitation of Temperature Rise and Uniformity of Temperature Distribution" *Journal of Power Sources*, vol- 182, pp-630–638, 2008.
- [3] Yeh L. "Review of Heat Transfer Technologies in Electronic Equipment," *Journal of Electron Package*, pp-117-333, 1995.
- [4] W. Wu, X. Yang, G. Zhang, X. Ke, Z. Wang, W. Situ, X. Li, J. Zhang, "An Experimental Study of Thermal Management System Using Copper Mesh-Enhanced Composite Phase Change Materials for Power Battery Pack," *Journal of Energy*, vol-113, pp-909-916, 2016.
- [5] B. Mortazavi, H. Yang, F. Mohebbi, G. Cuniberti, T. Rabczuk, "Graphene or h-BN Paraffin Composite Structures for the Thermal Management of Li-ion Batteries: A Multiscale Investigation," *Journal of Applied Energy*, vol-202, pp-323-334, 2017
- [6] Fereshet Samimi, Aziz Babapoor, Mohammad Mehdi Azizi, Gholamreza Karimi, "Thermal Management Analysis of Li Ion Battery Cell Using PCM Loaded with Carbon Fibers," *Journal of Energy*, vol-96, pp-355-371, 2016.
- [7] Zhonghao Rao, Yutao Huo, Xinjian Liu, Guoging Zhang, "Experimental Investigation of Battery Thermal Management System for Electric Vehicle Based on Paraffin/Copper Foam," *Journal of Energy Institute*, vol-88, pp-241-246, 2014.
- [8] Zichen Wang, Zhuqian Zhang, Li Jia, Lixin Yang, "Paraffin and Paraffin /Aluminum foam composite PCM Heat Storage Experimental Study Based on Thermal Management System of Li ion Battery," *Journal of Applied Thermal Engineering*, vol-78, pp-428-436, 2015.
- [9] Abid Hussain, C. Y Tso, Christopher Y.H.Chao, "Experimental Investigation of Passive Thermal Management System for High Powered Li ion batteries Using Nickel Foam Paraffin Composite," *Journal of Energy*, vol-115, pp-209-218, 2016.

- [10] W.Q.Li,Z.G.Qu,Y.L.He,Y.B.Tao, “Experimental Study of Passive Thermal Management System for High Powered Li-ion Batteries Using Porous Metal Foam Saturated with PCM,”*Journal of Power Sources* ,vol-255,pp 9-15, 2014.
- [11] Jiateng Zhao,Peizhao LV,Zhonghao Rao, “Experimental Study on Thermal Management Performance of PCM Coupled with Heat Pipe for Cylindrical Power Battery,” *Journal of Thermal and Fluid Sciences*,vol-82,pp-182-188, 2016.
- [12] Changhong Wang, “Heat transfer Enhancement of PCM Composite Material Copper Foam/Paraffin,”*Journal of Renewable Energy*, vol-96,pp-960-965,2016.
- [13] Shahbeddin K.Mohammadian, Seyed Moein Rassoulinejad-Mousari,Yuwen Zhang, “Thermal Management Improvement of an Air-Cooled High Power Li Ion battery by Embedding Metal Foam,” *Journal of Power Sources*,vol-296,pp-305-313,2015.
- [14]N.Javani,I.Dincer,G.F.Naterer,G.L.Rohrauer, “Modelling of Passive Thermal Management System for Electric Vehicles Battery Pack with PCM between Cells,”*Journal of Applied Thermal Energy*,vol-73,pp-307-316,2014.
- [15] Charles-Victor Hemery, Franck Pra, Jean Francois Robin, Philippe Marty, “Experimental Performances of a Battery Thermal Management System Using a Phase Change Material,” *Journal of Power Sources*, vol-270, pp-349-358,2014.
- [16] Belen Zalba, Jose M. Marin, Luisa F. Cabeza, Harald Mehling, “Review on Thermal Energy Storage with Phase Change Materials, Heat Transfer Analysis and Applications,” *Journal of Applied Thermal Engineering*, vol-23, pp-251-283,2003.
- [17] Tairan Yang, Naixing Yang, Xiongwen Zhang, Guojun Li, “Investigation of the Thermal Performance of Axial-Flow Air Cooling for the Lithium-Ion Battery Pack,”*Journal of Thermal Sciences*,vol-108,pp-132-144,2016.
- [18] Hassan Fathabadi, “High Thermal Performance Lithium-Ion Battery Pack Including Hybrid Active-Passive Thermal Management System for Using in hybrid/Electric Vehicles,” *Journal of Energy*,vol-70,pp-529-538,2014

Network Application Classification Using Deep Learning Algorithm in Software Defined Networks

Muhammad Basit Umair ^{1,a}, Zeshan Iqbal^{2,b}

¹*Department of computer science, University of Engineering and Technology, Taxila*

²*Department of computer science, University of Engineering and Technology, Taxila*

Email Address: ^a basitumair@gmail.com, ^b zeshan.iqbal@uettaxila.edu.pk

Abstract--Network application classification is quintessential for a wide range of network operations, network security monitoring, misconfiguration, and intrusion detection in network. Network application classification has the ability to solve fundamentals to numerous network management activities. As the popularity of software-defined network (SDN) is evolving technology and a suitable environment for easily applying in an efficient monitoring policy. In SDN architecture, the control plane separates from forwarding devices and making networks programmable. The emergence of deep learning methods and SDN provides a new way for application classification. In this study, a deep learning-based application classification method is proposed that can classify network traffic affectively. The experimental setup confirms that, the proposed model achieves a better classification accuracy of 99.10% using a convolutional neural network (CNN).

Keywords: Internet application classification, machine learning, traffic management, QoS aware application classification

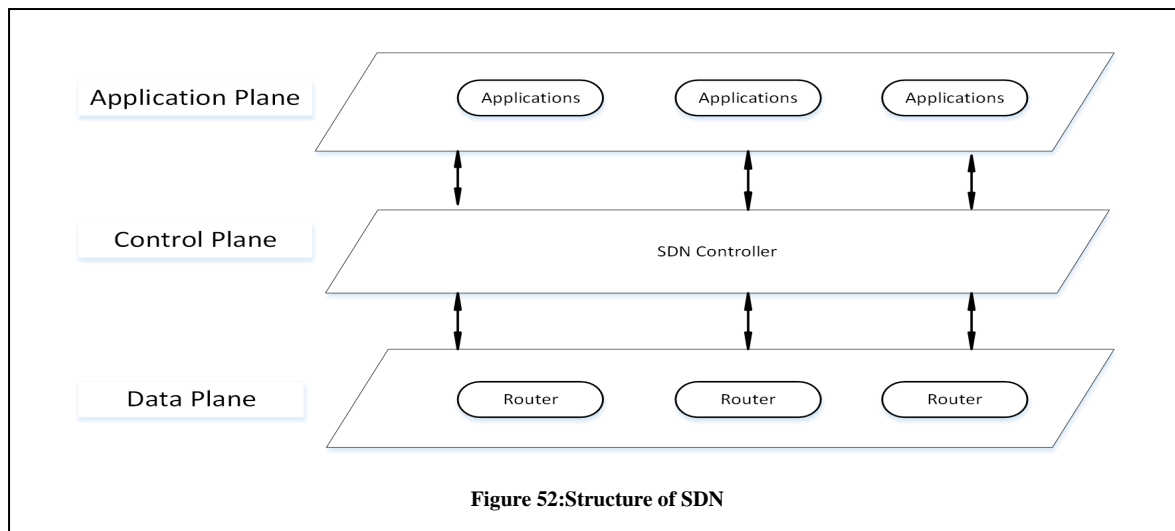
I. INTRODUCTION

Accurate application classification is an essential step of analyzing the nature of the traffic. Internet application classification is useful for intrusion detection, network management tasks and anomalies in the network traffic. Numerous numbers of internet application classification approaches has been suggested in the last few years included the port-based classification approach, payload-based classification approach and flows statistics-based classification [1].

In the port-based classification approach, registered port numbers in the range (1024-49151) are used that are identified by internet assigned names and numbers authority (IANA). Port based method is not useful due to their own limitations as the dynamic ports are used by different protocols [2]. Payload-based classification algorithms look at the packets' contents to identify the type of traffic . When a set of unique payload signatures is collected by an algorithm this approach results in high performance [3]. Payload-based classification is not useful when there is a fully encrypted data. In recent years, in this field, learning-based approaches get new interest. Machine learning approaches can be categorized into supervised methods, unsupervised methods and semi-supervised classification methods. In unsupervised learning approaches, output classes are not known, and the clustering method is used.

Software-defined networking (SDN) is an evolving standard, in which the control function is decoupled from the data plane and makes the network programmable. SDN is a suitable

environment for applying efficient monitoring policies, traffic classification and network management functions [4].



The programmability function of the SDN network which enables to make the network programmable. In a term, SDN aims at simplifying network management, promoting innovation, improving the use of network resources, and optimizing networking performance. OpenFlow is uses standardized protocols one of the south bound's most popular API is used between the control plane and data plane [5]. The emergence of the SDN brought new opportunities for classification of traffic and selection of features. SDN provides a global view of the controller is easy to extract network traffic statistical attributes from switches. Because of the OpenFlow protocol's mechanism design, it can be customized to collect flow features and indicate forwarding policies for each switch [6]. Our aim is to use deep learning algorithm to overcome the limitations in traditional classification approaches in SDN.

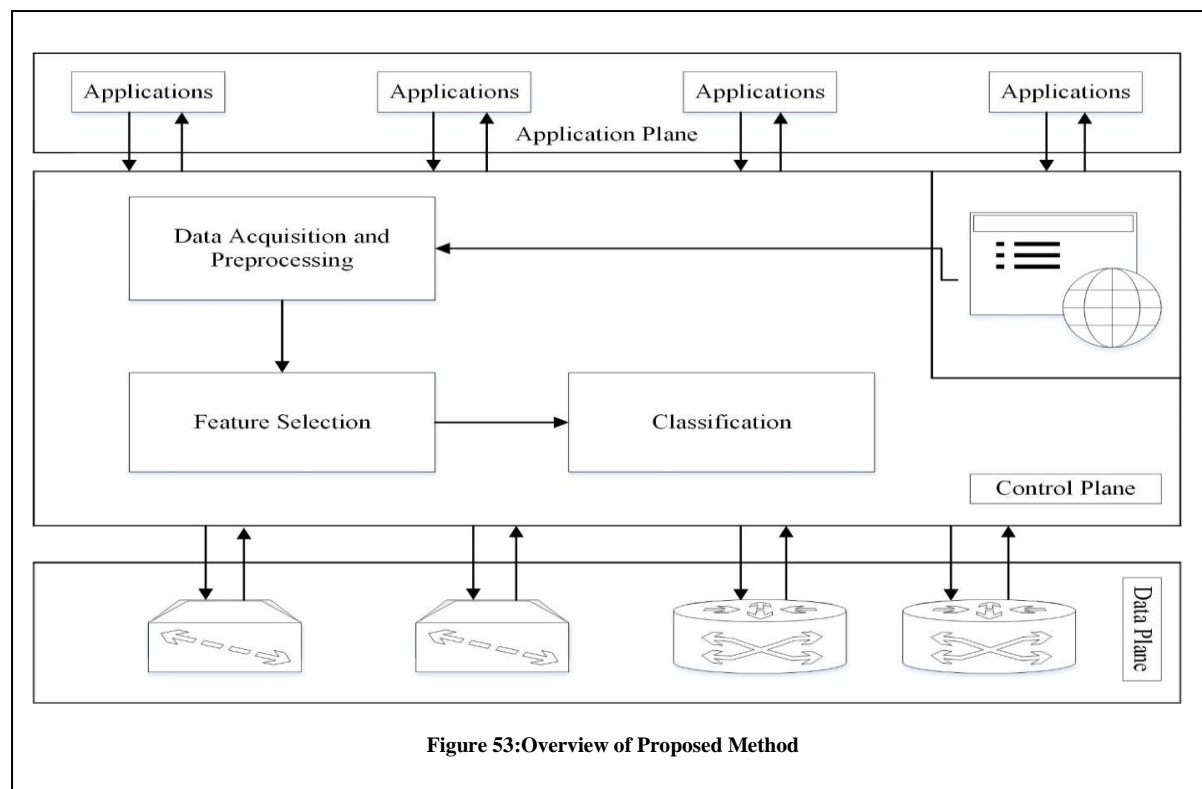
This research work motivates us in use of machine learning model based on statistical information. Optimal features are selected though chi-square test. A thorough comparison has been provided along with CNN in classifying the network application into different classes. A detailed analysis has been provided regarding the network traffic classification using deep learning-based approach.

II. LITERATURE REVIEW

There are different classification techniques has been applied by different researchers. Some researchers focused on port-based methods and payload-based methods. This research focused on deep learning methods.

Lopez-Martin et al. [7] applied a statistics based supervised learning method. A model based on deep learning that is a combination of RNN and CNN was proposed. Different features were

extracted from the header of packets and build a feature vector of every flow. More than 25000 flows and more than 100 distinct services were used to train this methodology.



Zhang et al. [8] suggested a novel network application classification model with deep learning and SDN architecture. A model for was proposed by combining the auto-encoder and softmax regression. To extract features autoencoder was used and softmax model was used as a classifier.

Sun et al. [9] introduced a TrAdaBoost method that utilized the labeled traffic data that was collected from different sources for classification. The maximum entropy model (Maxent) was used as the base classifier and implements the source of knowledge from the source domain to the target domain. Ertam et al. [10] proposed an extreme learning-based method for network traffic classification. Kernel-based extreme machine learning approach is on the extreme machine learning approach that was applied to the data.

Shi et al. [11] presented a feature optimization approach which was named EFOA for the optimal feature selection and optimization approach. A series of experiments were performed on the University of Cambridge Moore dataset [12]. First of all, the correlation of the original flow statistics was evaluated and removed the irrelevant features. After that relevant features were passed to feature generation model to get robust features and that model was based on

deep belief network (DBN) and implemented by unsupervised methods and at the last redundant features were removed.

III. METHODOLOGY

In this paper, a novel architecture is presented to classify the network traffic. In the proposed methodology the first step is data collection and pre-processing, and the second step is the classification. The detail of every step is given below steps.

1. DATA COLLECTION AND PRE-PROCESSING

In the present section, a description of the datasets used in the proposed method for testing and relevant pre-processing steps are described. We have selected publicly available Moore dataset for research purposes [12]. There are twelve input features server_port, client_port, min_segm_size, actual_data_pkts a b, mean_data_ip a b, inter-arrival time_pkt, src_mac, dst_mac, src_ip, dst_ip, initial_window_bytes a b, rtt_samples_a b and correspondence class. Six classes WWW, P2P, MAIL, INTERACTIVE, DATABASE, VOIP, ATTACK, SERVICES and BULK are included in the experiment [13]. After the acquisition of data, pre-processing is an important step. Data pre-processing is useful to handle the missing values in the dataset and standardize the data. The first important step in Moore dataset is to convert categorical data into numeric values using the OneHotEncoder Sikit-learn library. A further step is to make the values in a range using a standard scalar.

$$X' = \frac{X - X_{\text{MIN}}}{X_{\text{MAX}} - X_{\text{MIN}}} \quad (1)$$

2. FEATURE SELECTION

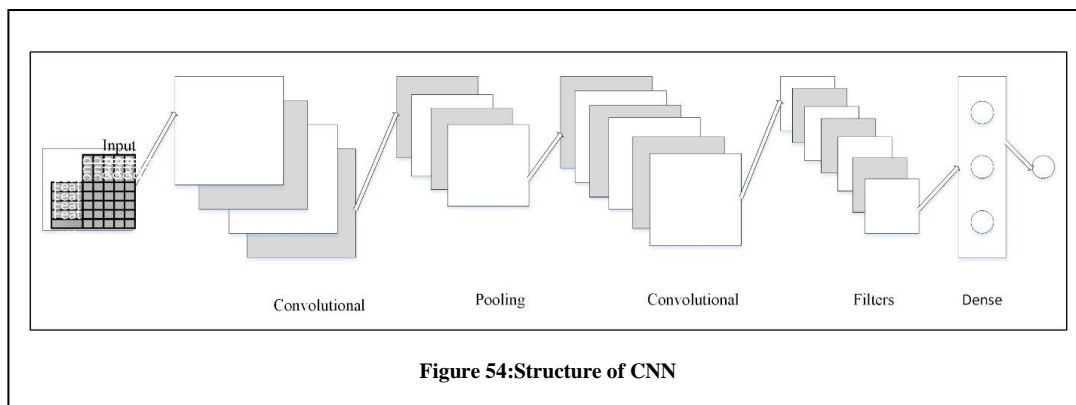
A statistical method known as chi-square is used in this proposed method to select most important features in a dataset. The major objective of the is to reduce dimensions from high dimension to low dimensions. In this methodology, we used the chi-square feature selection method to find best features from the dataset. The value of t is calculated by Eq (2)

$$t(C, E) = \frac{(C - E)^2}{E} \quad (2)$$

where c represents the count and E represent the Expected. After the selection of features these features set are passed to deep learning model.

3. CLASSIFICATION

We trained a CNN to classify the network. CNN models are used for image classification. The traffic data also consists of numeric values and image data also consists of numeric values, so



it
can
be

used for network traffic classification. There are four Conv1D layers, four Dropout, one MaxPooling1, one Flatten and two fully connected layers. Convolutional layer creates a features map after applying filter. The dropout layer provides regularization and preventing overfitting [14]. We added dense layer with softmax activation function. In softmax output can be represented as posterior probabilities. In softmax output can be represented as posterior probabilities. In the proposed method both datasets used belong to multi-class data so that softmax is used at the output layer of neural network classifier. Mathematically softmax is represented by Eq (3)

$$\text{softmax}(b_m) = \frac{e^{b_m}}{\sum_{n=1}^N e^{b_n}} \quad \text{for } m, n = 1, 2, 3, \dots, N \quad (3)$$

Here b_m and b_n represents the element and a represents the N-dimensional output vector. The softmax(b) represents N-dimensional vector after mapping.

CNN has a strong capability of classification, so it obtained better results than the other traditional machine learning methods. The accuracy is calculated for both training data and test data. The dataset is divided into a 7:3 ratio which means, that 70% training set, and 30% test set for the purpose of classification. The structure of CNN is given in **Error! Reference source not found.**

IV. EXPERIMENTAL SETUP

All of the simulations are tested in real-time. Python programming language is used in the experimental evaluation for various numerical libraries. The Sikit-learn is a python library used for scientific purposes. WEKA tool is also used for the analysis of the dataset [15].

V. EVALUATION METRICS

There are four evaluation metrics in this proposed framework. The detail of each parameter is given in Table 1.

TABLE 2: PERFORMENCE PARAMETRS

Parameter	Definition	Mathematical Expression
-----------	------------	-------------------------

Accuracy	Accuracy is a metric in which the number of predictions our model got right over the total number of predictions in a dataset.	$Acc = \frac{TP + TN}{TP + FN + FP + FN}$
Precision	Precision is the measure of classifier exactness.	$Percision = \frac{TP}{TP + FP}$
Recall	The recall is the measure of classifier completeness.	$Recall = \frac{TP}{TP + FN}$
F1-score	F1-score is defined as the weighted average of precision and recall.	$F1 - score = 2 * \frac{Precision * Recall}{Precision + Recall}$

VI. RESULTS

Different experiments are conducted to find out better results in application classification using CNN. For the data mining perspective, the network application classification is the multiclass problem. Four evaluation metrics are calculated, to find out the performance of the proposed method. The accuracy is calculated on the test data.

TABLE 3:AVERAGE RESULTS USING CNN

Classifier	Accuracy	Precision	Recall	F1-score
CNN	99.10%	99.07%	99.10%	99.09%

From

TABLE 3, it is observed that the average accuracy of 99.10% is achieved using the CNN model.

Similarly,

parameters recall of and obtained using

Classifier	Accuracy	Precision	Recall	F1-score
CNN	99.10%	99.07%	99.10%	99.09%

other precision, f1-score are a CNN.

Class	Accuracy	Precision	Recall	F1-Score
WWW	99.87%	99.24%	99.87%	99.56%
P2P	78.94%	91.84%	78.95%	84.91%
MAIL	81.00%	76.42%	81.00%	78.64%

TABLE

INTERACTIVE	100.0%	97.22%	100.0%	98.59%
BULK	100.0%	100.0%	100.0%	100.0%
SERVICES	91.80%	94.92%	91.80%	93.33%
DATABASE	98.12%	98.73%	98.13%	98.43%
VOIP	55.20%	61.63%	55.21%	58.24%
ATTACK	79.91%	86.06%	79.91%	82.87%

4:RESULTS OBTAINED FOR EACH CLASS

In

TABLE 4, evaluation metrics for each class is given. From

TABLE 4, it observed accuracy of 'WWW' high due to majority of in the

Class	Accuracy	Precision	Recall	F1-Score
WWW	99.87%	99.24%	99.87%	99.56%
P2P	78.94%	91.84%	78.95%	84.91%
MAIL	81.00%	76.42%	81.00%	78.64%
INTERACTIVE	100.0%	97.22%	100.0%	98.59%
BULK	100.0%	100.0%	100.0%	100.0%
SERVICES	91.80%	94.92%	91.80%	93.33%
DATABASE	98.12%	98.73%	98.13%	98.43%
VOIP	55.20%	61.63%	55.21%	58.24%
ATTACK	79.91%	86.06%	79.91%	82.87%
Class	Accuracy	Precision	Recall	F1-Score
WWW	99.87%	99.24%	99.87%	99.56%
P2P	78.94%	91.84%	78.95%	84.91%
MAIL	81.00%	76.42%	81.00%	78.64%
INTERACTIVE	100.0%	97.22%	100.0%	98.59%
BULK	100.0%	100.0%	100.0%	100.0%
SERVICES	91.80%	94.92%	91.80%	93.33%
DATABASE	98.12%	98.73%	98.13%	98.43%
VOIP	55.20%	61.63%	55.21%	58.24%
ATTACK	79.91%	86.06%	79.91%	82.87%

can be that the the class is the the samples dataset and accuracy of

'MULTIMEDIA' is low due to minority numbers of the samples in the dataset. As a network application problem is a multi-class problem so there are multiple output classes and four evaluation metrics are calculated to evaluate the performance of the proposed framework.

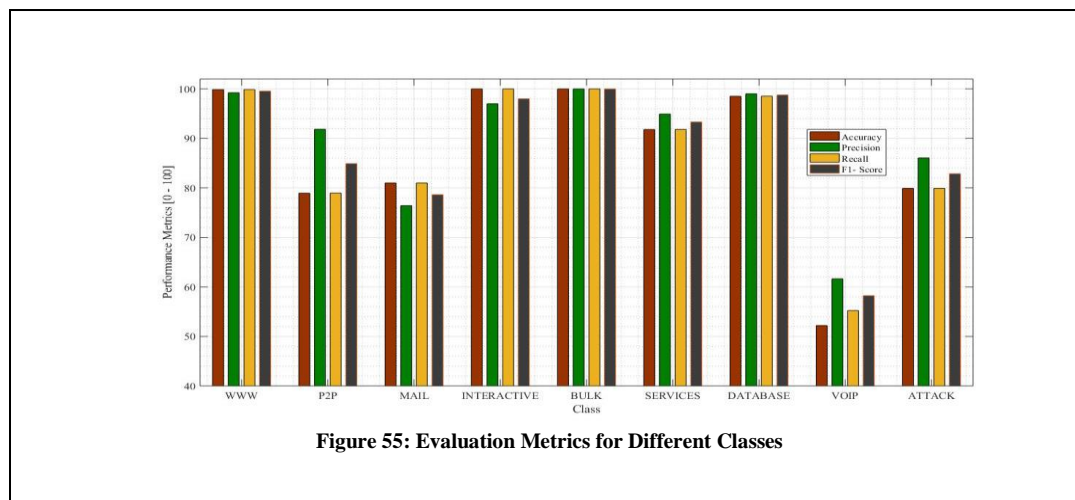


Figure 55: Evaluation Metrics for Different Classes

In Figure 4, evaluations metrics for different classes are shown. The accuracy class ‘WWW’ is high due to majority number of samples and class ‘VOIP’ is low due to minority number of samples.

VII. CONCLUSION AND FUTURE WORK

In this research paper, we introduced a framework for application classification. In this methodology features are selected through chi-square test. The CNN comprised of multiple layers and it has better classification accuracy. To check the performance of this proposed methodology, four evaluation metrics calculated. These experimental results indicate that, our proposed method achieved better accuracy than the existing technique.

In this research, we discussed the first application of CNN for the network traffic classification in SDN. Although we designed and validate our algorithm on Moore dataset based on SDN architecture and in the future, we planned to implement in real-time SDN environment.

REFERENCES

- [1] F. Pacheco, E. Exposito, M. Gineste, C. Baudoin, and J. Aguilar, “Towards the deployment of Machine Learning solutions in network traffic classification: A systematic survey,” *IEEE Commun. Surv. Tutorials*, 2018.
- [2] K. Zeilenga, “Internet Assigned Numbers Authority (IANA) Considerations for the Lightweight Directory Access Protocol (LDAP),” 2002.
- [3] A. W. Moore and K. Papagiannaki, “Toward the accurate identification of network applications,” in *International Workshop on Passive and Active Network Measurement*, 2005, pp. 41–54.
- [4] B. A. A. Nunes, M. Mendonca, X.-N. Nguyen, K. Obraczka, and T. Turetli, “A survey of software-defined networking: Past, present, and future of programmable networks,” *IEEE Commun. Surv. Tutorials*, vol. 16, no. 3, pp. 1617–1634, 2014.
- [5] N. McKeown *et al.*, “OpenFlow: enabling innovation in campus networks,” *ACM SIGCOMM Comput. Commun. Rev.*, vol. 38, no. 2, pp. 69–74, 2008.
- [6] F. Hu, Q. Hao, and K. Bao, “A survey on software-defined network and openflow: From concept to

- implementation,” *IEEE Commun. Surv. Tutorials*, vol. 16, no. 4, pp. 2181–2206, 2014.
- [7] M. Lopez-Martin, B. Carro, A. Sanchez-Esguevillas, and J. Lloret, “Network traffic classifier with convolutional and recurrent neural networks for Internet of Things,” *IEEE Access*, vol. 5, pp. 18042–18050, 2017.
- [8] C. Zhang, X. Wang, F. Li, Q. He, and M. Huang, “Deep learning–based network application classification for SDN,” *Trans. Emerg. Telecommun. Technol.*, vol. 29, no. 5, p. e3302, 2018.
- [9] G. Sun, L. Liang, T. Chen, F. Xiao, and F. Lang, “Network traffic classification based on transfer learning,” *Comput. Electr. Eng.*, vol. 69, pp. 920–927, 2018.
- [10] F. Ertam and E. Avci, “A new approach for internet traffic classification: GA-WK-ELM,” *Measurement*, vol. 95, pp. 135–142, 2017.
- [11] H. Shi, H. Li, D. Zhang, C. Cheng, and X. Cao, “An efficient feature generation approach based on deep learning and feature selection techniques for traffic classification,” *Comput. Networks*, 2018, doi: 10.1016/j.comnet.2018.01.007.
- [12] A. Moore, D. Zuev, and M. Crogan, “Discriminators for use in flow-based classification,” 2013.
- [13] W. Li, M. Canini, A. W. Moore, and R. Bolla, “Efficient application identification and the temporal and spatial stability of classification schema,” *Comput. Networks*, vol. 53, no. 6, pp. 790–809, 2009.
- [14] N. Srivastava, G. Hinton, A. Krizhevsky, I. Sutskever, and R. Salakhutdinov, “Dropout: a simple way to prevent neural networks from overfitting,” *J. Mach. Learn. Res.*, vol. 15, no. 1, pp. 1929–1958, 2014.
- [15] M. Hall, E. Frank, G. Holmes, B. Pfahringer, P. Reutemann, and I. H. Witten, “The weka data mining software: An update, software available at <http://www.cs.waikato.ac.nz/ml/weka>,” *SIGKDD Explor.*, vol. 11, no. 1, 2009.

Fabrication and characterization of methylene blue based sensors

Asad Ullah Khan^{1,a} and Muhammad Tahir^{2,b}

¹*Faculty of Engineering Sciences, Ghulam Ishaq Khan Institute of Engineering Sciences and Technology,
Topi 23640, Pakistan*

²*Department of Physics, Abdul Wali Khan University, Mardan 23200, Pakistan*

Email address: ^{a)} asadullah2657@gmail.com and ^{b)} tahir@awkum.edu.pk

Abstract— Methylene blue (MB), a small organic molecule, was used as an active layer to fabricate temperature and humidity sensors. For measuring the sensing properties of the fabricated devices, their capacitance was measured as a function of temperature and humidity. The response and recover times were measured. The morphology and ultraviolet (UV-vis) studies of the MB thin film were also carried out.

Keywords—Methylene Blue, humidity sensor, temperature sensor.

I. INTRODUCTION

Today's research in the fabrication of sensors have wide range of applications for different purposes [1]. Several sensors have been assembled using organic and inorganic molecules, ceramics or other materials for the measurement of light, pressure, humidity and temperature [2, 3]. Temperature and humidity sensors have great importance in our daily life which comprises goods, fresh foods, storage of medicine, environment and safety purposes for industrial and laboratory research. Inorganic material sensors are complex and expensive, due to which the inorganics are replaced by the organic materials which are low cost, reliable and have long-term stability [4]. Pure organic semiconductor have been studied for the sensing purpose of humidity and temperature. In order to increase the sensitivity, the organic semiconductor methylene blue is used for fabrication.

Methylene blue (MB) is a dark green crystalline powder with semiconducting properties. Here methylene blue is selected for the artifacting of multifunctional sensor due to its conjoined arrangement, reliability, indelible stability, low-priced and is easily soluble in water. The moderate boiling point $\sim 110^{\circ}\text{C}$ of methylene blue (MB) makes the sensor useful for different temperatures due to high sensitivity.

In this work an organic multiuse sensor have been formulated and inspected for the application of humidity and temperature sensing. The Ag/MB/Ag sensor has been checked for the sensing properties suchlike humidity and temperature to give fast recovery and response. To study improvement in quality of sensor, another Au/MB/Au sensor was formulated and examined with contrast to the Ag/MB/Ag. The observation of both sensors proved superior temperature sensitivity of Ag/MB/Ag than Au/MB/Au sensor. The sensitivity of sensor also depends upon the applied frequency, that's why sensitivity has been calculated at two particular frequencies of 120 Hz and 1 KHz.

II. EXPERIMENTAL WORK

The organic small molecule methylene blue (MB) was acquired from the market. Structural formula of MB is displayed in Fig. 1. Its molecular mass is 319.851 g/mol and molecular formula is $\text{C}_{16}\text{H}_{18}\text{N}_3\text{ClS}$, respectively. In this work, the active layer of MB material have been used for the formulation of Ag/MB/Ag and Au/MB/Au multifunctional sensors. For formulation of device 100nm thin Ag and Au electrodes have been deposited on the glass substrates in such a way that 50 μm inter-electrode gap was maintained by masking the sample. The Ag and Au electrodes were deposited on the glass substrates through thermal evaporator. The evaporator model used was EDWARDS AUTO 306. Pressure maintained in vacuum chamber was approximately 10^{-5} mbar, while rate of deposition on substrate was ~ 0.1 nm/s, respectively. The thickness of electrode film was measured through IN SITU FTMS monitor connected with vacuum chamber. A 16 wt. % solution of MB has been prepared in de-ionized water at room temperature using magnetic stirrer for two hours. The solution were then spin-coated at 1000 rpm for 20 sec separately on two Ag and Au electrodes deposited substrates, in such a way that inter-electrodes gap was concealed by solution. Spin coated thin film were annealed for two hours using hot plate. Schematic layouts for formulated devices are displayed in Fig. 2 (a) and 2 (b). The UV-Visible spectroscopy of MB solution were performed using LAMBDA 35 UV/Vis-spectrometer, Perkin Elmer Instruments. Temperature-capacitance (T-C) and relative humidity-capacitance measurements were made using self-made temperature and humidity setup.

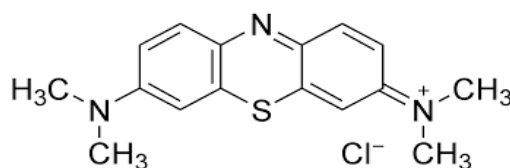


Fig. 1. Molecular formula of MB.

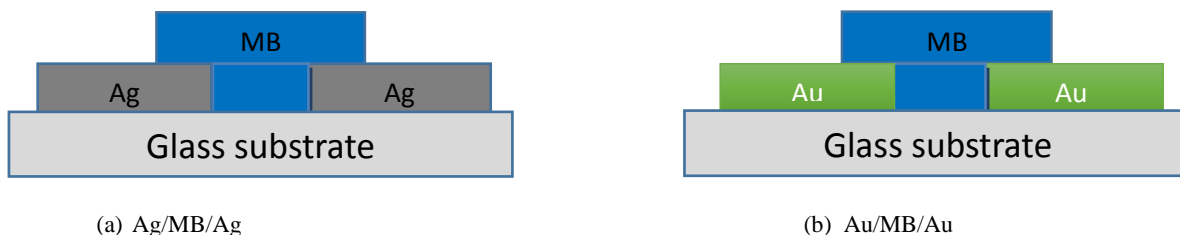


Fig. 2. Cross-sectional view of surface-type formulated sensors.

III. RESULT AND DISCUSSION

The morphology of sensitive thin film have great effect on the behavior of sensor [5]. The surface of MB thin film has been investigated by AFM as shown in Fig. 3. The sensing properties of MB thin film are linked with the topographical parameters such as grain size, grain boundaries, shape and orientation/distribution of grains throughout the film. The microstructure shown reveal that surface of MB is dispersed due to which the film can adsorb more water and exhibit high accurate sensitivity.

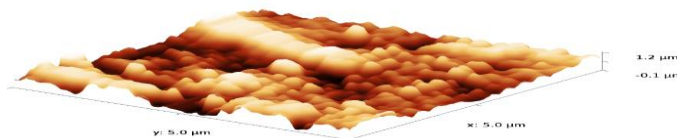
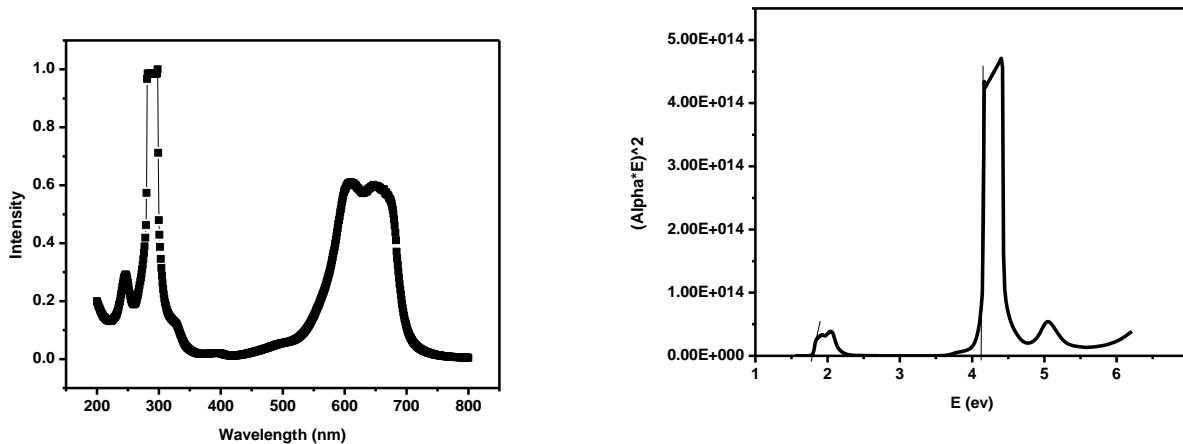


Fig. 3. AFM image of MB.

Fig. 4 (a). UV-Vis graph of MB.
 Band gap of MB.

Fig. 4 (b).

The measured UV-vis graph of MB solution is shown in Fig. 4 (a). The intensity peaks shows the absorption of light having specific wavelength. The graph show peaks in ultraviolet region at 298 nm as well as in visible region at 613 nm and 655 nm. The spectrum also confirms the broad wavelength absorption of MB covering some UV region and large visible region approximately 500-700 nm. This feature indicates the potential use of MB for photovoltaic applications. Similarly, Fig. 4 (b) shows relation between $(\alpha E)^2$ and E_g . According to the Tauc's equation, $\alpha E = (E_g - E)^m$, where m is the number indicating direct or indirect bandgap semiconductor. In this case, MB is an indirect bandgap material therefore $m=1/2$. In the figure, different peaks can be observed and the slope of each peak intersection on horizontal axis (E_g) is actually giving the value of the bandgaps. Here the values of bandgaps are measured to be 1.7 and 4.1 eV.



Figs. 5 (a) and 5 (b) show the change of capacitance with change in temperature (°C). Variation in capacitance with change in temperature was carried out by placing the sensor over hot iron while the temperature was measured by thermocouple. *C-T* characteristics of Ag/MB/Ag at 120 Hz and 1 kHz are shown in Fig. 5 (a). *C-T* characteristics of Au/MB/Au sensors at 120 Hz and 1 kHz are displayed in Fig. 5 (b). The capacitance at 1 kHz and 120 Hz were measured in pF and nF, respectively, as shown in Fig. 8. When the temperature was raised from 30 to 70 °C, the capacitance of Ag/MB/Ag increased from 66.3 to 67.6 pF at 1 kHz and at 120 Hz the capacitance raised from 0.069 to 0.075 nF. Furthermore, when the capacitance of Au/MB/Au increased from 67.8 to 71.9 pF at 1 kHz by increasing the temperature from 32 to 71 °C and at 120 Hz the capacitance increased from 0.073 to 0.088 nF. The raise in capacitance with respect to temperature is by reason of raising charge carriers energy [6].

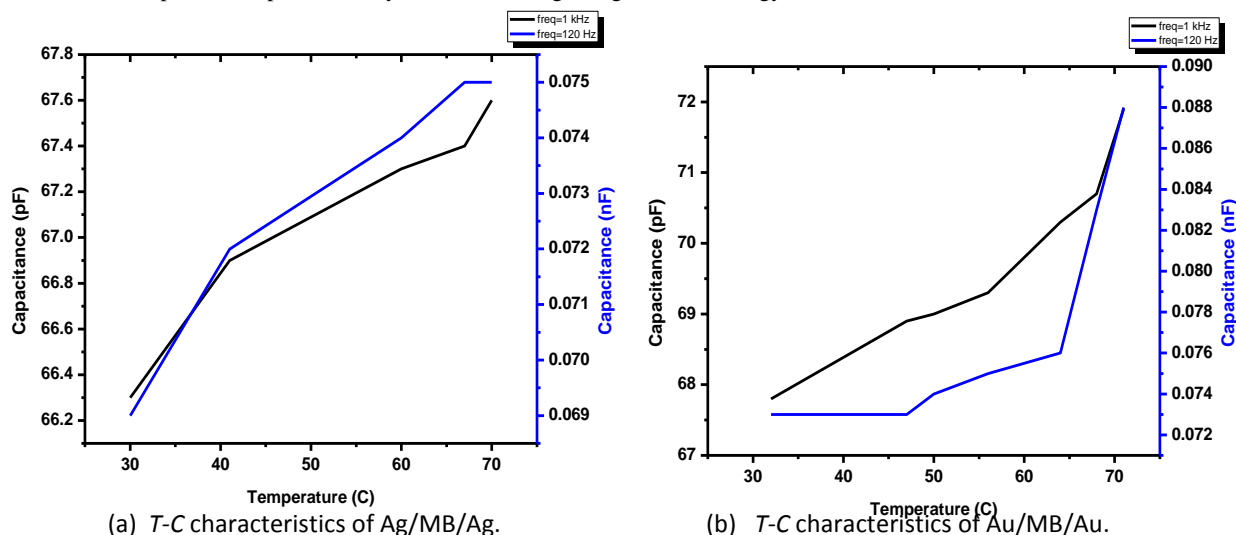


Fig. 5. *T-C* characteristics at 1 kHz and 120 Hz.

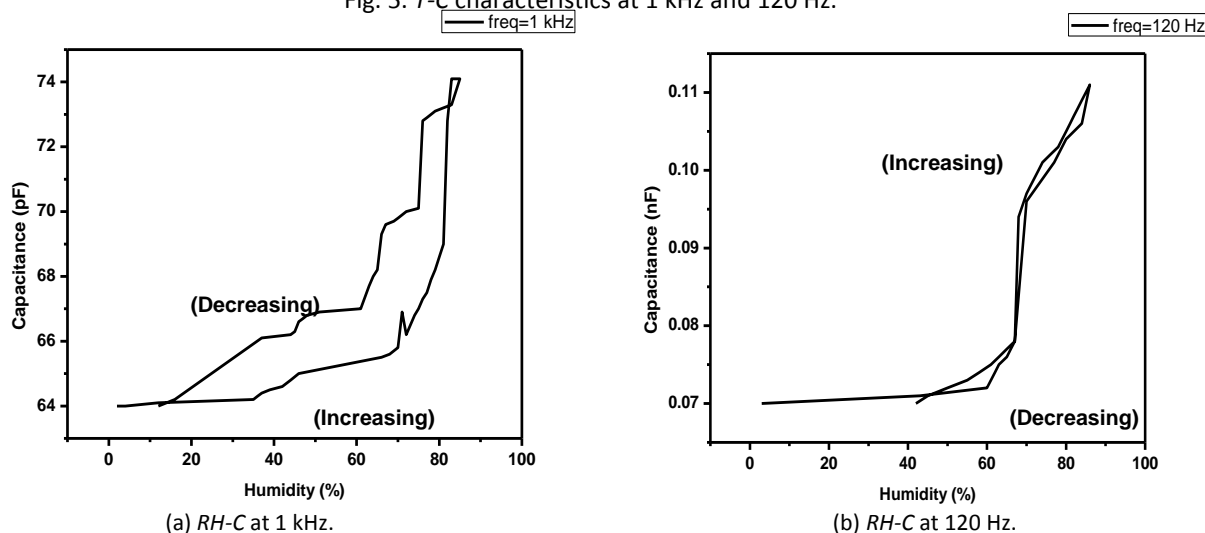


Fig. 6. Humidity-capacitance characteristics of Ag/MB/Ag.

The changing of capacitance (*C*) as a function of relative humidity (RH %) is shown in Fig. 6 (a) at 1 kHz and in Fig. 6 (b) at 120 Hz, respectively of the Ag/MB/Ag at room temperature. In figure, raising in capacitance is shown with increase in RH % level, as well as reducing of capacitance with decrease in RH %. The increase is because of water molecules adsorbed by active thin layer of MB due to which the dielectric constant of thin layer increases. The capacitance and dielectric constant have direct relation with each other, the greater the dielectric constant of material, higher will be capacitance and conversely materials having low dielectric constant have low capacitance [7]. As capacitance depends upon applied frequency, hence capacitance-RH % characteristic of Ag/MB/Ag sensor has been investigated at two particular frequencies of 1 kHz and 120 Hz. The high sensitivity of sensor occurs at low frequency i.e. 120 Hz. While for higher frequency, sensitivity is low because of polarization of adsorb water which show little change in dielectric constant [8]. Molecules of water are polar and by applying electric field its dipole moment increases. The dipole moment is given by:

$$P = \alpha E \quad (1)$$

Where E represent electric field applied to electrodes and α is polarizability of the material, its value is 6.1×10^{-30} Cm for water [9]. The schematic device in Fig. 2 (a) shows Ag electrodes, which act as parallel plates of capacitor and MB act as dielectric constant. Relation between the capacitance and dielectric constant can be expressed as,

$$\frac{C_s}{C_0} = \left(\frac{\epsilon_w}{\epsilon_d} \right)^n \quad (2)$$

Where C_s represent capacitance of semiconductor, C_0 is initiative capacitance. ϵ_d and ϵ_w are material permittivities in dry and wet air, where n indicates morphology of material's dielectric. The water's relative permittivity is much greater than organic semiconductor materials [10]. By increasing humidity level adsorption of water molecules increase on surface of thin film increases which results in high sensitivity of the sensors.

Figs. 6 (a) and 6 (b) reveal that humidity sensor prepared by Ag electrodes display high sensitivity at 1 kHz as compared to 120 Hz, but the high accuracy is at 120 Hz as compared to 1 kHz. The capacitance rapidly increases with increase in RH %. At 1 kHz the capacitance changes from 64 pF to 74.2 pF by increasing the RH from 2 to 81 %, while by decreasing RH from 81 to 2 %, the capacitance decreases from 74.2 pF to 66.1 pF. At 120 Hz the capacitance changes from 0.07 nF to 0.11 nF by increasing RH from 40 to 81 %, and follow relatively same path at decreasing RH from 81 to 40 %, which show the high accurate sensitivity of the sensor at 120 Hz.

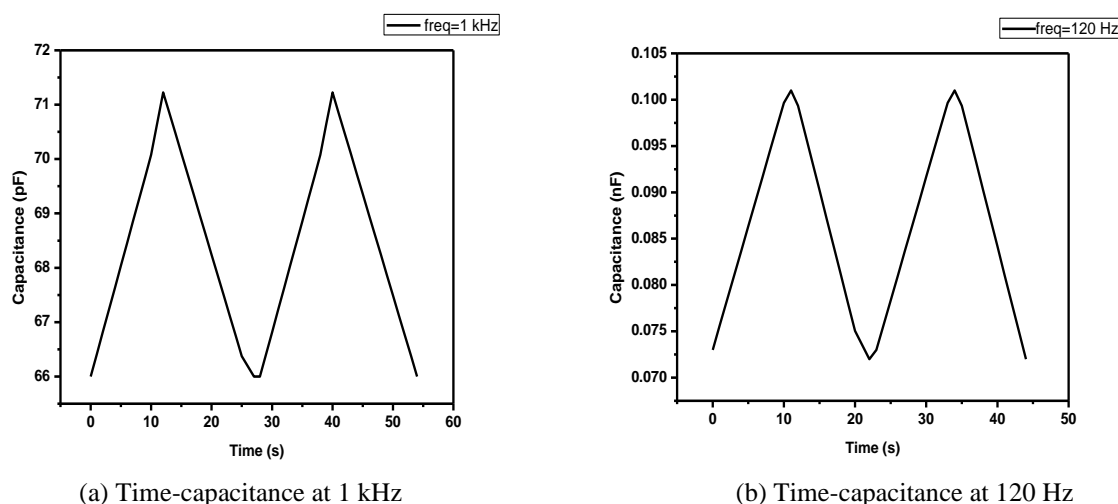


Fig. 7. Response and recovery time measurement of Ag/MB/Ag.

The response and recovery of the fabricated sensor is measured at 1 kHz and 120 Hz having silver electrodes at room temperature. The relationship is shown in Figs. 7 (a) and 7 (b). The sensor give response by increasing capacitance from 66 pF to 71.2 pF in 12 sec by immediately transfer from low humidity to high humidity chamber, which results in a decrease of the capacitance due to desorption of water from thin MB deposited film [11]. Similarly, the recovery of sensor is shown by decreasing of capacitance from 71.2 pF to 66 pF in 15 sec by immediately transfer from high humidity to low humidity chamber at 1 kHz, respectively. The same cycle was repeated again as shown in Fig. 7 (a). As the MB have rough surface, by increasing humidity the surface absorb water due to which the capacitance increases. Similarly by decreasing the humidity through passing dry nitrogen gas, the gas will absorb water from the surface of MB, and the surface becomes dry due to which the capacitance decreases.

Similarly, at 120 Hz the sensor gives response by increasing capacitance from 0.073 nF to 0.101 nF in 11 s by immediately transfer from low humidity to high humidity chamber. The recovery is shown by decreasing of capacitance from 0.099 nF to 0.072 nF in 11 s by immediately transfer from high humidity to low humidity chamber respectively. At 120 Hz, the response and recovery gives same time which shows the accurate sensitivity of sensor at 120 Hz. The same cycle is repeated again as shown in Fig. 7 (b).

IV. CONCLUSION

The fabricated sensors based on MB Au/MB/Au and Ag/MB/Ag have been studied for their temperature and humidity sensing properties. It was established that both of the devices exhibited sensitivity to humidity and temperature within a range of 35-85 RH% and 30-70 °C, respectively. Due to interfacial states at the junction between MB and metal contacts, the response of the devices is non-linear to humidity and temperature. The key parameters of the sensor such as response/recovery times and repeatability of the results have been studied which showed minor deviations. The humidity response and recovery time were measured to 12 s and 15 s, respectively. The bandgap of MB was 1.7 and 4.1 eV which suggests its potential applications in the field of organic semiconductor devices.

REFERENCES

1. Tahir, M., et al., *Perylene diimide: Synthesis, fabrication and temperature dependent electrical characterization of heterojunction with p-silicon*. Physica B: Condensed Matter, 2013. **426**: p. 6-12.
2. Sayyad, M., et al., *Fabrication and study of NiPc thin film based surface type photocapacitors*. J. Optoelectron. Adv. Mater, 2008. **10**: p. 2805-2810.

3. Su, P.-G. and C.-L. Uen, *A resistive-type humidity sensor using composite films prepared from poly (2-acrylamido-2-methylpropane sulfonate) and dispersed organic silicon sol*. *Talanta*, 2005. **66**(5): p. 1247-1253.
4. Su, P.-G. and C.-P. Wang, *Flexible humidity sensor based on TiO₂ nanoparticles-polypyrrole-poly-[3-(methacrylamino)propyl] trimethyl ammonium chloride composite materials*. *Sensors and Actuators B: Chemical*, 2008. **129**(2): p. 538-543.
5. Tahir, M., et al., *Enhancement in the sensing properties of methyl orange thin film by TiO₂ nanoparticles*. *International Journal of Modern Physics B*, 2014. **28**(05): p. 1450032.
6. Janssens, S., et al., *Separation of intra-and intergranular magnetotransport properties in nanocrystalline diamond films on the metallic side of the metal-insulator transition*. *New Journal of Physics*, 2011. **13**(8): p. 083008.
7. Ahmad, Z., et al., *Humidity-dependent characteristics of methyl-red thin film-based Ag/methyl-red/Ag surface-type cell*. *Physica E: Low-dimensional Systems and Nanostructures*, 2008. **41**(1): p. 18-22.
8. Bondarenka, V., et al., *Thin films of poly-vanadium-molybdenum acid as starting materials for humidity sensors*. *Sensors and Actuators B: Chemical*, 1995. **28**(3): p. 227-231.
9. Griffiths, D.J., *Introduction to electrodynamics*. 2005, American Association of Physics Teachers.
10. Saleem, M., et al., *Cu (II) 5, 10, 15, 20-tetrakis (4'-isopropylphenyl) porphyrin based surface-type resistive-capacitive multifunctional sensor*. *Sensors and Actuators B: Chemical*, 2009. **137**(2): p. 442-446.
11. Steele, J., M. Taschuk, and M. Brett, *Response time of nanostructured relative humidity sensors*. *Sensors and Actuators B: Chemical*, 2009. **140**(2): p. 610-615.

Effect of Fines on the Engineering Properties of Lawrencepur Sand

Hammad Haider^{1,a} and Naveed Ahmad^{2,b}

¹MSc Student, Civil Engineering Department, University of Engineering and Technology, Taxila, Pakistan

²Assistant Professor, Civil Engineering Department, University of Engineering and Technology, Taxila, Pakistan

Email address: ^{a)} hammad.haider1@uettaxila.edu.pk and ^{b)} naveed.ahmad@uettaxila.edu.pk

Abstract—A lot of work has been done to study the effect of different parameters on the engineering properties of clean sand and a clear understanding exists about role of these parameters. Keeping in view the presence of fines with sands at construction sites, some researchers have studied the effect of fines on engineering properties of their local sands and have obtained different trends with different optimum percentages. In this study, Lawrencepur sand is used and effect of fines having same mineral composition is studied. From the results, it is found that fines increase cohesion, decrease internal friction angle, whereas a transition has been observed in dry density and optimum moisture content values.

Keywords—Lawrencepur sand, cohesion, angle of internal friction, optimum moisture content

I. Introduction

The response of clean sand has been studied extensively in the past. Researchers have studied effect of particle shape, size, density, mineralogy etc on behavior of clean sands. With the particle angularity, there is increase of angle of internal friction, whereas with increasing effective size, there is reduction in internal friction angle [1]. There is increase in peak friction and dilatancy angle as the angularity and particle surface roughness increase [2]. With rising particle regularity the soil appears to be more prone to liquefaction [3]. Data reveals that increasing irregularity of particle results in fading of stiffness and an uprising trend in the frictional stage critical angle [4]. As there is decrease in specimen density and increase in mean stress, peak state friction angle (ϕ_p), CS friction angle (ϕ_{cs}), and dilatancy angle (ψ) decrease [5]. As it is quite rare to have clean sand at our construction sites, there was a need to study the behavior of sand silt mixtures. Researchers studied effect of both silt and clay on friction angle of sand and observed a decrease in phi in both the cases, whereas cohesion was increased [6]. With the increase of fines, internal friction angle reduced and cohesion increased [7]. With the decrease of the fine aggregates, the cohesion reduced and internal friction angle raised [8]. The behavior of a silty sand cannot be predicted accurately, based purely on its silt content, but we need to compare that content of silt with the limiting silt content of the base sand [9]. The fines

between sand to sand contacts increase the soil resistance to shearing [10]. At 30% fines, the e_{min} and e_{max} obtain minimum values in sand fine mixtures [11]. At 18% fines, the e_{min} and e_{max} obtain minimum values in sand fine mixtures [7]. With the rise of fines, first Maximum Dry Density (MDD) rises then reduces, whereas Optimum Moisture Content (OMC) reduces then rises [12].

II. Materials and Method

A. Material used

In this study, locally available sand collected from Lawrencepur, Attock was used. To get a true representation of the sand available in the region, disturbed samples were obtained from various locations and were mixed thoroughly. The material has coefficient of uniformity (C_u) 2.89 and coefficient of curvature (C_c) 1.11. The sieve analysis is shown in Fig. 1.

To avoid the effect of mineral composition, fines were prepared by grinding the same sand in Los Angeles Abrasion machine. Samples with different percentage of fines content were prepared and tested in Soil Mechanics and Foundation Engineering laboratory in UET Taxila, Pakistan.

B. Sample Preparation Method for Direct Shear Test

All experiments were carried out in accordance with the ASTM standards. For direct shear test, samples were prepared keeping constant density for all the percentages of fines. Sample height was 20 mm and cross-sectional area was 36 cm² (each side is 6 cm). Axial strain at 1.5 mm/min rate was used in all the tests using ELE strain-controlled machine.

III. Test Results and Discussion

Modified compaction tests were performed for all percentages of fines and variation of optimum moisture content and maximum dry density with fines is shown in Fig. 2 and Fig. 3, respectively. It has been observed that initially optimum moisture content reduces with rise in fines content, obtaining minimum value around 20% fines followed by a rise in value with further rise in fine content. Contrary to this, a rise in the value of maximum dry density was observed initially, reaching a peak value around 20% fines content and decreasing thereafter.

The effect of fines on minimum (e_{min}) and maximum (e_{max}) void ratio is shown in Fig. 4. It has been observed that e_{min} and e_{max} initially decrease with fine content, achieving a minimum value near 20% fines followed by rise in void ratio with further rise in fine content. Literature shows a similar behavior as reported by previous researchers using their local sands but optimum percentage of fines was found different by different researchers.

Fig. 5 shows effect of fines content on cohesion of sand-silt matrix and it has been observed that cohesion keeps increasing with fines content. Although, rate of increase of cohesion was greater for initial percentage of fines content and was reduced for higher percentages.

Effect of fines content on angle of internal friction is shown in Fig. 6. Initially, an increase in friction angle value was observed up to 10% as in this range the fines are used to fill up the voids

between clean sand particles, increasing resistance to sliding. As the percentage of fines

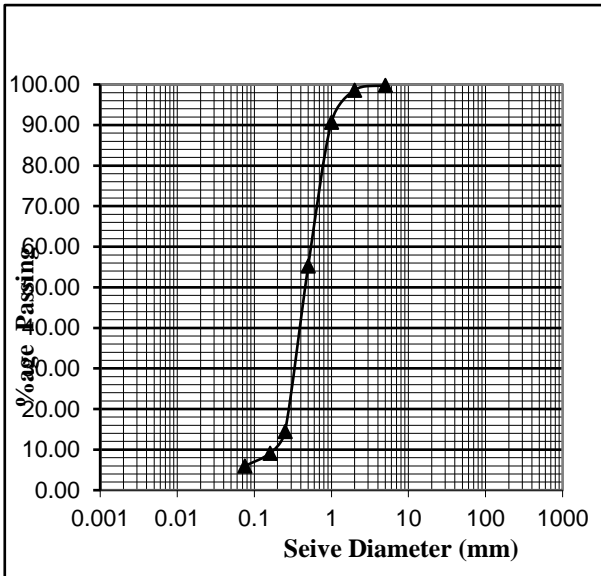


Fig. 1 Particle Size Distribution Curve

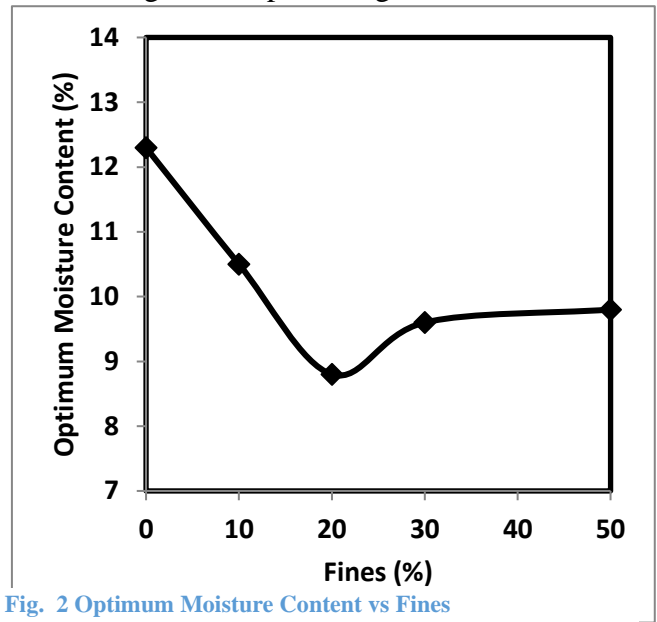


Fig. 2 Optimum Moisture Content vs Fines

increases further, fines start to reduce particle to particle contact between sand particles, thus reducing the friction angle values.

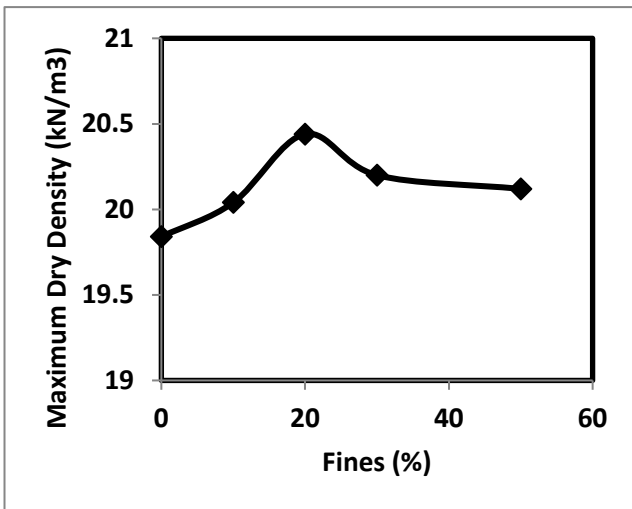


Fig. 3 Maximum Dry Density vs Fines

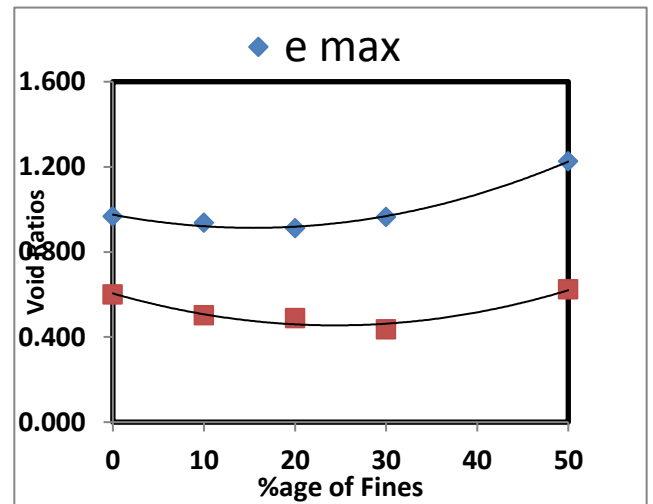


Fig. 4 Void vs Fines

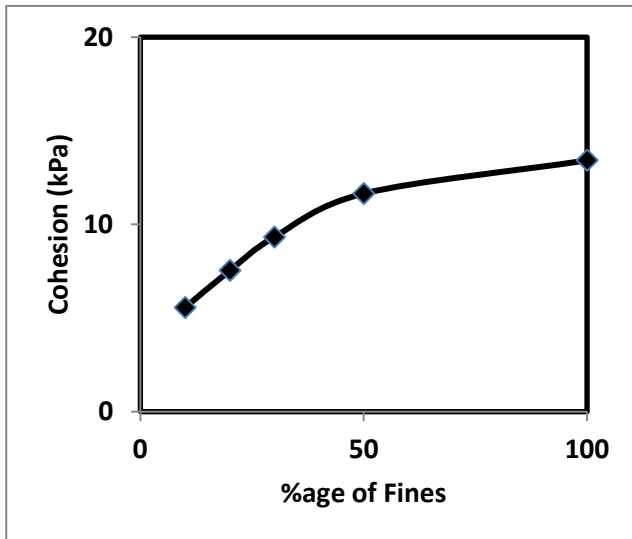


Fig. 5 Cohesion vs Fines

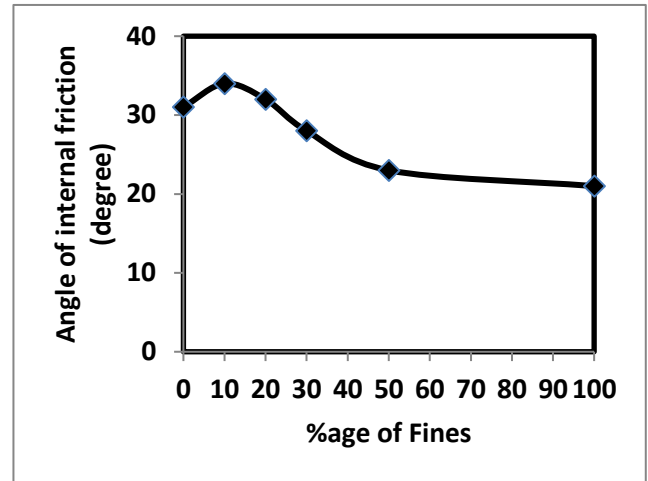


Fig. 6 Angle of Internal Friction vs Fines

IV. Conclusions

- As percentage of fines increase, optimum moisture content (OMC) reduces upto 20% of fines and then rises.
- As percentage of fines increase, maximum dry density (MDD) rises upto 20% of fines and then reduces.
- Maximum and minimum void ratio values reduce upto 20-30% of fines and then increase again.
- As percentage of fines increase, a slight increment in the Cohesion value has been observed that might be due to apparent cohesion. And rise in the internal friction angle was observed upto 10-20% fine content, followed by a constant decrease in its value.

V. References

- [1] Koerner, Robert M. "The behavior of cohesionless soils formed from various minerals." (1968).
- [2] Alshibli, Khalid A., Maha F. Jarrar, Andrew M. Druckrey, and Riyadh I. Al-Raoush. "Influence of particle morphology on 3D kinematic behavior and strain localization of sheared sand." *Journal of Geotechnical and Geoenvironmental Engineering* 143, no. 2 (2017): 04016097.
- [3] Yang, J., and X. D. Luo. "Exploring the relationship between critical state and particle shape for granular materials." *Journal of the Mechanics and Physics of Solids* 84 (2015): 196-213.
- [4] Cho, Gye-Chun, Jake Dodds, and J. Carlos Santamarina. "Particle shape effects on packing density, stiffness, and strength: natural and crushed sands." *Journal of geotechnical and geoenvironmental engineering* 132, no. 5 (2006): 591-602.

- [5] Alshibli, Khalid A., and Mehmet B. Cil. "Influence of particle morphology on the friction and dilatancy of sand." *Journal of Geotechnical and Geoenvironmental Engineering* 144, no. 3 (2018): 04017118.
- [6] Thian, S. Y., and C. Y. Lee. "Undrained response of mining sand with fines contents." *International Journal of Civil & Structural Engineering* 1, no. 4 (2011): 844-851.
- [7] Phan, Vu To-Anh, Darn-Horng Hsiao, and Phuong Thuc-Lan Nguyen. "Effects of fines contents on engineering properties of sand-fines mixtures." *Procedia engineering* 142 (2016): 213-220.
- [8] Kim, Daehyeon, Myung Sagong, and Yonghee Lee. "Effects of fine aggregate content on the mechanical properties of the compacted decomposed granitic soils." *Construction and Building Materials* 19, no. 3 (2005): 189-196.
- [9] Polito, Carmine P., and James R. Martin II. "Effects of nonplastic fines on the liquefaction resistance of sands." *Journal of Geotechnical and Geoenvironmental Engineering* 127, no. 5 (2001): 408-415.
- [10] Shen, C.K., Vrymoed J.L. and Uyeno C.K. (1977) "The effect of fines on liquefaction of sands," Proceedings of the 9th International Conference on Soil Mechanics and Foundation Engineering, Tokyo, 2, pp. 180 – 189.
- [11] Belkhatir, Mostefa, Tom Schanz, and Ahmed Arab. "Effect of fines content and void ratio on the saturated hydraulic conductivity and undrained shear strength of sand–silt mixtures." *Environmental earth sciences* 70, no. 6 (2013): 2469-2479.
- [12] Fatima, Zainab & Mukahveena, Sreedhar. (2017). Influence of Plastic Fines on Compaction and CBR Characteristics of Soil Mixtures. *International Journal of Engineering Research and*. V6. 10.17577/IJERTV6IS070131.

Impact of Collar and Roughness on Bridge Pier Scouring

Sabir Hussain^{1,a}, Usman Ghani^{2,b} and Mujahid Iqbal^{3,c}

¹University of Engineering and Technology Taxila,
Civil Engineering Department

² University of Engineering and Technology Taxila,
Civil Engineering Department

³ University of Engineering and Technology Taxila,
Civil Engineering Department

Email address: ^{a)} sabirhussain.pk36@gmail.com, ^{b)} usman.ghani@uettaxila.edu.pk

and ^{c)} mujahid.iqbal@uettaxila.edu.pk

Abstract— Local scouring is one of the main causes of bridge failure across the world. Bridge failure causes interruption of social interaction, economical loss in the form of repairing and in severe case the loss of lives. In this research work oblong shape collar having width 2.5 times the diameter of pier and gravels roughness with size; $d_{50}=6.32\text{mm}$ are used as a countermeasure on plain circular shape pier. Both the collar and pier roughness were tested on the circular shape pier at different flow rate and corresponding scouring was measured by using point gauge. All the experiments were carried out in a laboratory flume having width, length and depth is 0.96m, 20m and 0.75m respectively. The results exhibited that 55.10% scouring is reduced with the presence of oblong shape collar on pier and 22.40% scouring is reduced with pier roughness. It is concluded that pier with collar was found to be effective scouring reducer as compared to pier with roughness.

Keywords— component, bridge pier, local scour, collar, roughness, countermeasure.

I. INTRODUCTION

Local scouring, around the bridge piers, is a significant and crucial process that leads towards bridge failure. In this regard, it becomes essential to predict the local scouring, around the bridge piers, in an accurate and precise way. Otherwise, the local scouring will result in collapsing the whole bridge structure leaving a serious death toll and injuries as its aftermath [1]. The local scouring problem have been studied by many hydraulic researchers under different flow conditions. Based on the research carried out, several methods have been introduced and implemented to counter local scouring, around the bridge piers [2]. Countermeasure techniques around the bridge pier for the local scouring are classified into two categories: armoring and flow altering techniques. There are multiple armoring techniques like riprap stones around the bridge pier, reno mattresses, cable tied blocks, gabions, tetrapod's, dolos, and concrete mats or bags. The flow altering technique includes sills, sacrificial piles, slots, low vanes, ring column [3]. The local scouring around the bridge pier can be reduced by using the collars and geobags. The collars and geo- bags are efficient for reducing the scouring around the bridge piers when experimentally studied. When the experimental data of collars and geobags were compared with the data on simple bridge pier,

the results showed that percentage of scour reduction is more by using the combination of collar and the geobags than the simple pier. Moreover, the efficiency of collars is better than the geobags when both are used independently [4]. The experimental work was conducted to achieve different optimum techniques like slot and both the slot and sill. The experimental work was performed on the circular pier to check the local scouring. The local scouring was reduced by the using of slot and the combination of sill and slot. It was concluded from the results that the maximum local scour depth reduced by the slot was up to 30%. On the other hand, when combined countermeasure technique opted — slot and bed sill — the maximum scour reduction in front of pier was up to 45%. From the experimental results, it can be stated that the combination of slot and bed sill is more efficient and effective in order to diminish the local scouring, around the bridge piers [5]. Several researchers are, currently, working to belittle the local scouring, around the bridge piers. Experimental work performed to minimize the local scour on a bridge pier by countermeasure technique such as sacrificial pile and the sacrificial piles with perforation in this research. The holes with different orientation in perforated piles were tested, a sacrificial and the sacrificial perforated pile were positioned at the upstream. The results concluded from the experiments were that scour depth can be reduced up to 89%, when the combination of the pile with 45°-hole angle and the sacrificial perforated pile with the 45°- hole angle and the diameter of hole equals to 0.43 times diameter of pile. This research study may be used for the protection of bridge pier from the effect of scouring [6]. The local scour around the bridge pier was controlled by using the rectangular shape of the collars. Experimental work conducted on the rectangular shape of the collar to find out the approximate collar dimensions for the reduction of scouring around the bridge pier. Effects of the Rectangular collars with different dimension on a circular shape pier were investigated in the flume at the upstream and downstream side of the pier. The optimum width of the collar was estimated about 2.8 times of the pier diameter. The scour depth reduced up to 98% at 72 h by using the collar sizes [7]. The main cause of bridge collapse is the local scour around the bridge pier. There are many countermeasure techniques are adopted to protect the bridge pier from scouring. Experiments were conducted on the bridge pier with the anti-scour collar. Three parameters including height of the collar, diameter of the collar and the collar protection range were investigated. From the results it is concluded that with the increase in collar height the effect of protection decreases and with the increase in external collar diameter the effect of protection increases. It is suggested that anti-scour collar is more effective and efficient to protect the bridge pier from scouring [8]. In this study, the effect of oblong shape collar and pier roughness on the scouring around the bridge pier is investigated and compare the results of collar and roughness effect on the local scouring around the pier.

II. EXPERIMENTAL WORK:

A. Channel description and Preparation

Hydraulic laboratory of Civil Engineering Department at University of Engineering and Technology Taxila was used to carried out experimental work. All experiments were performed on 0.96m wide and 20m long rectangular channel. The side walls and bed of the channel were made up of transparent glass and concrete foundation respectively. The bed of the channel was prepared with sand material having size $d_{50}=0.57\text{mm}$ and was levelled horizontally. To avoid the unwavering water level in the test section the sand bed should be appropriately level. An adjustable tailgate was installed at the extreme downstream of the channel to control the water level and discharge was controlled by using flow control valve fixed at the start of the channel. At the periphery of test section, a 15cm thick uniform and cohesion less sand material was used as

a bed. The unit weight of sand is 26.5kN/m³, when $d_{50} \geq 0.6\text{mm}$. The ratio of $\frac{D}{d_{50}} \geq 50$ is satisfied, the impact of the sediment roughness is avoided by this value [9][10]. The sediment particles with the standard deviation ($\sigma_g=d_{85}/d_{50}$) was <1.3 [10][11] to reduce the sediment non-uniformity effect on scour hole. Furthermore, to stop the ripple evolution the bed particles with the diameter was 0.57mm. (Ettema 1980; Raudkivi and Ettema1977; Lanc ,a, Simarro, and Fael 2015).

B. Experimental Procedure

After preparing the channel bed, a plain vertical circular shape pier was installed at the centerline of the channel at a distance of 3.5m downstream from the entrance of channel. An adjustable tailgate was installed at the extreme downstream of the channel to control the water level and discharge was controlled by using flow control valve fixed at the start of the channel. After completing all necessary work, flow was assumed to flow in the channel. The sediments start to scour around the bridge pier when the water was allowed to flow in the test section. Scouring around bridge piers was investigated at four different flow rate e.g. $Q= 0.02304\text{cumecs}$, $Q= 0.0288\text{cumecs}$, $Q= 0.03456\text{cumecs}$ and $Q= 0.04032\text{cumecs}$ and at every discharge value, 15cm depth of water in the test section was maintained by using tailgate. The running time of each trial was fixed for 3 hours and after this time flow was assumed to stopped. After drained out water from channel, the resultant scouring around the bridge pier was measured by using point gauge. After measuring scouring depth around bridge pier (shown in Fig.1, a), the bed of channel was again leveled for next trials. Then next two case; oblong shape collar and pier roughness (shown in Fig.1, b & c) were tested as a countermeasure at same flow conditions. The width of oblong collar was kept 2.5 times the diameter of pier, while for the case of pier roughness, gravels with size $d_{50}=6.32\text{mm}$ was used as a roughness material. Schematic diagrams of pier with different conditions is shown in figure 1.

Figure 1: Schematic diagrams of pier with different conditions; (a) plain circular pier, (b) pier with oblong shape collar, (c) pier with roughness.



III. RESULT AND DISCUSSION

A. Variation of Scour Depth with velocity:

In all cases, it is observed that by increasing the velocity of flow the depth of scour around the pier also increases (shown in Fig.2), but this trend decreases afterward. The reason behind this decreasing trend is, due to submergence of sediments the shear force between particles decreases and ultimately lead to

decrease critical velocity of sediments. Due to decreasing critical velocity of sediments, the sediment from the upstream moves towards the scour hole, that causes the reduction of the scour depth.

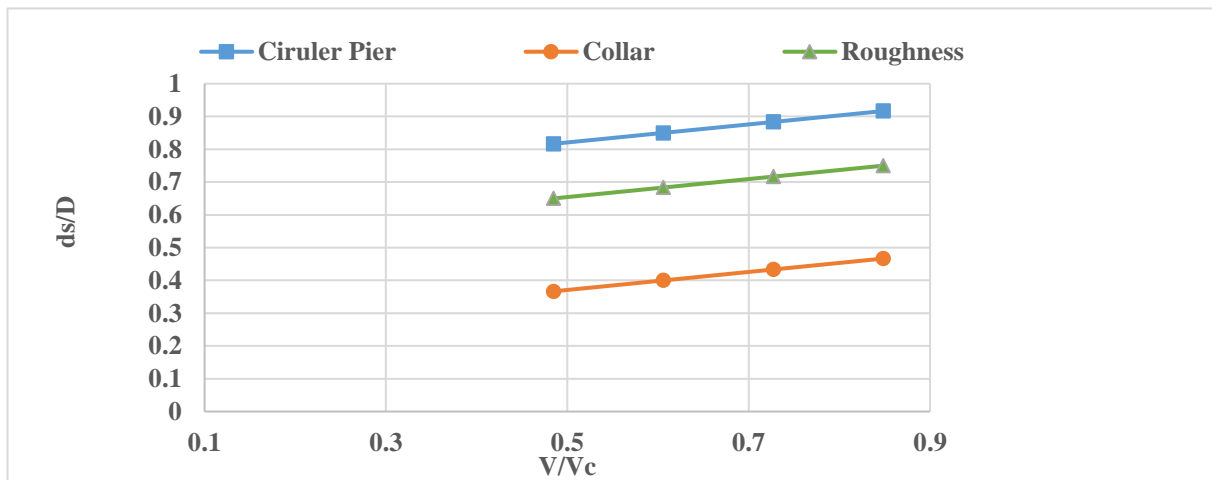


Figure 2: Variation of scour depth with velocity ratio (V/Vc) for plain circular pier, pier with collar and roughness with time interval of 3h.

B. Variation of Scour Depth with Discharge:

It is also examined that by increasing the discharge, the scour depth around the pier also increases. The figure (Fig.3) shows the trend of scouring depth with discharge for all cases: plain circular pier, pier with oblong shape collar and pier with roughness.

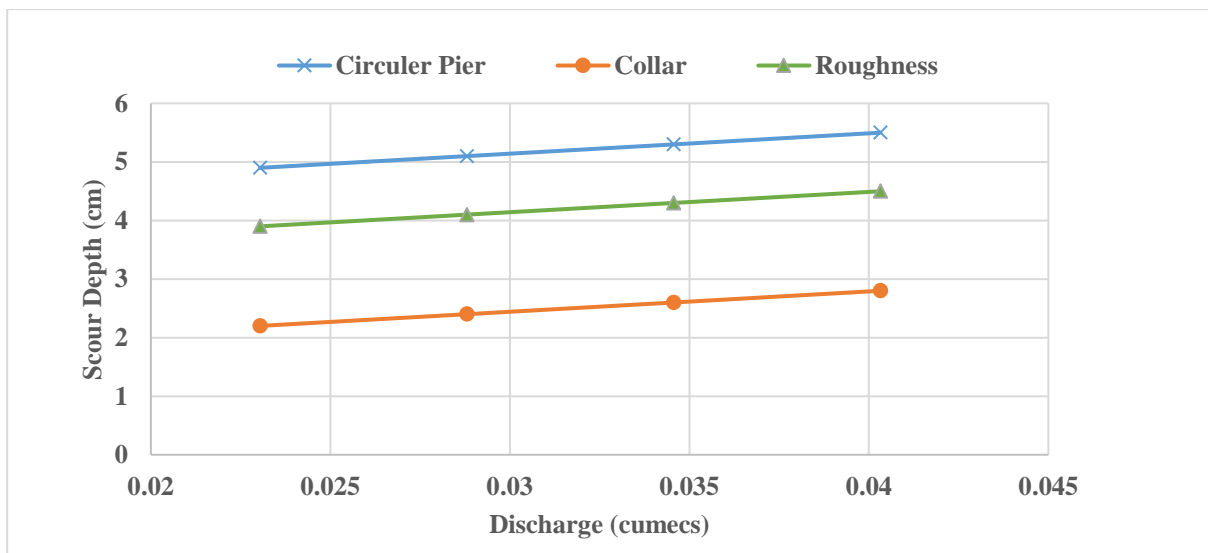


Figure 3: Variation of scour depth with discharge for plain circular pier, pier with collar and roughness with time interval of 3h.

C. Scouring comparison among plain circular pier, pier with collar and roughness

The scour comparison among plain circular pier, pier with roughness and pier with oblong collar is plotted at maximum velocity. It is shown in figure 4.

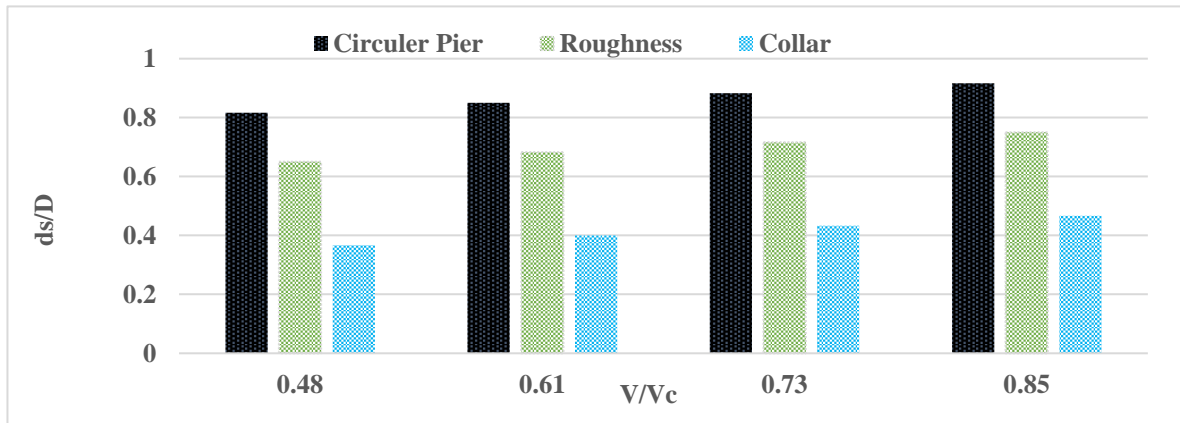


Figure 4: Comparison of scour depth versus variation in velocities for plain circular pier, pier with collar and roughness

D. Percentage Reduction comparison between pier with collar and roughness

The percentage scouring comparison is plotted between pier with oblong shape collar and pier with roughness at maximum scouring depth. It is shown in figure 5.

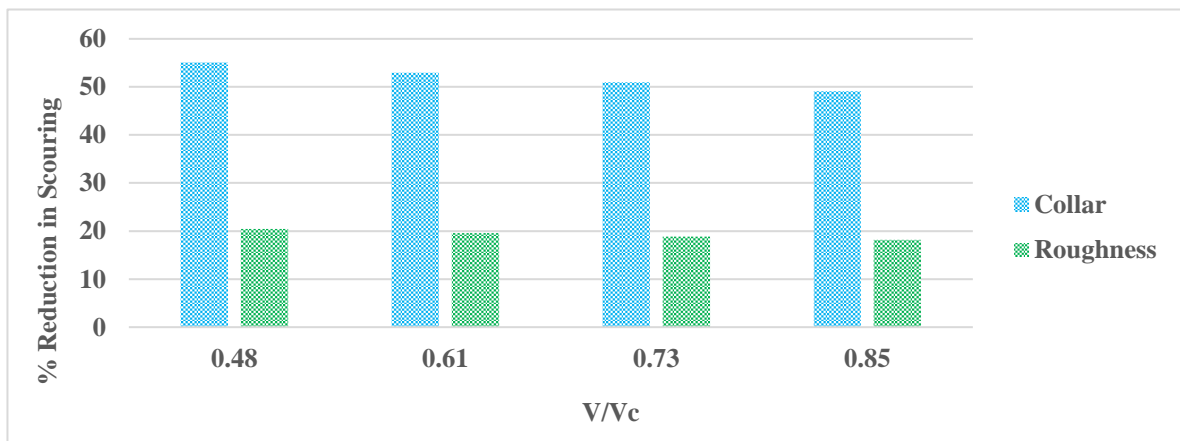


Figure 5: Percentage reduction comparison between scouring depth and V/ Vc for the case of pier with collar and pier with roughness.

IV. CONCLUSION:

The current research concluded that:

1. With the increase in discharge the scour depth around the bridge pier also increases and vice versa.
2. The scour depth around the bridge pier decreases by providing the oblong collar or roughness on pier.
3. The percentage of reduction of scour for the case of pier with collar reduced up to 55.10 %, while for the case of pier with roughness reduced up to 20.40 %.
4. The pier with collar is found to be more efficient technique to reduce the scouring as compared to providing roughness on pier.

V. REFERENCE:

- [1] Al-Shukur A-H K and Hadi Obeid Z 2016 Experimental Study of Bridge Pier Shape To Minimize Local Scour *Int. J. Civ. Eng. Technol.* **7** 162–71
- [2] Of S E, As I, By O, Melville B W and Hadfield A C 1999 OF 1221–4
- [3] TANG H W, DING B, CHIEW Y M and FANG S L 2009 Protection of bridge piers against scouring with tetrahedral frames *Int. J. Sediment Res.* **24** 385–99
- [4] Akib S, Liana Mamat N, Basser H and Jahangirzadeh A 2014 Reducing local scouring at bridge piles using collars and geobags *Sci. World J.* **2014**
- [5] Grimaldi C, Gaudio R, Calomino F and Cardoso A H 2009 Countermeasures against local scouring at bridge piers: Slot and combined system of slot and bed sill *J. Hydraul. Eng.* **135** 425–31
- [6] Elnikhely E A 2017 Minimizing scour around bridge pile using holes *Ain Shams Eng. J.* **8** 499–506
- [7] Jahangirzadeh A and Akib S 2015 Eksperimentinis tyrimas tilto tauro sprastasiens matmenims nustatyti *Balt. J. Road Bridg. Eng.* **10** 89–96
- [8] Wang S, Wei K, Shen Z and Xiang Q 2019 Experimental investigation of local scour protection for cylindrical bridge piers using anti-scour collars *Water (Switzerland)* **11**
- [9] Melville B W and Raudkivi A J 1977 Caracteristiques de l'ecoulement dans des conditions d'affouillement localisees au voisinage immediat des piles d'un pont *J. Hydraul. Res.* **15** 373–80
- [10] Taylor P, Chiew Y M and Melville B W 2010 Local scour around bridge piers Local scour around bridge piers AfTouillements locaux au pied des piles de pont B ^ 37–41
- [11] Raudkivi A J 1986 Functional trends of scour at bridge piers *J. Hydraul. Eng.* **112** 1–13

Investigating the Permeability of coarse and fine asphalt mixtures

M Haroon ^a, Imran Hafeez ^b, Shafeeq Ahmad ^c,

^a *Research Scholar, Civil Engineering department, UET Taxila*

^b *Professor, Civil Engineering department, UET Taxila*

^c *Highway research and training center, Burhan
email a, muhammadharoon1995@yahoo.com
b, imranhafeez783@yahoo.com*

ABSTRACT-A study has been conducted to investigate the drainability of four different types of asphalt mixtures that are used for pavement surface layers. These mixes include SP-A, MS-2B, NHA-A and NHA-B gradation. One type of Bitumen are used as ARL and two types of aggregate source are used as Margalla and Uban Shah. Four types of permeability apparatus are used as Italian (6inch dia), European (5inch dia), in situ-permeameter (4 inch dia) and water pressurized permeameter. These devices work on falling head principles. The focus is given to determine the effect of different NMAS on permeability and permeameters cogency and viability. The study reveals that increase in void size with random formation of increased structural connections increase the permeability. If size of permeability apparatus increases its permeability also increases and also if pressure is applied its permeability increases. While NHA A is more permeable as compared to other permeable asphalt mixes. While NHA B mixes offered less permeability while NHA A offered more permeability, due to specific gradation. Study reveals that permeability is dependent on interconnection of air voids, sample size gradation and head pressure.

Keywords

1. Introduction

Permeability of Asphalt mixtures is dependent on different parameters, Type of mix, effective porosity, direction of flow, gradation of mix, air voids, packing of aggregates, size & shape of aggregates. The interconnectivity of air voids affects permeability of asphalt mixtures. The equipment used for measurement of permeability also effects to the permeability, method of testing and accuracy of the observations obtained from the particular equipment.. The reason described is that as the coarser particle contribute to large air voids and the chance of connectivity of these voids enhances, on the other hand the finer gradation have voids of smaller size, these voids have minimum linkages as interconnected path become longer and squeezes the channel of movement of moisture. Sometime moisture get entrapped into these voids and proposes difficulties for the streamline flow of water or moisture in the finer mixes. The equipment used in the study of permeability have a wide range of complexion in terms of size of equipment. The mechanism of operation and limitations during observations of measurements.

the many field and lab testing devices available. For field testing, there are five designs that have been used in published research. They all calculate the coefficient

Abdullah et al. 1998 proposed different factors that affect the permeability of an asphalt pavement during its service life as: segregation of the mix during placing; temperature of mix during cessation rolling; temperature of mix during pneumatic rolling; weight of breakdown roller; Tire or contact pressure of pneumatic roller; ambient temperature during placing of mix; Void content of the compacted mix & amount of traffic before winter rains.

In addition to fine mixes, Chou bane et al. (1998) also studied coarse mixes and concluded coarse mixes with air voids greater than 6% are susceptible to excessive permeability. Early work on permeability indicated a pavement with air voids greater than 8% was susceptible to excessive permeability. This threshold of 8% was also confirmed by Brown et al. (1998).

Chen et al. 2004, The mix properties are discussed one by one for better understanding of permeability of asphalt mixtures. Asphalt pavement are excessively vulnerable to moisture problems in the early pavement service life, for example stripping of binder and cracking due to increase in pore pressure and permeation to succeeding granular base layers as explained.

Waters, T 2004, In this study, a new term, "normalised air voids", has been introduced, which accommodates both the voids and the size of the particles within the mix. The permeability of asphalt has been correlated with the normalised air voids. Asphalt has been categorised on the basis of permeability, with categories ranging from very low permeability to free-draining. Normalised air voids have also been found to have a correlation with road surface texture. In asphalt design, a balance needs to be reached between low permeability and good surface texture.

Kanitpong et al. 2005, researched permeability in fine graded mixes and recommended the minimum density should be set at 93.8% (6.2% air voids) to control permeability in fine graded Superpave mixes.

The phenomenon of moisture damage effects were examine by Carol et al. 2008a and Caro et al 2008b. The common factor that determines permeability is the amount of air voids contained in the specimen. In asphalt pavements, air void content is reduced using compaction to increase the density of the pavement. Therefore, the degree of compaction (density) should be related to the permeability of the pavement.

the device developed by the Florida Department of Transportation (FDOT), the other uses the Corelok device. The FDOT device also uses Darcy's Law, while the Corelok device uses a volumetric approach to calculated permeability. There have been recent studies

on directional permeability that use X-Ray CT imaging to develop a computer model of an HMA core sample. A numerical fluid flow model based on the Kozeny-Carman equation along with the X-Ray CT imaging gives the permeability (k) for the cores/asphalt samples used in the study. Permeability (k) measurement based on Kozeny- Carman formulation (Kozeny 1927, Carman 1938, 1956) equation used in different studies is equation 1. In equation 1 we see that the k value is linear parameter of the voids/pores present the mix.

$$K = (\gamma / \mu) (1 / CK-C) (1 / S_0^2) [e^3 / (1+e)] \dots\dots(1)$$

Where γ is the unit weight of the permeant (usually water), μ is the dynamic viscosity of the permeating fluid, CK-C is an empirical coefficient, S_0 the specific surface area of the soil/asphalt per unit volume of particles, and e is the void ratio, hereafter denoted as (e). The equation 2 developed by Vardanega & Waters (2011, 2015) based on the equation developed by the

$$k = 0.46(R_p)^{3.70} [R^2 = 0.74; n = 467] \dots\dots\dots(2)$$

Where k has units of mm/s and R_p has units of mm and where R_p is the representative pore size (RPS), Where, $R_p = (2/3) [AV (\%)/100] [D_{75} (\text{mm})]$.

$$k = 0.269(R_p)^{3.67} \dots\dots\dots(3)$$

$$k = 0.154(R_p)^{4.12} \dots\dots\dots(4)$$

The different devices used by the researchers have used Darcy's equation or Kozeny Carman formulation and have developed their model based on the previous studies.

Rohid Rosli Hanin et al, 2013, investigates the effect of lift thickness on permeability and the time available for compaction (TAC) of hot-mix asphalt (HMA) mixes under tropical climate condition. A total of 14 HMA mixes consisting of various types, gradations, and nominal maximum aggregate sizes (NMAS) were selected. The results also suggest that the TAC for a 25 mm lift is 13 min, 23 min for 32 mm, 32 min for 38 mm, and is expected to be more than 50 min for 44 mm and above & effect of lift thickness on permeability and the time available for compaction of hot mix asphalt pavement under tropical climate condition was determined. J. Vardanega et al, 2018, This research presents two laboratory databases assembled from data sourced from the literature. Using a database of permeability tests on fine-grained soils, the ability of the Kozeny-Carman void ratio function to interpret the data is examined alongside a simple power-law relationship

A second database of permeability measurements on asphalt concrete specimens is used to re-examine the 'representative pore size' concept as a method of predicting the coefficient of permeability. The influence of nominal maximum aggregate size (NMAS) on the coefficient of permeability is also studied.

Er. ankush verma et al 2018, The primary objective of the present study is to determine general magnitude of permeability of bitumen mixes at different conditions. Additionally, the permeability characteristics of field-prepared field compacted (FPFC) cored specimens are evaluated and compared with laboratory-prepared laboratory compacted (LPLC) specimens. Field cores are extracted from on-going paving projects and evaluated for

permeability using a fabricated falling head laboratory permeameter. Marshall Mix prepared in the laboratory as per the site specification and compacted with impact compactor at varying compactive efforts, and finally subjected to permeability testing.

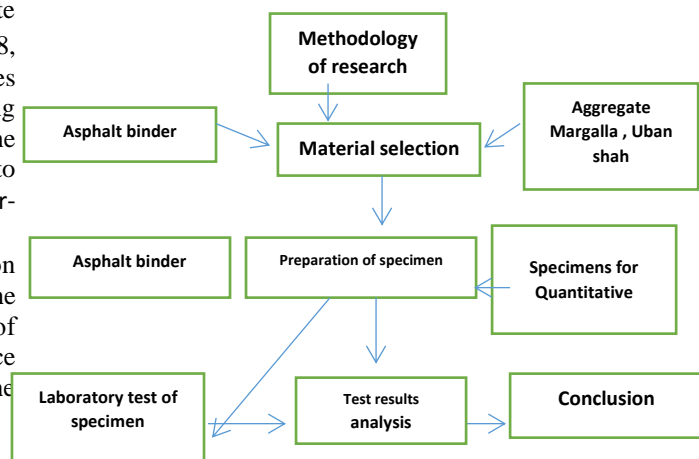
Sheldon A .et al 2019 Numerous theoretical models were evaluated and the selected model is based on regression analysis of field data. Initially, predominant variables influencing layer permeability were found to be void proportion, binder content as well as aggregate grading and packing. Subsequently, regression analyses of data showed that within reasonable variation of the other variables, layer permeability is strongly correlated to aggregate grading and packing, as described by rational Bailey ratios, hence the focus of refining the model on the latter parameters.

2. Objective of research study

The main objectives of this Research is

- To determine the Permeability of fine and coarse graded asphalt mixtures.
- To compare and develop relationship permeability measuring devices.
- To develop relationship between air void and permeability.

3. Research methodology



A research study was divided into three phases. In first phase ,to prepare asphalt mixture,single asphalt binder ,two aggregate quarries. Based on petrography results aggregate quarries were selected. Margalla and Uban Shah aggregate quarries contain, calcium carbonate, dolomite, and granite minerals respectively. Asphalt binder i.e commonly used in flexible pavements of Pakistan was taken from Attock Oil Refinery (ARL) Pakistan. In second phase of research study specimens were prepared for quantitative test regime. While in last phase all laboratory tests were performed to asses moisture sensitivity of asphalt mixture. The flow chart of Research Methodolgy has been given in Fig.1.

4. Materials & Methods

4.1 Bitumen

The selected asphalt binder is commonly used in Pakistan road network and basically consists of four generic fractions based on molecular size and chemical reactivity. These four groups consist of saturates, aromatics, resins and asphaltenes. As aromatics are the 40-65% of total asphalt binder volume that is the main reason of the non polar behavior of asphalt binder.

Bitumen of grade-60/70 was utilized with the source of Attock Oil Refinery was finalized and arranged provision of bitumen in the lab. . Material properties of asphalt binder has been given in Table 1. Master curve of ARL is given in Fig.2. The basic objective of construction of master curve was to characterize the binder over a wide range of temperature and loading frequencies. This objective was achieved by conducting frequency sweep test on DSR. Single reference temperature is generally taken in a construction of master curve. Time and temperature superposition principle or principle of reduce variable that essentially describe the equivalency of time and temperature are the basis behind the construction of master curve. Master curve at reference temperature of 30oC has been constructed to complete the characterization of binders as shown in Figure2, where values in terms of log of reduced frequency(fr) are plotted against complex modulus G*.

4. Materials & Methods

4.1 Bitumen, The selected asphalt binder is commonly used in Pakistan road network and basically consists of four generic fractions based on molecular size and chemical reactivity. These four groups consist of saturates, aromatics, resins and asphaltenes. As aromatics are the 40-65% of total asphalt binder volume that is the main reason of the non polar behavior of asphalt binder.

Bitumen of grade-60/70 was utilized with the source of Attock Oil Refinery was finalized and arranged provision of bitumen in the lab. . Material properties of asphalt binder has been given in Table 1. Master curve

of ARL is given in Fig.2. The basic objective of construction of master curve was to characterize the binder over a wide range of temperature and loading frequencies. This objective was achieved by conducting frequency sweep test on DSR. Single reference temperature is generally taken in a construction of master curve. Time and temperature superposition principle or principle of reduce variable that essentially describe the equivalency of time and temperature are the basis behind the construction of master curve. Master curve at reference temperature of 30oC has been constructed to complete the characterization of binders as shown in Figure2, where values in terms of log of reduced frequency(fr) are plotted against complex modulus G*.

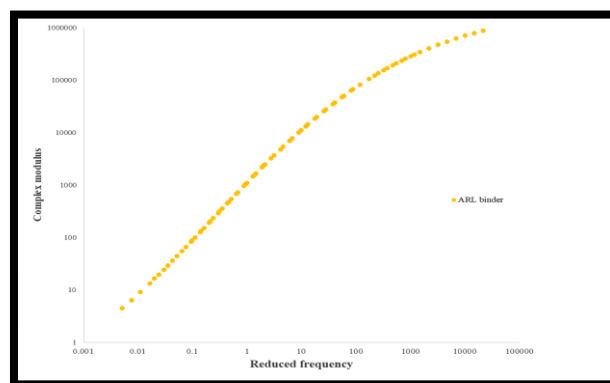


Fig.2. Master curve ARL

Basic necessary testing of bitumen was carried out including penetration grade at 25, Softening Point, Ductility, Flash and Fire Point and Specific Gravity. All results are with in the limits.

**Table 1
Material properties of asphalt binder**

Test Description	Asphalt binder ARL 60/70
Penetration ASTM D6	61.0
Softening point ASTM D36	48.4
Flash & Fire (*C) ASTM D92	328-362
Specific Gravity ASTM D70	1.023

4.2 Aggregate

Asphalt mixture contains about 95% of aggregate by weight as a constituent . The properties of coarse and fine aggregates are therefore important and directly affect the performance of asphalt mixtures. Aggregate quarries were selected on the petrography of rock source. Amount of silica (SiO₂) is responsible for acidic or basic behavior of rock. Acidic nature rock commonly

rich in silica while basic nature aggregate quarries contain less amount of silica. Two different types of aggregate quarries are locally available in Pakistan i.e Margalla and Uban Shah aggregate quarries are basic in nature. Nominal maximum aggregate size (NMAS) which is defined as one sieve size larger than the first sieve to retain more than 10 per cent of the material is one of the commonly used parameter in the analysis of aggregate packing characteristics. NMAS of NHA-A and NHA-B gradation is 19.0 mm, for gradation SP-A and MS-II it is 12.5 mm. Selected aggregate quarries location has been shown in Fig.3. Chemical properties of aggregate is shown in Fig. 4.

Different tests were conducted to measure the physical and mechanical properties of aggregate in the laboratory. Aggregate engineering properties have been summarized in Table 2. It may be noted from Table 2 that fractured particles of all aggregate source are 100%. While having less than 15% of flakiness and elongation index. Aggregate engineering properties have been summarized in Table 2.



Fig.3. Location Map of Aggregate Quarries (<https://geology.com/world/pakistan-satellite-image.shtml>)

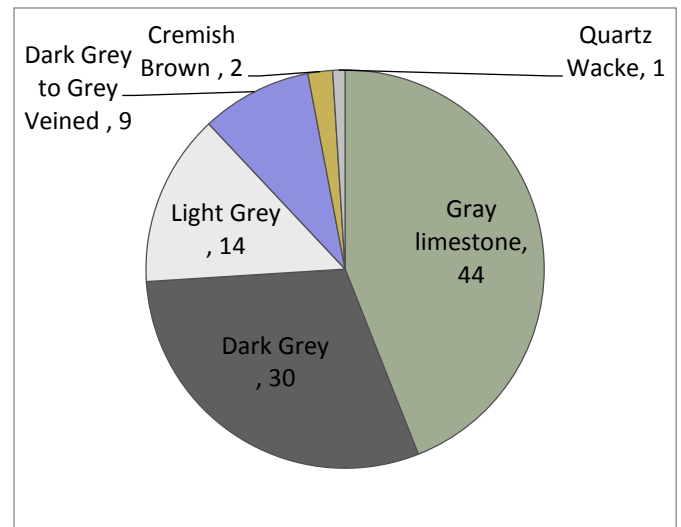
As shown in Fig.3. Margalla represent northern part of country. While Uban Shah represents the southern part of Sindh, Pakistan.

Table 2
Engineering properties of aggregate

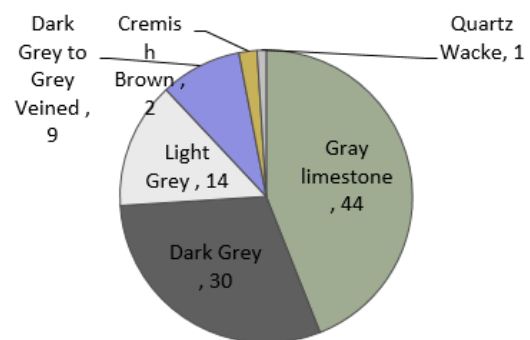
Test title	Standard	Margalla	Uban shah	Limits
Fractured Particles (%)	ASTMD 5821	100	100	90 min
Flakiness Index (%)	BS 812.108	4.84	10	10 max
Elongation Index (%)	BS 812.109	6.4	10	10 max
Water absorption(%)	ASTM C127	0.95	0.97	2 max
Los angeles abrasion(%)	ASTM C131	23	26	30 max
Sand equivalent (%)	ASTM D 2419	73	70	50 min
Soundness (%)	ASTM C88	2.5	3.2	8 max

The complete testing of aggregates like water absorption test, Los-Angeles Abrasion sand equivalent and soundness was conducted and found within the limits. .

No aggregate quarry has loss angles abrasion value more than 30% and sand equivalent value less than 70%.



UBAN SHAH



MARGALLAH

Fig.4. Mineral Composition of Different Aggregate Quarries
<http://nceguop.edu.pk/GeologicalBulletin>

4.2.1 Aggregate Gradation

Various types of gradation is used e.g average gradation, bailey gradation etc. But, we are adopting average technique because of its compatibility with desired project. We selected 2 different quarry sources having 3 different sizes of aggregates for their exact blending. Both Coarse and fine aggregates were sieved in 13 different sizes of sieves ranging from 0.075mm to

37.5mm. To check their percentage of passing . Two types of aggregate sources were selected; one is UBAN SHAH and other is MARGALLA.. The aggregate gradation is shown in Table 3 and Table 4 .

4.3 Asphalt Mixture

Bituminous mix design for pavement construction helps in producing a mix that is workable, durable, strong, and economical in nature. One of the widespread use of bitumen is in the pavement design and construction. There are different types of bitumen mixes for example Open-graded, Well graded or dense graded, Gap-graded and Unbounded bituminous mix that can be prepared. All of them have different properties and serviceability. This study comprises of dense graded mix that further sub-divided in coarse and fine graded. This hot asphalt mix is the most common mix used because it can provide great impermeable characteristics allowing water to run away from the surface area. These have all ranges of aggregates and are sufficiently packed. It facilitate the proper filling of voids in a systematic manner. This type of asphalt is ideal for all traffic conditions and has great performance under structural conditions, friction, andfor surfacing and repairing needs. It offers good compressive strength and tensile strength. The name comes from the aggregate size used while mixing the raw materials to produce the asphaltic composition.

Marshall mixture design method has been used for asphalt mix design . The first step in sample preparation is to determine optimum binder content . Three trials of aggregate –asphalt binder blends , with five sample for each blend and a total of fifteen specimens were prepared for each mixture. By evaluating each trial blend’s performance, optimum binder contents (OBC) of asphalt mixtures were determined. Stability test standard method was used to prepare the mixture in accordance with ASTM D6927.

Samples were to be fulfilled adequately. Samples were prepared on gyratory compactor in which 7000gm of aggregate and bitumen are used Different. mixes detail are given in Table 5. Which show the different asphalt mixture with different sources.

Table 5. Different types of asphalt mixes

Type of Mix	Source of Agg	Source of bitumen	Grade of bitumen	Maximum size (mm)	Nominal Max size(m m)	GM B	V A	Stability
Coarse Graded								
NH A-A	Margallah	ARL	60/70	25	19	2.392	3.0	1362
Fine Graded								
MS-2B	Margallah	ARL	60/70	19	12.5	2.340	4.9	1554
NH A-B	Uban shah	ARL	60/70	19	12.5	2.370	4.51	1291
SP-A	Margallah	ARL	60/70	19	12.5	2.338	4.53	1424

Further divided NHA classified groups of mixes are selected for this research. These are categorized at the basis of maximum & nominal particle sizes used. For example NHA class A has the highest size 25mm and nominal max size 19mm ,while GMB,VA and Stability values are with in the limits.

4.5 Permeability Testing

There are different types of permeameter FDOT permeameter, NCAT field permeameter, WPI modified NCAT permeameter. These differ from each other due to, use of epoxy membrane to seal core, sizes & dia of stand pipe dia, Correction factors, air voids connectivity, density and most important handling of specimen. But, In-situ falling head permeameter is the most quickest and easiest method to find the permeability accurately and the results obtained from this test doesnot deviate more than two to three percent of the results obtained from modified NCAT permeameter. The Falling Head-Permeameters used to study permeability are, Insitu-Permeameter diameter 5" to (EN 12697-40) 80-B0093/E, in-situ permeameter Italian Highway system compatible 6" Dia, Drainig Pavements 4" (80-B0093) and water pressurized permeameter as mention in Fig.5.

It has been inferred from Fig.5. that, Insitu-Permeameter has diameter of 5 inch, while in-situ permeameter Italian Highway system compatible has diameter 6 inch, while Drainig Pavements have 4 inch diameter and water pressurized permeameter.

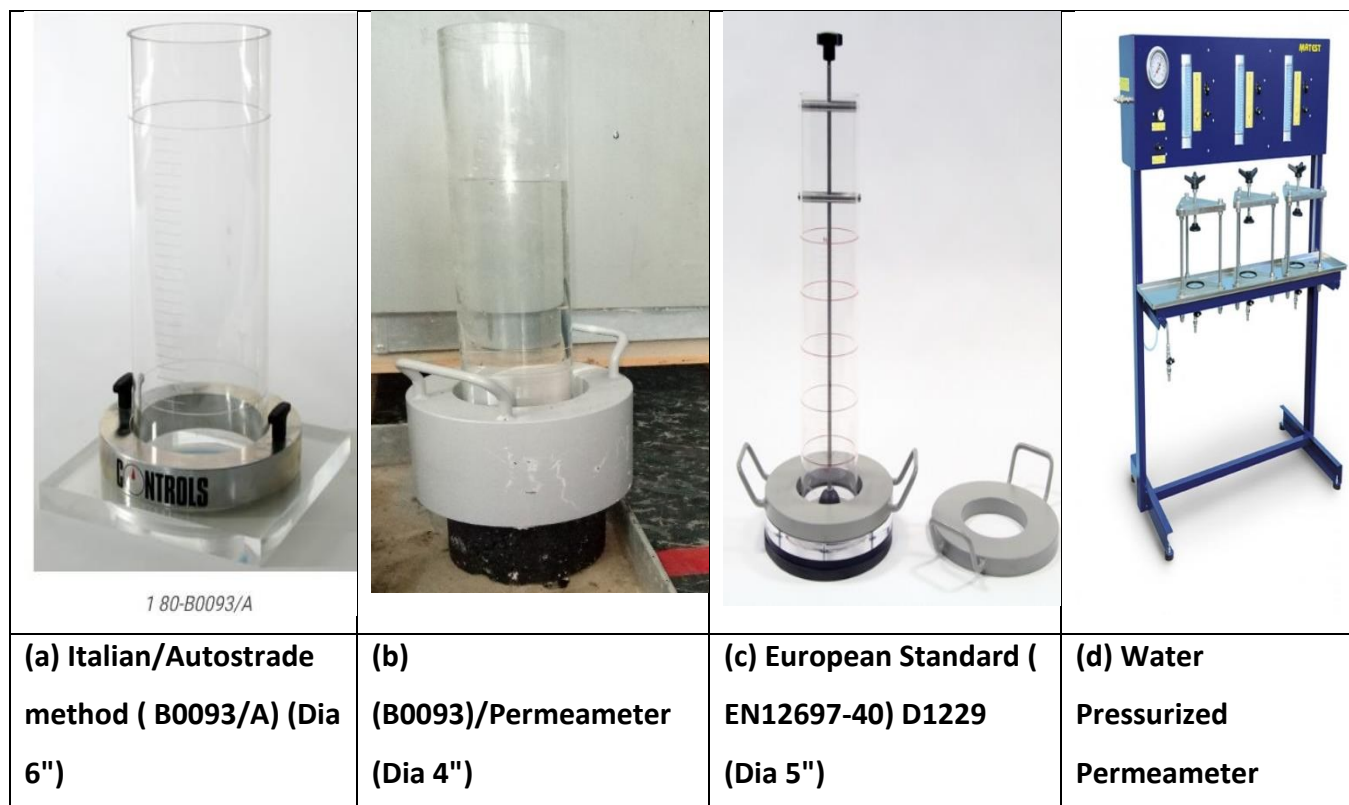


Fig.5. Different permeability apparatus

Permeability measured using Darcy's relation of laminar in following relationship .

$$k = \frac{al}{At} \ln \left(\frac{h1}{h2} \right) tc$$

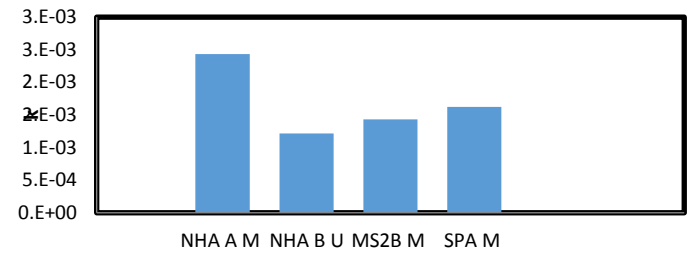
Where:

A=Cross-sectional Area of Sample in mm;
 L=Height/Length of Sample in mm; a= Cross-sectional Areas of Stand Pipe in mm; h1=Initial Head across test specimen; h2= Final Head across test specimen; t= Time Elapsed from start to Reading; tc= Temperature correction for viscosity of water while recording observations. As all measurements were taken at room temperature, so tc is taken equals to one. The permeability values ranges from 0 to 50 x 10E-5 mm/sec shows the impermeable pavements as per literature review. However the criteria for Super-Pave fine aggregate mixtures up to 8% air voids should not exceed 15 x 10E-3 mm/sec, and not a single value is exceeding from the design limitation.

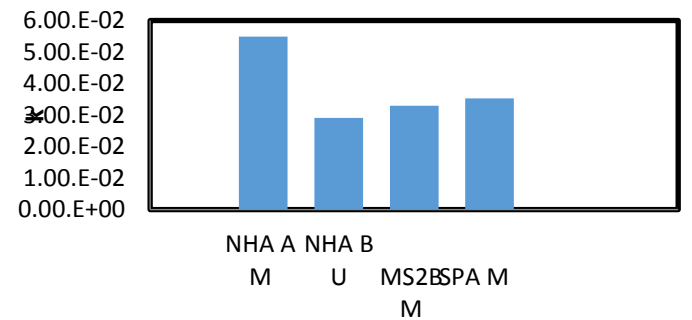
5.1 Permeability of asphalt mixes

We can see that 4'' permeability apparatus , asphalt mixes have low value of k and its take more time to flow water so it is a permeable. While 5'' permeability apparatus, asphalt mixes have greater k value as compared to 4 '' so it take less time to water flow so it is impermeable. While 6'' permeability apparatus have k value is more as compared to 4'' and 5'' so its take less time to flow water so it is permeable. While water pressurized permeameter have less k value as compared to other apparatus. In Fig 6 ,we can see that 4'' permeameter results have less value of K is impermeable while 5'' and 6'' permeameter has some mixes K value is less and those are impermeable and water pressurized permeameter has 60% of the results are the permeable and 40% result are impermeable ,NHA B U NRL 60/70 asphalt mix has less value of K

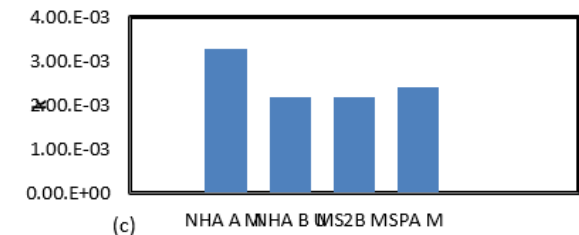
all of these permeability devices so it is impermeable. Other asphalt mixes result are given in Fig.6 .



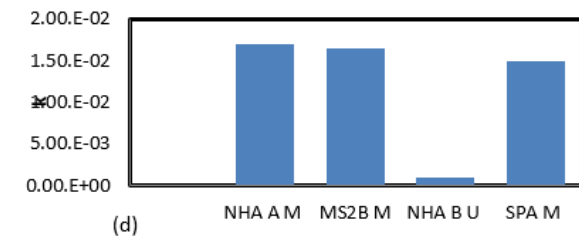
(a)



NHA A M NHA B U MS2B M SPA M



NHA A M NHA B U MS2B M SPA M



NHA A M MS2B M NHA B U SPA M

Fig.6. Effect of permeameter on permeability of asphalt mixture (a) 4'' (b) 5'' (c) 6'' (d) water pressurized permeameter

5.2 comparison between time and permeability

It may be noted from Fig.7 that 4'' permeameter takes more time to flow as compared to 5'' permeameter. In Fig.8, we see that time is change, as asphalt mix is changed. so we see that NHA B take more time to flow while NHA A takes less time to flow. we also see that size of apparatus changes, permeability value also changes, time also changes, air void and gradation also impact on permeability.

Water pressurized permeameter also impact on permeability as pressure apply permeability also changes. As compared to other permeability apparatus, water pressurized permeability less and time also less as other apparatus.

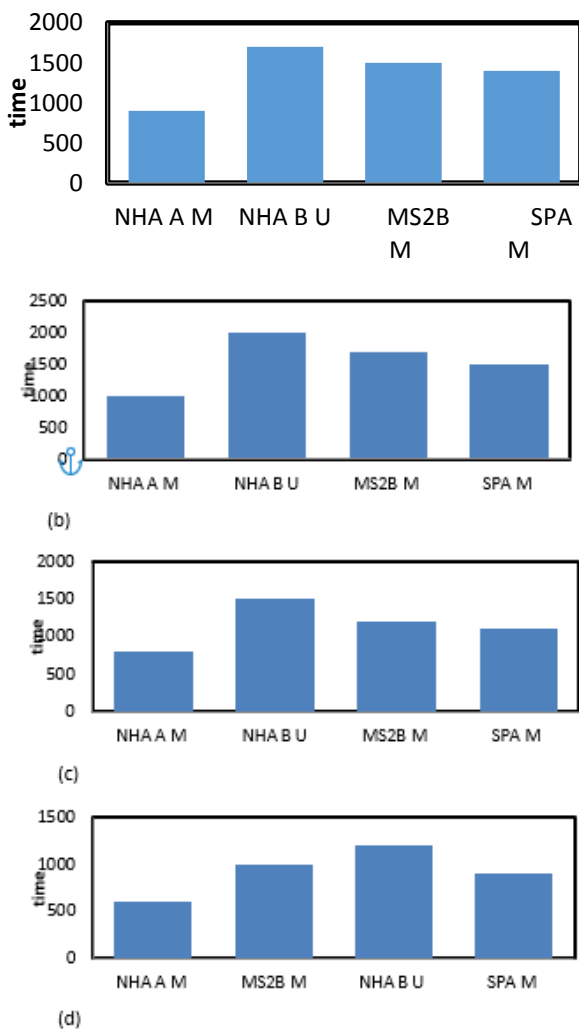


Fig.7. effect of permeameter on permeability of asphalt mixture

(a) 4'' (b) 5'' (c) 6'' (d) water pressurized permeameter

6. Acknowledgements

The authors thank the Taxila institute of transportation engineering and HRTC to provide friendly environment to conduct

7. REFERENCES

Abdullah, W.S., Obaidat, M.T. and Abu-Sa'da, N.M. 1998. "Influence of Aggregate Type and Gradation on Voids of Asphalt Concrete Pavements". *Journal of Materials in Civil Engineering*, 10(2): 76-85.

Bhattacharjee, S. and Mallick, R.B. 2002. An Alternative Approach for the Determination of Bulk Specific Gravity and Permeability of Hot Mix Asphalt (HMA). *International Journal of Pavement Engineering*, 3(3): 143-152.

Brown, E.R., Hainin, M.R., Cooley, A. and Hurley, G. 2004a. Relationships of HMA in-place air voids, lift thickness, and permeability Volume One. NCHRP web document, 68 <http://onlinepubs.trb.org/onlinepubs/nchrp/nchrp_w68v1.Pdf> (19 Nov. 2016).

Brown, Ray, Hainin M., Cooley Allen, Hurley Garham. "Relationship of Air Voids, Lift Thickness, and Permeability in Hot Mix Asphalt Pavements", Washington, DC: Transportation Research Board, 2004.

Chapuis, R.P. and Aubertin, M. 2003. On the use of the Kozeny-Carman equation to predict the hydraulic conductivity of soils. *Canadian Geotechnical Journal* 40(3): 616- 628.

Chapuis, R.P. and Aubertin, M. 2003. On the use of the Kozeny-Carman equation to predict the hydraulic conductivity of soils. *Canadian Geotechnical Journal* 40(3): 616- 628.

Chen, J.-S., Lin, K.-Y. And Young, S.-Y. 2004. Effects of Crack Width and Permeability on Moisture-Induced Damage of Pavements. *Journal of Materials in Civil Engineering*, 16(3): 276-282.

Cooley, Allen, Prowell Brian, Hainin Mohd and Buchanan M. "Bulk Specific Gravity Round-Robin Using the Corelok Vacuum Sealing Device", Report No.

02-11, National Center for Asphalt Technology (NCAT), 2002.

Gogula, A., Hossain, M., Romanoschi, S. and Fager, G.A. 2003. "Correlation between Laboratory and Field Permeability Values for the Super-pave Pavements". In Proceedings of the 2003 Mid-Continent Transportation Research Symposium, Ames, Iowa, August 2003. < <http://www.ctre.iastate.edu/pubs/midcon2003/gogulasupe rpave.pdf> > (19 Nov. 2016).

Goodbye, Hazen; Hello, Kozeny-Carman. *Journal of Geotechnical and Geo environmental Engineering*, 129(11): 1054-1056.

Haddock, J.E. and Prather, M. 2004. Investigation of permeability on Indiana SR-38. *Journal of Performance of Construction Facilities*, 18(3): 136-141

Hainin, M.R., Yusoff, N.I.Md., Satar, M.K.I.M.S. and Brown, E.R. 2013. The effect of lift thickness on permeability and the time available for compaction of hot mix asphalt pavement under tropical climate condition. *Construction and Building Materials*, 48: 315-324.

Harris, Christopher. "Hot Mix Asphalt Permeability: Tester Size Effects and Anisotropy", M.A.Sc. Virginia Polytechnic Institute and State University, Blacksburg, Virginia, 2007.

Kanitpong, K., Benson, C.H. and Bahia, H.U. 2001. Hydraulic conductivity (permeability) of laboratory-compacted asphalt mixtures. *Transportation Research Record* 1767, Pa- per No. 01-2997, Transportation Research Board, Washing- ton, DC, 25-32.

Li, Hui, Kayhanian Masoud and Harvey John. "Comparative field permeability measurement of permeable pavements using ASTM C1701 and NCAT permeameter methods", *Journal of Environmental Management*, Vol. 118, 2013, pp. 144-152.

Mallick, R.E., Cooley, L.A., Jr., Teto, M.R., Bradbury, R.L. and Peabody, D. 2003. An Evaluation of Factors Affecting Permeability of Superpave Designed Pavements. Report no. 03-02, National Centre for Asphalt Technology, Auburn University, and Auburn, Ala.

Masad, E., Al-Omari, A. and Lytton, R. 2006. Simple Method for Predicting Laboratory and Field

Permeability of Hot- Mix Asphalt. *Transportation Research Record* 1970, Transportation Research Board, Washington, DC, pp. 55- 63.

Maupin, G. W. "Asphalt Permeability Testing in Virginia", *Transportation Research Record: Journal of the Transportation Research Board*, Vol. 1723, No. 1, 2000a, pp. 83-91

Maupin, G.W. Jr. 2009. Personal Communication. McLaughlin, J.F. and Goetz, W.H. 1955. Permeability, Void Content, and Durability of Bituminous Concrete. *Highway Research Board Proceedings*, 34: 274-286. Masad, E., Birgisson, B. and Al-Omari, A. 2004. Analytical Derivation of Permeability and Numerical Simulation of Fluid Flow in Hot Mix Asphalt. *Journal of Materials in Civil Engineering*, 16(5): 487-496.

Mogawer, Walaa S., Mallick Rajib B., Teto Matthew R., and Crockford W. C. "Evaluation of Permeability of Superpave Mixes", *The New England Transportation Consortium*, 2002.

Mohammad, L.N., Herath, A. and Huang, H. 2003. Evaluation of Permeability of Super-pave ® Asphalt Mixtures. *Transportation Research Record* 1723, Paper No. 03-4464, Transportation Research Board, Washington, DC, pp. 50- 58. Mullen, W.G. 1967.

Impact of aging and moisture damage on bond strength of asphalt mixtutre

Hafiz Muhammad Abubakar ^{1, a}, Syed Bilal Ahmed Zaidi ^{2, b} and Muhammad Sohail Jameel ^{3, c}

¹ Research Scholar, Department of Civil Engineering, University of Engineering and Technology, Taxila, 47050, Pakistan

² Assistant professor, Department of Civil Engineering, University of Engineering and Technology, Taxila, 47050, Pakistan

³ Research Scholar, Department of Civil Engineering, University of Engineering and Technology, Taxila, 47050, Pakistan,

Email address: ^{a)} gaziabubakar74@gmail.com, ^{b)} bilal.zaidi@uettaxila.edu.pk and ^{c)} sohailjamil10@yahoo.com

Abstract— Bond strength in asphalt mixture should be adequate throughout the service period of a pavement for better performance. Bitumen due to some external factors, such as temperature and heat changes its capacity to resist moisture damage and bonding properties due to aging. To analyze the effect of aging on bond strength of asphalt mixture, binder is aged using the rolling thin film oven test (RTFOT) and pressure aging vessel (PAV). Dynamic Shear Rheometer (DSR) is used to check the stiffening of the virgin binder compared to aged binder. Bitumen Bond Strength (BBS) and Rolling Bottle Test (RBT) is performed to check the interaction between binder and aggregate as a result of aging of binder. BBS test on virgin and aged binder is performed at 24 hours of dry and wet conditioning. BBS test results have shown an improvement in Pull of tensile strength (POTS) after RTFOT and PAV aging at 24 hours of dry and wet conditioning. In dry conditions virgin and RTFOT aged binder follows cohesive nature of failure and PAV aged binder follows adhesive failure pattern. In wet conditions cohesive nature of failure is observed in virgin, RTFOT and PAV aged binder. RBT results have shown increase in percent retained coating of binder after RFTFOT and PAV aging. It is found that aging increases the resistive property to moisture damage and bond strength of binder.

Keywords— Asphalt mixture, rolling thin film oven test, pressure aging vessel, Dynamic shear rheometer, Bitumen bond strength test, rolling bottle test.

Introduction

As bitumen gets aged its chemical properties changes. Its oily components with change in temperature and pressure gets removed and bitumen loses its ductility due to which its bonding characteristics gets changed. Cracking phenomena in the pavement mostly occurs due to aging of binder which makes mixture brittle and as the pavement loaded it becomes more prone to cracking. So, impact of bond strength and aging of binder play an important role in pavement performance.

Aging of bitumen is a phenomenon in asphalt pavement structures that contributes to deterioration due to stiffening of binder. Over the bitumen losses its ductility due to removal oily components and other saturates bitumen becomes hard and stiff. Moisture damage occurs due to stripping phenomena in asphalt mixtures and it contributes to further deterioration of pavement. So, it is very important to analyze the effect of aging on bond strength and resistance to moisture damage. As the cracks appears on surface of pavement moisture enters in cracks and may severely damage the underneath structure of pavement.

Problem statement

Usually it is not possible to characterize the bonding behavior of bitumen after aging. Very little-known effort is made on this aspect in the past. It is a known fact that aging enhances the stiffness of the binder. As binder in asphalt mixture is aged, pavement may be subjected to surface cracks and moisture get enters into it. But stiffness weather improves the bonding property and causes a greater resistance against moisture or causes a decrease in bonding strength. In this study the effect of aging of binder on bonding properties of bitumen were checked.

Aims and objectives

- To check the stiffness of binder after RTFOT and PAV aging
- To depict the impact of aging on moisture damage of asphalt mixture
- To analyze the bond strength and mechanism involved in bonding behavior of bitumen before and after aging.

Literature review

Aging of bitumen is a phenomenon in asphalt pavement structures that contributes to deterioration. Over the time bitumen changes its chemical characteristics that may cease the pavement performance [1, 2]. Asphalt mixture as the most important materials for pavement and their physical and chemical properties have a direct influence on performance of mixture. The lack of bonding between them can cause a major damage to pavement structure. Asphalt adhesion is directly affected by the chemical changes in the bitumen [3, 4]. Bitumen aging can be divided in two phases, short and long-term aging. Short term aging occurs during mixing and transporting and compaction of mixture while long term aging occurs during service period due to loading, pressure and environmental effects and is limited to few millimeters of pavement surface. Aging promote the chances of cracking in the pavement. Aging make bitumen brittle and stiff, this stiffness may cause the fatigue cracking decreasing the life span of pavement[5-7].

A force that link the two unlike materials is called adhesion. In case of asphalt mixture adhesion is the required energy that is needed to get rid of the link between the bitumen and aggregate. Adhesion is also a most important phenomena in asphalt mixtures which also contribute to serviceability of pavement structure[8, 9]. Four basic theories have been theorized to justify the bonding of asphalt mixture which are mechanical adhesion theory, molecular orientation theory, surface energy theory and chemical reaction theory. Chemical reaction theory explains the adhesion in context of viscosity of bitumen, more viscous bitumen has greater concentration of polar molecules(asphaltenes) create greater adhesion with aggregates due to greater adhesion tension [10-12]. A study has shown an improvement in moisture damage resistance after oxidative aging [13]. Another work study evaluated the combined effect of aging and water damage to asphalt mixture indicating the poor performance of asphalt mixture in unaged condition [14]. A work have shown decrease in moisture damage resistance after RTFOT and PAV treatment of binder and bonding strength[15]. Another study has shown that aging promotes generation of surfactants and acids which damage the moisture resistive performance of mixture [16]. A work on adhesion of binder and aggregates has shown under the moisture conditions a virgin binder usually follow the cohesive nature of failure and a severely aged binder follows an adhesive nature of failure in bond strength test[17].

Research Methodology

Materials

Properties of bitumen are shown in Table 5.

Table 1: Properties of Virgin Binder

Property	Reading (Penetration Grade 60/70)
Mean penetration value (1/10 mm) (ASTM D5)	62
Ductility (ASTM D113)	Above 100 cm
Flash point (ASTM D3143/3143M-13)	269°C
Softening point (ASTM D36)	52°C

Bitumen of Attock refinery penetration grade 60/70 is used as binder for each of Limestone (Margala crush) and sandstone (Sargodha crush) which is used as a substrate. Properties of aggregates used are listed in **Error! Reference source not found.** and **Error! Reference source not found..**

Table2: Aggregate type, Composition and Nature

Aggregate Type	Components	Rock Type	Nature
Sandstone	40.848 SiO ₂	Sedimentary Rock	Acidic
Limestone	Calcite 65%, Silica 30%	Fossiliferous Limestone	Basic

Table3: Physical properties of aggregates

Property	Limestone	Sandstone
Water absorption (%)	1.32	1.00
Specific gravity	2.83	2.72
Bulk density(kg/m ³)	1508	1533
Voids (%)	45.56	42.80
Impact value (%)	16.50	11.60
Crushing value (%)	29.80	17.90
Compressive strength (MPA)	26.30	21.10
Splitting tensile strength (MPA)	2.25	2.00
Flexural strength (MPA)	4.90	4.78

Testing Plan

- Dynamic shear rheometer (DSR) according to standard AASHTO T315 [18]
- Rolling Bottle Test (RBT) according to standard EN 12697-11:2012 [19].
- Bitumen Bond Strength test (BBS) according to standard ASTM D 4541[20]

The workflow diagram for this research study is shown in Figure 21.

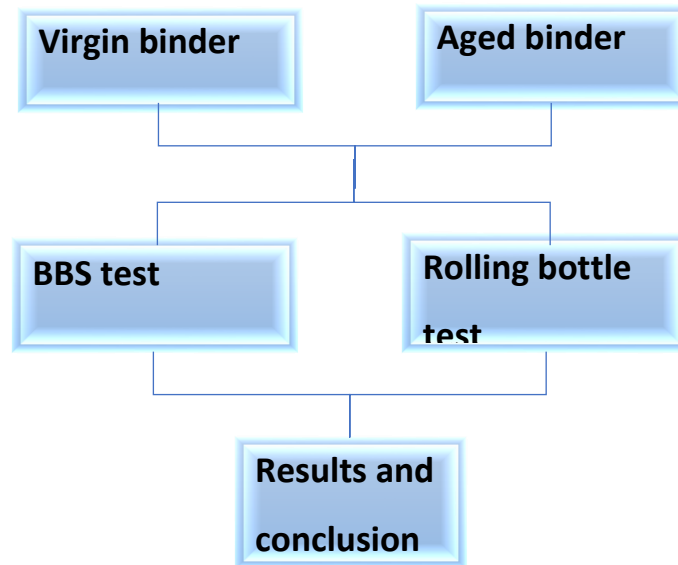


Figure 21: Workflow diagram

Tests Descriptions

Dynamic shear rheometer

Rheology of virgin and aged bitumen are determined using the frequency sweep. Test is taken at the various intermediate and high temperatures which ranges from (22, 34, 46, 58, 70, 82°C) and at frequency range (0.1 to 10Hz) and at a constant strain level oscillatory shear is applied. Rheological parameters are obtained using excel and master curves are plotted at the temperature of 58°C using the sigmoidal function

$$\text{Log}|G^*| = \delta + \frac{\alpha}{1 + e^{\beta + \gamma(\text{Log}f_r)}} \quad (3)$$

Where δ is the minimum complex shear modulus, α is the difference between maximum and minimum complex shear modulus value, G^* is the complex shear modulus, γ , β are the shaped functions parameters of sigmoidal function and f_r is the reduced frequency.

Rolling Bottle Test

Rolling bottle test is proved to be most suitable method as for adhesion[21]. In rolling bottle test two type of mixtures are prepared using sandstone and limestone aggregates with each of 60/70 and 80/100 penetration grade bitumen. The is conducted using the standard procedure of EN 12679-11. 162g of aggregate passing 9.6mm and retained on 6.3mm is cleaned with deionized water

to remove any material present on the surface of aggregates and placed in oven for 60 minutes at 60°C and is mixed with 8g of bitumen and mixture is prepared heated to a limit that bitumen is properly coated on aggregates. The mixture then is placed in rolling bottle by separating single aggregate one by one poured into the rolling bottle and placed on rolling machine for 72h. The test is performed at 20°C and machine is rolled at 60rpm. Reading is taken after 6h,24h,48h,72h. Pictures of sample are taken by a camera of 13 megapixel and pictures are taken at fixed distance of 18cm. Two reading for each mixture is taken by two observers to get the appropriate results. At the end mean is taken for each time of rolling to get the final percentage of coating of bitumen.

BBS test

BBS test consists of an adhesion tester, pressure pipe, piston, plate, and stubs made of metal that are used to pull off from reaction plate over the bitumen and the pressure is noted to calculate the pull of tensile strength (POTS) by the following formula.

$$POTS = \frac{(BP \times Ag) - C}{A_{ps}} \quad (4)$$

BP is representative of burst pressure (psi), Ag is the contact area between gasket and plate having value 4.06 in², C is a constant having value 0.286 in², A_{ps} is the area of pull of stub having value 0.1963 in². Aggregate plates having thickness of 2" are cut by a saw cutter having some specific dimension are cleaned by deionized water to remove the dust or any raw material on surface of plate. These plates are placed in an oven with temperature of 60°C for a period of 60 minutes to remove the absorbed water. Stubs are placed in oven for 20 minutes at 60°C to remove of the oils present on it. Binder is heated in oven for 5 minutes at 160°C and immediately placed on the stub which is pressed on the plate vertically. Pressure on adhesion device is provided not more than 120psi. circular spacer is placed on the stub and piston tightened on the stub and a pressure is given at a rate of 2-6psi/s. The pressure at which the stub is pulled out of the plate is used to calculate the POTS value. Penetration grade 60/70 is tested with limestone and sandstone.

Aging of Bitumen

RTFOT aging

Binder short term aging is done by using the rolling thin film oven test using the procedure of standard AASHTO T240. There are eight glass bottles and one bottle are filled with 35g of bitumen and cooled in the cooling rack for a period of 60-180 minutes. After cooling bottles are taken in RTFOT oven and is rotated at 15 rpm for 85 minutes. during at 325°F (163°C) and air flow in is kept bottles at 244 in³/min (4000 ml/min)[22].

PAV aging

Binder is aged for long term aging is by pressure aging vessel of pressure 300psi(2.07MPa) and at a temperature of 110°C(230° F). Pans of each is 50-gram capacity are kept in a pan holder and then moved in the pressure aging vessel for 20 hours. After 20 hours of treatment samples are taken from the vessel and degassed to perform the tests [23].

Table 4: Properties of binder after Long- term and Short-term aging

Type of Aging	Short Term Aging	Long Term Aging
Mean Penetration Value (1/10 mm) (T49-03)	57	53
Ductility (T51-00)	62 cm	56 cm
Flash Point (T48-99)	Above 300°C	Above 300°C
Softening Point (T53-96)	39°C	31°C

Results and Discussion

DSR test Results

Figure 22 is shown for complex shear modulus and reduced frequency. As the binder is aged the curve shifts upward indicating an increase in stiffness of binder. For RTFOT aged binder the curve is higher than virgin binder and PAV aged it goes further up indicating a more increase in stiffness after PAV aging. Higher value of G^* means elastic response is slowed and loss of ductility. The upward movement of curve with aging is an indication that stiffness of binder is increasing with aging of binder. RTFOT treated binder is more stiff than virgin binder and PAV aged binder is stiffer than RTFOT aged and virgin binder.

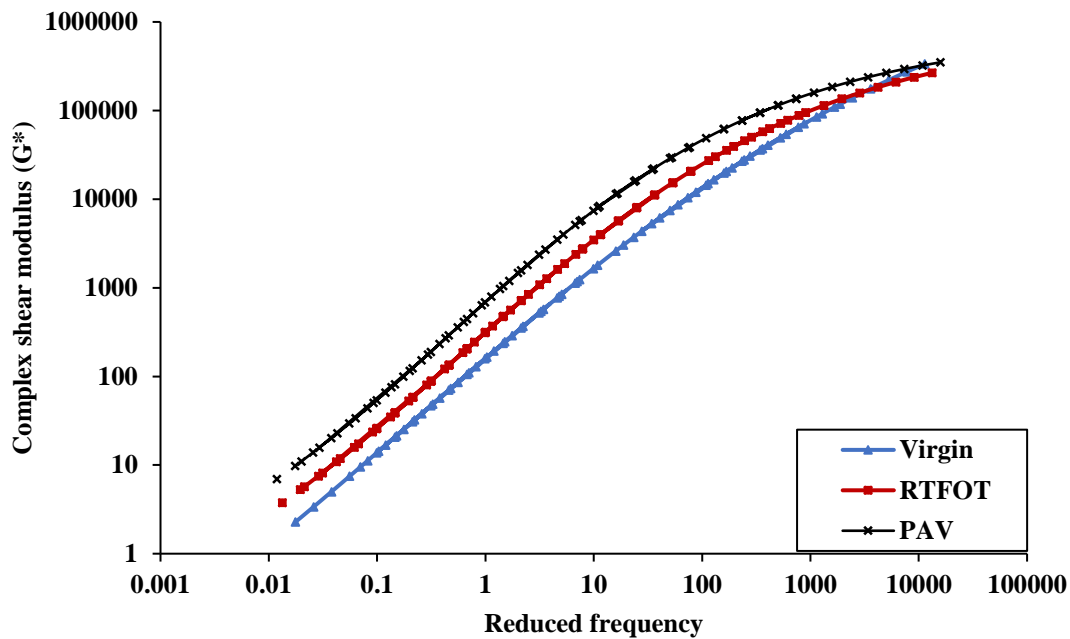


Figure 22 : Relationship between G^* and reduced frequency for 60/70 pen grade

Rolling bottle test results

Rolling bottle test results are shown as percentage of bitumen coating. **Error! Reference source not found.** and **Error! Reference source not found.** shows decreasing value for limestone and sandstone in which aged binder coating is increased for 6h of rolling. For 24hours, 48hours and 72hours the value of bitumen coating is following the same trend of lower coating of binder for virgin binder is less than for aged binder. For both limestone and sandstone virgin percent retained coating is less than RTFOT aged and PAV aged binder. So, aging decreases the moisture damage in terms of stronger adhesive bond between aggregates and bitumen.

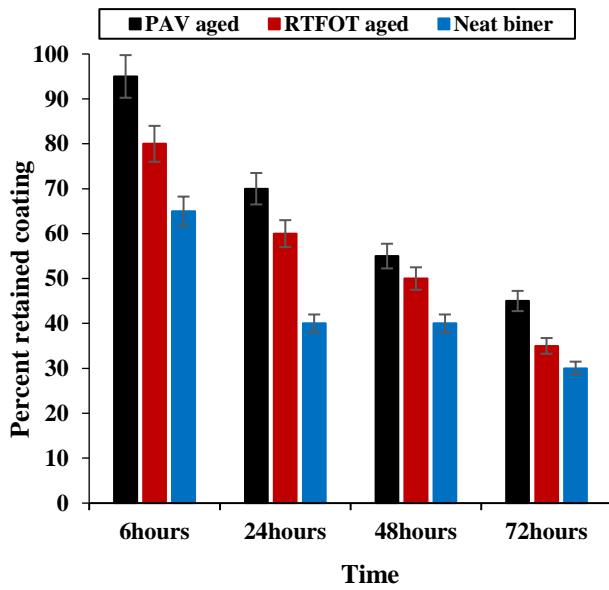


Figure 23: Percent retained coating of 60/70 pen grade for limestone

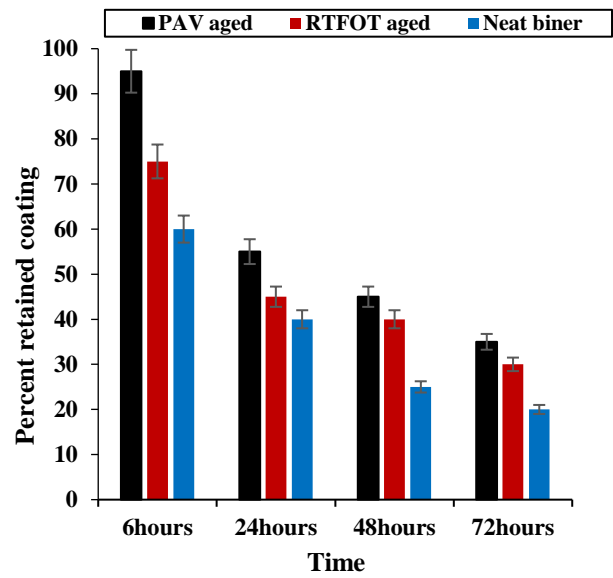


Figure 24: Percent retained coating of 60/70 pen grade for sandstone

BBS test results

From **Error! Reference source not found.** and **Error! Reference source not found.** it's clear that POTS value for unaged binder penetration grade 60/70 with limestone and sandstone at 24 hours of dry conditions is less and for aged binder its improved. In case of virgin binder its lower than both RTFOT aged and PAV aged binder. In case of short term aging it is higher than virgin and for long term or PAV aged its higher than both virgin and RTFOT aged binder. For virgin and RTFOT failure pattern is cohesive and for PAV treated binder it follows only adhesive nature of pattern.

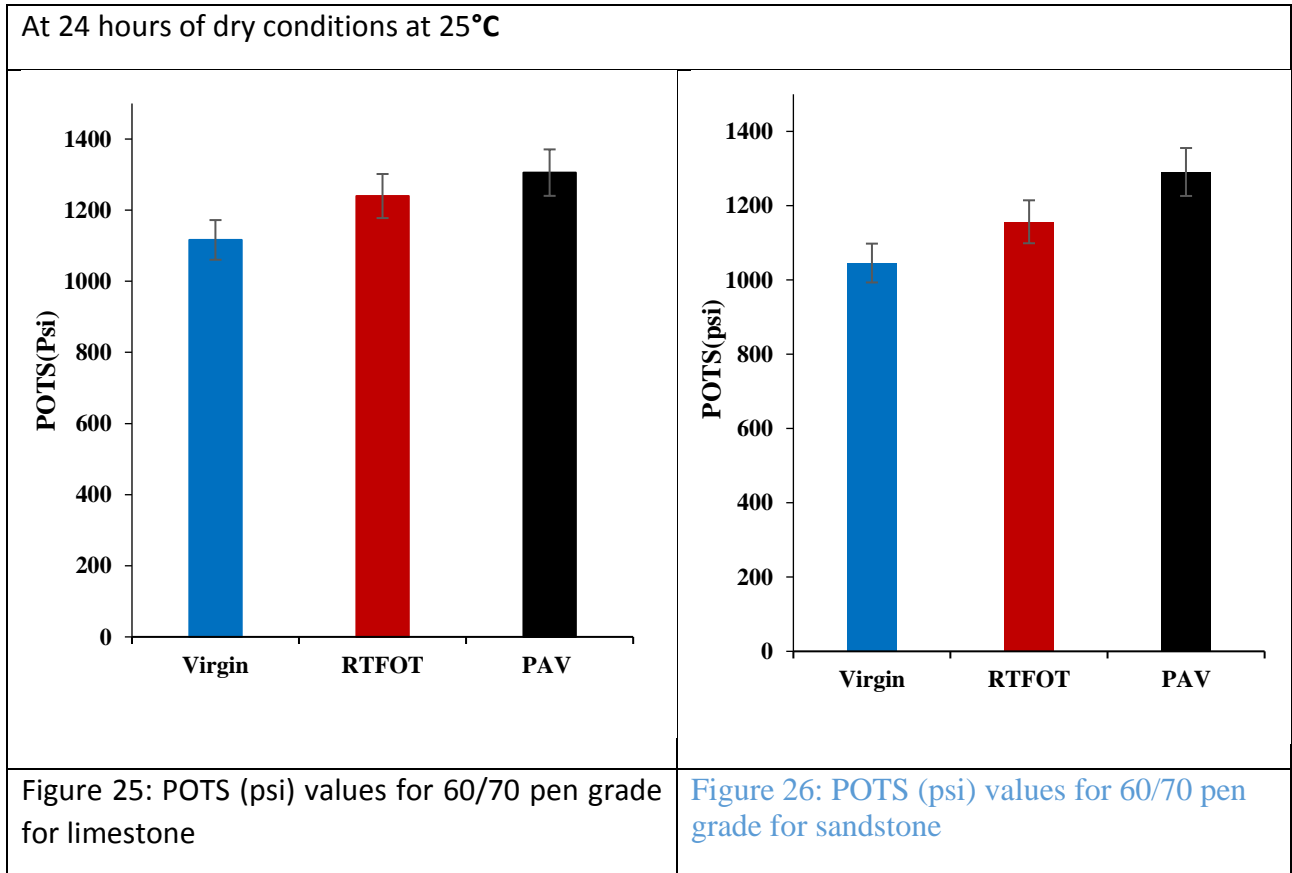


Figure 27 and Figure 28 shows the POTS values for 24 hours of wet conditions in which virgin POTS are lower than RTFOT aged binder and PAV aged binder. Virgin, RTFOT and PAV treated binder all follows only cohesive nature of failure pattern.

A 24 hours of wet conditions at 25°C

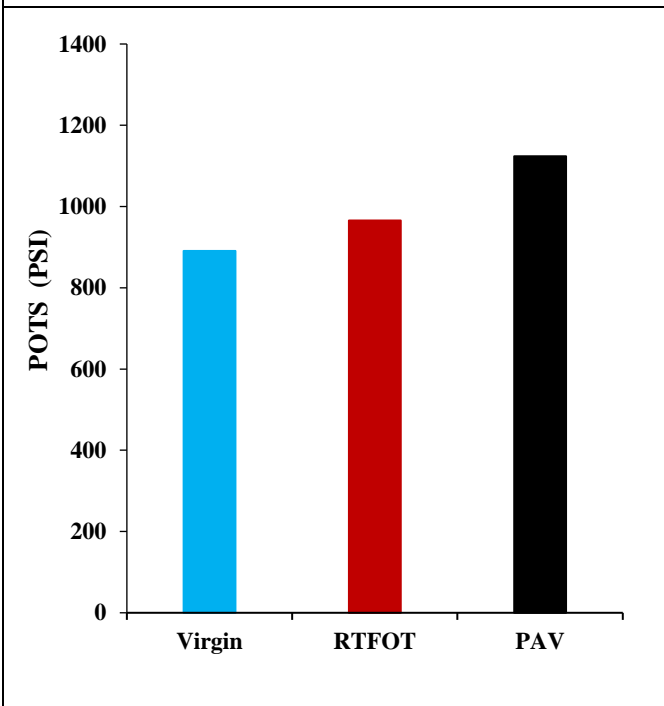


Figure 27: POTS (psi) values for 60/70 pen grade for limestone

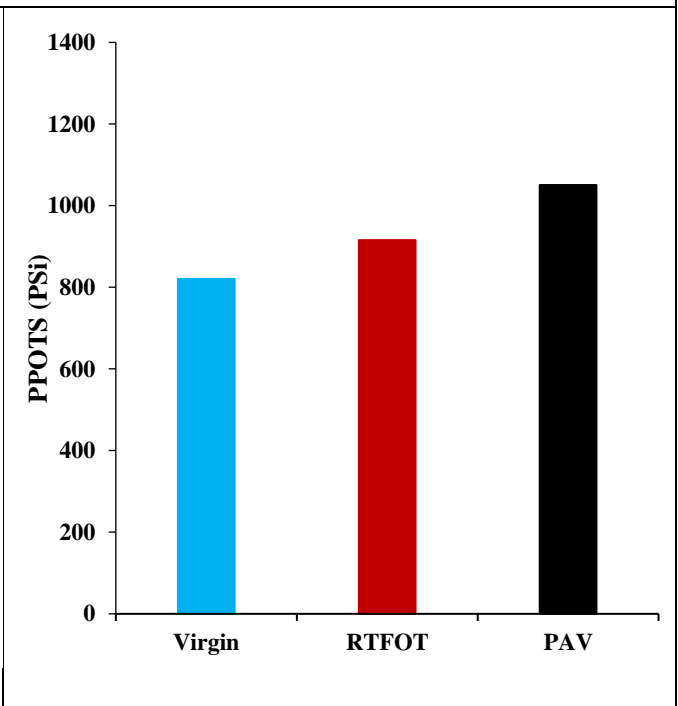


Figure 28: POTS (psi) values for 60/70 pen grade for sandstone

CONCLUSION

From above results it is clear that as

- As bitumen gets aged its complex shear modulus increases. As a result of improvement in complex shear modulus stiffness increases. Bitumen lost most of its oily components responsible for ductile behavior.
- Stiffness improves the POTS and Adhesion of bitumen and aggregates increases as it gets aged. As a result of aging pull of tensile strength of bitumen improves and on the other other hand it causes in loss of ductility of bitumen. Due to loss in ductility, aging results in embrittlement mode of failure. Pull of tensile strength increases due to brittle behavior of binder. Virgin and short-term aged binder follows cohesive nature of failure and long-term aged binder follows adhesive nature in dry conditions and in wet conditions cohesive only failure is observed.
- Rolling bottle test results shows that as bitumen gets aged its adhesion with individual particles increases but stripping phenomena in bitumen aggregate system may increase due to loss of ductile nature. Resistance to moisture damage increases due to aging of binder.

Rolling bottle test is a visual observations of percentage coating and coating is observed on individual particles and stripping is caused due to cohesive failure within the bitumen binder.

References

1. Petersen, J.C., *A review of the fundamentals of asphalt oxidation: chemical, physicochemical, physical property, and durability relationships*. Transportation Research Circular, 2009(E-C140).
2. Yang, Z., et al., *Effect of aging on chemical and rheological properties of bitumen*. Polymers, 2018. **10**(12): p. 1345.
3. Yao, H., et al., *Performance of asphalt binder blended with non-modified and polymer-modified nanoclay*. Construction and Building Materials, 2012. **35**: p. 159-170.
4. Zhao, S., et al., *Characterizing rheological properties of binder and blending efficiency of asphalt paving mixtures containing RAS through GPC*. Journal of Materials in Civil Engineering, 2014. **26**(5): p. 941-946.
5. Hofko, B., et al., *Alternative approach toward the aging of asphalt binder*. Transportation Research Record, 2015. **2505**(1): p. 24-31.
6. Huang, S.-C., et al., *Ageing characteristics of RAP binder blends—what types of RAP binders are suitable for multiple recycling?* Road materials and pavement design, 2014. **15**(sup1): p. 113-145.
7. Ongel, A. and M. Hugener, *Aging of bituminous mixes for rap simulation*. Construction and Building Materials, 2014. **68**: p. 49-54.
8. Copeland, A.R., *Influence of moisture on bond strength of asphalt-aggregate systems*. 2007.
9. Mohd Jakami, F., *Adhesion of asphalt mixtures*. 2012.
10. Curtis, C.W., *Investigation of asphalt-aggregate interactions in asphalt pavements*. American Chemical Society, Fuel, 1992. **37**: p. 1292-1297.
11. Hicks, R.G., *Moisture damage in asphalt concrete*. Vol. 175. 1991: Transportation Research Board.
12. Santagata, F., et al. *Modified PATTI test for the characterization of adhesion and cohesion properties of asphalt binders*. in *Sixth International Conference on Maintenance and Rehabilitation of Pavements and Technological Control (MAIREPAV6) International Society for Maintenance and Rehabilitation of Transportation Infrastructure Transportation Research Board*. 2009.
13. Li, B., et al., *Effect of short-term aging process on the moisture susceptibility of asphalt mixtures and binders containing sasobit warm mix additive*. 2015. **2015**.
14. Das, P.K., et al., *Coupling of oxidative ageing and moisture damage in asphalt mixtures*. 2015. **16**(sup1): p. 265-279.
15. Al Masri, Z.A.B., et al., *Evaluating the Effect of Binder Aging and Mineral Fillers on Moisture Susceptibility of Asphalt Concrete Using Surface Free Energy*.
16. Thomas, K.P., et al., *Surfactants in aged asphalt and impact μ on moisture susceptibility of laboratory-prepared mixes*. 2006. **7**(4): p. 477-490.
17. Asif, S.A., et al., *Study of adhesion characteristics of different bitumen–aggregate combinations using bitumen bond strength test*. 2018. **41**(5): p. 430-440.
18. Holsinger, R., A. Fisher, and P. Spellerberg, *Precision Estimates for AASHTO Test Method T308 and the Test Methods for Performance-Graded Asphalt Binder in AASHTO Specification M320*. 2005.
19. Dickinson, L.L., A.T. Blachly, and A.J. George, *Evaluation of Asphalt Stripping Tests*. 1990: Federal Highway Administration.

20. Astm, D., *4541, Standard Test Method for Pull-Off Strength of Coatings Using Portable Adhesion Testers*. Annual Book of ASTM Standards, 2002: p. 1-13.
21. Paliukaitė, M., et al., *Evaluation of different test methods for bitumen adhesion properties*. 2016. **14**: p. 724-731.
22. AASHTO, *Standard method of test for effect of heat and air on a moving film of asphalt binder (rolling thin-film oven test)*. 2009.
23. Behera, P.K., A. Singh, and M. Amaranatha Reddy, *An alternative method for short-and long-term ageing for bitumen binders*. Road materials and pavement design, 2013. **14**(2): p. 445-457.

Effect of Load and Fuel Price Variation on Genco Agent in Day Ahead Auction

Nisha Hareem
Center for Advanced Studies in
Energy
National University of Science
and Technology (NUST)
Islamabad, Pakistan
nishahareem7@gmail.com

Kashif Imran
Center for Advanced Studies in
Energy
National University of Science
and Technology (NUST)
Islamabad, Pakistan
kashifimran@uspcae.nust.edu.pk

Abdul Kashif Janjua
Center for Advanced Studies in
Energy
National University of Science
and Technology (NUST)
Islamabad, Pakistan
kashif@uspcae.nust.edu.pk

Abstract— In electricity markets, participants undertake distributed decision making under dynamic environment. Agent based modeling and simulation is suitable for analysis of such distributed decision making. Self-centric GenCo agents have a chance to learn from results of day-ahead auction and adjust their bids for the next day. Reactive reinforcement learning algorithms have capabilities to learn optimal response of GenCo agents to dynamic conditions of day-ahead auction. This paper explores change in convergence behavior of learning algorithm when market environment was made more dynamic, by introducing stochastic load profiles and variable generation cost coefficients, to model load variability and fuel price changes in real world markets. The results show that as variation in load profile increases, algorithm generally take more days to converge but average number of simulation runs that converge remain within a small range. As fuel price variation increases, convergence becomes tough and gets delayed but a greater number of simulation runs achieve convergence.

Keywords— reinforcement learning, electricity market, convergence rate, strategic bidding

I. INTRODUCTION

The electricity market is a platform where electricity is exchanged between the participants at a fixed price according to the electrical system capacity. The electricity market consists of two types of markets, one is a wholesale market and another one is the retail market. In the wholesale power market, there are three major participants include an Independent System Operator (ISO) and traders consisting of Load-Serving Entities (LSEs) and Generation Companies (GENCOs) are distributed across the buses of the transmission grid. In the wholesale market, price is set by a market-clearing algorithm that considers generators' bids and offers of the load. In the wholesale market, electricity is purchased and sold on a day-ahead basis to avoid the price volatility of the real-time market.

In the day-ahead market, the price is determined at each node to maintain the equilibrium between supply and demand. In this

situation, a supplier can increase its profit by exerting its market power and using a bidding strategy. Therefore, the optimal bidding strategy has become the most important goal of generation companies (GENCOs) to achieve their maximum profit in the electricity market. In a centralized market, decision making for generation dispatch is made through one central point without any competition in the market. In this market, the structure operator suffers from an incentive problem in bidding. However, the decentralized market, which includes renewable sources producers, is flexible and deals with the criteria of energy consumption, the safety of supply, environmental compatibility and economy.

As the market moves from centralized to decentralized structure, competition increases to achieve maximum profit and participants face increasing risk. Many problems arise like participants have to do operations planning and develop suitable bidding strategies to survive in the market. Therefore, a well-organized and efficient computational and intelligent system is required to develop a bidding strategy for obtaining maximum profit in the market. GENCOs and LSEs are involved in forecasting participant behavior and market outcomes to learn how to maximize their profit in such a decentralized market. GENCO sells its power to LSEs at a profitable rate which depends on many parameters in a competitive market like optimal bidding, load demand, and fuel price variation. In the case of decentralization, market profit and prices are volatile and unpredictable [1].

To study the conduct of complex market environment and restructure the economic consequences of the power industry, different agent-based simulation tools are used like MESCAM, MATREM, AMES, EMCAS and MAST [2]. MESCAM (Multi-agent Simulator of Competitive Electricity Markets) tool helps to study restructuring options for a wholesale power market. Similarly, MATREM (Multi-Agent Trading in Electricity Market) allows the simulations regarding the participants' behavior and resulting outcomes of the electricity market. EPOCHS is an agent-based distributed simulation environment that combines multiple research and commercial off-the-shelf systems. However, the current study chooses Agent-Based

Modeling of Electricity System (AMES) because it is open-source software. AMES is a computational agent-based laboratory to study participant behaviors in the wholesale energy market [3]. Different machine learning techniques are useful for modeling optimal bidding of GENCO but a Reinforcement Learning (RL) algorithm is used in AMES.

Different pricing strategies from distribution companies are introduced to the user on an hourly, daily and monthly price basis. Limited knowledge is available to the user and the fuzzy Q-learning techniques should be adapted for optimal pricing policy. The customer learns the best way to maximize the utility and minimize price at a peak, hence increasing market stability [4]. Convergence period and price depends upon many parameters like the pseudorandom number and parameter k . The convergence of clearing price is inversely proportional to the period number [5]. The convergence of the algorithm in peak hours and high demand is higher than the spot price [6]. Market participants use Q-learning for bidding strategy in the auction of the balancing market by considering the marginal cost. Uniform price auction and pay as bid auction are modeled for balancing the market. Pay as a bid is more adaptable for market-clearing [1].

The wholesale electricity market has been operating under varied capacity conditions. High market efficiency was attained using double auction by learning through modified Roth Erev learning. Learning helps infra marginal traders to bid which is close to the true reservation price [7]. For bidding strategies and actions performed in the day-ahead market, a multi-agent simulation tool like MASCEM is developed. Reinforcement learning (RL) the methodology is used in which players observe the changing environment and bid accordingly [2].

AMES was designed to study the restructured wholesale market in which trading strategies of traders are expected to improve over time because of machine learning algorithms [3]. Variant Roth Erev algorithm is implemented in the AMES market framework and according to data is predicted robustly in mixed strategic equilibrium as compared to static equilibrium. Improved net earnings were obtained with the proposed Roth Erev RL algorithm for GENCO optimal bidding strategy [8]. The improvement was established despite other learning agents in a repeated volatile auction environment [9]. GENCO's bidding strategy is made on multidimensional and continuous action space.

Due to the decentralization of electricity market, the ambiance becomes dynamic and decision-making processes fluctuate so the convergence of learning algorithms may be adversely affected. In this study, the main purpose is to explore the GENCO agent's strategic behavior in a volatile market environment. It can be achieved by changing the learning of algorithms for reinforcing the Variant Roth Erev learning. Hence, the effect of load-based variation and price variation on reinforcement learning algorithm convergence is mainly focused on the current study.

II. METHODOLOGY

A. Reinforcement Learning

Originally, Alvin Roth and Ido Erev developed an algorithm and afterward refined their algorithms to model how people react in repeated activity against different strategic participants. The Roth Erev algorithm has been created to update the decision possibility when an agent fails to choose among different actions [9].

The method of optimal bidding of the GENCO agent is modeled by the Roth Erev algorithm in the AMES framework [10]. Instead of considering the environmental conditions in which the learning agent is located, training is based exclusively on the selected last action along with the reward which is earned from the proposed action. A probability distribution occurs on every selected action. In the RL technique, the GENCO agent may consider many market parameters like day time, prices of fuel and load prediction before making an offer choice. VRERL works by combining all the propensities values followed by converting these values into probability distribution into the action domain. Suppose $q(t)$ be the propensity for the action choice j at the time (t) .

$$P_j(t) = \frac{q_j(t)}{\sum_{m=1}^n q_m(t)} \quad (1)$$

The parameters used in reinforcement learning algorithm are described as follows [9]:

a. Boltzman Constant

In the beginning, the probability of choosing any action is the same as an initial propensity. Due to the corresponding propensity, the Boltzman constant measures the probability of action that is selected. Similarly, if the supply offer m has the highest propensity value then the degree to choose this probability action j of supply offer increases.

b. Experimentation

The purpose of the experimental factor is to inhibit a GENCO agent from selecting a single supply offer at a very initial stage. It provides the opportunity to GENCO agent to more frequently experiment with the new supply offers.

c. Recency

The recency factor is used to reduce the choice of previously selected supply bid for a prolonged time. This permits the GENCO agent to ignore previously acquired earnings from the supply offer and helps them to submit new supply offer and consequently learn the present market state.

III. AGENT BASED ENERGY MARKET SIMULATION

The experiment is performed on dynamic 5 bus test system in AMES as shown in Figure 1 [9].

The system consists of five GENCOs G1, G2, G3, G4 and G5 that have maximum operating capacity of 110MW, 100MW, 520MW, 200MW and 600MW respectively. G3 is considered as potential load pocket with respect to LSEs because it has LSEs on local and adjacent buses. G4 is expensive due to costly generation technology whereas G1, G2, G5 have moderate generation costs.

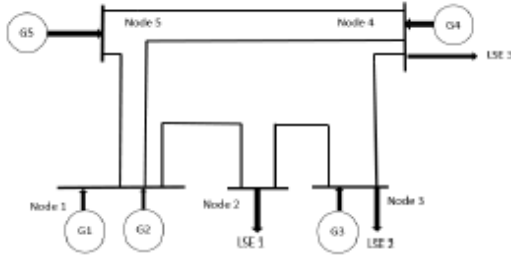


Figure 1 Five Bus Test System

At the start of day 1 of the day ahead market without any strategic learning for the day D, the daily load profile is submitted by means of demand bids. The three LSE's inelastic daily load profile shown in Figure 2 remains the same from day to day.

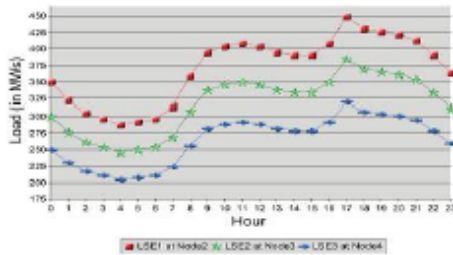


Figure 1: Daily Load Profile

Actual marginal cost function of generator i is represented as

$$MC_i(pG_i) = a_i + 2 \cdot b_i \cdot pG_i \quad (2)$$

Generator i reports a supply offer $s_i^T(D)$ at the beginning of each day D to the AMES ISO for day $D+1$ aimed at day ahead market. This supply offer is considered as reported marginal cost function.

$$MC_i^R(pG_i) = a_i^R + 2 \cdot b_i^R \cdot pG_i \quad (3)$$

The whole process of the model is listed below as follows:

- On Day 1, each GENCO chooses its supply offer from the action domain and submits to ISO while each LSE submits its demand bids to ISO.

- The ISO solves the DC OPF considering all nodal constraints and thermal limits. At the end of the day, each GENCO calculates its profit based on 24 hourly dispatch volumes and LMPs resulting from market clearing.
- The supply choice probability and the propensity is updated by using reinforcement learning.
- Using action choice probability, GENCO selects the best supply bid for the following day.
- ISO clears the market from the GENCO supply and LSE demand bids thereby solve the DC OPF solution yet again and this process is repeated every day [9].

For the specific interval of 24-hour simulation, consumer has an opportunity to submit offer for demand reductions. Volatility and system marginal price can be modified through demand side bidding price.

IV. RESULTS AND DISCUSSION

For this study in AMES, we used 5 bus system that has the same 24 hourly load profiles and generation cost coefficients for all days of day-ahead market simulation. We programmed in Java language and extended the underlying code of AMES to develop two case studies that separately explored the effects of variation in load demand and fuel price on convergence parameters of learning algorithms. Two parameters are considered namely the average number of days taken by a learning algorithm to converge and the number of simulation runs that converged. In Case Study 1, the load was allowed to vary within $\pm 0\%$, $\pm 1\%$, $\pm 2\%$, $\pm 3\%$, $\pm 4\%$ and $\pm 5\%$ from nominal 24 hourly load profile and convergence results were recorded. In Case Study 2, generation cost coefficients were allowed to vary within $\pm 0\%$, $\pm 1\%$, $\pm 2\%$, $\pm 3\%$, $\pm 4\%$ and $\pm 5\%$ from nominal generation cost coefficients to analyze convergence behavior. Erev Roth learning algorithm starts its learning from a certain seed value. Whenever data of a test case like 5 bus system is loaded in AMES to run a simulation, a GUI opens and comes loaded with the same seed value each time. However, the seed value is editable and can be changed in two ways; it can be manually entered or randomly generated. We investigated convergence behavior in three ways: (i) by using pre-loaded seed value all the time; (ii) selecting a fixed set of 50 random numbers for manual entry; and (iii) randomly generating seed value for each simulation run.

Whenever pre-loaded seed value was used for a particular simulation scenario, simulation results remained the same. However, when seed value was varied within a fixed set and manually entered or randomly generated in GUI, simulation results varied within each simulation scenario. Therefore, such a simulation scenario was run 200 times and all results were recorded. Note that each simulation was allowed to run for a

maximum of 1000 days if the learning algorithm did not converge earlier than 1000 days. Number of days taken by a learning algorithm to converge were averaged over 200 runs and average values are presented as results in this paper.

Case Study 1

In the base case, there is no load variation and all 5 GENCOs use the original Variant Roth Erev Reinforcement learning VRERL provided in the AMES framework. An average number of days specify that the experiment is run on different variations and then the average is taken of sample space. Runs that converge mean how many samples converge on the specified day.

The maximum days to run the simulation is 1000 days to take 200 samples on each point. The result shows that with the same random number, the learning of the GENCO agent with no load change is fixed and there is a slight increase in an average number of days of convergence as the load differs.

Different random numbers are generated and 50 random numbers are selected and run the modified Variant Roth Erev Reinforcement learning algorithm (VRERL) provided in the AMES framework. When the load is changed within a specified limit range, the learning of agents becomes tough and the average number of days to converge is increased. In figure 3-6 shown below, graph x-axis represents the different variation points and the y-axis represents the average number of days at which the learning of agents is converged.

The experiment is performed on the 5-bus system with a randomly chosen random number for 1000 days. Each time generates a new pseudorandom number and runs the experiment. The simulation runs for 200 times on each point of variation. The result shows that with each new random number generation, the learning of the GENCO agent decreases and becomes tough. Similarly, a number of runs in an experiment that converged out of the given sample space is also observed. The straight line indicates that when variation in load is increased with a fixed set of a random number, the learning algorithm converged at the same values. Likewise, randomly chosen number convergence rate decreases in a dynamic environment. This decreasing trend is due to the random environment.

Case Study 2

When fuel price vary and experiment run with the same random number, learning of algorithm doesn't affect thereby an average number of days to converge remains constant.

The experiment is performed on the 5-bus system with a fixed set of random numbers for 1000 days. A fixed set of random number and randomly chosen random number are used to run the modified Variant Roth Erev Reinforcement learning algorithm provided in the AMES framework. When fuel price

is varied within a specified limit, the learning of agents becomes a tough and the average number of days to converge increases. When fuel price variation increases, the rate at which the learning algorithm converges to a specified number of day (1000) decreases.

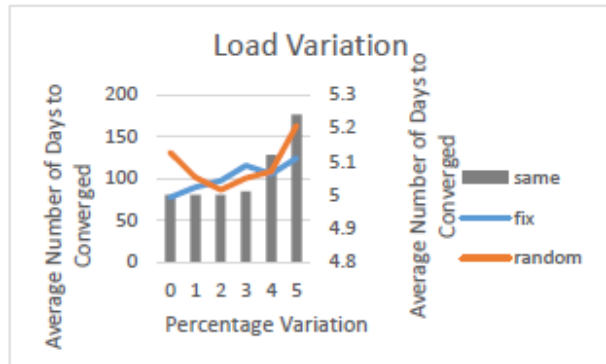


Figure 2 Average Number of Days to Converge in Load Variation

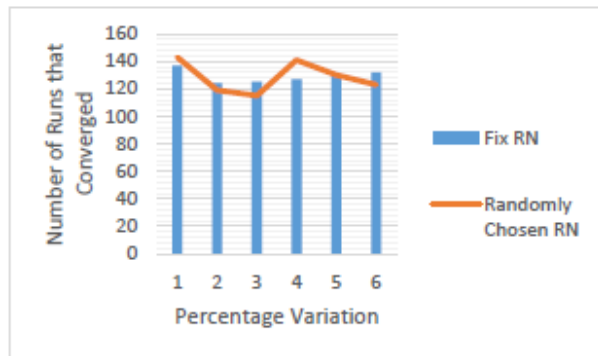


Figure 3 Number of Runs that Converged in Load Variation

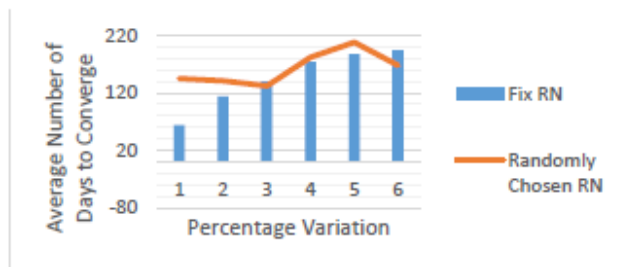


Figure 4 Average Number of Days to Converged in Fuel price Variation

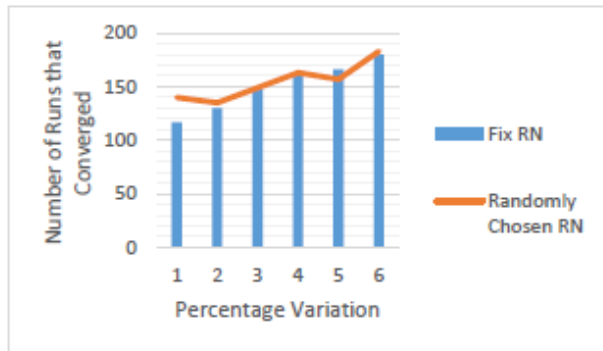


Figure 5 Number of Runs that Converged in Fuel Price Variation

v. Conclusion

The deregulated electricity markets have resulted in distributed decision making among market participants under a dynamic environment. Agent-based modeling and simulation are suitable for analysis of such distributed decision making. Optimal bidding in the day-ahead market by GenCos requires distributed decision making by self-centric GenCo agents who have a chance to learn from results of the day-ahead auction and adjust their bids for the next day. A reactive reinforcement learning algorithm has capabilities to learn the desired behavior of GenCo agents to respond to dynamic conditions of the day-ahead auction. For a fixed 24 hourly load profile of LSEs and constant generation cost coefficients of GenCos in AMES, Erev Roth learning algorithm learns optimal bidding for a GenCo agent and converges successfully. For this study, we explored change in convergence behavior of learning algorithm when market environment was made more dynamic, by introducing stochastic load profiles and variable generation cost coefficients, to model load variability and fuel price changes in the real world. This paper has demonstrated that when variation in load and fuel price increases, learning of GENCO agent becomes tough and gets delayed but the algorithm has convergence stability even under dynamic loads and fuel prices in the market environment.

References

- [1] B. Jie, T. Tsuji, and K. Uchida, "An analysis of market mechanism and bidding strategy for power balancing market mixed by conventional and renewable energy," *Int. Conf. Eur. Energy Mark. EEM*, pp. 1–6, 2017.
- [2] Z. Vale, T. Pinto, I. Praça, and H. Morais, "MASCEM: Electricity markets simulation with strategic agents," *IEEE Intell. Syst.*, vol. 26, no. 2, pp. 9–17, 2011.
- [3] H. Li and L. Tesfatsion, "The AMES wholesale power market test bed: A computational laboratory for research, teaching, and training," *2009 IEEE Power Energy Soc. Gen. Meet. PES '09*, pp. 1–8, 2009.
- [4] M. Sharifi and H. Kebriaei, "A study on pricing strategies for residential load management using fuzzy reinforcement learning," *2015 Int. Conf. Cogn. Comput. Inf. Process.*, pp. 1–6, 2015.
- [5] Z. X. Jing, H. W. Ngan, Y. P. Wang, and Y. Zhang, "Market Simulation."
- [6] F. Kalantzis and N. T. Milonas, "Market integration and price dispersion in the European electricity market," *2010 7th Int. Conf. Eur. Energy Mark. EEM 2010*, pp. 1–6, 2010.
- [7] J. Nicolaisen, V. Petrov, and L. Tesfatsion, "Market power and efficiency in a computational electricity market with discriminatory double-auction pricing," *IEEE Trans. Evol. Comput.*, vol. 5, no. 5, pp. 504–523, 2001.
- [8] B. I. Erev and A. E. Roth, "American Economic Association Predicting How People Play Games: Reinforcement Learning in Experimental Games with Unique, Mixed Strategy Equilibria Author (s): Ido Erev and Alvin E. Roth Source: The American Economic Review, Vol. 88, No. 4 (Sep)," vol. 88, no. 4, pp. 848–881, 2016.
- [9] A. Y. F. Lau, D. Srinivasan, and T. Reindl, "A reinforcement learning algorithm developed to model GenCo strategic bidding behavior in multidimensional and continuous state and action spaces," *IEEE Symp. Adapt. Dyn. Program. Reinf. Learn. ADPRL*, pp. 116–123, 2013.
- [10] N. Chrysanthopoulos and G. P. Papavassilopoulos, "Learning Optimal Strategies in a Stochastic Game With Partial Information Applied To Electricity Markets."

Investigating the wet-chemical growth of CdS quantum-dots on metal-sulfide interfacial layers deposited by ALD

Ijaz Ali^{1,a}, and Muhammad Abdul Basit^{2,b}

¹*Department of Materials Science and Chemical Engineering, Hanyang University, Ansan 15588, Republic of Korea*

²*Department of Materials Science and Engineering, Institute of Space Technology, Islamabad 44000, Pakistan*

Email address: ^aijazalibehar@gmail.com, ^bm.abdulbasit@mail.ist.edu.pk

Abstract—Owing to their unique and tunable optoelectronic characteristics, Quantum-dots (QDs) are considered as the most efficient nanoscale materials for various advanced applications including solar cells. Expansive and technologically complicated photovoltaic devices such as thin film solar cells and/or dye-sensitized solar cells are under-replacement solely due to the evolution of QDs, introducing newer family of solar cells including perovskite and QDs-sensitized solar cells (QDSCs). The technological progress of these devices is so far slow and a lot of optimization is required regarding the optimal deposition and energy harvesting of QDs without detrimental electronic issues of back-transfer of charge carriers and electron-hole recombination. In this work, we have focused the issue of lower energy harvesting in thin films deposited by wet-chemical methods such as successive ionic layer adsorption and reaction (SILAR) by introducing atomic layer deposited (ALD) ZnS, SnS and MoS₂ IL on TiO₂-deposited Si-wafer. The aim was to in-depth analyze the nucleation and growth trend in QDs, considering CdS as a reference material owing to its stability for atomic force microscopic (AFM) examination. It was deduced that all metal-sulfide layers deposited by ALD enhance the deposition of CdS QDs and can prove beneficial for optoelectronic devices incorporating QDs, however their increased deposition is importantly classified in terms of coverage and size of QDs, differently. Considering the results of our study it will be beneficial for optimizing the QDs based devices in general and CdS QDSCs, in particular.

Keywords—*Quantum-dots, SILAR, ALD, nucleation, atomic force microscopy*

Comparative Analysis of Temperature Excursion Hybrid Techniques for Electronic Devices

Tanzeel Ur Rehman^{1,a}, Abid Hussain^{1,b} and Muhammad Mehboob^{1,c}

¹*Department of Mechanical Engineering, University of Engineering and Technology, Taxila*

Email address: ^{a)} tanzeel.ur.rahman@gmail.com , ^{b)} abid.hussain@uettaxila.edu.pk and ^{c)} muhammadmehboob49@yahoo.com

Abstract—Phase Change Materials (PCMs) are becoming popular in thermal management of electronic devices for their safe operation and to prevent premature failure. PCMs have high latent heat of fusion but low thermal conductivity. High latent heat enables them to absorb a large amount of heat from the hot surfaces during their phase transition. In this experimental study, a hybrid thermal management system using copper foam with PCM and forced air convection is designed and tested experimentally. Copper foam and forced air convection is aimed to enhance the thermal conductivity and to improve the temperature uniformity within the PCM. The results are then compared with two other modes of cooling, pure PCM and composite PCM (copper foam along with PCM). Results indicate that addition of air as cooling medium reduces the temperature of the electronic device compared with the other two patterns. The hybrid system appeared to be 25.6% more effective than pure PCM and 15.6% more effective than the composite PCM.

Keywords—Phase Change Materials, hybrid, copper foam, air, temperature

Introduction

A large amount of heat generates in electronic devices during their operation. According to Hetsroni et al. 50-60 °C is the safe temperature limit for electronic

devices [1]. Hosseineizadeh et al. showed that chances of failure become 100% in electronic devices when their temperature goes beyond 10-20 °C [2]. So to dissipate this heat, various active and passive thermal management systems (TMS) are used for their safe operation. The heat transfer medium plays a very important role in the performance of the TMS [3]. Active thermal management systems generally involve forced convection of air or a fluid. Forced air convection is the widely used method because of its reliability, low cost and safe operation [4]. Air, however requires extremely high velocity [5], because of their low thermal conductivity [6]. Passive systems do not involve any supplemental cooling source. An example of passive system is the PCM. PCMs are those materials that absorb and retain a large amount of heat during their phase transition and keep the temperature within the melting range of the PCMs [7][8] and release this heat when their temperature falls below phase change temperature. Pure paraffin, is one of the most effective PCM because of its large latent heat

capacity and low cost. Sharma et al. [9] experimentally proved that paraffin wax is the most stable PCM. However, PCMs have very low thermal conductivity [10]. Due to low thermal conductivity, the thermal management system may fail under extreme conditions when the ambient temperature is high [11]. So highly thermal conductive materials are added into PCM to increase and enhance their thermal conductivity [12][13]. Recent development shows that metallic foams are very efficient in enhancing the thermal conductivity of the PCMs [14][15] due to their large surface area and high porosity. So composites PCMs are prepared using metal foams as their skeleton in which PCM such as paraffin is filled [16][17]. This kind of composite PCM has high thermal conductivity compared with pure paraffin [18].

From the literature review, it appears that under stressful conditions, neither passive nor active thermal management is sufficient to remove the heat from the device [19][20][21]. Ling et al. [21] suggested a mixed TMS that combined PCM with forced air convection. However, studies investigating the combined effect of passive and active cooling have been inadequate.

The current research involves experimental study of a hybrid thermal management system consisting of a composite PCM combined with force air convection. The effectiveness of the system was proved experimentally with other modes of cooling.

Experimental setup

Experimental setup consists of a cavity, an electric heater, copper metal foam, PCM, a variable speed electric fan, k-type

thermocouples, data acquisition system (DAQ) and a laptop with necessary software installed.

The cavity used in this experiment has inner dimensions of 102 x 102 x 30 mm and was made from a 3 mm thick plexiglass sheet to only allow one dimensional heat transfer. To allow natural and forced air convection, the cavity was open from the top. The cavity was made slightly larger (2 mm) from inside than the size of the electric heater. This allows easy installation and removal of electric heater and metal foam and also makes space for electric wires.

A flexible square-type silicone rubber fiberglass insulated heater was used to represent an electronic device and is a source of heat for the experiment. The heater has dimensions of 100 x 100 x 1.5 mm. The heater was placed inside the bottom of the cavity during the experiment.

PCM (paraffin wax), having melting temperature between 39 to 41 °C and thermal conductivity of 0.2 W/m.K was used to absorb the heat from the electric heater. Copper foam having dimensions of 100 x 100 x 20 mm and thermal conductivity of 398 W/m.K was used to enhance the thermal conductivity of the paraffin. The composite PCM was prepared by pouring the molten paraffin into the copper foam.

Electric fan made by Foxconn having size 100 x 100 mm was used for the forced air-convection to enhance the rate of heat transfer from the composite PCM.

Maximum input voltages for the fan are 12 volts and it was operated at the same voltage. The fan was suspended one inches above the plexiglass to allow easy passage for the air.

A k-type thermocouple having temperature sensitivity between $-50\text{ }^{\circ}\text{C}$ to $1350\text{ }^{\circ}\text{C}$ was placed at the center and at a depth of 10 mm inside the Copper foam and Composite PCM to measure the temperature.

A variable voltage power supply was used to power both, the electric heater and the fan.

The data acquisition system made by “National Instruments” was used to record the temperature inside the composite PCM at equal intervals of time.

A laptop with installed necessary softwares for the DAQ system was attached to the DAQ via a USB cable.

The experimental setup is shown in the figure.

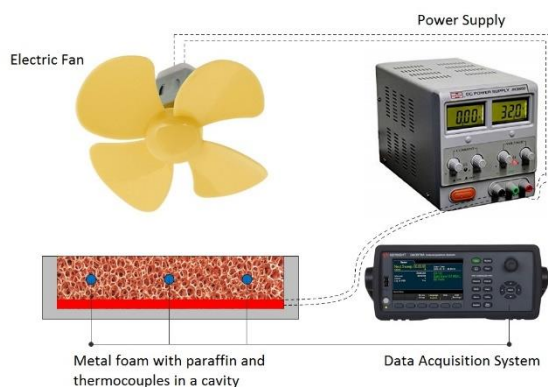


Fig. 1. Experimental setup

Results and Discussion

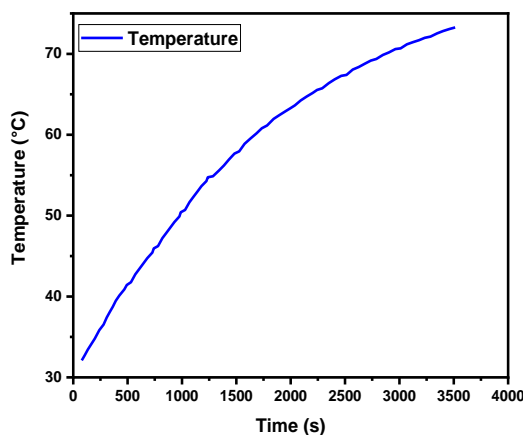


Fig. 2. Temperature, without any thermal management system

The above graph is for electric heater without any thermal management system. The graph shows that the temperature increases rapidly and in a very short time interval of approximately 3200 seconds (53.3 min.) reaches $72\text{ }^{\circ}\text{C}$ which is not a very safe temperature for operating electronic devices. We also see that it took approximately 480 seconds (8 minutes) for the electric heater to reach a temperature of $41\text{ }^{\circ}\text{C}$ which is temperature where the phase transition of the pure PCM ends.

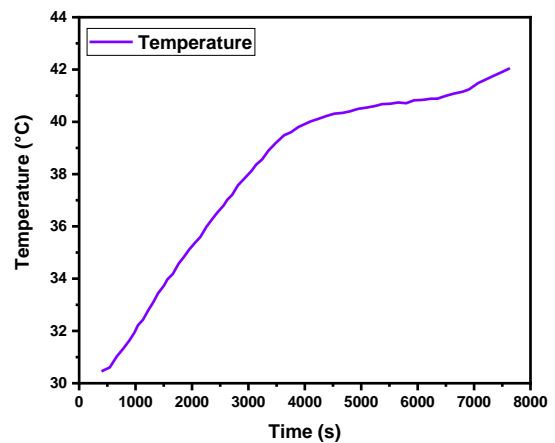


Fig. 3. Temperature variation of pure paraffin

The above temperature graph which is for pure paraffin, reveals that it took approximately 3400 seconds (56.6 min.) for pure paraffin to reach a temperature of $39\text{ }^{\circ}\text{C}$ where melting of PCM starts and took 3200 seconds (53.3 min.) to complete the melting phase and to reach $41\text{ }^{\circ}\text{C}$ where the melting or transition phase completes. The total time to reach $41\text{ }^{\circ}\text{C}$ was 6645 seconds (110.75 min). Compared with no thermal management system, pure paraffin absorbed a large amount of heat and appeared 1280% more efficient.

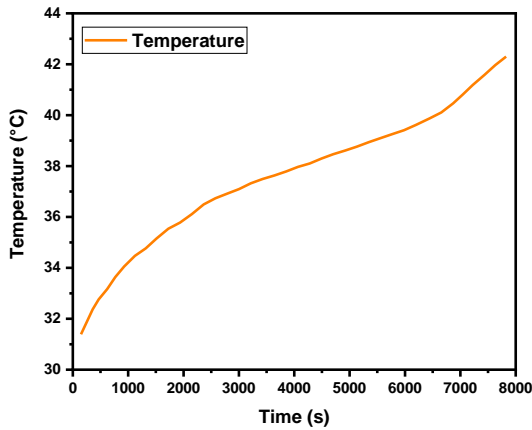


Fig. 4. Temperature variation of composite PCM

The above temperature profile is for composite PCM consisting of Copper foam and pure paraffin. From the graph we conclude that it took approximately 5500 seconds (91.6 min.) for the composite PCM to reach the saturation temperature of 39 °C and 7223 seconds (120.38 min) to reach a temperature of 41 °C. The composite PCM performed 9% better than the pure PCM in reaching a temperature of 41 °C. This increase in efficiency was due to the increase in the thermal conductivity of the PCM with the addition of copper foam.

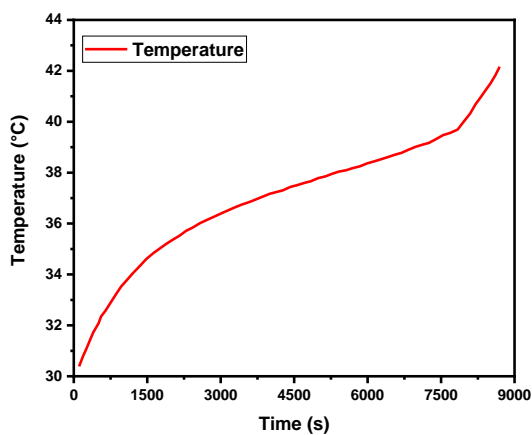


Fig. 5. Temperature variation of hybrid thermal management system

The above graph is for the hybrid thermal management system consisting of a fan and a composite PCM. From the graph we

conclude that it took approximately 6900 seconds (115 min.) for the proposed thermal management system to reach the saturation temperature of 39 °C and 8350 seconds (139.16 min) to reach 41 °C. By drawing a comparison between the three thermal management systems to reach a temperature of 41 °C, the hybrid system appears to be 25.6% more efficient than pure paraffin and 15.6% more efficient than composite PCM.

Conclusion

- The purpose of this experimental study was to compare the effectiveness of active and passive thermal management systems.
- From the graphs and discussion above, we conclude that without any thermal management system, the temperature of electronic device will rise beyond acceptable limits which will ultimately result in the failure of the device. On the other hand pure paraffin, due to its low thermal conductivity, loses its effectiveness earlier than composite PCM.
- With the addition of copper foam in pure paraffin, the thermal conductivity of paraffin increases and composite PCM appears 9% better than pure paraffin. While comparing the hybrid thermal management system with air as cooling medium, we see a 25.6% and 15.6% increase in efficiency respectively, compared with pure paraffin and composite PCM. So we conclude with the addition of air, the hybrid thermal management system performed better compared with the other passive systems mentioned here.

REFERENCES

- [1] G. Hetsroni, A. Mosyak, Z. Segal, and G. Ziskind, "A uniform temperature heat sink for cooling of electronic devices," *Int. J. Heat Mass Transf.*, vol. 45, no. 16, pp. 3275–3286, 2002, doi: 10.1016/S0017-9310(02)00048-0.
- [2] S. F. Hosseinizadeh, F. L. Tan, and S. M. Moosania, "Experimental and numerical studies on performance of PCM-based heat sink with different configurations of internal fins," *Appl. Therm. Eng.*, vol. 31, no. 17–18, pp. 3827–3838, 2011, doi: 10.1016/j.applthermaleng.2011.07.031.
- [3] A. Pesaran, "Battery Thermal Management in EVs and HEVs : Issues and Solutions," *Adv. Automot. Batter. Conf.*, p. 10, 2001.
- [4] T. Wang, K. J. Tseng, and J. Zhao, "Development of efficient air-cooling strategies for lithium-ion battery module based on empirical heat source model," *Appl. Therm. Eng.*, vol. 90, pp. 521–529, 2015, doi: 10.1016/j.applthermaleng.2015.07.033.
- [5] H. Park, "A design of air flow configuration for cooling lithium ion battery in hybrid electric vehicles," *J. Power Sources*, vol. 239, pp. 30–36, 2013, doi: 10.1016/j.jpowsour.2013.03.102.
- [6] R. T. Jacobsen and E. W. Lemmon, "Viscosity and Thermal Conductivity Equations for Nitrogen, Oxygen, Argon, and Air," *Int. J. Thermophys.*, vol. 25, no. 1, pp. 21–69, 2004.
- [7] S. A. Khateeb, M. M. Farid, J. R. Selman, and S. Al-Hallaj, "Design and simulation of a lithium-ion battery with a phase change material thermal management system for an electric scooter," *J. Power Sources*, vol. 128, no. 2, pp. 292–307, 2004, doi: 10.1016/j.jpowsour.2003.09.070.
- [8] S. Al-Hallaj and J. R. Selman, "Thermal modeling of secondary lithium batteries for electric vehicle/hybrid electric vehicle applications," *J. Power Sources*, vol. 110, no. 2, pp. 341–348, 2002, doi: 10.1016/S0378-7753(02)00196-9.
- [9] A. Sharma, S. D. Sharma, and D. Buddhi, "Accelerated thermal cycle test of acetamide, stearic acid and paraffin wax for solar thermal latent heat storage applications," *Energy Convers. Manag.*, vol. 43, no. 14, pp. 1923–1930, 2002, doi: 10.1016/S0196-8904(01)00131-5.
- [10] Z. Rao and S. Wang, "A review of power battery thermal energy management," *Renew. Sustain. Energy Rev.*, vol. 15, no. 9, pp. 4554–4571, 2011, doi: 10.1016/j.rser.2011.07.096.
- [11] R. Kizilel, A. Lateef, R. Sabbah, M. M. Farid, J. R. Selman, and S. Al-Hallaj, "Passive control of temperature excursion and uniformity in high-energy Li-ion battery packs at high current and ambient temperature," *J. Power Sources*, vol. 183, no. 1, pp. 370–375, 2008, doi: 10.1016/j.jpowsour.2008.04.050.
- [12] H. T. Cui, "Experimental investigation on the heat charging process by paraffin filled with high porosity copper

- foam,” *Appl. Therm. Eng.*, vol. 39, pp. 26–28, 2012, doi: 10.1016/j.applthermaleng.2012.01.037.
- [13] A. Sari and A. Karaipekli, “Thermal conductivity and latent heat thermal energy storage characteristics of paraffin/expanded graphite composite as phase change material,” *Appl. Therm. Eng.*, vol. 27, no. 8–9, pp. 1271–1277, 2007, doi: 10.1016/j.applthermaleng.2006.11.004.
- [14] S. A. Khateeb, S. Amiruddin, M. Farid, J. R. Selman, and S. Al-Hallaj, “Thermal management of Li-ion battery with phase change material for electric scooters: Experimental validation,” *J. Power Sources*, vol. 142, no. 1–2, pp. 345–353, 2005, doi: 10.1016/j.jpowsour.2004.09.033.
- [15] W. Q. Li, Z. G. Qu, Y. L. He, and Y. B. Tao, “Experimental study of a passive thermal management system for high-powered lithium ion batteries using porous metal foam saturated with phase change materials,” *J. Power Sources*, vol. 255, pp. 9–15, 2014, doi: 10.1016/j.jpowsour.2014.01.006.
- [16] A. Bhattacharya, V. V. Calmidi, and R. L. Mahajan, “Thermophysical properties of high porosity metal foams,” *Int. J. Heat Mass Transf.*, vol. 45, no. 5, pp. 1017–1031, 2002, doi: 10.1016/S0017-9310(01)00220-4.
- [17] R. Baby and C. Balaji, “Experimental investigations on thermal performance enhancement and effect of orientation on porous matrix filled PCM based heat sink,” *Int. Commun. Heat Mass Transf.*, vol. 46, pp. 27–30, 2013, doi: 10.1016/j.icheatmasstransfer.2013.05.018.
- [18] Z. Chen, D. Gao, and J. Shi, “Experimental and numerical study on melting of phase change materials in metal foams at pore scale,” *Int. J. Heat Mass Transf.*, vol. 72, pp. 646–655, 2014, doi: 10.1016/j.ijheatmasstransfer.2014.01.003.
- [19] Z. Rao, S. Wang, and G. Zhang, “Simulation and experiment of thermal energy management with phase change material for ageing LiFePO₄ power battery,” *Energy Convers. Manag.*, vol. 52, no. 12, pp. 3408–3414, 2011, doi: 10.1016/j.enconman.2011.07.009.
- [20] R. Sabbah, R. Kizilel, and J. R. Selman, “Active (air-cooled) vs . passive (phase change material) thermal management of high power lithium-ion packs : Limitation of temperature rise and uniformity of temperature distribution,” vol. 182, pp. 630–638, 2008, doi: 10.1016/j.jpowsour.2008.03.082.
- [21] Z. Ling, F. Wang, X. Fang, X. Gao, and Z. Zhang, “A hybrid thermal management system for lithium ion batteries combining phase change materials with forced-air cooling,” *Appl. Energy*, vol. 148, pp. 403–409, 2015, doi: 10.1016/j.apenergy.2015.03.080.
- [82]

Effects of Combined Use of Metakaolin, Silica fume and Coconut Fibers on Different Properties of Cement Composite

Mian Syed Nawab^{1,a} and Muhammad Yaqub^{2,b}

¹*M.Sc Scholar, Civil Engineering Department, University of Engineering and Technology, Taxila
(47050) Pakistan*

²*Professor, Civil Engineering Department, University of Engineering and Technology, Taxila
(47050) Pakistan*

Email address: ^{a)} engrsyed555@gmail.com ^{b)} muhammad.yaqub@uettaxila.edu.pk

Abstract—This research work presents the effects of combined use of metakaolin, silica fume and coconut fibers on different properties of cement mortar composites. The proportion of 0.8:0.2:1 (Cement: Pozzolans: Sand) was kept fixed with water to binding materials ratio varies from 0.35 to 0.60 depending on the coconut fibers content to fulfil the need of workability requirements. In this study total 180 specimens of various sizes were casted in two different phases, in phase-I, 54 specimens each nine specimens of the same percentage of 20% cement replaced with silica fume and metakaolin were casted for maximum compressive strength to get optimum value for metakaolin and silica fume combination. In phase-II, further 126 fibers reinforced mortars specimens were casted with optimum value of metakaolin and silica fume obtained in phase-I with varying content of coconut fibers 0%, 3%,6%,9%,12% and 15% by weight of binder and replacing the composition of sand. The samples were then investigated for compressive strength, modulus of rupture (MOR), water absorbing capacity and moisture content at 7day, 14day and 28day curing age.

Keywords— metakaolin, silica fume, coconut fibers, compressive strength, flexural strength, water absorption and moisture content.

I. INTRODUCTION

Cement mortar composite is one of the most versatile construction material and has wide application in plastering, masonry work, repairing of damaged concrete structures, filling or patching, floor leveling, rendering and also in the development of precast structures and products. It is much important to achieve high performance cement composite for utilization in many applications, like for concrete repair instantly, pavements, flooring, roof treatment, high compressive strength precast structures and rehabilitation applications. Metakolin has been proved to be effective in improving

both early and also long term mechanical and physical properties of the composite cement paste and concrete, a replacement range of 10 to 15% metakaolin has showed very effective results in this regard [1]. The value of compressive strength of composite increases varying in the range between 20 to 30% with 5-15% cement replacement by silica-fume [2]. Artificial and natural fibers were used for reinforcing the matrix to improve the toughness, ductility, flexural strength, resistance to fatigue and impact resisting nature. Natural fibers are cheaper, renewable, abundantly available and show very little health concern during processing and handling [3]. Among all natural fibers because of highest toughness, low water absorption and abundantly availability as an agricultural waste, the use of coconut fiber as a reinforcement in low cost structure is of great interest from last few decades. Metakaolin has positive impacts while silica fume has negative impacts on the workability but their co-addition of metakaolin and silica fume can reduce the negative impact of silica fume, secondly

concerning strength, metakaolin and silica fume both have positive impacts, but the combination of silica fume and metakaolin has the significant impacts which improves the strength more than the rise in strength due to sole incorporation of metakaolin or silica fume [4]. This research was aimed to investigate the impacts of combined addition of metakaolin and silica fume as a replacement of some proportion of cement and natural coconut coir fibers as reinforcement for the composite cement.

II. EXPERIMENTAL PROGRAMME

A. *Materials and preparation of samples*

Ordinary Portland Cement (Dewan brand), local coarse river sand, local natural coconut fibers, metakaolin, silica fume and water reducing agent were used in casting of samples. The proportion 0.8:0.2:1 (cement: pozzolans: sand) was kept fixed with water to binder ratio varies from 0.35 to 0.60 depending on the coconut fibers content and to fulfil the need of workability requirements. Admixture Ultra 235 is used at the rate of 0.7% by weight of the cementitious materials. Samples were prepared in two phases, In phase-I plain cement mortar samples each nine samples of the same percentage of cement replacement with silica fume (SF) and metakaolin (MK) were casted for each of the six combination 0% SF-0% MK, 20% SF-0% MK, 0% SF-20% MK, 10% SF 10%MK, 5% SF 15% MK, 15% SF-5% MK to obtain optimum combination in term of compressive strength. In phase two, fibers reinforced cement mortar samples were casted with optimum value of silica fume and metakaolin combination obtained in phase-I and with varying content of coconut fibers 0%, 3%, 6%, 9%, 12% and 15%.to test for physical and mechanical properties, proportions of cement mortar composites are presented in Table 1. All the ingredients are measured by mass. The increase in water to cementitious materials ratio in fibers reinforced mortar mix is done to cover the additional water required by the coconut fibers in the mortar mix.. For preparation of coconut fibers reinforced mix, all the ingredients of the composite were placed in the mixer pan in three layers. In first layer, fine aggregates were placed in the mixer pan, then fiber were dispersed above them manually, followed by cement and

finally pozzolans were added. This same procedure of laying was repeated for second and third layer. The mixer was run for three and half minutes. Then about one 3rd portion of the total water required for the mixture was added to the mixture, and the concrete mixer machine was run for three and half minutes again. The mixing process was observed carefully to avoid balling of coconut fibers and segregation of mortar ingredients. All the samples were poured into molds in three properly compacted layers. After a period of 24 hours take the specimens from molds and put them for curing in water tank immediately.

TABLE I. SAMPLE PROPORTIONS

<i>Sample No.</i>	<i>Water to binder ratio</i>	<i>Fiber content (%)</i>
1	0.35	0
2	0.40	3
3	0.45	6
4	0.50	9
5	0.55	12
6	0.60	15

B. Testing Procedures

The casted specimens were carefully handled to be safe from any damage which could affect the results. Compression test on the samples was performed by Universal testing machine (UTM) with the rate of loading 1.8KN/s. The size of sample used for compressive strength test is 160 mm x 40 mm x 40 mm. MOR (Modulus of rupture) tests were conducted on the sample size of 400 mm x 100 mm x 16 mm strip beam. The strip was supported on both ends and load is applied on its one over third of its span length (3rd point loading flexural test) up to the failure loading. The flexural strength or MOR is then calculated. The size of specimen used for water absorption test and moisture content test is same which is 100 mm x 100 mm x 40 mm. To calculate the moisture content of composite, composites were placed in an oven at 100°C temperature for 24 hours and then the change samples weight before and after samples were placed in an oven was measured. For determination of water absorption, composite were placed in water for 24 hours and then the change in weight of samples before and after watering was noted. All tests mechanisms have complied according to BS 5669 Part 1: 1989.

III. RESULTS AND DISCUSSION

A. Compressive strength of plain cement composite

The compressive strengths of plain cement composites were determined at 7day, 14day and 28day and the results are presented in Fig.1. It was observed that among all the mortar composites, the composite cement with 10% silica fume and 10% metakaolin gives the highest values of compressive strength at 7day, 14day and 28day, the value of compressive strength at 7 days is 59.2Mpa at 14 days is 67.8Mpa and at 28 days is 75.3Mpa. It was indicated from the results that 10% silica fume and 10% metakaolin combination give better results than pure use of either 20% silica fume or 20% metakaoline. From the comparision with controlled samples we found that this optimum combination increase the 7 days compressive strength by 13.6 %, 14 day strength by 20.4% and 28 days strength by 28.3%.

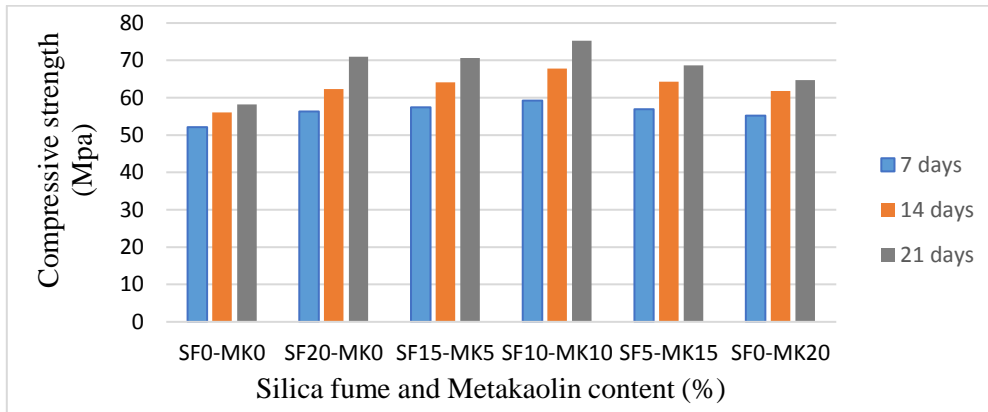


Fig.1. Compressive strength for different Silica fume (SF) and Metakaolin (MK) combination

B. Compressive strength of coconut fiber reinforced composite

The behaviors of the composite having optimum value of metakaolin and silica fume combination obtained in phase-I reinforced with different proportion of coconut fibers is determined by compression test at 7day,14day and 28day, all the results are presented here in Fig.2.

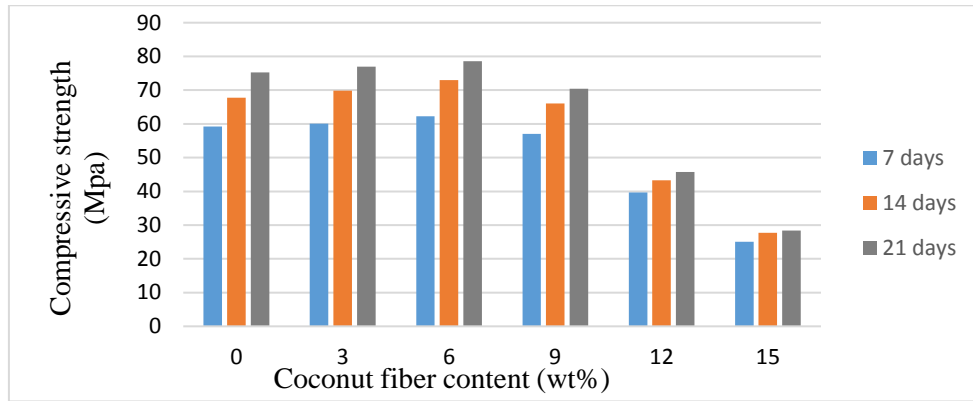


Fig.2 Comparison of compressive strength for different percentage of coconut fiber content

It was observed from the results that among all the coir reinforced cement composites, the mortar fibers reinforced specimens having 6% fibers content shows the highest value of compressive strength at all the three ages 7day, 14day and 28day which are 62.3Mpa, 73Mpa and 78.6Mpa respectively. After 6% content of coconut fibers the results obtained at 9% , 12% and 15% decreases significantly and the lowest values of compressive strength results at all the three ages are obtained at 15% coconut fiber content which are 25.1Mpa, 27.1Mpa and 28.4Mpa at 7, 14 and 28day respectively. The values of compressive strength obtained here are showing similar trend to the work of Alida [5].

C. Modulus of rupture (MOR)

Modulus of rupture (MOR) results are obtained at 7day, 14day and 28day which are presented here in Fig.3. The highest value of 16.7MPa obtained from the mortar specimens having 6% fibers content and at 28 day curing age. From all results obtained after 7, 14 and 28 days curing duration, it is found that modulus of rupture of composite increased with rise in percentage of fibers content. However after 6% content further addition of fibers decreased the flexural strength of the specimens. The reason is that at low content of fibers with uniform distribution has ability to bridge the micro structure of cracks significantly and also produced fibers balling effects so leads to good cracks arrest in the cement mortar specimen [6-8]. However, the use of natural coir fibers above 6 % leads to coir fibers agglomeration so result in strength reduction.

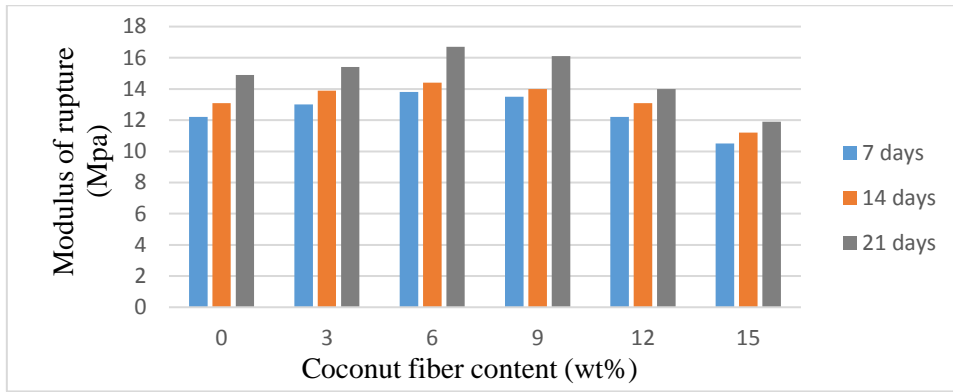


Fig.3. Comparison of modulus of rupture for different percentage of coconut fiber content

D. Moisture content of mortar composites

Moisture content values for all mortar specimens at 7day, 14day and 28day curing durations are determined and are presented in Fig.4

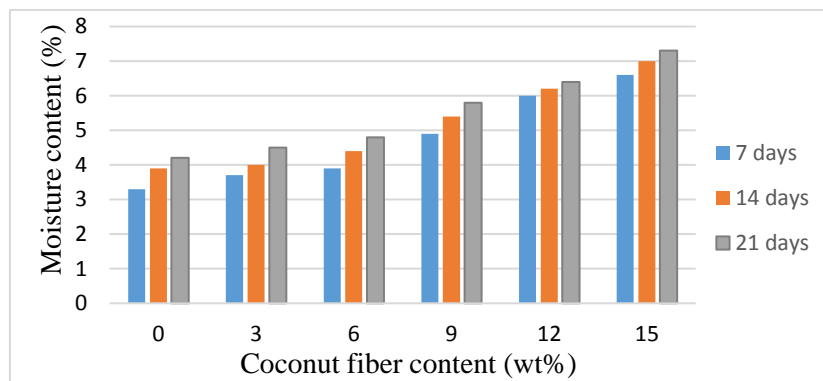


Fig.4. Comparison of moisture content for different percentage of coconut fiber content

From graphical representation, it was noted that the cement mortar specimens with 15% fibers content after curing age of 28 days gives 7.7% moisture content value which is the highest among all specimens and the lowest value is 3.3 % which is corresponding to control composites at 7 day of curing age.

It was noted from the graph that for less percentage of fiber content from 0 to 6% the moisture content increases gradually at a slower rate but after 6% there is a sudden rise in the moisture content of the composites.

E. Water absorption of mortar composites

The 7day, 14day and 28day water absorption results are determined and presented in Fig.5, It was noted that the water absorption capacity of composites increases with increases in coconut fibers content and also noted that the capacity of absorbing decreases with curing age. The cement mortar specimens reinforced with 15% fiber content have the highest value which is 4.5% whereas the reference sample having no coconut fiber indicated the lowest value which is 0.76%. Cement composites produced by using high fibers content showed the high value of water absorption which attributed to fall in the composites density and so resulted in higher rate of porosity of the mortar [9].

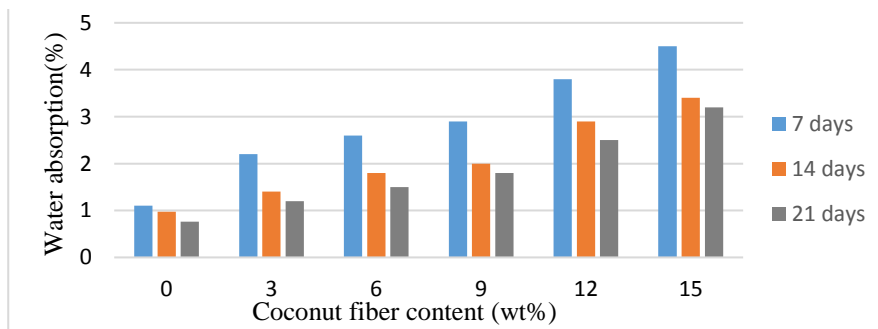


Fig.5. Comparison of water absorption for different percentage of coconut fiber content

IV. CONCLUSION

This experimental study is carried out to analyze the behaviors of the cement composite having 20% cement replaced by silica fume and metakaolin reinforced with a range of different proportion of natural coconut fibers. 54 specimens were casted and tested in phase 1 to get optimum value of silica fume and metakaolin combination in term of compressive strength of cement mortar, Then in phase 2 comparative study was undertaken considering various parameters of the cement mortar reinforced with a range of coconut fibers to get the optimum value of fibers content. Based on test results presented in this research work, the following important conclusions may be drawn:

- The optimum value for silica fume and metakaolin combination for compressive strength of the plain mortar composites is 10%SF and 10MK which give highest compressive strength (75.3Mpa) among all the six combinations (0SF-0MK, 20SF-0MK, 15SF-5MK, 10SF-10MK, 5SF-15MK and 0SF-20MK) of metakaolin and silica fume for 20% cement replacement.
- In case of natural coconut fiber reinforcement cement composite, It was found that 6% coconut fiber content give better results among all the six combinations (0%, 3%, 6%, 9%,12% and 15%) in term of compressive strength(78.6Mpa) and Modulus of rupture(16.7Mpa).
- Reference sample shows lowest moisture content value which is 3.3% addition of fiber increases the moisture content gradually for low content 51 up to 6% and after that the rise in moisture content is rapid and give highest value at 15% fiber content.
- .Reference sample show lowest water absorption of 0.76 % compared to coconut fibers reinforced composites and increase with increase in fibers content, it was observed that water absorption capacity of composites decreases with curing age of the specimens.

REFERENCES

- [1] K.Z. Farhan and W.A. Gul, "Impact of Metakaolin on Cement Mortar and Concrete": A Review. International Journal of Civil Engineering and Technology, 8(4), 2017, pp. 2157–2172
- [2] Harjinder Singh, Shikha, Bansal," Effect of Silica fume on the strength of cement mortar" : International Journal of Research in Engineering and Technology 2015
- [3] Zulkifli, R., M.J. Mohd Nor, A.R. Ismail, M.Z. Nuawi, S. Abdullah, M.F. Mat Tahir and M.N. Ab. Rahman, 2009. Comparison of Acoustic Properties between Coir Fiber and Oil Palm Fiber, European Journal of Scientific Research, 33(1): 144-152
- [4] S.H. Chu, A.K.H. Kwan, "Co-addition of metakaolin and silica fume in mortar: effects and advantages": Construction and Building Materials 197 (2019) 716-724 1228.
- [5] A .Alida, J. B. Shamsul, M. N. Mazlee, H. Kamarudin "Composite Cement Reinforced Coconut Fiber: Physical and Mechanical Properties and Fracture Behavior": Australian Journal of Basic and Applied Sciences (2011), p. 1228.
- [6] J. L. Pehanich, P. R. Blankenhorn, and M. R. Silsbee: Cement Concrete Research (2004), p. 59.
- [7] G. Ramakrishna & T. Sundarajan: Cement and Concrete Composites Vol. 27 (2005), p. 547.
- [8] W. H. Zhu, B. C. Tobias, R. S. P. Coutts, & G. Langfors: Cement and Concrete Composites

Vol.16 (1994), p.3

[9] A. Ashori, T. Tabarsa & S. Sepahvand: Construction and Building Materials, Vol.26 (2012), p.131.

Paper Title Investigating the wet-chemical growth of CdS quantum-dots on metal-sulfide interfacial layers deposited by ALD

Ijaz Ali^{1,a}, Tae Joo Park^{2,b} and Muhammad Abdul Basit^{3,c}

¹ Department of Materials Science and Chemical Engineering, Hanyang University, Ansan 15588, Republic of Korea

² Department of Materials Science and Engineering, Institute of Space Technology, Islamabad 44000, Pakistan

Email address: ^{a)} ijazalibehar@gmail.com , ^{b)} tjp@hanyang.ac.kr and ^{c)} m.abdulbasit@mail.ist.edu.pk

Abstract—Owing to their unique and tunable optoelectronic characteristics, Quantum-dots (QDs) are considered as the most efficient nanoscale materials for various advanced applications including solar cells. Expansive and technologically complicated photovoltaic devices such as thin film solar cells and/or dye-sensitized solar cells are under-replacement solely due to the evolution of QDs, introducing newer family of solar cells including perovskite and QDs-sensitized solar cells (QDSCs). The technological progress of these devices is so far slow and a lot of optimization is required regarding the optimal deposition and energy harvesting of QDs without detrimental electronic issues of back-transfer of charge carriers and electron-hole recombination. In this work, we have focused the issue of lower energy harvesting in thin films deposited by wet-chemical methods such as successive ionic layer adsorption and reaction (SILAR) by introducing atomic layer deposited (ALD) ZnS, SnS and MoS₂ IL on TiO₂-deposited Si-wafer. The aim was to in-depth analyze the nucleation and growth trend in QDs, considering CdS as a reference material owing to its stability for atomic force microscopic (AFM) examination. It was deduced that all metal-sulfide layers deposited by ALD enhance the deposition of CdS QDs and can prove beneficial for optoelectronic devices incorporating QDs, however their increased deposition is importantly classified in terms of coverage and size of QDs, differently. Considering the results of our will be beneficial for optimizing the QDs based devices in general and CdS QDSCs, in particular.

Keywords—Quantum-dots, SILAR, ALD, nucleation, atomic force microscopy

Introduction

ALD is an outstanding thin film deposition techniques owing to its unique set of characteristics comprising of sub-nanoscale thickness control [1]. Conventionally, oxide based materials such as Al₂O₃, SiO₂, HfO₂, TiO₂ and ZnO etc. were deposited using ALD [2]–[4]. Later on, metal sulfides were also tested for development and application of ALD films in various technological fields [5]. Importantly, Dasgupta et al. [6] extended the applications of ALD by depositing PbS based QDs directly. It is to highlight here that it had been very challenging to replace the oxygen based anionic precursors (i.e., O₂, H₂O or ozone) with sulphur-based precursors H₂S. ALD deposition of metal-sulfides of any compositional kind is associated with deterioration of precursor channels and contamination of gas lines inside the ALD equipment. Overcoming these

challenges, researchers soon managed to deposit CuInS₂ [7] absorbing layer for solar cells by ALD, which avowed the potential of ALD for deposition of metal-sulfide based films as well. With the evolution of metal-sulfides deposition, ALD became more influential in the technological application of solar cells, particularly QDSCs [6], [8], [9]. Since QDSCs have great potential to meet the modern day energy crisis by offering low-cost and facile development of solar cells, there is a need to uplift its performance in terms of power conversion efficiency (PCE) which is still lower than commercialized Si-based and thin film based solar cells [10]. One of the way to enhance the performance of solar cells (particularly QDSCs) is to enhance the deposition of absorbing materials so that maximum energy is absorbed from incident light and there is no waste of energy in the form of reflected and/or transmitted light.

To realize such kind of higher deposition of QDs is still under investigation for QDSCs, as QDSCs mainly have mesoporous TiO₂ network [8], [11], [12]. Therefore, the deposition of QDs inside and/or over a substrate need to be explored so that the enhancements strategies are revealed in more effectual way. In this work, we have attempted the deposition of CdS over ZnS, SnS and MoS₂ ALD films and exposed their role for the nucleation and growth of CdS QDs. It was deduced that increase in the deposition of QDs is not always useful as it may have detrimental increase in their size instead of covering more and more surface of the substrate. Energy dispersive spectroscopy (EDS) couples with atomic force microscope (AFM) was used to outline the dynamics of QDs growth over ZnS, SnS and MoS₂.

Materials and Methods

Atomic layer deposition of ZnS, SnS and MoS₂

Atomic layer deposition of all films was carried out on a TiO₂-coated Si-substrate [13]. The idea behind the substrate selection was to provide a similar surface (though planar) for secondary deposition of QDs as in QDSCs. The development of such analogous surface was carried out in accordance with previous reports [10]. Diethyl zinc (DEZ) and H₂S; Tetrakis(dimethylamino) Tin (TDMASn, Sn[N(CH₃)₂]₄) and H₂S, and Mo(NMe₂)₄ and H₂S were respectively used for the deposition of ZnS, SnS and MoS₂ by using ALD of traveling-wave type (CN-1 Co.). Further details of ALD process can be obtained from references [13].

Wet-chemical deposition of CdS QDs

CdS QDs were deposited on TiO₂-deposited Si-substrates without (considered as reference sample in this study) and with (either ZnS or SnS or MoS₂) ALD film via SILAR process [10], [12]. Briefly, all substrates were first immersed in 0.05 M solution of Cd(NO₃)₂ in water for 1 min (for the adsorption of Cd-ions on the surface of substrates). Then the poorly attached Cd-ions were washed away using water, leaving behind strongly attached Cd-ions. During the second main step of SILAR, each substrate film was separately introduced to an aqueous solution of 0.05 M Na₂S so that S-ions react with pre-adsorbed Cd-ions, forming individual CdS QDs. The substrates were washed again. The same process was repeated for five times and resultant samples were analyzed further. MIRA 3-TESCAN modelled scanning electron microscope (FESEM) available at Institute of Space Technology (IST) Islamabad, Pakistan was used for high-magnification imaging and statistical estimation of composition using energy dispersive spectrometry (EDS, Horbia). Flex-AFM of IST was utilized to record the deposition characteristics of CdS QDs for each sample.

Results and Discussion

Fig. 1 shows the 3-dimensional atomic force microscopic outlook of TiO₂-deposited Si-substrates after the deposition of CdS QDs via SILAR. It can be seen in Fig. 1a that the reference sample without any interfacial layer (w/o IL) produced larger grains of QDs as compared to ZnS IL (Fig. 1b). While

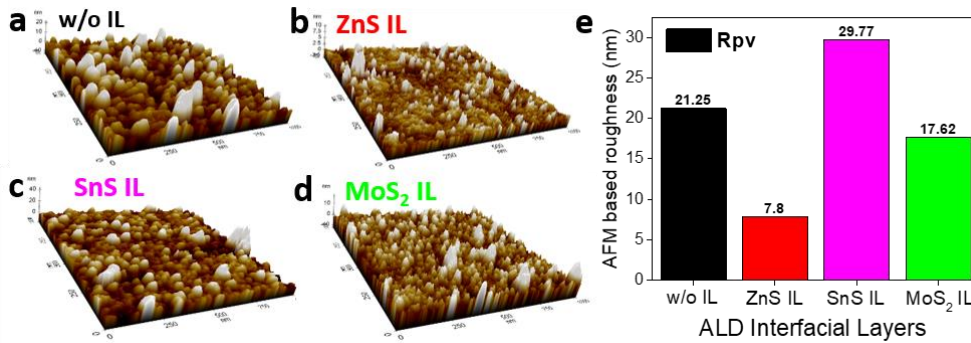


Figure 29. Atomic force microscopic analysis of CdS-quantum dots deposition on TiO₂ deposited Si-substrate (a) without and with (b) ZnS, (c) SnS and (d) MoS₂ interfacial layers. (e) Corresponding peak to valley roughness (R_{pv}) values

SnS IL produced the even thicker CdS layer (Fig. 1c), which is evident from its scale bar along Y-axis that is extended to 40 nm from 20 nm for reference sample. It means that much higher deposition of CdS occurred due to the presence of the SnS on TiO₂-deposited Si-substrate, even higher than that for ZnS IL. Contrarily, MoS₂ showed a number of small QDs over its surface which again means higher deposition of CdS, however the scale bar at Y-axis this time remained lower (Fig. 1d). This was why the AFM based roughness value associated with MoS₂ IL remained even lower than w/o IL sample. It is important to clear at this point that there are two possible routes for the increase in the deposition of CdS over surface. i.e., (1) In the horizontal direction, which is termed as coverage from here onwards [12]-[14]. (2) In the vertical directions, which is termed as growth from here onward. It is easy to understand that the coverage of the CdS QDs on any IL is associated with its nucleation directly, while growth is the secondary phenomena which preferably occurs on pre-existing nuclei. Assuming that ILs provide nucleation sites or preferred surface for CdS to grow, we can easily see that there was a contrasting behavior between all the ILs. CdS QDs with high coverage but low growth were produced in case of ZnS and MoS₂ IL, while SnS IL offered high growth with least nucleation which is evident from roughness values of ZnS (7.8 nm), SnS (29.77) and MoS₂ (17.62).

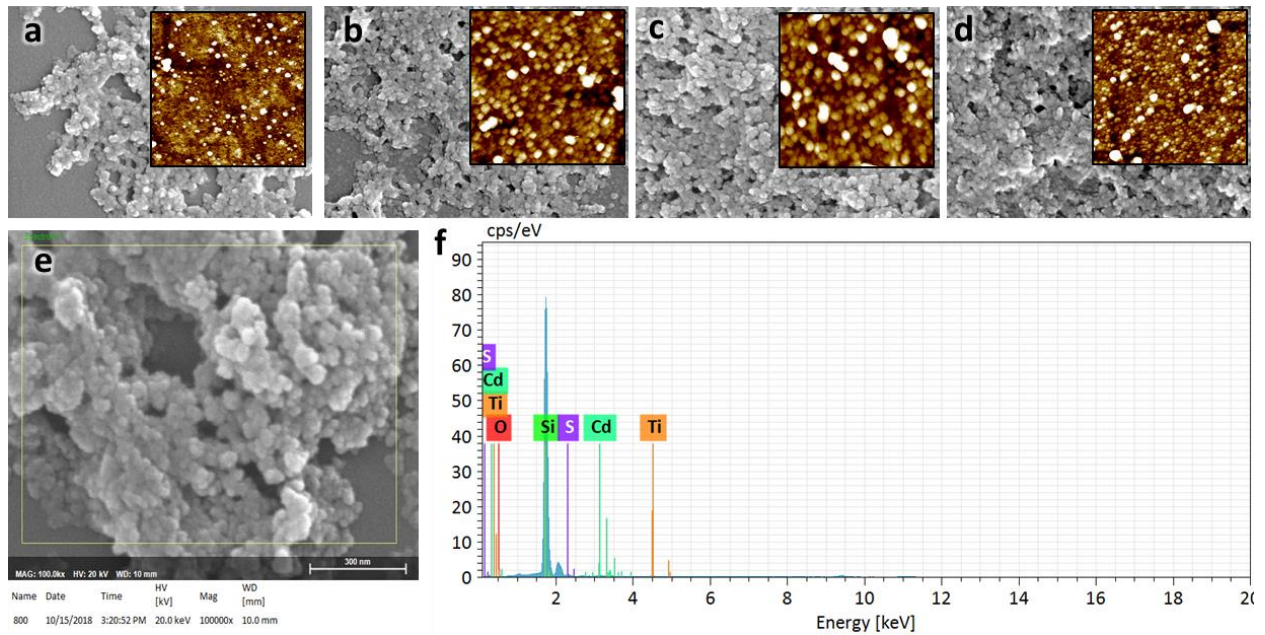


Figure 30 2D-scanning electron microscopic imaging of CdS-quantum dots deposited over TiO₂ deposited Si-substrate (a) without and with (b) ZnS, (c) SnS and (d) MoS₂ interfacial layers (inset shows 2D-images taken by Nanosurf Flex-AFM). Energy dispersive spectroscopy of standard TiO₂ deposited Si-substrate having CdS QDs. CdS QDs were deposited via successive ionic layer adsorption and reaction (SILAR) process.

The same trend in deposition of CdS QDs was reflected from FE-SEM images (Fig. 2a-d) where higher CdS QDs was observed in case of all ILs and optimal in case of MoS₂. Insets are showing the 2D-AFM imaging of each sample and affirm the effectuality of ALD ILs for enhanced deposition of CdS QDs. But as mentioned earlier, higher deposition may lead to detrimental charge carrier recombination inside QDs, we remained focused to separate between CdS QDs having more coverage, which are always expected to produce more light harvesting with lesser internal defects [10], [14]. Therefore, we further performed EDS-analysis for determination of the composition of all samples. In a typical EDS scan, we recorded the spectroscopic signals originating from TiO₂ (i.e., Ti and O), Si-substrate (Si mainly), and CdS (Cd and S). However, a peak existing at about 2 was neglected as it belonged to Pt which is an auxiliary component EDS-tested surfaces and introduced during the sample preparation for SEM.

Due to the limitation, all EDS maps are not presented here, however corresponding analysis is summarized in Fig. 4. We can directly see that amongst all three ILs, SnS sample reflected the maximum atomic percentage of Cd in it. Which is replication of the AFM trend where it had maximum roughness value of 29.77 nm. While ZnS resulted in lowest peak for Cd, as well as S showing lowest increase in the deposition of CdS QDs relative to TiO₂-deposited Si-substrate sample w/o IL (Fig. 3a). In case of MoS₂ IL, TiO₂-deposited Si-substrate additionally contrastingly showed highest peak for S, even higher than that of SnS having optimal Cd peak. It reflects that the signal of S is belonging to both ILs and CdS in all cases. This was why MoS₂ having two times higher presence of S in its stoichiometric film resulted highest peak, i.e. two sulfur atoms are bonded with each Mo in MoS₂, unlike ZnS and SnS. In literature [12], [14], a concomitant comparison of Cd and Ti in the form of Cd/Ti is often included to get rid of this confusion. Cd/Ti ratio direct defines the quantitative trend in the deposition of CdS QDs. It is evident that SnS IL avowed optimal value of ~3 for Cd/Ti, which roughly means that roughly 3 atoms were stacked over each Ti atom as a consequence of 5 cycles of SILAR deposition. Same

fact was evident from AFM where the Y-axis reached to a level of ~40 nm showing higher growth. However, in this comparison the most interesting fact existed between ZnS and MoS₂. Both ILs showed almost similar Cd/Ti values while AFM roughness value was higher for MoS₂ (17.62 > 7.8 nm) than ZnS. Even the surface roughness value for reference sample w/o IL remained higher than that for ZnS IL, while it had lower Cd/Ti ratio. These results depicted that the deposition of CdS over ZnS was superior in terms of coverage (i.e. nucleation) than all other samples.

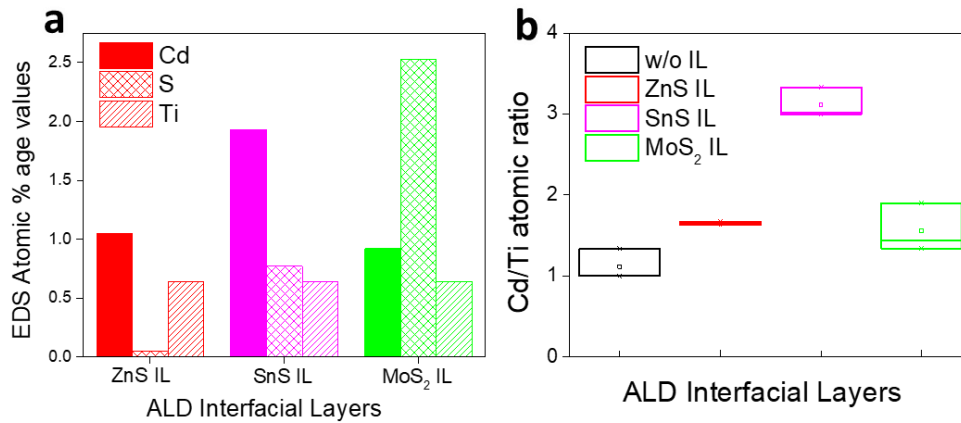


Figure 31 EDS-based (a) atomic percentage values of Cd, S and Ti over various ALD interfacial layers and the (b) consequent Cd/Ti ratio comparison showing the enhanced deposition of CdS QDs via SILAR

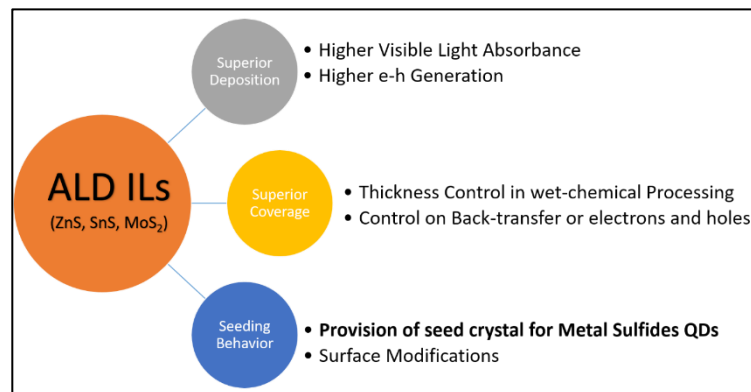


Figure 32 Various areas where ALD ILs can play influential role in devising the devices

As discussed earlier, the aim of the study was to analyze the deposition dynamics in-depth and to evaluate that which type of IL favors higher QDs deposition with more coverage; we deduced that ALD ZnS IL possesses beneficial role for deposition of CdS QDs and can prove valuable for various optoelectronic applications [15], [16] summarized in Fig. 5. However, we have applied ZnS IL for QDSCs successfully and the results will be reported elsewhere.

ACKNOWLEDGMENT

The authors are thankful to the Nanodevice Engineering Laboratory (NEL), Hanyang University South Korea for the provision of TiO₂-deposited Si-substrates and atomic layer deposition of ZnS, SnS and MoS₂.

REFERENCES

- [1] R. W. Johnson, A. Hultqvist, and S. F. Bent, "A brief review of atomic layer deposition: from fundamentals to applications," *Mater. Today*, vol. 17, no. 5, pp. 236–246, Jun. 2014, doi: 10.1016/j.mattod.2014.04.026.
- [2] K. E. Roelofs *et al.*, "Effect of Al₂O₃ Recombination Barrier Layers Deposited by Atomic Layer Deposition in Solid-State CdS Quantum Dot-Sensitized Solar Cells," *J. Phys. Chem. C*, vol. 117, no. 11, pp. 5584–5592, Mar. 2013, doi: 10.1021/jp311846r.
- [3] T. C. Li *et al.*, "Surface Passivation of Nanoporous TiO₂ via Atomic Layer Deposition of ZrO₂ for Solid-State Dye-Sensitized Solar Cell Applications," *J. Phys. Chem. C*, vol. 113, no. 42, pp. 18385–18390, Oct. 2009, doi: 10.1021/jp906573w.
- [4] K. Sridharan, E. Jang, Y. M. Park, and T. J. Park, "Superior Photostability and Photocatalytic Activity of ZnO Nanoparticles Coated with Ultrathin TiO₂ Layers through Atomic-Layer Deposition," *Chem. – Eur. J.*, vol. 21, no. 52, pp. 19136–19141, 2015, doi: 10.1002/chem.201502876.
- [5] N. P. Dasgupta, X. Meng, J. W. Elam, and A. B. F. Martinson, "Atomic Layer Deposition of Metal Sulfide Materials," *Acc. Chem. Res.*, vol. 48, no. 2, pp. 341–348, Feb. 2015, doi: 10.1021/ar500360d.
- [6] N. P. Dasgupta *et al.*, "Atomic Layer Deposition of Lead Sulfide Quantum Dots on Nanowire Surfaces," *Nano Lett.*, vol. 11, no. 3, pp. 934–940, Mar. 2011, doi: 10.1021/nl103001h.
- [7] N. Schneider, M. Bouttemy, P. Genevée, D. Lincot, and F. Donsanti, "Deposition of ultra thin CuInS₂ absorber layers by ALD for thin film solar cells at low temperature (down to 150 °C)," *Nanotechnology*, vol. 26, no. 5, p. 054001, Jan. 2015, doi: 10.1088/0957-4484/26/5/054001.
- [8] M. A. Basit, M. A. Abbas, E. S. Jung, J. H. Bang, and T. J. Park, "Improved light absorbance and quantum-dot loading by macroporous TiO₂ photoanode for PbS quantum-dot-sensitized solar cells," *Mater. Chem. Phys.*, vol. 196, pp. 170–176, Aug. 2017, doi: 10.1016/j.matchemphys.2017.03.057.
- [9] C. Ding *et al.*, "Understanding charge transfer and recombination by interface engineering for improving the efficiency of PbS quantum dot solar cells," *Nanoscale Horiz.*, vol. 3, no. 4, pp. 417–429, Jun. 2018, doi: 10.1039/C8NH00030A.
- [10] M. A. Abbas, M. A. Basit, T. J. Park, and J. H. Bang, "Enhanced performance of PbS-sensitized solar cells via controlled successive ionic-layer adsorption and reaction," *Phys. Chem. Chem. Phys.*, vol. 17, no. 15, pp. 9752–9760, Apr. 2015, doi: 10.1039/C5CP00941C.
- [11] M. A. Basit, M. A. Abbas, J. H. Bang, and T. J. Park, "Efficacy of In₂S₃ interfacial recombination barrier layer in PbS quantum-dot-sensitized solar cells," *J. Alloys Compd.*, vol. 653, pp. 228–233, Dec. 2015, doi: 10.1016/j.jallcom.2015.08.237.
- [12] M. A. Basit, M. A. Abbas, E. S. Jung, Y. M. Park, J. H. Bang, and T. J. Park, "Strategic PbS quantum dot-based multilayered photoanodes for high efficiency quantum dot-sensitized solar cells," *Electrochimica Acta*, vol. 211, pp. 644–651, Sep. 2016, doi: 10.1016/j.electacta.2016.06.075.
- [13] M. A. Basit *et al.*, "Enhanced PbS quantum dot loading on TiO₂ photoanode using atomic-layer-deposited ZnS interfacial layer for quantum dot-sensitized solar cells," *Mater. Chem. Phys.*, vol. 220, pp. 293–298, Dec. 2018, doi: 10.1016/j.matchemphys.2018.09.006.
- [14] F. U. Hassan, U. Ahmed, M. Muhyuddin, M. Yasir, M. N. Ashiq, and M. A. Basit, "Tactical modification of pseudo-SILAR process for enhanced quantum-dot deposition on TiO₂ and ZnO nanoparticles for solar energy applications," *Mater. Res. Bull.*, vol. 120, p. 110588, Dec. 2019, doi: 10.1016/j.materresbull.2019.110588.

- [15] M. I. Aziz, F. Mughal, H. M. Naeem, A. Zeb, M. A. Tahir, and M. A. Basit, "Evolution of photovoltaic and photocatalytic activity in anatase-TiO₂ under visible light via simplistic deposition of CdS and PbS quantum-dots," *Mater. Chem. Phys.*, vol. 229, pp. 508–513, May 2019, doi: 10.1016/j.matchemphys.2019.03.042.
- [16] E. Jang *et al.*, "Atomic layer deposition with rotary reactor for uniform hetero-junction photocatalyst, g-C₃N₄@TiO₂ core-shell structures," *RSC Adv.*, vol. 9, no. 57, pp. 33180–33186, Oct. 2019, doi: 10.1039/C9RA05958J.